Search for Heavy Majorana Neutrinos at the LHC

Dissertation
zur Erlangung des Doktorgrades
an der Fakultät für Mathematik, Informatik und Naturwissenschaften
Fachbereich Physik
der Universität Hamburg

vorgelegt von

Jonas Neundorf

Hamburg
2024

Gutachter der Dissertation	Prof. Dr. Krisztian Peters Prof. Dr. Gregor Kasieczka
Zusammensetzung der Prüfungskommission	Prof. Dr. Krisztian Peters Prof. Dr. Gregor Kasieczka Prof. Dr. Caren Hagner Prof. Dr. Sven-Olaf Moch PD Dr. Roman Kogler
Vorsitzender der Prüfungskommission Datum der Disputation	Prof. Dr. Sven-Olaf Moch 13. 3. 2024
Vorsitzender des Fach-Promotionsausschusses Physik Leiter des Fachbereichs Physik Dekan der Fakultät MIN	Prof. Dr. Markus Drescher Prof. Dr. Wolfgang Parak Prof. Dr.-Ing. Norbert Ritter

Abstract

The origin of neutrino masses is one of the open questions of particle physics. This thesis presents work on the high-energy equivalent of neutrinoless double-beta decay. Two phenomenological studies investigate sensitivity to the $\mu^{\pm}\mu^{\pm}jj$ final state at the LHC. An extensive study based on a fast simulation of the ATLAS detector is presented. Results of this study are interpreted in the context of the Type I Seesaw model and as limits on the Weinberg operator. Assuming $300\,\mathrm{fb}^{-1}$ of data collected at $\sqrt{s} = 13\,\mathrm{TeV}$, LHC experiments could probe heavy Majorana neutrinos with masses exceeding 20 TeV, while being more sensitive than previous searches for masses above approximately 700 GeV. LHC experiments could be significantly more sensitive than the NA-62 experiment towards the Weinberg operator, but would not be able to compete with indirect limits from neutrino oscillations.

Following up on this, a search for the Type I Seesaw model and the Weinberg operator in the $\mu^{\pm}\mu^{\pm}jj$ final state with the ATLAS experiment is presented. In $140\,\mathrm{fb}^{-1}$ of data collected at $\sqrt{s} = 13\,\mathrm{TeV}$, no significant excess above the SM expectation is found. Upper limits at 95 % confidence level are placed on the muon neutrino – heavy neutrino mixing element $|V_{\mu N}|^2$ as a function of the heavy Majorana neutrino mass m_N as well as on the effective Majorana mass $|m_{\mu\mu}|$.

The LHC and its experiments will be upgraded to increase luminosity by approximately a factor of 10. For this, the ATLAS experiment will receive a new tracking detector, the Inner Tracker (ITk). New sensor modules are subject to an extensive quality control procedure, which includes thermal cycling. This thesis presents tests of the prototype of the thermal cycling setup used for endcap modules as well as work on the automation of the test setup.

Zusammenfassung

Eines der großen Rätsel der Teilchenphysik ist der Ursprung der Neutrinomassen. In dieser Dissertation wird dieses Rätsel im hochenergetischen Äquivalent des neutrinolosen Doppelbetazerfalls untersucht. Zwei phänomenologische Studien erkunden die Sensitivität der LHC-Experimente auf neue Physik im $\mu^{\pm}\mu^{\pm}jj$-Endzustand. Als Teil dieser Studien wird eine Analyse basierend auf einer schnellen Simulation des ATLAS-Experiments präsentiert. Ihre Ergebnisse werden im Rahmen des Typ I Seesaw-Modells und des Weinberg-Operators interpretiert. LHC-Experimente könnten mit einem Datensatz von $300\,\mathrm{fb}^{-1}$ bei $\sqrt{s} = 13\,\mathrm{TeV}$ schwere Majorana-Neutrinos mit Massen m_N jenseits von 20 TeV untersuchen. Für Massen größer als etwa 700 GeV ist der untersuchte Endzustand sensitiver als bisherige Suchen. Auch der Weinberg-Operator könnte wesentlich präziser untersucht werden als durch die aktuellen Messungen des NA-62-Experiments, allerdings nicht präzise genug um einen Vergleich mit indirekten Messungen durch Neutrino-Oszillationen zu ziehen.

Im Hauptteil wird eine Suche nach dem Typ I Seesaw-Modell und dem Weinberg-Operator im $\mu^{\pm}\mu^{\pm}jj$-Endzustand mit dem ATLAS-Experiment präsentiert. Der $140\,\mathrm{fb}^{-1}$ große Datensatz bei $\sqrt{s} = 13\,\mathrm{TeV}$ enthält keine signifikante Abweichung von der Standardmodellvorhersage. Daher werden Ausschlussgrenzen sowohl auf den Myonneutrino–schweres Neutrino-Mischungsparameter $|V_{\mu N}|^2$ als Funktion der Masse des schweren Majorananeutrinos m_N als auch auf die effektive Majoranamasse $|m_{\mu\mu}|$ bestimmt.

Der LHC und die LHC-Experimente werden umfangreich modernisiert, um die Luminosität um ungefähr den Faktor 10 zu erhöhen. Als Teil dieser Modernisierung wird das ATLAS-Experiment einen neuen Spurdetektor, den Inner Tracker (ITk), erhalten. Neue Sensormodule für diesen Detektor werden einer umfangreichen Qualitätssicherung unterzogen, wozu Untersuchungen bei sich zyklisch ändernden Temperaturen gehören. Diese Dissertation enthält Studien zur Inbetriebnahme des Prototypen des Teststandes zur Durchführung dieser Untersuchungen bei Endkappen-Module sowie zur Automatisierung dieses Teststandes.

Eidesstattliche Versicherung

Hiermit versichere ich an Eides statt, die vorliegende Dissertationsschrift selbst verfasst und keine anderen als die angegebenen Hilfsmittel und Quellen benutzt zu haben.

Hamburg, den 28. März 2024

Contents

List of Tables

List of Figures

1. Introduction

With the development of particle accelerators in the middle of the twentieth century, the field of particle physics emerged and developed rapidly. Newer accelerators reaching higher collision energies were able to produce a plethora of new particles, which we would now classify as mesons and baryons. The understanding of the theoretical foundations of this *particle zoo* evolved rapidly. In 1964, the quark model, albeit only with the three quarks known at that time, was proposed to bring order to the particle zoo that we still use today [1, 2, 3]. Similarly, the description of the fundamental forces developed quickly at that time. To unify the description of the electromagnetic and the weak forces, the W and Z bosons (and the photon) were proposed in the same decade [4, 5]. A while later, in 1973, the third quark generation was predicted to exist [6]. Perhaps a bit surprising to the modern reader is that the Higgs mechanism is as old as the quark model, having been developed in 1964, independently by three groups [7, 8, 9].

These theoretical predictions that are now part of the *Standard Model* of particle physics (SM) have long been a guideline for experiments. The W and Z bosons were discovered in 1983 [10, 11, 12], and after the top quark discovery in 1995 [13, 14], all quarks were found. With the discovery of the Higgs boson in 2012 [15, 16], nearly fifty years after it was proposed, the SM was finally complete.

Various precision measurements of the SM parameters have found good agreement with their values predicted from theory. However, we have also made many observations that cannot be explained with the standard model. Perhaps the most famous of these is *Dark Matter* (DM). When observing faraway galaxies, astronomers found that the distribution of the visible mass[1] does not explain at all the rotational speeds of the stars around their galactic centre [17]. A popular explanation for these is the presence of a new kind of particle that only interacts very weakly. Searches for various DM candidates are performed both at particle colliders and in purpose-built experiments.

Perhaps the most compelling sign for *physics beyond the SM* (BSM) was the observation of neutrino oscillations. Exactly as the charged leptons, neutrinos come in three different flavour: ν_e, ν_μ and ν_τ. When measuring neutrinos at different distances from their source, the flavour composition was found to be different. The observed neutrinos oscillate between different flavour states [18]. The explanation for these observations is that the flavour eigenstates we measure are different from the mass eigenstates [19]. From the frequency of the neutrino oscillations, it is then possible to determine the mass differences of the three neutrino mass states. We can now safely say that at least two of the three neutrino types observed in nature have a mass. Measurements of the KATRIN experiments have set an upper limit to the neutrino masses [20]. However, it is not yet

[1] Which is concentrated mostly in the stars.

clear whether one of the three types is massless or which of the three is the lightest and which the heaviest. These measurements are in direct conflict with the SM as the SM predicts neutrinos to be massless.

A popular way to explain neutrino masses is the addition of a set of heavy, sterile[2] neutrinos to the SM. In the *Seesaw* mechanism, they are of Majorana nature, i. e. their own antiparticle. They mix with the massless SM neutrinos and generate two sets of neutrinos masses: The light ones we observe in nature and heavy ones at a yet unknown mass scale. The Majorana nature of these sterile neutrinos would allow for processes that violate lepton number conservation, thus having a signature distinctly different from SM physics.

For example, two simultaneous β decays in the same nucleus could occur without an outgoing neutrino if there were Majorana neutrinos. Currently, the best limits on these *neutrinoless double-β decays* ($0\nu\beta\beta$) come from the GERDA experiment [21, 22, 23]. However, the main limitation of GERDA and similar experiments is that due to the low energy in nuclear decays, they are only sensitive to couplings between the Majorana neutrinos and electrons. The underlying theories allow also couplings to muons and τ leptons.

Accessing these heavier leptons is possible only at colliders. Currently, the largest collider is the *Large Hadron Collider* (LHC), colliding two proton beams with an energy of 6.5 TeV each, with four experiments hosted around its ring. Two of them, ATLAS and CMS, are general-purpose detectors suitable for a variety of searches and measurements. The other two, LHCb and ALICE, are specialised for the study of bottom quarks and heavy ion collisions, respectively.

This thesis covers three topical parts. It presents two phenomenological studies showing that the LHC is sensitive to $0\nu\beta\beta$-like processes: In these processes, heavy Majorana neutrinos are created in the t-channel, which allows very high masses of $\mathcal{O}(20$ TeV) to be probed. As a comparison, previous searches were considering only s-channel production, which is sensitive only to masses of $\mathcal{O}(1$ TeV). Following that, the author performed a search with the ATLAS experiment for Majorana neutrinos in final states with two muons of the same electric charge. For the first time in ATLAS, such a search has been performed in the t-channel. But without a functioning detector, such searches are not possible. The third part of this thesis then presents the author's contribution to the ATLAS detector upgrade. In particular, work on the characterisation and automation of a thermoelectrical test stand is shown. It will be used as part of the quality control during the production of new tracking sensors for the High-Luminosity LHC era.

1.1. Author's contributions

Particle physics is a group endeavour – work is performed both in small teams and in huge collaborations that involve scientiest from many different countries. The ATLAS collaboration has 3000 members that contribute to the maintenance, operation and upgrade of the experiment as well as to event reconstruction and calibration of the detector.

[2] I. e. not interacting with the SM gauge bosons.

These tasks are carried out by dedicated working groups inside the collaboration and this thesis relies on the work performed in these groups.

The author has contributed to the upgrade of the detector by working on the thermal cycling test setup for new endcap detector modules. In close collaboration with the engineering team of the DESY ATLAS group, the author planned and conducted tests of the prototype. Additionally, the author wrote automation software for the test setup.

The author worked on a phenomenological study that explored the potential for LHC searches for the Type I Seesaw model and Weinberg operator. He made the first next-to-leading order calculation of the t-channel cross section of the Type I Seesaw model. The author then designed an analysis using a fast simulation of a LHC detector. The author defined a set of cuts and conducted a statistical analysis to determine the sensitivity of LHC experiments towards the Type I Seesaw model and the Weinberg operator. The results have been published in *Physical Review D* [24, 25].

The author was the main contributor to a search for the aforementioned processes with the ATLAS experiment. On this search, the author generated simulations of the signal models and designed control and validation regions for the main backgrounds. He made major contributions to the statistical analysis of this search, which was subsequently completed by two other doctoral researchers, Benjamin Wilson and Gareth Bird. The author has also contributed to the analysis software framework and the functional form estimate of the fake lepton background. This search was published in *European Physical Journal C* [26].

2. Theoretical Background

Particle physics investigates phenomena that happen at subatomic distances and high energies. These phenomena are described in the language of *quantum field theory* (QFT). All currently known particles and their interactions are described by the Standard Model (SM), which will be outlined in Section 2.1. However, some observations cannot be explained within the SM and are instead by addressed by new theories. Section 2.2 will give an overview of such new theories that try to explain the origin of neutrino masses.

2.1. The Standard Model

The SM describes all currently known elementary particles and their interactions through the electromagnetic, weak and strong forces. The fourth fundamental force, gravity, does not yet have a QFT description and thus cannot be combined with the SM. However, gravity is also many orders of magnitude weaker than any of the other three forces[1], thus its influence can be safely neglected.

2.1.1. Particles of the Standard Model

Particles can be grouped into two categories based on their spin. *Bosons* have integer spin. Those with spin 1, the *gauge bosons*, mediate the fundamental forces. The *photon* (γ) is a massless, electrically neutral particle that mediates the electromagnetic interaction. Similarly, the gluon (g) of the strong interaction is also massless, but, due to its colour charge, can self-interact. Finally, the $W^{\pm}$ and Z bosons with masses of 80.39 GeV and 90.19 GeV, respectively, mediate the weak interaction. A single scalar (i. e. spin zero) boson, the Higgs boson, exists in the SM and is responsible for the electroweak symmetry breaking.

Then, *fermions* have spin $\frac{1}{2}$ and are modelled as spinor fields. They make up all known matter and can be grouped further into two categories. *Leptons* take part only in the electroweak interaction, while *quarks* have a colour charge and thus also take part in the strong interaction. Both are organised into three generations, where each generation has higher mass than the previous generation, but the same electric and colour charge as well as quantum numbers. Anti-fermions have the same mass, but opposite charge and chirality.

[1] The Coulomb force acting on two protons 1 fm apart is $F_{\text{Coulomb}} = \frac{1}{4\pi\epsilon_0}\frac{e^2}{r^2} = 230\,\text{N}$, while their gravitational attraction is merely $F_{\text{G}} = G\frac{m_{\text{p}}^2}{r^2} = 1.9 \cdot 10^{-34}\,\text{N}$.

Quarks are either up-type with an electric charge[2] of $+\frac{2}{3}$ or down-type with a charge of $-\frac{1}{3}$. The up (u), charm (c) and top (t) quark form the former group, while the down (d), strange (s) and bottom (b) quark form the latter. Each quark carries a colour charge[3] of either red (r), green (g) or blue (b). Anti-quarks carry an anti-colour, both are denoted by decorating the symbol with a $^-$. Quarks with right-handed chirality have weak isospin $I_3 = 0$ and form a singlet

$$u_R, d_R, c_R, s_R, b_R, t_R. \tag{2.1}$$

Left-handed quarks with weak isospin $I_3 = +\frac{1}{2}$ form an isospin doublet

$$\begin{pmatrix} u \\ d' \end{pmatrix}_L, \begin{pmatrix} c \\ s' \end{pmatrix}_L, \begin{pmatrix} t \\ b' \end{pmatrix}_L \tag{2.2}$$

where the q' quarks denote the eigenstates of the weak interaction. They are obtained from the mass eigenstates via the *Cabibbo-Kobayashi-Maskawa* (CKM) matrix

$$\begin{pmatrix} d' \\ s' \\ b' \end{pmatrix} = \begin{pmatrix} V_{ud} & V_{us} & V_{ub} \\ V_{cd} & V_{cs} & V_{cb} \\ V_{td} & V_{ts} & V_{tb} \end{pmatrix} \cdot \begin{pmatrix} d \\ s \\ b \end{pmatrix}. \tag{2.3}$$

Note that free quarks have never been observed. This is due to *colour confinement*: No object with a colour charge can propagate as a free particle. Assuming e.g. a quark-antiquark pair, as the distance between the two increases, so does the QCD potential. At some point, it is energetically more favourable to form a new $q\bar{q}$ pair. Therefore, quarks are observed only in bound states, the *hadrons*. Hadrons that consist of a $q\bar{q}$ pair are called *mesons*, while a qqq bound state is known as a *baryon*.

The SM also contains three leptons with an electric charge of -1, the electron (e), muon (μ) and tau (τ) and three corresponding neutral leptons, the electron neutrino (ν_e), muon neutrino (ν_μ) and tau neutrino (ν_τ). Again, they are organised by chirality into left-handed weak isospin doublets with $I_3 = +\frac{1}{2}$

$$\begin{pmatrix} e \\ \nu_e \end{pmatrix}_L, \begin{pmatrix} \mu \\ \nu_\mu \end{pmatrix}_L, \begin{pmatrix} \tau \\ \nu_\tau \end{pmatrix}_L \tag{2.4}$$

and right-handed singlets with weak isospin $I_3 = 0$

$$e_R, \mu_R, \tau_R. \tag{2.5}$$

The SM does not predict the existence of right-handed neutrinos.

[2]By convention, electric charges are given as multiples of the positron charge.

[3]Note that *colour* is just a name for this degree of freedom of the quarks, it shares nothing with the colours from daily life except for the name.

2.1.2. Forces and Bosons

Out of the four fundamental forces in nature, three are part of the SM and will be introduced in this section. A description of forces should be valid no matter where the measurement is conducted, i. e. it should be *gauge invariant*. The theory should be invariant both under *global transformations* that affect all points in space in the same way as well as under *local transformations* that affect different points in space differently. All forces in the SM are required to be gauge invariant.

Electromagnetism and the Photon

The electromagnetic interaction is described by the theory of Quantum Electrodynamics (QED). It can describe the movement of a fermion $\psi(x)$ according to the *Dirac equation* $(i\gamma^\mu\partial_\mu - m)\psi(x) = 0$, which can be derived from the Lagrangian

$$\mathcal{L}_{\text{Dirac}} = \bar{\psi}(\gamma^\mu\partial_\mu - m)\psi. \tag{2.6}$$

Here, γ^μ are the Dirac matrices and $\bar{\psi} = \psi^\dagger\gamma^0$ denotes the adjoint spinor. QED should be gauge invariant under $U(1)$ transformations, i. e. a simple phase shift

$$\psi(x) \to \psi' = e^{i\alpha(x)}\psi(x). \tag{2.7}$$

However, the Lagrangian of Equation (2.6) is not invariant under this phase shift:

$$\begin{aligned}
\mathcal{L}_{\text{Dirac}} \to \mathcal{L}'_{\text{Dirac}} \quad & = e^{-i\alpha(x)}\bar{\psi}(x)(\gamma^\mu\partial_\mu - m)e^{i\alpha(x)}\psi(x) \\
& = e^{-i\alpha(x)}\bar{\psi}(x)\gamma^\mu\partial_\mu e^{i\alpha(x)}\psi(x) - e^{-i\alpha(x)}\bar{\psi}(x)me^{i\alpha(x)}\psi(x) \\
& = \bar{\psi}(x)\gamma^\mu\partial_\mu\psi(x) + \bar{\psi}(x)\gamma^\mu\partial_\mu\alpha(x)e^{i\alpha(x)}\psi(x) + m\bar{\psi}(x)\psi(x) \\
& = \mathcal{L}_{\text{Dirac}} + \bar{\psi}(x)\gamma^\mu\partial_\mu\alpha(x)e^{i\alpha(x)}\psi(x)
\end{aligned}$$

The invariance is violated by the derivative term. It needs to be replaced by the *covariant derivative*, which behaves properly under $U(1)$ transformations and thus preserves gauge invariance:

$$D_\mu^{\text{QED}} = \partial_\mu + iqA_\mu(x). \tag{2.8}$$

Here, a field A is introduced that is required to transform as

$$A_\mu \to A'_\mu = A_\mu - \frac{1}{q}\partial_\mu\alpha(x) \tag{2.9}$$

where $\alpha(x)$ is the same transformation as in (2.7). The parameter q describes the coupling strength between the field A and the fermion ψ. In QED, the coupling strength q is simply the electric charge of the fermion and the field A describes the photon. The Lagrangian of the photon field is given by

$$\mathcal{L}_{\text{photon}} = -\frac{1}{4}F_{\mu\nu}F^{\mu\nu} = -\frac{1}{4}(\partial_\mu A_\nu - \partial_\nu A_\mu)(\partial^\mu A^\nu - \partial^\nu A^\mu). \tag{2.10}$$

Adding a mass term $mA_\mu A^\mu$ would break gauge invariance, which shows that the photon has to be a massless particle. Combining (2.6) and (2.10) gives the Lagrangian of QED:

$$\begin{aligned}\mathcal{L}_{\text{QED}} &= \mathcal{L}_{\text{Dirac}} + \mathcal{L}_{\text{photon}} \\ &= \bar{\psi}(\gamma^\mu D_\mu^{\text{QED}} - m)\psi - \frac{1}{4}F_{\mu\nu}F^{\mu\nu}. \end{aligned} \tag{2.11}$$

Strong Interaction: The Gluon

Quarks are also fermions and thus also described by the Dirac Lagrangian (Equation (2.6)). In addition to an electric charge, they carry a *colour* charge, which can be either *red*, *green* or *blue* for quarks, antiquarks carry a respective anticolour. A change of the colour state, e. g. from *red* to *blue*, should not change the strength of the strong interaction. In other words, the Lagrangian of *Quantum Chromodynamics* (QCD) should be invariant under a transformation

$$\psi(x) \to \psi'(x) = e^{\frac{1}{2}ig_S\alpha^a(x)\lambda^a}\psi(x). \tag{2.12}$$

Here, λ^a are the eight Gell-Mann matrices that are the generators of the $SU(3)$ symmetry group. The requirement of gauge invariance necessitates the introduction of a covariant derivative

$$D_\mu^{\text{QCD}} = \partial_\mu + i\frac{1}{2}ig_S\lambda^a G_\mu^a. \tag{2.13}$$

which introduces the gluon field G_μ^a. It has to transform as

$$G_\mu^k \to G_\mu'^k = G_\mu'^k - \partial_\mu\alpha_k - g_S f_{ijk}\alpha_i G_\mu^j. \tag{2.14}$$

The Gell-Mann matrices do not commute, but rather obey the commutation relation $[\lambda_i, \lambda_j] = 2if_{ijk}\lambda_k$ where f_{ijk} denotes the *structure constants* of $SU(3)$. This non-commutation also leads to an additional term in the field strength tensor

$$G_{\mu\nu}^i = \partial_\mu G_\nu^i - \partial_\nu G_\mu^i + g_S f_{ijk} G_\mu^j G_\nu^k. \tag{2.15}$$

From the last term of $G_{\mu\nu}^i$, it can be seen that gluons carry a colour charge and can interact with each other. Combining these pieces, the Lagrangian of QCD is

$$\mathcal{L}_{\text{QCD}} = \sum_f \bar{\psi}^f(\gamma^\mu D_\mu^{\text{QCD}} - m)\psi^f - \frac{1}{4}G_{\mu\nu}^i G_i^{\mu\nu}. \tag{2.16}$$

Here, the sum is over all quark flavours. The addition of a gluon mass term would break gauge invariance again, therefore the gluon also has to be a massless particle.

Electroweak Interaction

Unlike QED or QCD, the weak interaction breaks parity symmetry. Thus, mirror-asymmetry needs to be an integral part of the theory. The $W^\pm$ bosons of the weak

interaction only couple to left-handed particles and right-handed anti-particles, as selected by the chirality projection operator

$$\psi_{L/R} = \frac{1}{2}(1 \mp \gamma^5)\psi. \tag{2.17}$$

The weak interaction is invariant under local $SU(2)$ phase transformations. The $SU(2)$ group is generated by the Pauli spin matrices and gives rise to the weak isospin I_W. Due to the invariance requirement, three W boson fields W_μ^k with $k = 1, 2, 3$ are present in this theory. It would be tempting to identify W_μ^3 with the neutral Z boson. However, the W only couples to left-handed particles, unlike the Z boson. A solution was proposed by Glashow, Salam and Weinberg [4, 5, 27] in the form of electroweak unification. The $U(1)$ symmetry of QED is replaced with a new $U_Y(1)$ symmetry, where Y is the weak hypercharge. This theory is invariant under transformations

$$\psi(x) \to \psi'(x) = \exp[ig'\frac{Y}{2}\zeta(x)]\psi(x) \tag{2.18}$$

and introduces a new gauge field B_μ that couples to the weak hypercharge. The observed $W^\pm$ and Z bosons as well as the photon are then linear combinations of these four gauge fields. The definition of the neutral bosons makes use of the *Weinberg angle* θ_W

$$\begin{pmatrix} W_\mu^+ \\ W_\mu^- \\ Z_\mu \\ A_\mu \end{pmatrix} = \begin{pmatrix} \frac{1}{\sqrt{2}} & -\frac{i}{\sqrt{2}} & 0 & 0 \\ \frac{1}{\sqrt{2}} & \frac{i}{\sqrt{2}} & 0 & 0 \\ 0 & 0 & \cos\theta_W & -\sin\theta_W \\ 0 & 0 & \sin\theta_W & \cos\theta_W \end{pmatrix} \cdot \begin{pmatrix} W_\mu^{(1)} \\ W_\mu^{(2)} \\ W_\mu^{(3)} \\ B_\mu \end{pmatrix}. \tag{2.19}$$

The Lagrangian for the electroweak interaction includes only the fermion kinetic term and gauge boson interaction terms

$$\mathcal{L}_{\mathrm{EW}} = \bar{\psi} D_\mu \psi - \frac{1}{4} W_{k\mu\nu} W_k^{\mu\nu} - \frac{1}{4} B_{\mu\nu} B^{\mu\nu}. \tag{2.20}$$

Here, the covariant derivative

$$D_\mu = \partial_\mu - ig\frac{\sigma_k}{2}W_\mu^k - ig'\frac{Y^W}{2}B_\mu \tag{2.21}$$

is required to preserve gauge invariance. The field tensors are

$$\begin{aligned} W_{k\mu\nu} &= \partial_\mu W_{k\nu} - \partial_\nu W_{k\mu} + g\epsilon_{klm} W_{l\nu} W_{m\nu} \\ B_{\mu\nu} &= \partial_\mu B_\nu - \partial_\nu B_\mu. \end{aligned}$$

Electroweak Symmetry Breaking

The Lagrangian of the electroweak interaction would loose its gauge invariance by adding a mass term. However, the $W^\pm$ and Z bosons as well as quarks and charged leptons have been measured to have a mass. The boson masses are acquired from a scalar

field through the mechanism of electroweak symmetry breaking, also known as Higgs mechanism. Assume a complex $SU(2)$ doublet scalar field

$$\phi = \begin{pmatrix} \phi^+ \\ \phi^0 \end{pmatrix} = \frac{1}{\sqrt{2}} \begin{pmatrix} \phi_1 + i\phi_2 \\ \phi_3 + i\phi_4 \end{pmatrix}. \tag{2.22}$$

Here, ϕ^+ is a field with a positive electric charge and ϕ^0 is a neutral field. This field has the Lagrangian

$$\mathcal{L}_{\text{Higgs}} = (D_\mu \phi)^\dagger (D_\mu \phi) - V(\phi) \tag{2.23}$$

with the potential

$$V(\phi) = \mu^2 \phi^\dagger \phi + \lambda (\phi^\dagger \phi)^2 \tag{2.24}$$

and the electroweak covariant derivative D_μ defined in Equation (2.21). A ground state of this potential can only exist for $\lambda > 0$. However, μ^2 can be either positive or negative If it were positive, the field ϕ would describe a scalar particle with mass μ and a four-point self-interaction. On the other hand, if μ^2 is negative, $\mu^2 \phi^\dagger \phi$ cannot be interpreted as a mass term. Then, the potential will have its minimum at $\phi^\dagger \phi = \frac{-\mu^2}{2\lambda} =: \frac{v^2}{2}$, where v is the vacuum expectation value (VEV) of the Higgs field. While this is an infinite set of minima, the ground state is chosen to be $\phi = \frac{1}{\sqrt{2}} \begin{pmatrix} 0 \\ v \end{pmatrix}$ and then the Higgs field is expanded around this minimum

$$\phi(x) = \frac{1}{\sqrt{2}} \begin{pmatrix} 0 \\ v + h(x) \end{pmatrix}. \tag{2.25}$$

By choosing the *unitary gauge*, the other three components ϕ_1, ϕ_2, ϕ_4 of Equation (2.22) that describe massless fields are absorbed by the weak gauge bosons. This allows to write the Lagrangian of the Higgs field as

$$\mathcal{L}_{\text{Higgs}} = (D_\mu \phi)^\dagger (D_\mu \phi) - \mu^2 h^2 - \lambda v h^3 - \frac{1}{4} \lambda h^4. \tag{2.26}$$

Inserting the definition of the covariant derivative D_μ of the electroweak interaction will result in mass terms for the electroweak bosons. Their masses depend only on their couplings to the Higgs field g_W, g' and the VEV v:

$$\begin{aligned} m_W &= \frac{1}{2} g_W v \\ m_Z &= \frac{v}{2} \sqrt{g_W^2 + g'^2} \\ m_A &= 0. \end{aligned}$$

The ratio of the coupling strengths $\frac{g'}{g_W} = \tan \theta_W$ connects back to the definition of the fields in Equation (2.19).

In a similar way, fermion masses are generated by the Yukawa coupling between fermion field and the Higgs field:

$$\mathcal{L}_{\text{Yukawa}} = \sum_f -g_f (\bar{\psi}_L^f \phi \psi_R^f + \bar{\psi}_R^f \bar{\phi} \psi_L^f). \tag{2.27}$$

Here, the sum is over all fermion generations. Note that for a fermion to have a mass, it needs to have both a left- and a right-handed component. The Yukawa coupling g_f is a free parameter and determined from the observed fermion masses.

$$g_f = \sqrt{2}\frac{m_f}{v}. \tag{2.28}$$

2.1.3. Summary of the Standard Model

The Lagrangian of the SM is the sum of its four constituent Lagrangians introduced in the previous section.

$$\mathcal{L}_{\text{SM}} = \mathcal{L}_{\text{QCD}} + \mathcal{L}_{\text{EW}} + \mathcal{L}_{\text{Higgs}} + \mathcal{L}_{\text{Yukawa}} \tag{2.29}$$

This Lagrangian is invariant under transformations of the SM gauge group SU(3) $\times$ $SU(2) \times U(1)$. It is described by eighteen free parameters.

- The Yukawa couplings g_f of the six quarks and three charged leptons.
- Three coupling constants g_S, g, g' that determine the strength of the gauge interactions.
- Mass m_h and VEV v of the Higgs field.
- The CKM matrix can be parametrised by four parameters.

All known elementary particles and their interactions are described by the SM and its eighteen parameters.

2.1.4. Open Questions of Particle Physics

The predictions of the SM have been confirmed in multiple experiments (see e. g. [28, 29]). However, several phenomena have been observed that cannot be explained within the SM. Among the most pressing open questions are

- **the origin of neutrino masses.** Neutrino flavour oscillations have been observed by several experiments [18, 30, 31, 32, 33]. They arise from mass differences between the three different types of neutrinos – which shows that at least two of the three neutrinos observed in nature have a mass. However, neutrinos should be massless according to the SM.
- **the baryon asymmetry of the universe.** The universe as we know it today contains significantly more matter than antimatter. In the SM, several processes violate the CP symmetry. However, the currently known CP violating processes are not enough to explain the abundance of matter in the universe.

- **the nature of Dark Matter.** Measurements of the rotations speeds of stars in many different galaxies have shown that these do not agree with the visible mass distributions. Currently, the best explanation is the existence of a class of particles without electromagnetic interactions, the *Dark Matter* (DM). The only known particle that fits this description is the neutrino. However, their mass is way too small to create the amount of DM needed to explain the observations. In a similar vein, some *Dark Energy* is required to explain the structure of galaxy clusters.

- **Gravity.** The SM describes only three of the four fundamental forces. Currently, there is no quantum field theory of gravity.

2.2. Neutrino Masses

Neutrinos are particles that take part in neither the strong nor the electromagnetic interaction. They do take part in the weak interaction, which couples only to left-handed particles and right-handed anti-particles. If a right-handed neutrino existed, it would be *sterile*, i. e. it would not take part in any SM gauge interaction. However, the SM describes all known interactions of particles, thus it does not contain any sterile neutrinos.

Fermion masses are generated via the Yukawa coupling (Equation (2.27)). It couples the left-handed lepton doublets with the right-handed lepton singlets. This coupling leads to a mass term for charged leptons after spontaneous symmetry breaking. But since there are no right-handed neutrinos in the SM, they do not have a Yukawa coupling. Therefore, there is no mass term for them and neutrinos are massless particles in the SM.

However, the observation of neutrino oscillations has shown that at least two of the three neutrinos have a mass. Therefore, this section will briefly introduce the relation between neutrino oscillations and neutrino masses and then introduce some models that try to explain the origin of neutrino masses.

2.2.1. Neutrino Oscillations

Similar to the case of the quarks (cf. Section 2.1.1), the weak interaction eigenstates of the neutrinos $(\nu_e, \nu_\mu, \nu_\tau)$ are different from the mass eigenstates ν_1, ν_2, ν_3. The weak interaction eigenstates are obtained by a rotation from the mass eigenstates.

It has been observed that the weak eigenstate of a neutrino is not constant, but changes along its propagation. For example, a ν_e that is created at some point in space-time may be measured as a ν_μ at a different point with a probability $P(\nu_e \to \nu_\mu)$. In a simplified model with only two flavours ν_e, ν_μ and two mass eigenstates ν_1, ν_2, the mass eigenstates need to be rotated by an angle θ_{12} to obtain a ν_e The time evolution of this state is given as

$$|\psi(\mathbf{x}, t)\rangle = \cos\theta_{12}|\nu_1\rangle e^{-ip_1 x} + \sin\theta_{12}|\nu_2\rangle e^{-ip_2 x}. \tag{2.30}$$

Here, p_1 and p_2 are the four-momenta of the respective mass eigenstates. The phase in the exponent can alternatively be expressed as a function of the propagation distance L and time T

$$\phi_i = p_i x = E_i T - \mathbf{p}_i L. \tag{2.31}$$

Using Equation (2.30), the probability of a change of neutrino flavour is found to be

$$P(\nu_e \to \nu_\mu) = \sin^2(2\theta_{12}) \sin^2\left(\frac{\Delta\phi_{12}}{2}\right). \tag{2.32}$$

Assuming that the momentum of the two mass eigenstates is identical ($p_1 = p_2 = p$), the phase difference can be expressed as[4]

$$\Delta\phi_{12} \approx \frac{m_1^2 - m_2^2}{2p} \cdot L \tag{2.33}$$

Since neutrinos propagate effectively at the speed of light, $T \approx L$ is assumed in natural units. With $p = E_\nu$, the oscillation probability can be written as

$$P(\nu_e \to \nu_\mu) = \sin^2(2\theta_{12}) \sin^2\left(\frac{(m_1^2 - m_2^2)L}{4E_\nu}\right). \tag{2.34}$$

The amplitude of the flavour oscillation depends on the mixing angle θ_{12}, whereas the oscillation period depends on the difference of the squared masses $m_1^2 - m_2^2$. For small mass differences, an effect of neutrino oscillations is visible only over large distances.

In the three-flavour case, the rotation from the mass to the weak eigenstates is described by the *Pontecorvo-Maki-Nakagawa-Sakata* (PMNS) *matrix*.

$$\begin{pmatrix} \nu_e \\ \nu_\mu \\ \nu_\tau \end{pmatrix} = \begin{pmatrix} U_{e1} & U_{e2} & U_{e3} \\ U_{\mu 1} & U_{\mu 2} & U_{\mu 3} \\ U_{\tau 1} & U_{\tau 2} & U_{\tau 3} \end{pmatrix} \begin{pmatrix} \nu_1 \\ \nu_2 \\ \nu_3 \end{pmatrix} \tag{2.35}$$

The PMNS matrix is a complex unitary 3×3 matrix, which can be parametrised by three real angles θ_{ij} and a complex phase δ.

$$U_{\text{PMNS}} = \begin{pmatrix} 1 & 0 & 0 \\ 0 & c_{23} & s_{23} \\ 0 & -s_{23} & c_{23} \end{pmatrix} \begin{pmatrix} c_{13} & 0 & s_{13}e^{-i\delta} \\ 0 & 1 & 0 \\ -s_{13}e^{i\delta} & 0 & c_{13} \end{pmatrix} \begin{pmatrix} c_{12} & s_{12} & 0 \\ -s_{12} & c_{12} & 0 \\ 0 & 0 & 1 \end{pmatrix} \tag{2.36}$$

Here, the short-hand notations $c_{ij} = \cos\theta_{ij}$ and $s_{ij} = \sin\theta_{ij}$ are used. Also in the three-flavour case, the probabilities for neutrino oscillations depend on the mass differences $\Delta m_{ij}^2 = m_i^2 - m_j^2$. The PMNS matrix allows CP violation via the parameter δ.

Since neutrino oscillations are sensitive only to the mass differences, the spectrum of neutrino masses can be ordered in two different ways. The *normal ordering* (NO) assumes $m_1 < m_2 < m_3$, whereas the *inverted ordering* (IO) is $m_3 < m_1 < m_2$. Measurements show that $\Delta m_{21} \ll |\Delta m_{31}^2| \approx |\Delta m_{32}^2|$, which excludes other mass orderings.

[4]Note that the same result can also be obtained by assuming equal energy E_ν or equal speed β.

2.2.2. Mechanisms for Neutrino Mass Generation

The SM needs to be extended to create a neutrino mass term. A common method is to extend the SM by m sterile neutrinos ν_s. With these sterile neutrinos, two different mass terms can be constructed.

The *Dirac* mass term introduces a coupling between sterile and SM neutrinos.

$$\mathcal{L}_{M_\nu,\text{Dirac}} = -M_{Dij}\bar{\nu}_{si}\nu_{Lj} \tag{2.37}$$

Here, M_D is a complex $3 \times m$ matrix. This Lagrangian gives rise to a Yukawa coupling for neutrinos, so they could gain their mass in the same way as the charged leptons. Also, the Dirac mass term conserves the lepton number, but not the lepton flavour number. Thus, neutrino oscillations remain possible. However, it cannot explain why the observed neutrinos are so much lighter than the charged leptons.

Alternatively, one can postulate that the sterile neutrinos are *Majorana* particles, i. e. their own antiparticles. The Lagrangian

$$\mathcal{L}_{M_\nu,\text{Majorana}} = -\frac{1}{2}M_{Nij}\bar{\nu}_{si}\nu_{sj}^C \tag{2.38}$$

contains two sterile neutrino fields and a symmetric $m \times m$ matrix M_N. The Majorana mass term breaks the lepton number symmetry by two units.

Both Lagrangians can be combined to

$$\mathcal{L}_{M_\nu} = -\frac{1}{2}\begin{pmatrix}\bar{\nu_L}^C & \bar{\nu_s}\end{pmatrix}\begin{pmatrix}0 & M_D^T \\ M_D & M_N\end{pmatrix}\begin{pmatrix}\nu_L \\ \nu_s^C\end{pmatrix} + \text{h. c.}, \tag{2.39}$$

where $(\bar{\nu^C}, \bar{\nu_s})^T$ is a $3+m$-dimensional vector and *h. c.* indicates the hermitian conjugate of the previous expression. The matrix M_ν in this equation is symmetric and complex. It can be diagonalised to obtain the mass eigenstates.

Apart from the Dirac and Majorana mass terms, neutrino masses can also be introduced by some other new physics process. These are in general modelled by an operator of dimension 5 or higher and would violate the lepton number symmetry of the SM.

2.2.3. The Seesaw Mechanism

The eigenvalues of M_ν in equation Equation (2.39) will give the masses of observable neutrinos. The eigenvalue problem has two solutions

$$m_\pm = \frac{M_N}{2} \pm \frac{1}{2}\sqrt{M_N^2 + M_D^2} = \frac{1}{2}\left(M_N \pm M_N\sqrt{1 + \frac{4M_D^2}{M_N^2}}\right). \tag{2.40}$$

Assuming $M_N \gg M_D$, the two solutions for a light (ν) and a heavy (N) neutrino state are

$$|m_\nu| \approx \frac{M_D^2}{M_N} \quad \text{and} \quad m_N \approx M_N. \tag{2.41}$$

This is where the name *seesaw mechanism* arises: the heavier the heavy neutrino N is, the lighter is the light neutrino ν.

Assuming that the Majorana term exists, the seesaw mechanism predicts that there is a light and a heavy neutrino for each neutrino generation. The light neutrino will have masses way smaller than the other fermions in the SM, whereas the other state will be very massive.

To illustrate, assume that $|m_\nu| \approx 0.1\,\text{eV}$, which is compatible with the current experimental limits on neutrino masses. If the Dirac mass was of the same order of magnitude as the electron mass, i. e. $M_D = \mathcal{O}(1\,\text{MeV})$, Equation (2.41) would postulate that $m_N = \mathcal{O}(10\,\text{TeV})$. Alternatively, if the Dirac mass was closer to the mass of the τ lepton or quarks, i. e. $m_D = \mathcal{O}(1\,\text{GeV})$, one would have $m_N = \mathcal{O}(10^7\,\text{TeV})$.

2.2.4. Weinberg Operator

The other signal model considered in this thesis belongs to the category of generic operators of new physics. The *Weinberg operator* [34]

$$\mathcal{L}_5 = \frac{C_5^{ll'}}{\Lambda}[\phi \bar{L}_l^C][L_{l'}\phi] \tag{2.42}$$

is the lowest-dimension ($d = 5$ in mass) operator that can generate neutrino masses. Here, ϕ is the Higgs doublet of Equation (2.22), L_l denotes the lepton doublets of Equation (2.4) and $C_5^{ll'}$ is the Wilson coefficient. The new physics encoded by this operator violates lepton number by two units and lives at mass scales of Λ.

Even though the word operator is used in singular, the Weinberg operator is actually a family of operators. This becomes apparent when *opening up* the operator, i. e. looking at the potential interactions included in it. While in principle any number of new or existing particles could be involved in these diagrams, the following will only focus on interactions at tree-level. At tree-level, there are three options, but all of them involve two interaction vertices and introduce one kind of new particle (Figure 2.1). The new particle could be a right-handed neutral Majorana fermion, or right-handed neutrino. In this case, one would arrive at the Type I Seesaw mechanism outlined in Section 2.2.3. Alternatively, the new particle could also be a fermion weak isospin triplet, which would correspond to the Type III Seesaw mechanism. The third case introduces a new scalar multiplet, which has Yukawa couplings to both to the Higgs $\phi^\dagger\phi$ and lepton $\bar{L}^C L$ fields. Each of these options could be extended at an arbitrary number of loops.

The effective Majorana mass

$$m_{ll'} = C_5^{ll'}\frac{v^2}{\Lambda} \tag{2.43}$$

can be calculated by inserting the VEV v of the Higgs field into the Weinberg operator. The Weinberg operator is an effective field theory (EFT): New particles exist at mass scales that are too high to be resolved yet. However, they might show effects already at the energies reached by current experiments.

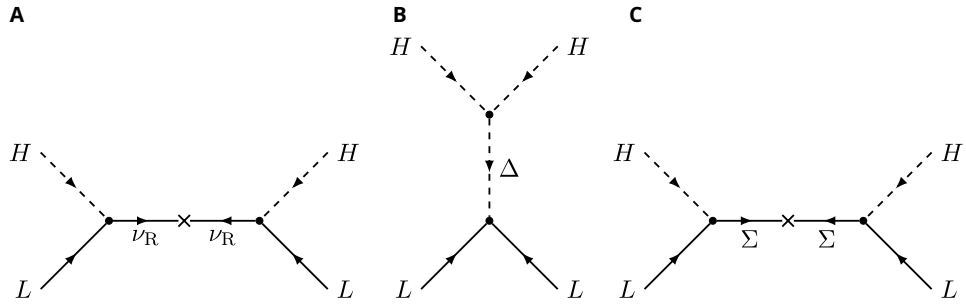

Figure 2.1.: Opening the Weinberg operator at tree-level yields three different options. (A) is a realisation of the Type I Seesaw model with a right-handed Majorana neutrino ν_R. (B) corresponds to the Type II Seesaw with a new scalar particle Δ and (C) demonstrates the Type III Seesaw with a fermion triplet Σ. In this Figure, L refers to the left-handed lepton doublet of Equation (2.4) and H to the Higgs doublet. Figure from [35].

3. The ATLAS Experiment and the Large Hadron Collider

3.1. The Large Hadron Collider

The *Large Hadron Collider* (LHC) [36] at CERN is the world's largest particle accelerator. It is hosted by a tunnel with a circumference of 26.7 km under the French-Swiss border area near Geneva. The tunnel consists of eight arcs and eight straight sections, each of the latter is ca. 0.5 km long. Four of these straight sections are used to host experiments. The general-purpose experiments ATLAS and CMS are on opposite sides of the ring. They collect data for precision measurements of the known particles and enable searches for hypothetical undiscovered particles. The third experiment at the LHC, LHCb, is specifically targeting b-quark physics, whereas the last large experiment, ALICE, is dedicated to the study of heavy ion collisions. In addition to these large experiments, the FASER, TOTEM and MoEDAL experiments are also located at the LHC. They are small experiments with a focus on a specific kind of physics and do not have their own interaction points. Instead, they detect particles created during collisions at the other experiments. The remaining four straight sections host equipment needed for the operation of the collider.

The LHC does not accelerate single protons, but *bunches*, groups of ca. $1.15 \cdot 10^{11}$ protons[1]. It is not possible to create bunches and accelerate them from zero to collision energy in the LHC. Instead, protons go through a long chain of other accelerators beforehand (cf. Figure 3.1). Hydrogen gas from a usual bottle is ionised and accelerated by the linear accelerator LINAC 2 to an energy of 50 MeV. In the *Proton Synchrotron Booster* (BOOSTER), the protons are accelerated to 1.4 GeV. Then, in the *Proton Synchrotron* (PS), the bunches are rearranged into 72 bunches separated by 25 ns, which will also be the bunch separation in the LHC. The *Super Proton Synchrotron* (SPS) will gather three or four fills of the PS and accelerate them to 450 GeV. From there, up to 2808 bunches are injected into the LHC and then accelerated to 6.5 TeV, leading to collisions at a centre-of-mass energy of $\sqrt{s} = 13\,\text{TeV}$. During Run 2, the LHC delivered an instantaneous luminosity of up to $2 \cdot 10^{34}\text{cm}^{-2}\text{s}^{-1}$ to the ATLAS and CMS experiments, twice of it's original design value.

Due to the high instantaneous luminosity, several pp collisions occur in each bunch crossing. At most one of these collisions, the *hard scatter*, is of interest. The other collisions result only in low-energy particles and are referred to as *in-time pile-up*. Ad-

[1] The LHC does also accelerate lead ions in dedicated fills, but proton-lead and lead-lead collisions are not of interest for this thesis.

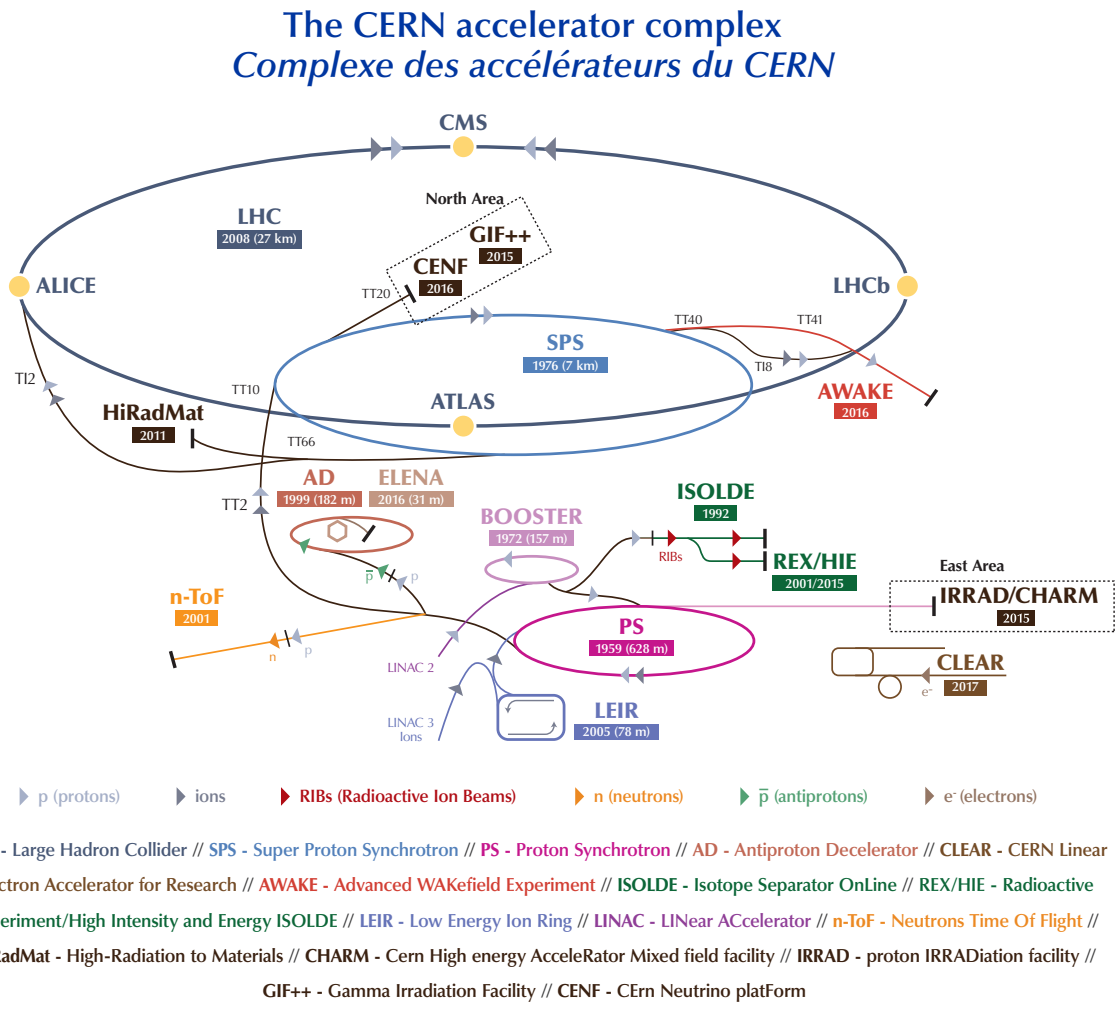

Figure 3.1.: Schematic of the CERN accelerator complex at the end of Run 2. Figure from [37].

ditionally, the calorimeters often contain energy from other bunch crossings, which is referred to as *out-of-time pile-up*.

3.2. The ATLAS Detector

The ATLAS Experiment is described extensively in [38]. The design of the experiment was determined by two physics goals, one being the search for the SM Higgs boson. By far the cleanest final state for a Higgs boson search is $h \to \gamma\gamma$, but also the leptonic final states of $h \to W^{\pm}W^{\mp}$ and $h \to ZZ$ were considered to be highly sensitive when the experiment was designed. Therefore, a good measurement and identification of electrons, muons and photons was needed. The other design goal of the ATLAS experiment was to

perform searches of *physics beyond the SM* (BSM). While there is a multitude of different BSM models, a common theme of these is that they are easiest to detect through their interactions with heavy SM fermions, in particular τ leptons and b quarks. Another common theme are new resonances at high mass, which would then decay and cause leptons or jets with transverse momenta as high as several TeV.

Combining these requirements leads to a multi-layered detector design that completely encloses the interaction point. The tracking detector is completely contained in a 2 T magnetic field provided by a solenoid. It bends the trajectory of charged particles passing the tracking system. Going outward from the beampipe, particles first traverse four layers of silicon pixel and another four layers of silicon strip detectors providing very high spatial resolution. The outer part of the tracking system is covered by straw-tube detectors. While their spatial resolution is worse than for the silicon detectors, the far larger amount of layers and the possibility to detect transition radiation compensate for that.

On the other side of the solenoid, the liquid Argon (LAr) calorimeter will measure the energy of electromagnetic particles with high resolution and granularity. In the barrel region, a scintillator-tile calorimeter measures the energy of jets. Calorimetry in the endcaps is done using a LAr calorimeter to measure both electromagnetic particles and hadrons.

All these parts are surrounded by three large air-core toroid magnets (one for the barrel and one for each endcap). Three layers of tracking chambers then allow to measure the momentum of muons and one layer of special trigger chambers can be used to quickly start detector readout.

Combining all these subsystems into one gives a truly gigantic particle physics experiment: The complete ATLAS detector (Figure 3.2) has a length of 44 m, measures 25 m in diameter and weighs approximately 7000 t. It is mounted in a cavern 100 m underground.

3.2.1. Coordinate System

ATLAS uses a right-handed Cartesian coordinate system with its origin at the nominal interaction point. While the z-axis is aligned with the beam, the x-axis points towards the centre of the LHC ring and the y-axis points upwards. When using cylindrical coordinates, the azimuthal angle ϕ is measured in the $x - y$ plane around the beam axis and the polar angle θ is the angle from the beam axis. The rapidity $y = 0.5 \cdot \ln\left((E + p_z)/(E - p_z)\right)$ is occasionally used. In the case of negligible masses, it is equivalent to the pseudorapidity $\eta = -\ln\tan(\theta/2)$. However, the main advantage of the pseudorapidity is that differences in this observable are invariant under Lorentz transformations. Consequentially, a common measure for the distance between two reconstructed objects is defined as $\Delta R = \sqrt{\Delta\eta^2 + \Delta\phi^2}$. Finally, the transverse momentum is defined as the momentum component perpendicular to the beam axis.

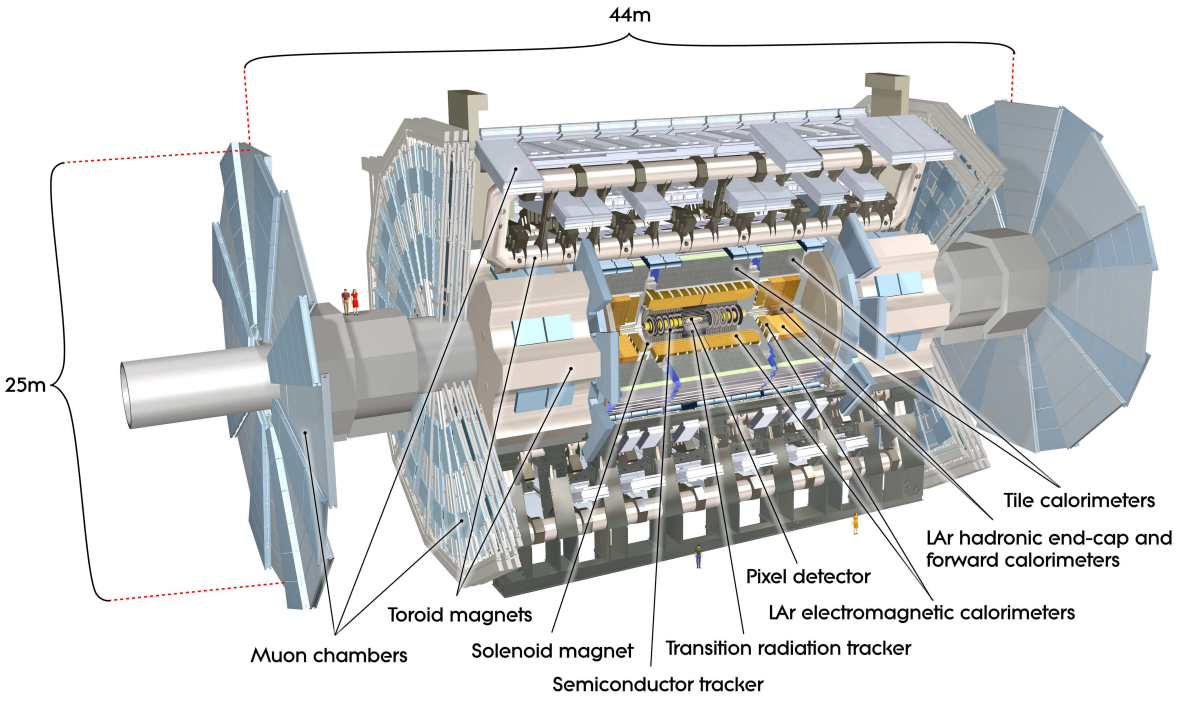

Figure 3.2.: Cut-away view of the ATLAS detector. Figure from [38]

3.2.2. Magnet System

Parts of the detector are placed inside an magnetic field which will deflect charged particles traversing it. From the magnitude of the deflection, the momentum of the particles can be calculated. All magnets used inside ATLAS are superconducting and operate at ca. 4.5 K. In the centre, a solenoid of 2.46 m inner diameter and 5.8 m length provides a 2 T magnetic field in the z direction. Outside of the solenoid, the magnetic flux is returned through the steel elements of the hadronic calorimeter and its support structure. In order to reduce the amount of dead material in front of the calorimeters, the solenoid has a thickness of only 5 cm. Further outside, three sets of toroid magnets provide a magnetic field for the muon system. The 25.3 m long barrel toroid is a huge structure that gives the ATLAS detector its characteristic outline. In the endcap, the toroids are smaller and inserted inside the barrel toroids (cf. Figure 3.2). The magnetic field of ca. 0.5 T in the barrel and ca. 1 T in the endcap is inhomogenous and needs to be mapped for the reconstruction of charged particle trajectories. Therefore, a total of 1840 sensors spread across the muon spectrometer measures the actual magnetic field to allow a precise momentum reconstruction.

3.2.3. Tracking

Inside the 2 T magnetic field of the solenoid lies the *Inner Detector* (ID, Figure 3.3). Each proton-proton collision is expected to produce 1000 particles that traverse the ID,

i. e. the region with $|\eta| < 2.5$. In order to keep the occupancy of the detector low, a layered design using different technologies is employed. The four inner layers consist of silicon pixel sensors measuring $50 \times 400\,\mu$m, the innermost of which is known as the *Insertable B-Layer* (IBL) [39, 40]. The sensors are mounted parallel to the beam axis with the long side in the z direction in the barrel and perpendicular to the beam axis in the endcap. This leads to a position resolution of $10\,\mu$m in the $R-\phi$ ($z-\phi$) plane and $115\,\mu$m in the z (R) direction in the barrel (endcap). With it, the tracking and b-tagging efficiencies of the ATLAS detector actually improve in Run 2 despite the higher luminosity. In total, there are now 86.42 million readout channels in the pixel detector.

The middle part of the Inner Detector consists of the four layers of the *Silicon Microstrip Tracker* (SCT). They provide another 6.3 million readout channels. Due to the lower track density, strip sensors with a width of $80\,\mu$m and a length of 6.4 cm can be used while still keeping the occupancy sufficiently low. The strip sensors are mounted in a "stereo" configuration with two sensors per layer: One sensor is aligned parallel to the beam axis (perpendicular to it in the endcap). The other sensor is mounted close to it, but rotated by an angle of 40 mrad. With this technique, a resolution of $17\,\mu$m in the $R-\phi$ ($z-\phi$) plane and of $580\,\mu$m in the z (R) direction can be achieved in the barrel (endcap).

Finally, the last layer of the Inner Detector is formed by the *Transition Radiation Tracker* (TRT). Each individual sensor here is a 4 mm diameter straw tube made from a custom composite material. At it's centre, a gold-plated tungsten wire is located and the tube is filled with a gas mixture of 70 % Xenon, 27 % carbon dioxide and 3 % oxygen. A charged particle passing through a tube will ionise the gas. Because of the 1.5 kV voltage between wire and tube, the ionisation charge is amplified and collected at the wire. An electron passing through the wall of the tube will emit *Transition Radiation* (TR) photons at low energy. These photons will be absorbed by the gas filling of the tube and create a significantly larger charge signal. Pions, on the other hand, do not cause transition radiation due to their higher masses.

The TRT has a position resolution of $130\,\mu$m in the plane perpendicular to the tubes and does not offer position information in the direction of the tubes. Also, there are only 351 000 readout channels. However, this disadvantage is compensated by the high number of layers: The TRT has 73 layers of straw tubes and a typical charged particle will leave at least 36 hits. For an electron with $p_{\mathrm{T}} > 2\,$GeV, seven to ten of these hits are typically from a TR photon. The discrimination between electrons and pions provided by the TRT significantly improves the electron reconstruction.

3.2.4. Calorimetry

The calorimeters of the ATLAS experiment are arranged symmetrically around the interaction point and cover the $|\eta| < 4.9$ range. Four subsystems leveraging different technologies are used to make precise measurements in the face of different requirements (Figure 3.4). Calorimeters perform destructive measurements by stopping all particles entering them. They are designed with a thickness of at least 22 radiation lengths X_0 in the electromagnetic and approximately 10 interaction lengths λ in the

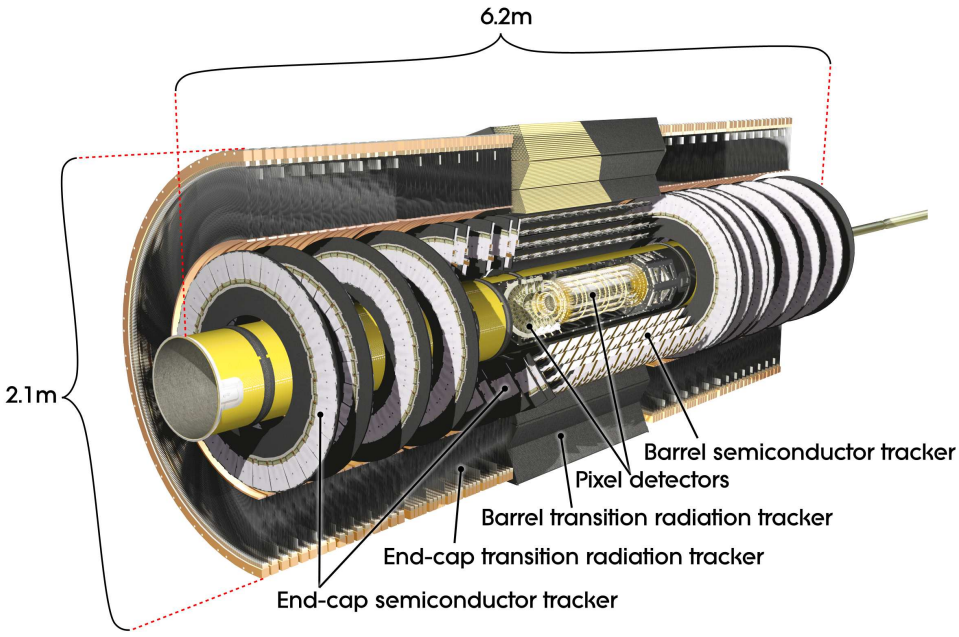

Figure 3.3.: Cut-away view of the Inner Detector. Figure from [38].

hadronic calorimeters. Thus, no particles except for muons and neutrinos can propagate beyond the calorimeters. All calorimeters in the ATLAS experiment are sampling calorimeters. They consist of multiple layers of a dense absorber material alternating with an active medium where the deposited energy can be measured.

Three out of the four subsystem use LAr as the active medium, which has a linear response and is not susceptible to radiation damage. Also, past experience has shown that the response doesn't change over time. In all subsystems, the readout regions are arranged in a way that they roughly point to the interaction region in the centre of the detector.

The *LAr electromagnetic calorimeter* is the innermost of the four calorimeters and surrounds the ID. It is split in a barrel ($|\eta| < 1.475$) and an endcap ($1.375 < |\eta| < 3.2$) part. The lead absorber plates are arranged in an accordion geometry in order to avoid gaps in the phi direction. In order to support the reconstruction of photons and electrons, the region $|\eta| < 2.5$ (which is also covered by the Inner Detector) has three layers of calorimeter cells with high granularity in the $\eta-\phi$ plane. At higher η, the EM calorimeter only has two layers and a coarser granularity.

Hadronic calorimetry is done using two different systems. The barrel region ($|\eta| < 1.7$) is covered by the only non-LAr calorimeter, the *tile calorimeter*. It consists of steel absorber plates and scintillating tiles arranged in radial direction. The scintillator tiles are connected with fibres to photomultiplier tubes located at the outer end of each layer. Three of these layers give the tile calorimeter a total thickness of $9.7\,\lambda$. In the endcap, the *LAr hadronic endcap calorimeter* (HEC) is located right behind the EM calorimeter in the same LAr cryostat. It uses copper absorber plates arranged in the radial direction

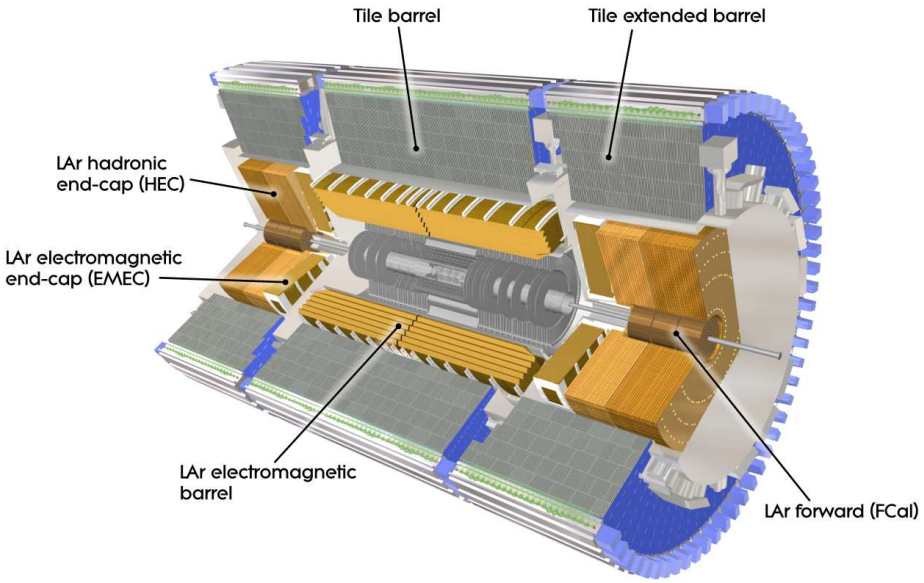

Figure 3.4.: Overview of the ATLAS calorimeters. Figure from [38].

and covers the $1.5 < |\eta| < 3.2$ range, thus overlapping a bit with both the tile and the forward calorimeter.

Finally, the *Forward Calorimeter* (FCal) closes the gap between the other calorimeter systems and the beam pipe (i. e. $3.1 < |\eta| < 4.9$). Because of the higher particle flux in the forward region, the LAr-filled gaps between the absorber plates are smaller in order to increase their density. The smaller gaps also lead to a faster signal than in the barrel and endcap calorimeters. Due to the limited space, the FCal cannot be as thick as the other calorimeters and thus needs especially dense material. Out of it's three layers, the first one is made of copper absorber plates, which have holes in the z direction. Into these holes, copper rods coated in fibre are inserted and the gap between those and the absorber plates is filled with LAr as active medium. The second and third layer of the FCal are optimised for hadronic calorimetry and use tungsten where the first layer used copper.

3.2.5. Muon System

The outermost part of the ATLAS detector is the muon system, the magnetic field for which is provided by a dedicated system consisting of air-core toroids. Three parts, one for the barrel and a smaller one for each endcap, consisting of eight coils each provide a magnetic field in the ϕ direction. This field is mostly perpendicular to the movement of the muons. Air-core toroids were chosen because they add only little material to the path of the muons, thus there is less multiple scattering and the resolution improves.

In order to accurately determine the muon momentum, the coordinate in the bending plane[2] has to be determined with high precision. Both the barrel and the endcap use three layers of *Monitored Drift Tube chambers* (MDT) to measure muons with $|\eta| < 2.7$ (cf. Figure 3.5). Each chamber contains three to eight layers of drift tubes filled with an Ar-CO_2 mixture and mechanical support. Integrated into the mechanical support structure is an alignment system. The magnetic field of the toroids can deform the muon system. Therefore, the position of the muon drift tubes needs to be monitored to allow a precise measurement of the particle trajectory. The knowledge gained about the position of the individual wires in the drift tubes then reduces the position resolution to 35 μm per chamber in the η plane.

MDTs work fine for particle counts up to ca. $150\,\mathrm{Hz}\cdot\mathrm{cm}^{-2}$. In the innermost layer of the endcap, this count is exceeded in the $2.0 < |\eta| < 2.7$ area. Therefore, this area is covered by *Cathode-Strip Chambers* (CSC) that can be used up to $1000\,\mathrm{Hz}\cdot\mathrm{cm}^{-2}$. These are multiwire proportional chambers where the cathode plates are segmented into strips which are read out. The cathode plates are segmented either in the R direction, parallel to the wires, or in the ϕ direction. In the latter, non-bending case, the strips are spaced further apart leading to a worse resolution.

While the MDT and CSC offer a good position resolution, their readout is too slow to be used for triggering. Therefore, special trigger chambers are mounted next to the MDT layers (see Figure 3.5). Their good time resolution and rapid readout allow to tag individual bunch crossings. In the barrel region ($|\eta| < 1.05$), *Resistive Plate Chambers* (RPC) are used. Two parallel plates serve as electrodes, separated by 2 mm of a gas mixture. Triggering the endcap region ($1.05 < |\eta| < 2.4$) is done with *Thin Gap Chambers* (TGC). These are wire chambers where the distance between individual wires (1.8 mm) is larger than the distance between the wires and the cathode plates (1.4 mm). Both types of trigger chambers measure the coordinate in the bending and non-bending plane, whereas the MDT only measure in the bending plane. During reconstruction, the position in the non-bending plane is obtained from the trigger chambers.

3.2.6. Trigger and Data Acquisition

The LHC collides protons with a frequency of 40 MHz. Each recorded event requires ca. 1 MiB of storage, recording every event would require adding several new hard disk drives per minute and a computing farm orders of magnitude larger than the existing. Clearly, this is a task not achievable within a somewhat realistic budget. Therefore, it has to be decided on the fly which events contain hints of interesting physics and should be stored permanently. The task of finding and recording interesting events is done by the *Trigger and Data Acquisition System* (TDAQ).

ATLAS uses a two-stage trigger system which is described in [41]. The *Level 1* (L1) trigger uses only coarse information to make a rapid first decision. The calorimeter is read out in *trigger towers* measuring ca. 0.1×0.1 in $\eta \times \phi$. The amount of energy deposited in the hadronic and electromagnetic calorimeters in combination with clus-

[2] I. e. the $r - z$ plane, perpendicular to the magnetic field.

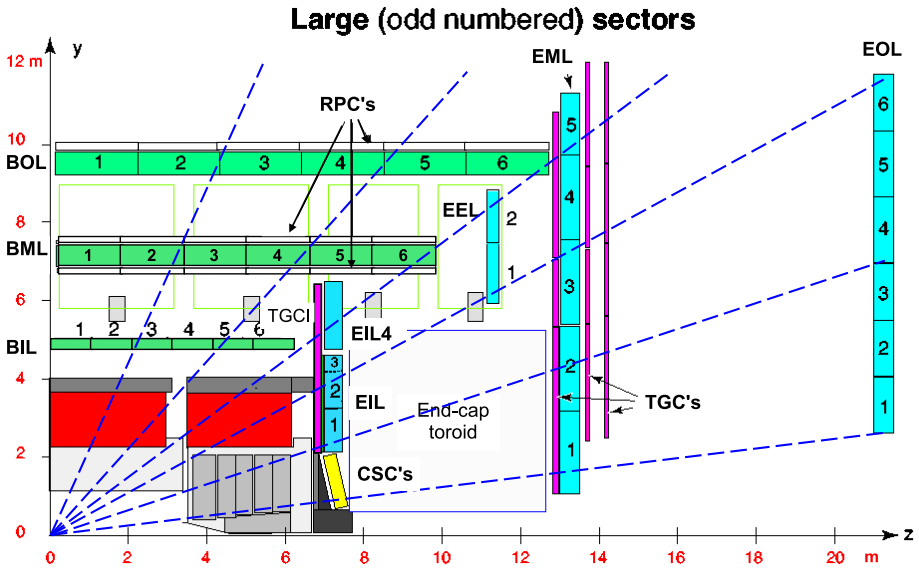

Figure 3.5.: Schematic of the ATLAS muon system in the bending plane. The dashed lines indicate tracks of infinite-momentum muons. MDT in the barrel are highlighted in green, in the endcap in blue. Figure from [38].

tering algorithms allows to distinguish between jets, electromagnetic particles and tau lepton candidates. The L1 trigger does not use tracking information and thus cannot distinguish electrons and photons. In the muon system, dedicated trigger chambers that can be read out rapidly (cf. Section 3.2.5) are used by the L1 trigger to identify events with muons. Approximately 2 μs pass between a bunch crossing and the decision of the L1 trigger. It deems ca. 100 000 events per second as interesting enough to warrant a more detailed check.

This more detailed investigation is done by the *High-Level Trigger* (HLT). It identifies *Regions of Interest* (RoI) based on the items identified by the L1 trigger and performs event reconstruction only in these RoI. In particular, this means that the HLT can also use information from the ID in its decision and e. g. trigger on b-jets. Roughly 1 200 events per second pass the HLT and are stored permanently.

The raw readout from the detector needs to be reconstructed before it can be used for physics analysis. A small part is reconstructed on the fly and used to monitor the data quality. This way, problems with the detector can be identified and mitigated quickly. A somewhat larger subset of the data is reconstructed early and used to calibrate the detector. Especially, this includes determining the exact position of the beams and identifying noisy segments of the detector, which are then subsequently masked during reconstruction. Once this evaluation is completed, the data taken during a single LHC fill is reconstructed in bulk [42].

3.3. Event Reconstruction

The first step towards a physics analysis of the collision is the *reconstruction* of physics objects from the detector readout. This is done in a two step procedure outlined in this section. At first, the basic building blocks are identified: tracks, their vertices, and calorimeter deposits. From these, dedicated algorithms reconstruct electrons, muons and jets. These algorithms run independently. Afterwards, the *overlap removal* procedure resolves ambiguous cases, where two or more objects of different type are reconstructed in close proximity and at least partially shared basic objects. Finally, the missing transverse momentum $E_{\mathrm{T}}^{\mathrm{miss}}$ is calculated, which gives a handle on particles escaping the detector undetected.

3.3.1. Basic Objects

Tracks

Track finding in ATLAS is done with two different algorithms [43]. At first, an *inside-out* algorithm is applied. A seed consisting of three hits in the pixel detector is used as a starting point. From there, a Kalman filter follows this track outward through all layers of the pixel and SCT. There are many track candidates and ambiguities between them need to be resolved based on the goodness of the track fit and the track morphology. For example, track candidates without a hit in the IBL are strongly disfavoured in this steps, since they are more likely to come from e. g. photon conversions. Tracks from secondary vertices will be reconstructed in a later step. After removing ambiguities, the tracks are extended to the TRT. Hits in the TRT compatible with a track from the silicon detector are added to it, but they are not used to readjust the track. The inside-out algorithm will reconstruct tracks starting at $p_{\mathrm{T}} > 400\,\mathrm{MeV}$ [44].

In a second step, an *outside-in* algorithm is applied to the hits that are not part of a track. Since the curvature of tracks with $p_{\mathrm{T}} > 500\,\mathrm{MeV}$ is nearly undetectable by the TRT, this algorithm starts by finding TRT hits in straight line pointing towards the beamline. This line is then propagated through the SCT and pixel detectors to find further track candidates. In particular, this method is able to identify tracks originating from secondary vertices. Both the inside-out and the outside-in algorithm work under the pion hypothesis. That means that they assume that the track originates from a pion e. g. when accounting for energy losses in the tracker layers.

Vertices

Vertices, i. e. the positions of the pp collisions in the event, are reconstructed from tracks that are compatible with originating from the interaction region [45]. For each of these tracks, the z coordinate of the closest approach to the average collision point is determined. The z position with the most tracks is used as a seed for the adaptive vertex fitting algorithm [46]. Tracks with a z coordinate more than seven standard deviations away from a vertex are used to seed a new vertex. This high threshold is meant to prevent a single vertex being split into two by outlying tracks.

Topological Clusters

A single particle frequently deposits energy in more than one calorimeter cell. Therefore, the energy deposits in the calorimeter are combined into *topological clusters* (topoclusters) [47]. The algorithm for finding topological clusters works in terms of the energy deposited relative to the noise of the calorimeter: $\zeta_{\text{cell}}^{\text{EM}} = E_{\text{cell}}^{\text{EM}} / \sigma_{\text{noise, cell}}^{\text{EM}}$. Seeds for the clustering algorithm need to contain an energy significantly deviating from the noise level: $|\zeta_{\text{cell}}^{\text{EM}}| > 4$. These cells form a protocluster, to which all neighbouring calorimeter cells are added. "Neighbouring" does also include cells in adjacent layers of the calorimeter that partially overlap. In the next phase of the clustering sequence, cells neighbouring cells in the protocluster with $|\zeta_{\text{cell}}^{\text{EM}}| > 2$ are added to the protocluster until no more cells passing this threshold are found. If a cell should be added to two protoclusters according to this procedure, the two protoclusters are merged. Cells that do not pass this threshold can still become part of a cluster, but do not expand it.

Protoclusters formed this way may be too large and contain actually more than one particle. Therefore, they are spit around cells with energy deposits of at least 500 MeV that are local maxima in the energy distribution inside the calorimeter.

3.3.2. Electrons

An electron leaves both a track in the ID and an energy deposit in the EM calorimeters. Their reconstruction is further complicated by energy losses due to bremsstrahlung. Thus, for an accurate reconstruction, the basic objects defined previously need to be combined [48, 49]. While topoclusters can be used as-is for electron reconstruction, the procedure for tracks is more elaborate. Reconstructed tracks that can be loosely matched to a topocluster are used, but they are subject to a new track fit. This fit is done under the electron hypothesis, i. e. allowing for higher energy losses in the layers of the ID and the emission of bremsstrahlung photons. The latter would manifest as an increase in the curvature of the track due to the now reduced electron energy.

Refitted tracks are then used to build superclusters. They are seeded from topoclusters with $E_{\text{T}} > 1\,\text{GeV}$ that are matched to a track. Around the barycentre of the supercluster, a window of $\Delta\eta \times \Delta\phi = 0.075 \times 0.125$ is placed. Topoclusters that also fall into this window are added as satellite clusters. The window is larger if the best track for a satellite cluster is the same as for the seed cluster.

In order to identify electrons among the reconstructed candidates, a likelihood-based procedure is employed that combines a variety of observables. These observables encode e. g. the shape of the electromagnetic shower in the calorimeters or properties of the track. For each, a probability density function binned in η and E_{T} is derived for signal and background. The likelihood function as product of the individual PDFs is then used to define three working points: loose, medium and tight. They are defined such that the *loose* WP has the highest efficiency of 93 %, *medium* identifies 88 % of the electrons as such and the *tight* working point has only 80 % for electrons with $E_{\text{T}} = 40\,\text{GeV}$. The efficiency increases with E_{T} and the less efficient working points offer a higher background rejection.

3.3.3. Muons

Muons are reconstructed using a combination of information from the ID, the MS and the calorimeter [50]. While track reconstruction in the ID has been covered before (Section 3.3.1), track reconstruction in the MS is done in a different way. At first, straight-line segments in the individual stations of the MS are identified. These segments are then combined into track candidates that roughly point towards the IP. A first χ^2 fit is used to remove outlying hits and add in missed hits along the track. Conflicts between overlapping track candidates are in general resolved by keeping the candidate with a higher quality. This final set of MS track candidates is then subject to a second χ^2 fit. This time, energy losses in the calorimeter are taken into account and the track is required to originate from the IP.

Tracks from the MS are then combined with information from the other subdetectors in order to reconstruct muons. A total of five different strategies is used in ATLAS:

- *Combined* (CB) muons are reconstructed by matching tracks from the MS to tracks in the ID. After performing the matching, a combined track fit that also takes into account energy losses in the calorimeter is performed. In the most forward part of the MS, at $|\eta| > 2.5$, MS tracks are combined with short track segments from the ID. These *silicon-associated forward* (SiF) muons form a subset of CB muons.

- *Inside-out combined* (IO) muons are formed in the opposite directions. Tracks from the ID are extrapolated towards the MS, where at least three hits aligned closely with the extrapolated track are required. The parameters of the muon are then determined by a combined track fit. Since this type of muon does not require a track in the MS, it performs better in regions with reduced coverage of the MS (e. g. at $|\eta| \lesssim 0.1$) or for low p_{T} muons.

- *Muon-spectrometer extrapolated* (ME) muons do not have a matching track in the ID. Instead, the MS track is extrapolated to the beamline. This muon type can make use of the full MS cove rate ($|\eta| < 2.7$).

- *Segment-tagged* (ST) muons consist of an ID track that is closely aligned with a track segment in the MS. However, muon parameters are obtained only from the ID track.

- *Calorimeter-tagged* (CT) muons require a track in the ID that is then extrapolated through the calorimeters. To qualify as a muon, a candidate needs to have energy deposits in the calorimeter that are consistent with a minimally ionising particle.

All these reconstruction strategies run in parallel. Then, this array of options is reduced to three muon identification working points for general use in ATLAS. When determining whether a muon candidate passes the requirements of a certain WP, two more observables are considered for CB and IO muons. These are the q/p compatibility defined as the ratio between the q/p difference $|q/p_{\mathrm{ID}} - q/p_{\mathrm{MS}}|$ and their respective

resolutions added in quadrature. Here q/p_{ID} is the electric charge q divided by the momentum as measured by the ID and q/p_{MS} is the equivalent in the MS. $\rho' = \frac{|p_{\mathrm{T,\,ID}} - p_{\mathrm{T,\,MS}}|}{p_{\mathrm{T,\,CB}}}$ can be used to check whether the p_{T} measurements in ID and MS are compatible.

The *loose* WP has the highest selection efficiency, but also the highest amount of fakes, whereas the *tight* working selects a very pure sample of muons with a reduced efficiency.

- The *medium* WP is the default choice for ATLAS analyses and a compromise between the other two working points. It accepts CB and IO muons within $|\eta| < 2.5$ that have a q/p compatibility smaller than seven. Outside of the ID acceptance, SiF and ME muons extend the coverage to the $2.5 < |\eta| < 2.7$ region. Muons passing the medium WP have $p_{\mathrm{T}} > 3\,\mathrm{GeV}$.

- The *loose* WP is more inclusive. In addition to all muons passing the medium WP, it also includes CT and ST muons in the $|\eta| < 0.1$ region. The pass-throughs for services in that part of the MS reduce the efficiency for CB muons. Additionally, requirements for IO muons with $p_{\mathrm{T}} < 7\,\mathrm{GeV}$ are loosened in order to improve the coverage at low p_{T}. However, muons passing this requirement also need to be tagged as ST muons in order to reduce the misidentification rate.

- Finally, the *tight* WP has stricter selection requirements than the medium WP. In particular, this means varying maximum values for the q/p compatibility and ρ' depending on p_{T} and η of the muon candidate Additionally, the χ^2/n_{dof} of the combined track fit as to be smaller than eight and muons passing this working point have $p_{\mathrm{T}} > 4\,\mathrm{GeV}$

In addition to these three commonly used WP, there are also two specialisations of the medium WP. The *low* p_{T} WP increases the efficiency for muons with $p_{\mathrm{T}} < 10\,\mathrm{GeV}$, whereas the *high* p_{T} WP improves the resolution for muons with $p_{\mathrm{T}} > 100\,\mathrm{GeV}$. However, the gain in resolution for the latter comes at the cost of a worse efficiency than the tight WP at similar rates of fake muons.

In order to select only prompt muons, i. e. those arising from SM bosons or BSM processes, *isolation* requirements are imposed. Non-prompt muons usually arise from the decay of hadrons with b or c quarks and thus are accompanied by significant activity. This activity can be determined eġ. with track-based observables. Either the sum of transverse momenta of all tracks within $\Delta R = 0.2$ is used (then labelled $p_{\mathrm{T}}^{\mathrm{cone20}}$) or alternatively, the radius can be determined dynamically. For this $p_{\mathrm{T}}^{\mathrm{varcone30}}$ observable, the transverse momenta of all tracks within $\Delta R = \min(10\,\mathrm{GeV}/p_{\mathrm{T}}^{\mu}, 0.3)$ are considered. Similarly, calorimeter-based isolation requirements considered the amount of energy deposited within e. g. $\Delta R = 0.2$. This analysis, however, uses an isolation criterion based particle flow [51] techniques. It uses the track-based observables defined above ($p_{\mathrm{T}}^{\mathrm{varcone30}}$ for $p_{\mathrm{T}}^{\mu} < 50\,\mathrm{GeV}$, $p_{\mathrm{T}}^{\mathrm{cone20}}$ above that) and the energy deposited by neutral particles within $\Delta R = 0.2$ inside the calorimeter. The latter can be obtained by using tracks to remove energy deposits from charged hadrons from the calorimeter measurements.

3.3.4. Jets

Due to colour confinement, quarks from the final state of an interaction will not propagate as such to the detector, like electrons or muons would. Instead, during hadronisation and parton shower, they form a collimated stream of hadrons. Thus, the whole stream of hadrons, called a *jet*, needs to be recognised and treated as one object. During Run 1 of the LHC and also in the earlier phases of Run 2, ATLAS reconstructed jets either only from tracks or only from topoclusters. Most analysis used the latter approach. The calorimeter can detect neutral particles, unlike the tracker. The energy resolution for a charged pion in the detector is specified [38] as

$$\frac{\sigma(E)}{E} = \frac{50\,\%}{\sqrt{E}} \oplus 3.4\,\% \oplus \frac{1\,\%}{E}, \tag{3.1}$$

whereas the design resolution of the track measurement is

$$\sigma(\frac{1}{p_\mathrm{T}}) \cdot p_\mathrm{T} = 0.036\,\% \cdot p_\mathrm{T} \oplus 1.3\,\%. \tag{3.2}$$

Energies and transverse momenta in both formulas are given in GeV. From these formulas, it is clear that the track resolution at low p_T (or low energy) is superior to the calorimeter resolution. In addition, tracks are associated with a vertex and thus allow the rejection of pile-up. Therefore, the jet reconstruction can be improved by combining information from the ID and the calorimeters.

Particle Flow

ATLAS uses the *particle flow* algorithm (often abbreviated as *PFlow*) to reconstruct individual hadrons in the jet. A schematic of this algorithm can be found in Figure 3.6 and a more thorough description in [51].

In the beginning, tracks are selected using *tight* criteria. In particular, this means at least nine hits in the Pixel and SCT detectors, with no missing hits in the Pixel detector. Tracks must fulfil $p_\mathrm{T} > 500\,\mathrm{MeV}$ and $|\eta| < 2.5$, in order to be fully inside the ID. Reducing the p_T threshold to 400 MeV, i. e. the standard threshold for tracks, would increase the computation time significantly without offering a large improvement in the jet resolution. A too high momentum of $p_\mathrm{T} > 40\,\mathrm{GeV}$ will also cause the track to be ignored by the algorithm. Tracks with such a high momentum are usually only poorly isolated and thus it would be difficult to remove the energy associated with it from a topocluster. But even in jets with $40\,\mathrm{GeV} < p_\mathrm{T} < 60\,\mathrm{GeV}$, such tracks are very rare. Also, tracks that are matched to an electron or muon identified at the medium WP without any isolation requirements are ignored. The algorithm to subtract calorimeter deposits is optimised for hadronic showers and would not handle leptons correctly.

These list of eligible tracks is then matched to the closest topocluster within

$$\Delta R' = \sqrt{\left(\frac{\Delta\phi}{\sigma_\phi}\right)^2 + \left(\frac{\Delta\eta}{\sigma_\eta}\right)^2}. \tag{3.3}$$

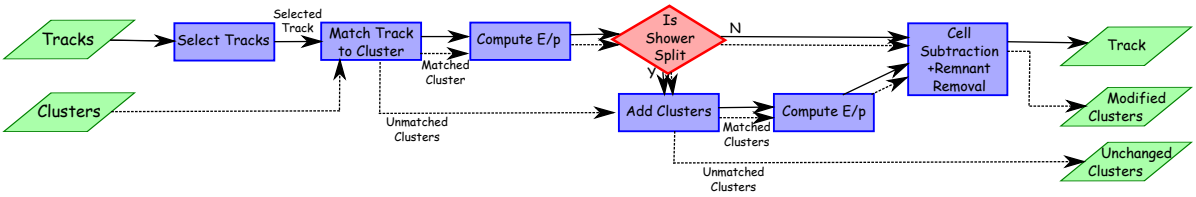

Figure 3.6.: Flowchart of the particle flow algorithm. Figure from [51].

Here, σ_ϕ and σ_η are the standard deviations of the distance of the constituent cells from the topocluster barycentre in each direction. They are required to be at least 0.05. A cluster-track pair needs to satisfy $\frac{E^{\text{cluster}}}{p^{\text{track}}} > 0.1$. If no suitable pair within $\Delta R' < 1.64$ is found, it is assumed that the track did not cause a topocluster.

After identifying pairs of tracks and topoclusters, the energy deposited by the former needs to be subtracted from the latter. Using single, well isolated pions as reference, the energy deposit $< E_{\text{dep}} >= p^{\text{track}} < E^{\text{cluster}}_{\text{ref}}/p^{\text{track}}_{\text{ref}} >$ expected from a track with given momentum can be obtained. If this is larger than the energy E^{cluster} deposited in the topocluster, it is removed completely. Otherwise, the energy expected from the track is subtracted from the topocluster. In case it contains significantly less energy than expected, it is assumed that the particle did create more than one topocluster and all topoclusters within $\Delta R < 0.2$ are matched with the track. The energy subtraction is then performed cell-by-cell, moving outward from the track of the particle extrapolated through the calorimeter. If the energy in the remnant of the topocluster is compatible with fluctuations in the parton shower, the remnant is removed completely. Otherwise, the remnant is kept, as it may also contain energy from another nearby particle.

Finally, this will create a collection of tracks and remaining topoclusters without any double-counting between the subdetectors.

Jet Clustering

The individual particle flow objects need to be combined into jets, because only a jet recovers the kinematics of the final state quark or gluon. There are several algorithms available for this purpose. A common requirement is that they are *infrared and colinear* (IRC) *safe*. Neither the presence or absence of a low energy (*infrared*) particle nor the *colinear splitting* of a high-energy particle should change the reconstructed jet. From the available algorithms, the anti-k_t algorithm [52] is widely used in ATLAS. It defines two distance measures, the distance d_{ij} between two particles or pseudojets[3] i and j and the distance to the beam d_{iB}. They are defined as

$$d_{ij} = \min(p^{2p}_{\text{T,i}}, p^{2p}_{\text{T,j}})\frac{\Delta^2_{ij}}{R^2} \tag{3.4}$$

$$d_{iB} = p^{2p}_{\text{T,i}}. \tag{3.5}$$

Here, $\Delta^2_{ij} = (y_i - y_j)^2 + (\phi_i - \phi_j)^2$ denotes the distance in the plane of rapidity y and azimuthal angle ϕ, whereas R is the radius parameter. ATLAS uses $R = 0.4$ by default.

[3] A pseudojet is a combination of particles that does not yet constitute a jet.

The exponent for the anti-k_t algorithm is $p = -1$, though different choices also lead to IRC safe jet algorithms. The case of $p = +1$ corresponds to the k_t algorithm [53], whereas $p = 0$ is also known as Cambridge/Aachen algorithm [54, 55]. Jet clustering is done by combining the two closest entities into a new pseudojet. If $d_{ib} < d_{ij}$, the pseudojet has been clustered into a jet and is removed from the list of particles and pseudojets. This clustering proceeds until no more jets can be found.

The anti-k_t algorithm has a few advantages over other jet algorithms. The distance measure is dominated by the particle with larger p_{T}, which makes it resilient towards the presence of additional low p_{T} particles, e. g. from pile-up. As a consequence of this, the size and shape in the $y - \phi$ plane is very regular, almost a circle.

Jet Energy Calibration

The energy of jets needs to be calibrated after clustering in order to account for the impact e. g. of pile-up or the jet composition on the measured energy. This correction is performed in several steps based on MC simulations, which are described extensively in [56] and summarised in Figure 3.7. Pile-up effects are mitigated first in an area-based correction, where the median p_{T} density $\rho =< p_{\mathrm{T}}/A >$ is used to subtract the expected p_{T} from pile-up, ρA, depending on the area of the jet. ρ is derived from k_t jets[4] within $|\eta| < 2$. However, due to the way ρ is derived, some dependency of the p_{T} of the anti-k_t jet on the pile-up is observed. This is mitigated by the residual correction, which compares the reconstructed and true jet p_{T} as a function of the number of primary vertices N_{PV} and the average pile-up μ.

Next, the reconstructed jet energy needs to be corrected to its truth value via the *Jet Energy Scale* (JES) correction. This is done by determining the average jet response $\mathcal{R}$ as the mean value of a Gaussian fit to the $E^{\mathrm{reco}}/E^{\mathrm{true}}$ distribution in dijet MC samples. The jet response is determined in bins of E^{true} and then numerically inverted to obtain it as a function of E^{reco}. This step is necessary because sampling calorimeters do not have a linear energy response.

The jet response varies depending on e. g. the transverse expansion of the jet, whether it was initiated by a gluon or a quark and, if the latter, also the flavour will have an impact on the jet response. In order to improve the resolution in these various cases, a *Global Sequential Calibration* (GSC) is applied. It does not vary the JES derived previously. Based on six different observables, such as the number of tracks or the fraction of energy deposited in the last electromagnetic or first hadronic calorimeter layer, a scale factor for each is determined and applied one after the other.

The final part of the calibration sequence is the *in-situ calibration*, which compensates the differences between simulation and data in the jet response. In principle, this is done by balancing the jet p_{T} against a well-calibrated reference object and then forming the ratio $c = \mathcal{R}^{\mathrm{data}}_{in\ situ}/\mathcal{R}^{\mathrm{MC}}_{in\ situ}$ of the jet responses in data and MC. At first, the η *intercalibration* calibrates jets in different eta regions of the detector against each other, especially those outside the most central region ($0.8 < |\eta| < 4.5$). The dijet asymmetry

[4] The k_t algorithm is chosen here because it creates jets that include a uniform, soft background.

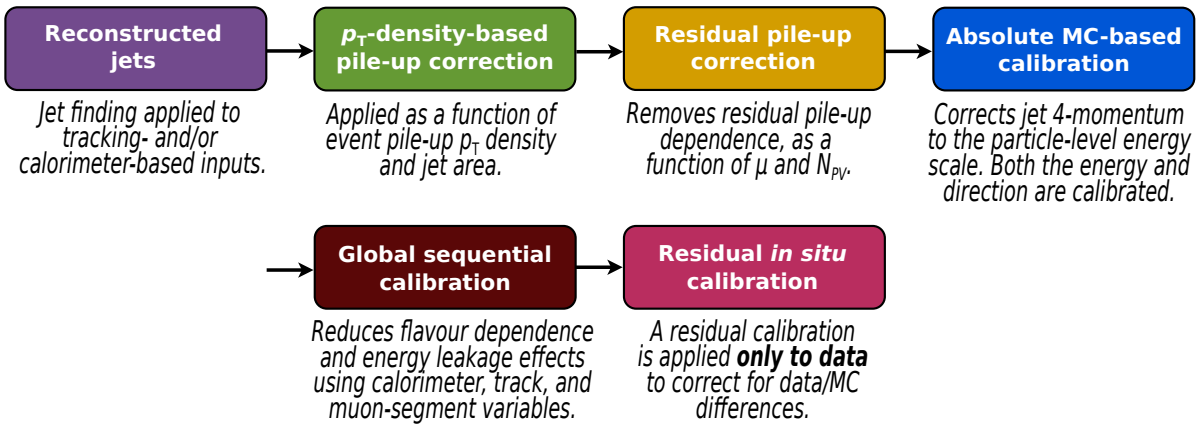

Figure 3.7.: Flowchart of the jet calibration procedure. Figure from [56].

is used to determine the difference in the jet response between the η regions. Using this differences, it is possible to transfer calibrations obtained in the central region of the detector to the forward regions. Next, the actual momentum calibration is performed in Z+jet and γ+jet events. Photons or the Z-boson reconstructed from an $e^{\pm}e^{\mp}$ or $\mu^{\pm}\mu^{\mp}$ pair serve as a reference object with a well-calibrated p_{T}. It is assumed that all $E_{\mathrm{T}}^{\mathrm{miss}}$ in this event originates from jet mismeasurement, so that the correct jet calibration will lead to $E_{\mathrm{T}}^{\mathrm{miss}} = 0$. Z+jet events allow to start the calibration in the range 17 GeV to 1 TeV, whereas γ+jet events have a higher threshold in order to avoid jets faking photons and cover the 25 GeV . . . 1.2 TeV range. Finally, the jet calibration is extended to even higher p_{T} using multijet events. For this, events with a single jet of very high p_{T} recoiling against jets of smaller, previously calibrated p_{T} are selected. Applying this procedure twice allows to extend the jet calibration up to 2.4 TeV.

A final check finds that the in-situ calibration does not change with N_{PV}, indicating that the pile-up corrections applied throughout the calibration chain indeed work as intended.

Pile-Up Suppression

Several pp collisions occur in each bunch crossing. So far, this has been accounted for only with an average-based subtraction of this pile-up. However, only jets originating from the hard-scatter vertex are of interest for the analysis. In the central region, tracking information from the ID can be used to differentiate hard-scatter jets from pile-up. The *Jet Vertex Tagger* (JVT) algorithm [57] combines two low-level observables to identify the fraction of jet momentum originating from the hard-scatter vertex. It assigns a score between zero for pile-up-like and one for hard-scatter-like jets to each jet. For forward jets (i. e. $|\eta| > 2.5$), no tracking information is available. Instead, the *forward JVT* (fJVT) algorithm [58] first selects central pile-up jets by requiring a JVT score smaller than 0.2. Assuming that each pile-up vertex has only one forward jet, the

forward jet p_{T} is compared to the $p_{\mathrm{T}}^{\mathrm{miss}}$ of each pile-up vertex. If they perfectly match, an fJVT score of 1 indicates that the forward jet is indeed a pile-up jet. On the other hand, a score close to zero indicates a hard-scatter forward jet.

Identification of Jets Originating from b-Quarks

The jet reconstruction presented so far is not able to identify the flavour of the quark that started a jet. However, knowledge of this is important for many measurements and searches, and for b quarks (to a lesser extent also c quarks), this is challenging but possible. ATLAS uses a two-staged approach described extensively in [59]. At first, a set of low-level algorithms extracts different properties of the tracks present in a jet, then a high-level algorithm combines them.

- The *IP2D* and *IP3D* algorithms investigate the signed impact parameter significance $S_{d_0} = d_0/\sigma_{d_0}$. d_0 is the transverse impact parameter, i. e. the closest approach of the track to the collision in the r direction. Negative values are possible if the closest approach is on the opposite side of the collision point. The IP3D algorithm also considers the longitudinal impact parameter significance S_{z_0}.

- The *RNNIP* algorithm uses a recurrent neural network (RNN) does additionally also consider the momentum fraction of a track and its distance towards the jet axis. It can exploit correlations between these two and calculate probabilities for a jet to originate from a b, c or light quark. These probabilities are then combined into a single score that is used as final discriminant.

- Secondary vertices are identified by the *SV1* algorithm. It uses an iterative fit to find secondary vertices inside a jet and can reject those arising from the decays of light hadrons or interactions with the detector material. Eight properties of the final reconstructed secondary vertex are then provided as input for the high-level taggers.

- The *JetFitter* tagger reconstructs the decay chain of the b (or c) hadron with a Kalman filter, making use of characteristic elements of this structure.

While all of these low-level algorithms can somewhat distinguish jets from b hadrons, the best discrimination is achieved by combining these. In Run 2, ATLAS uses a multi-layered feed-forward neural network for this purpose. The *DL1r* algorithm combines all of the low level algorithms presented above. It then calculates the probability of the jet originating from a b (p_b), c (p_c) or light (p_{light}) quark and combines them into a single discriminant.

$$D_{\mathrm{DL1r}} = \ln \frac{p_b}{f_c p_c + (1 - f_c) p_{\mathrm{light}}}. \tag{3.6}$$

Here, f_c is a tunable parameter which allows tuning the relative rejection power of the discriminant for c-jets and light-flavoured jets. While not of interest for this thesis, a similar discriminant can be formed to identify c jets without any changes to the neural network.

3.3.5. $E_{\mathrm{T}}^{\mathrm{miss}}$ Reconstruction

Neutrinos or hypothetical long-lived particles from BSM processes would escape the detector unnoticed and cannot be reconstructed directly. However, due to momentum conservation, the momenta of all outgoing particles should cancel in the $x-y$ plane. An imbalance here, the missing transverse momentum $E_{\mathrm{T}}^{\mathrm{miss}}$, would be a sign of escaping invisible particles. Its definition and performance is described in [60].

$$\vec{E}_{\mathrm{T}}^{\mathrm{miss}} = \sum_{i=e,\mu,\gamma,j} \vec{E}_{\mathrm{T}}^{\mathrm{miss,\,i}} + \vec{E}_{\mathrm{T}}^{\mathrm{miss,\,soft}} \tag{3.7}$$

The first, *hard term* in Equation (3.7) consists of reconstructed objects which have been calibrated and thus have a well-known four-momentum. Several $E_{\mathrm{T}}^{\mathrm{miss}}$ working points are defined, which differ in the pile-up rejection cuts applied to jets.

All basic objects that are not matched to a reconstructed object constitute the *soft term* of the $E_{\mathrm{T}}^{\mathrm{miss}}$. It can be either calculated from the calorimeter or from tracks. The track-based soft term (TST) includes all tracks with $p_{\mathrm{T}} > 400\,\mathrm{MeV}$ in the ID ($|\eta| < 2.5$) that are associated with a hard scatter vertex, i. e. $S_{d_0} < 2$ and $z_0 \sin\theta < 3.0\,\mathrm{mm}$. Tracks with a nearby electron, photon or hadronically decaying τ lepton are excluded. Similarly, isolated tracks with $p_{\mathrm{T}} > 120\,\mathrm{GeV}$ and no associated calorimeter deposit of compatible magnitude are excluded in order to remove mismeasured tracks.

$E_{\mathrm{T}}^{\mathrm{miss}}$ Significance

$E_{\mathrm{T}}^{\mathrm{miss}}$ can originate both from a real imbalance, caused e. g. by final-state neutrinos, or arise from mismeasurement of reconstructed objects. To distinguish these two cases, one can define an $E_{\mathrm{T}}^{\mathrm{miss}}$ significance. The most simple case, event-based $E_{\mathrm{T}}^{\mathrm{miss}}$ significance, uses the total activity in the event as a proxy for the $E_{\mathrm{T}}^{\mathrm{miss}}$ resolution: $\mathcal{S} = E_{\mathrm{T}}^{\mathrm{miss}}/\sqrt{E_{\mathrm{T}}}$. However, a more sophisticated approach, the *object-based $E_{\mathrm{T}}^{\mathrm{miss}}$ significance*, is now used in ATLAS and described in [61]. It considers the resolution of each object in order to determine the likelihood of observing a given $E_{\mathrm{T}}^{\mathrm{miss}}$ assuming a true invisible transverse momentum of $p_{\mathrm{T}}^{\mathrm{inv}}$.

$$\mathcal{S} = 2\ln\frac{\max_{p_{\mathrm{T}}^{\mathrm{inv}}\neq 0}\mathcal{L}(E_{\mathrm{T}}^{\mathrm{miss}}|p_{\mathrm{T}}^{\mathrm{inv}})}{\max_{p_{\mathrm{T}}^{\mathrm{inv}}=0}\mathcal{L}(E_{\mathrm{T}}^{\mathrm{miss}}|p_{\mathrm{T}}^{\mathrm{inv}})} \tag{3.8}$$

This equation can be simplified with three assumptions. Firstly, all objects are assumed to be measured independently. Then, the measured p_{T}^{i} is assumed to follow a Gaussian distribution around the true transverse momentum π_{T}^{i}. The resolution in the direction of the particle ($\sigma_{p_{\mathrm{T}}}$) and perpendicular to it ($p_{\mathrm{T}}\cdot\sigma_{\phi}$) can be expressed in the form of a covariance matrix $\mathbf{V}^{i}$. Finally, momentum conservation implies $p_{\mathrm{T}}^{\mathrm{inv}} = \sum_i \pi_{\mathrm{T}}^{i}$. With these three assumptions, the likelihood function follows a Gaussian distribution and the likelihood ratio in Equation (3.8) transforms to

$$\mathcal{S}^2 = \vec{E}_{\mathrm{T}}^{\mathrm{miss}\,T}\Big(\sum_i \mathbf{V}^{i}\Big)^{-1}\vec{E}_{\mathrm{T}}^{\mathrm{miss}}. \tag{3.9}$$

Note that the covariance matrices need to be rotated into xy coordinates before summation.

The performance of the object-based $E_{\mathrm{T}}^{\mathrm{miss}}$ significance has been tested by using it to separate $ZZ \to ee\nu\nu$ events from a $Z \to ee$ background. Depending on the exact selection used (number of jets, $E_{\mathrm{T}}^{\mathrm{miss}}$ thresholds), it performs usually significantly better than both the event-based $E_{\mathrm{T}}^{\mathrm{miss}}$ significance or a simple $E_{\mathrm{T}}^{\mathrm{miss}}$ cut, but never worse than the other two observables.

4. Testing the Endcap Module Thermal Cycling Setup

This chapter introduces the upgrades to the ATLAS tracking system planned for the HL-LHC. Then it proceeds to describe the author's involvement around commissioning the prototype of a thermoelectrical test stand for tracking detector modules and the automation of it.

4.1. The ITk Project

The HL-LHC will increase the luminosity to up to $7.5 \cdot 10^{34}\text{cm}^{-2}\text{s}^{-1}$, which will increase the number of simultaneous pp collisions (pile-up) to $< \mu >= 200$, eight times higher than the design value for the LHC. ATLAS is planned to collect an integrated luminosity of $250\,\text{fb}^{-1}$ annually for at least ten years. This very challenging environment would quickly exceed the radiation limits of the existing SCT and Pixel detector. Also, the occupancy[1] of the existing detector would be excessively high (approaching 100 % in the TRT), thus degrading the track finding performance significantly.

Therefore, the ATLAS collaboration will build the *Inner Tracker* (ITk), an all-silicon tracking detector replacing the existing Inner Detector. An extensive description of the ITk can be found in [62]. It is designed to operate well in the harsh environment at the HL-LHC. In particular, the occupancy will stay at $\lesssim 1\,\%$ in all layers of the ITk and a particle should typically transverse 13 layers of sensors for good track finding. Also, the tracking detector will cover the pseudorapidity $|\eta| < 4$, a significant improvement over the $|\eta| < 2.5$ coverage of the ID. Apart from the improved sensitivity to forward physics processes, this will also help e. g. with the $E_{\text{T}}^{\text{miss}}$ resolution or pile-up rejection.

4.1.1. The Pixel Detector

At small radii, sensors with $50 \times 50\,\mu\text{m}^2$ large pixels covering in total $12.74\,\text{m}^2$ are used. In the barrel region, they are arranged in five layers (cf. Figure 4.1), the inner two of which can be replaced separately due to radiation damage degradation. Similarly, the inner one of the four endcap rings can also be replaced.

[1] The percentage of readout channels marked as "hit" in any given bunch crossing.

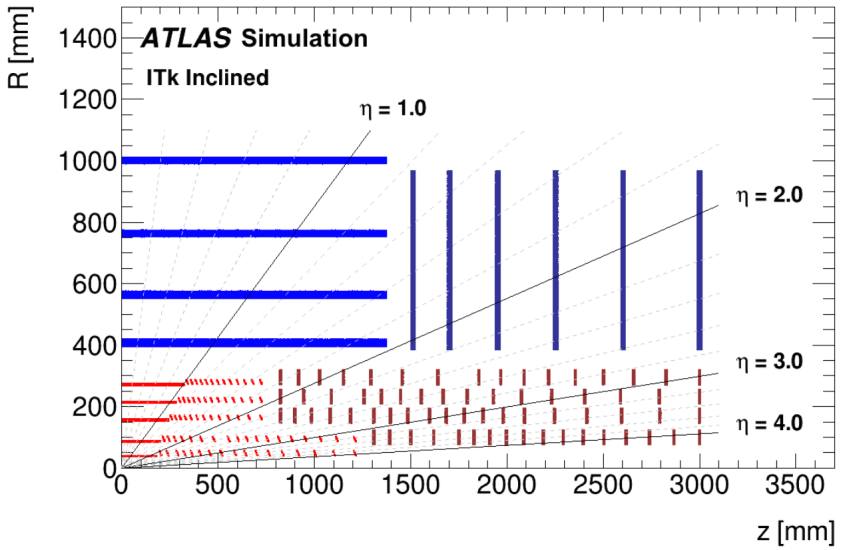

Figure 4.1.: Schematic layout of one quadrant of the ITk. Active elements of the Pixel detector are shown in red, those of strip detector in blue. Support structures are not shown. Figure from [62].

4.1.2. The Strip Detector

At higher radii, the barrel region contains four layers of strip sensors, whereas the endcap contains six disks each. Each layer consists has two sets of sensors, mounted on either sides of the support structure and at a slight angle to each other. This *stereo angle* improves the position resolution of the tracks along the strip direction. In total, the ITk strip detector will have ca. 60 million channels spread across 165 m^2 of silicon sensors. Sensors are oriented such that the resolution is highest in the ϕ direction, i. e. the strips are parallel to the beam axis in the barrel and perpendicular to it in the endcap.

4.1.3. The ITk Strip Endcap

In the endcap, the sensor modules are mounted on wedge-shaped carbon fibre structures called petals (Figure 4.2). These petals contain embedded coolant pipes, as well as connections for data and power. Petals are mounted slightly overlapping in rings within a carbon fibre global structure (Figure 4.3). On the outside of this structure, cables and pipes for data, power and cooling are carried from the petals to their respective supplies outside of the detector.

4.1.4. Endcap Strip Modules

The detector is assembled from *modules* with a size of roughly 100 cm^2. Figure 4.4 shows such a module consisting of a sensor (grey) and its readout and power electronics. Individual strip channels in the sensor have a length ranging from 1.5 to 5 cm, with the shortest strips being placed in the regions with highest particle flux. The pitch

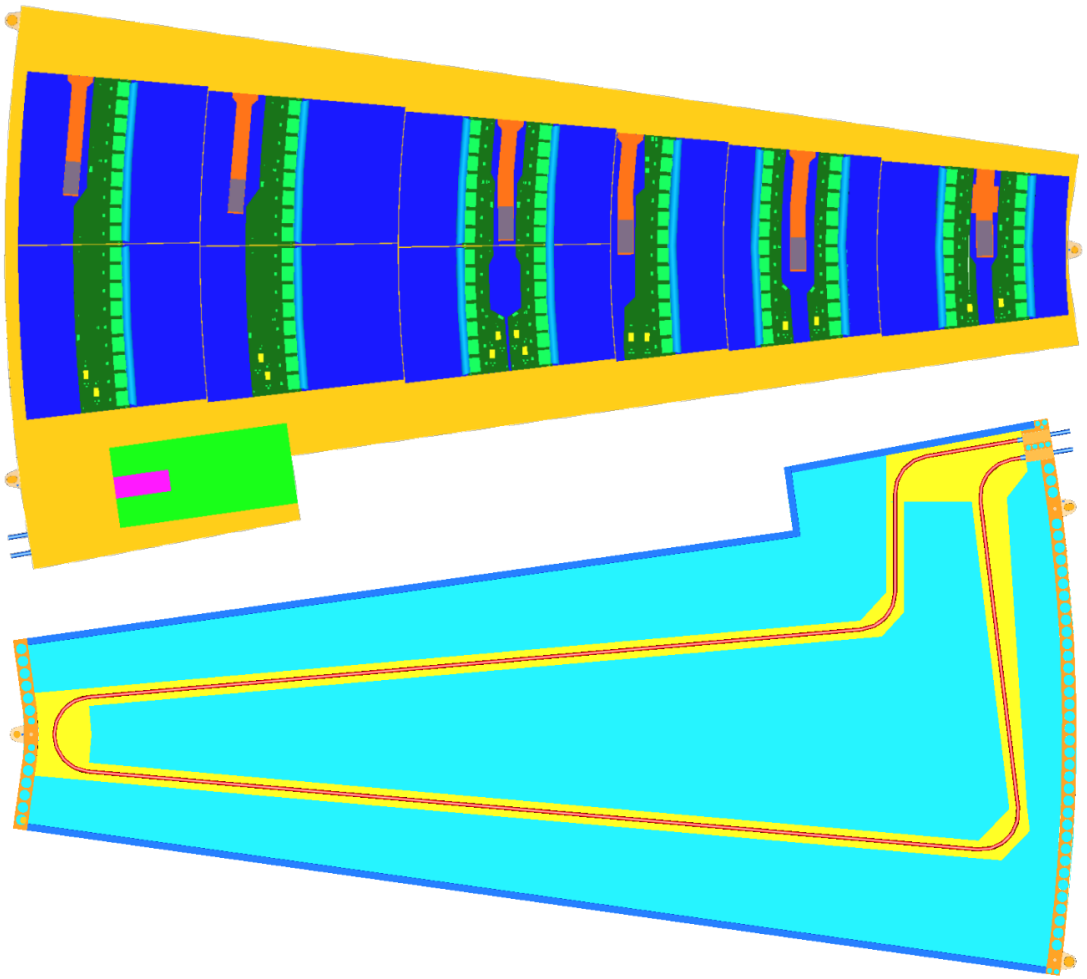

Figure 4.2.: Schematic view of a petal showing the modules mounted on the petal (top) and the position of the coolant pipes inside the petal (bottom). In this drawing, R5 modules are on the left (outer) side of the petal, whereas the R0 module is at the right in the innermost position. Due to the wedge-shape of the petal, all six module types differ in size and shape. Figure from [62].

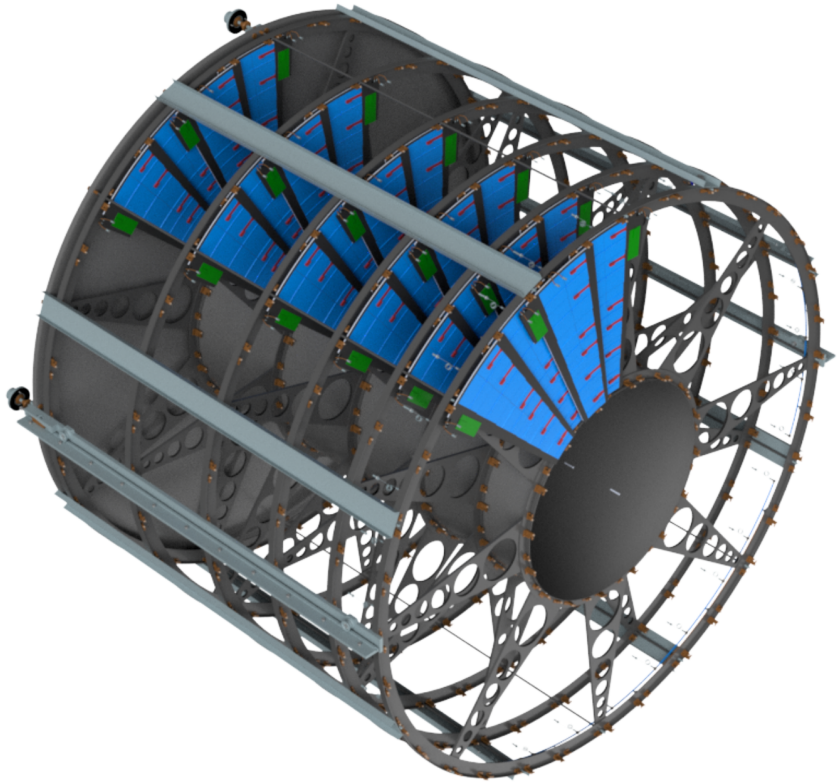

Figure 4.3.: Support structure of the ITk strip endcap. For illustration purposes, one *electrical service sector* is populated with petals. Figure from [62].

is relatively uniform across the whole radius and varies between 70 and 80 μm. On these sensors, two types of *Printed Circuit Boards* (PCB) are mounted. The *hybrids*, highlighted in green, hold several *ATLAS Binary Chips* (ABC) that read out individual sensor strips to which they are connected via wire bonds. One ABC and its wire bonds are highlighted in yellow. They relay the information to a single *Hybrid Controller Chip* (HCC, white outline), which communicates with the readout electronics outside of the module. Between the two hybrids is the powerboard, highlighted in red, which, as the name suggests, provides electrical power to both the hybrids and the sensors. In addition, it holds an *Autonomous Monitor and Control Chip* (AMAC), that can monitor both the powerboards and the hybrids and e. g. perform functionality and performance tests of the module.

The module shown in Figure 4.4 is mounted on a *test frame*, a rectangular PCB that holds the module during testing and has connectors for power and data. It can be equipped with foam protecting from electrostatic discharge and a Plexiglas cover in order to protect the module. A test frame with mounted Plexiglas cover is also called *transport box*, as the module can be safely transported in such an enclosure.

Due to the wedge shape of the petals, the endcap modules have to be shaped accordingly, which results in six different module geometries for the endcap. The innermost modules, called *R0*, are significantly smaller than the outermost modules, called *R5*.

4.2. Quality Control Tests of ITk Modules

It is essential that all components of the ITk perform well and reliably during operation. Therefore, extensive *Quality Control* (QC) of all involved components is performed. As part of this QC process, the assembled modules will have to be tested both at low and high temperatures according to the sequence shown in Figure 4.5. The low temperature tests will be conducted at the operating temperature of the detector of $-35\,^{\circ}\mathrm{C}$. Should the detector ever reach $+40\,^{\circ}\mathrm{C}$ during operation, the interlock system will automatically turn it off. But this also means that modules must remain operational at least up to this temperature. At each temperature extreme reached during cycling, a short *confirmation test* taking approx. 5 min is performed, which consists of

- **Noise Occupancy** — Measure the number of channels claiming a hit depending on the noise threshold.
- **Strobe Delay** — Measure the time between the command to inject a calibration pulse in the sensor and the actual pulse.
- **Three Point Gain** — Perform threshold scans for three injected charges (0.5 fC, 1 fC, 1.5 fC) and determine a response curve. Additionally, this test can also determine the input noise for each channel [62, Chapter 7].

In addition, two long *characterisation tests* with an expected duration of 1 h will be performed, one at $-35\,^{\circ}\mathrm{C}$ before the thermal cycling and another one at room temperature after cycling. These expand the characterisation tests by measurements of e. g. the

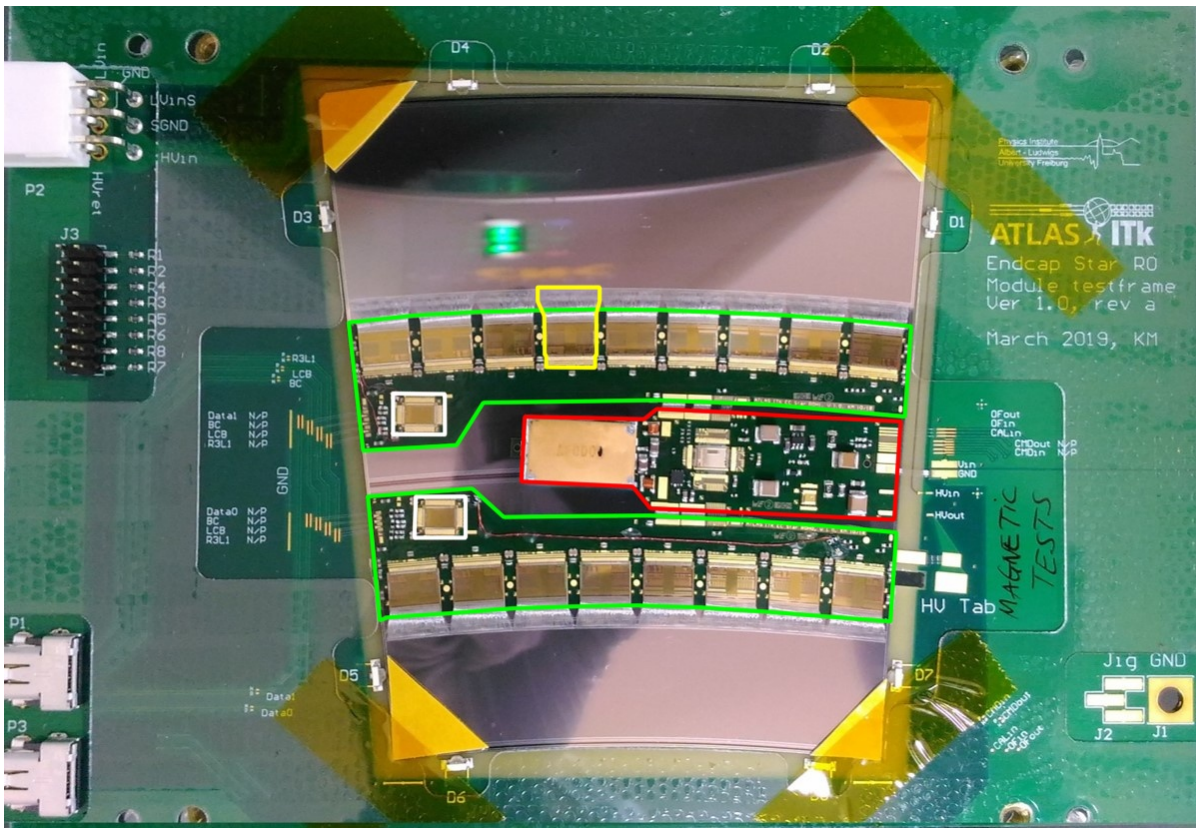

Figure 4.4.: Photograph of an endcap module on a test frame. The hybrids are highlighted in green, whereas the powerboard is marked red. Also highlighted are one ABC with its wire bonds (yellow) and the two HCCs (white).

leak current as a function of the bias voltage or an extended response curve test that includes more charges. With this sequence it is ensured that the assembled modules meet the performance requirements and can be used in the detector. Also, damages such as broken wire bonds can be identified, so that a module not passing these tests can possibly be repaired.

4.3. Design of the Endcap Thermal Cycling Setup

The DESY group has designed and built the test stand to perform the thermo-electrical tests described in Section 4.2 and produced all setups for endcap institutes.

The main driver for the performance goals of the thermal cycling setup (commonly referred to as *coldbox*) is that it can run one sequence as shown in Figure 4.5 overnight. Therefore, the sequence itself should not take longer than approximately 20 h. This will enable maintaining the production throughput at module production sites. In total, approximately 4 h of the sequence will be required to perform the necessary tests. A preliminary performance estimate of the chiller leads to a delay of 1 h after beginning the sequence until reaching −35 °C. In order to meet the overall time constraint, the

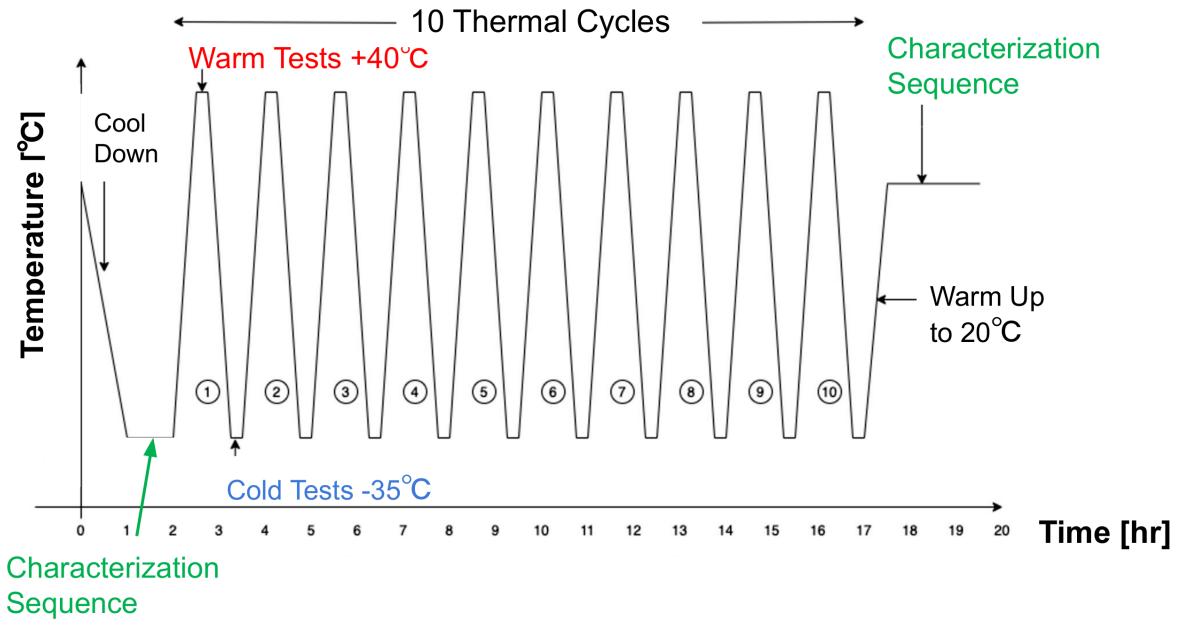

Figure 4.5.: Schematic of the thermal cycling sequence that will be used for module QC. Figure adapted from [63].

ten warm-cold cycles should not exceed a duration of 15 h, which leads to a design goal of 1 h per cycle.

Figure 4.6 shows a sketch of the coldbox with one side wall removed. On the inside, four transport boxes mounted on four *chucks* can be seen. These chucks are insulated from the side and the bottom against the air inside the coldbox, so that only their top plate is visible. They are connected to the coolant pipes. An external chiller (Julabo Dyneo DD-1000F [64]) will remove the waste heat from the copper chucks. On the front side (removed), valves are mounted to control the dry air flow. Inside the box, the dry air is first guided through a collar around the coolant return pipes and then distributed to the transport boxes and other positions inside the coldbox. The wall at the far end is occupied by feed-throughs for cables. The rightmost one is used for the temperature and humidity sensors mounted inside the box, whereas the other four have power and electrical data connections for one chuck and one module each. On the outside, several latches and one safety lock are visible, the latter one will prevent an opening of the box when the conditions inside are hazardous. This means in particular conditions when room air entering the coldbox would cause condensation or when high voltage is applied to the modules, as this would risk injury of the operator. The coldbox constitutes a Faraday cage, thus effectively shielding the modules against external noise sources.

The core element of the coldbox are the four chucks, an exploded view of which can be seen in Figure 4.7. From bottom to top, it consists of a copper base plate (part nr. 20), on which a second copper piece (10) is mounted. This contains serpentines on its underside so that the coolant will have a large contact area with the copper. On top

of this, four Peltier elements[2] (210) cool down the parts mounted above. The cooling of the modules is achieved by the Peltier elements. The coolant is required to remove heat from the warm side of the Peltier elements and thus increase their performance. They are held in place by a Teflon plate (50), which also provides additional insulation against the air in the box. A self-adhesive graphite foil is applied to the Peltier elements to improve the thermal contact. On top of the Peltier elements, two aluminium plates (40 and 30) with a graphite sheet (11) for better heat contact provide a place to mount the devices under test. In previous studies, it was found that this configuration reduces electric noise from the Peltier elements. Finally, a thermally conducting and electrically insulating foil (90) on top of the aluminium plate prevents any high voltage from the module inside the transport box (190) to reach the chuck.

The topmost aluminium plate (30) was designed to accommodate all six different types of modules used in the endcap.

4.4. Commissioning of the Prototype

The design of the coldbox needs to be thoroughly tested to ensure that it can meet the criteria for cycling defined in Figure 4.5. A variety of tests were performed with the prototype that investigated the choice and placement of insulation, the number of Peltier elements as well as operating conditions of Peltier element and chiller. Three sets of tests were conducted with the prototype. Section 4.4.1 presents tests performed with the first iteration of the thermal cycling setup design. Section 4.4.2 investigates the effect of insulation, whereas the final set of tests in Section 4.4.3 focuses on the operation of Peltier elements and the chiller.

When the tests presented in this section were performed, the specification of the requirements was not finalised yet. In particular, it was assumed that the target temperatures have to be measured with a temperature sensor integrated into the module instead of on the chuck. Also, the exact sensor placement, readout electronics and peripheral devices were not yet decided and evolved based on the needs of the measurements and available equipment.

4.4.1. Preliminary Tests

Preliminary Tests with a Mock Module

The first design of the coldbox underwent tests of the thermal performance in order to validate it, Figure 4.8 shows the interior of the coldbox during these. Major differences between that status and Figure 4.6 are that the chucks are not insulated from the sides and the coolant pipes have twice the diameter. The chucks are raised and insulated from below with a foam mat. Another foam mat is placed on top of the chucks as

[2]Peltier elements are electrical heat pumps using the Peltier effect to transfer heat by applying an electrical current. Their main advantages are the small size and lack of moving parts or cooling liquids.

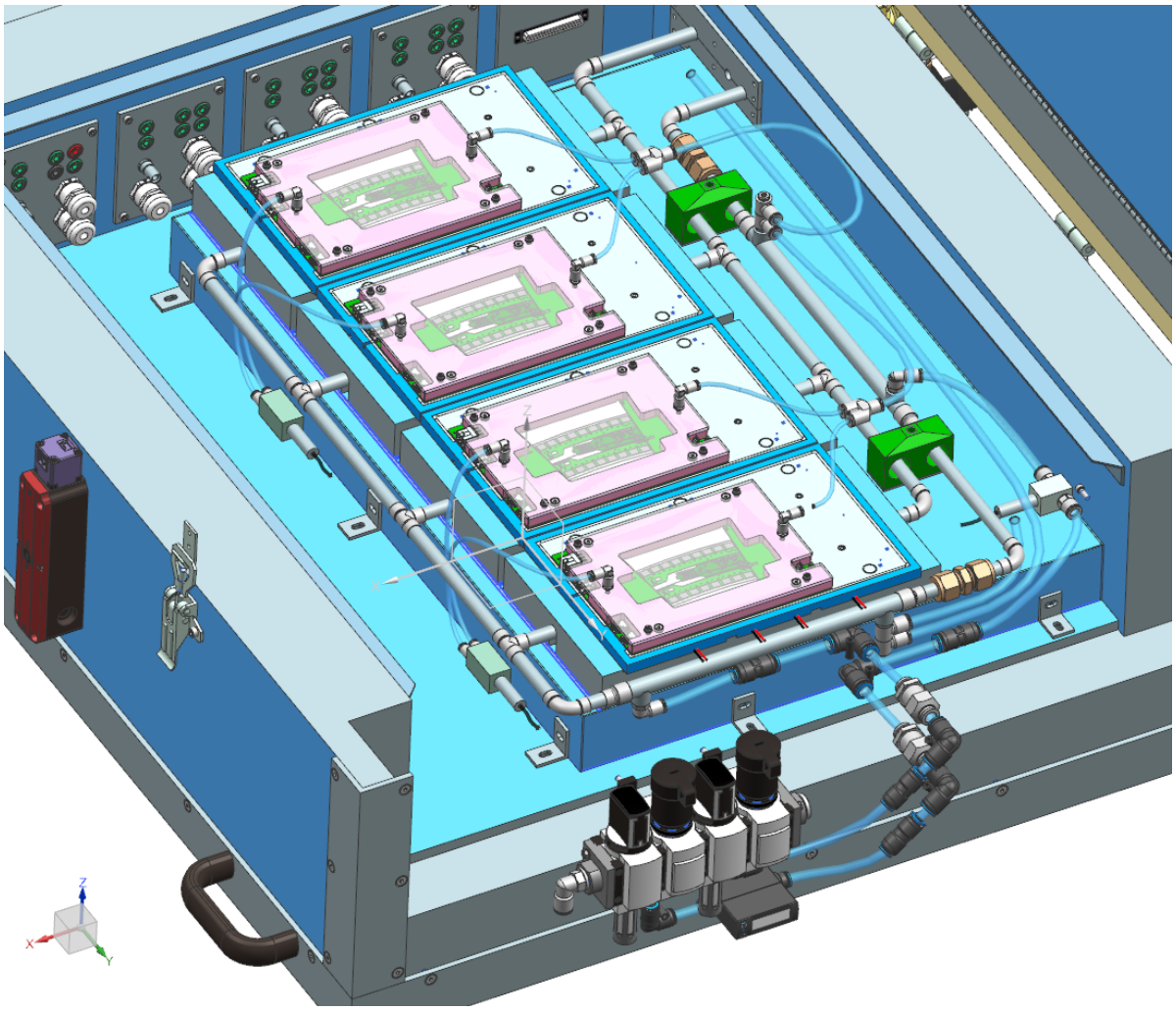

Figure 4.6.: CAD picture of the coldbox with one side wall removed. Figure by Sören Ahrens.

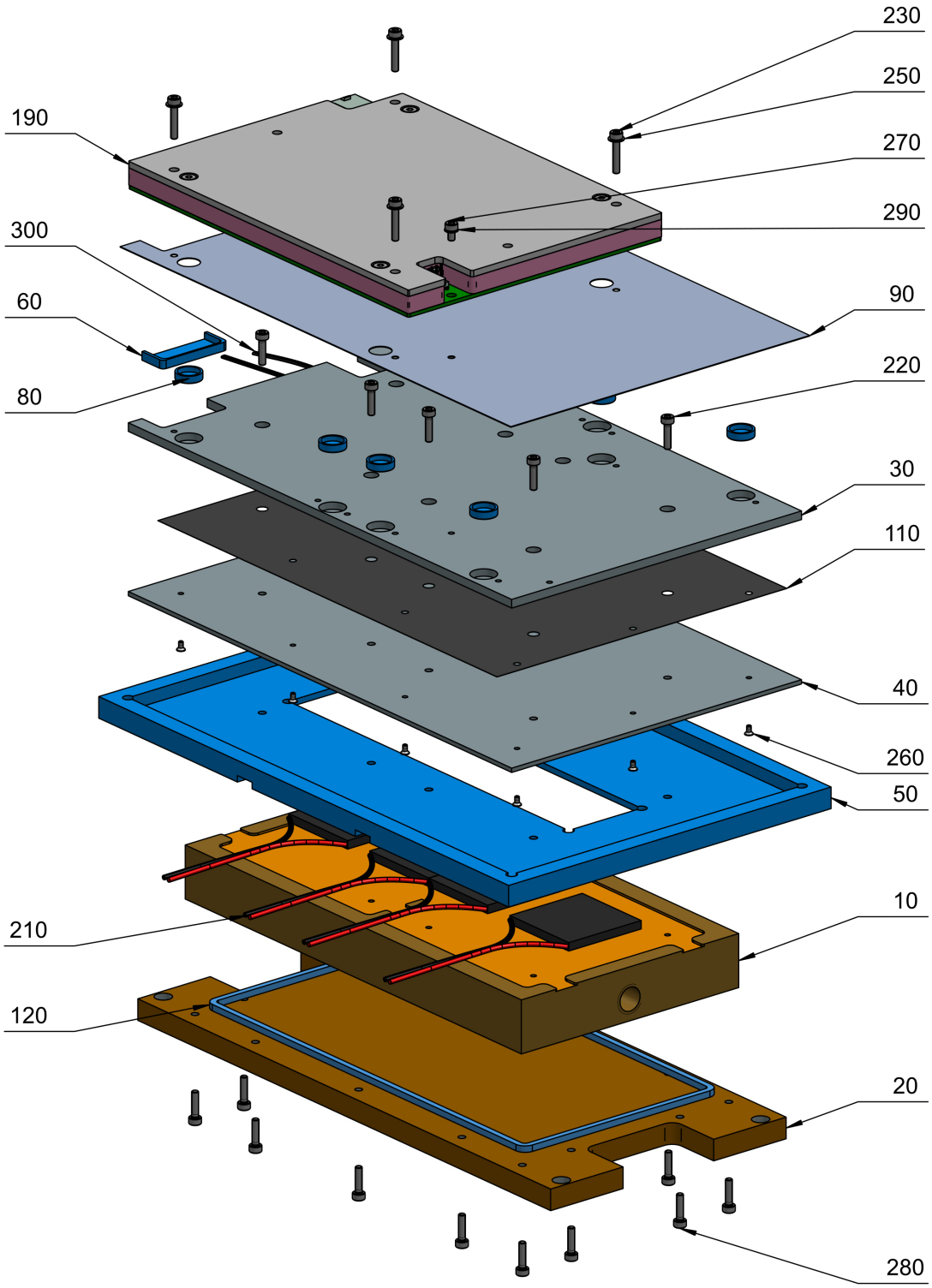

Figure 4.7.: Exploded view of a chuck. Figure by Sören Ahrens.

additional insulation. On chuck 3, the module is placed, whereas on chuck 2, a *mock module* consisting of an R0 test frame with a dummy silicon sensor, a heat-pad on top of the sensor, all enclosed in a module transport box, is mounted. The other chucks are equipped with heat-pads only. Each chuck was equipped with two $Q_C = 60\,W$ Peltier elements of type ETH-127-14-15 [65].

The Peltier elements were connected to one dual channel TTi CPX400DP [66] power supply, i. e. two chucks were connected to one channel. During this first test, the module was not available, thus is was replaced by a heat-pad. The other chucks were equipped with heat-pads mounted directly on top. In a real module, the sensor backplane[3] will be supplied with 550 V. The test frame on which the module is mounted has metallic thermal vias below the sensor in order to improve the thermal contact between module and chuck. However, this creates an electrical connection between the sensor backplane and the chuck. Therefore, chuck and test frame have to be separated with an electrical insulator. Kapton is a widely used insulator suitable for a huge temperature range and therefore an obvious choice. The thinnest available foil of only 25 μm thickness still has a breakdown voltage of 3 kV, more than sufficient for this use case. However, it is also a good thermal insulator with a thermal conductivity of only $0.2\,\frac{W}{m\cdot K}$ [67], therefore its effects on the thermal performance have to be investigated.

Using the chiller alone, the temperature on top of the chucks reaches $-23\,°C$ after approximately 1.5 h. For further cooling, the Peltier elements are supplied with a current between 2.7 A and 3.5 A. After reaching the minimum temperature, the heat-pads are turned on, delivering 8 W heat each. This is the waste heat of an R3 module, other modules have a lower waste heat of roughly 5.5 W.

Figure 4.9a shows the temperature insider the mock module and on the chuck during these tests. The mock module reached a temperature of $-37\,°C$ when placed on the Kapton foil, which is lower than the target temperature of $-35\,°C$. A whole cycle, i. e. heating the module from $-35\,°C$ to $+40\,°C$ and cooling it back down to $-35\,°C$ including the simulated tests, took approx 68 min.

In order to evaluate the influence of the Kapton foil on the temperature inside the mock module, the same test was run with the Kapton foil removed. Figure 4.9b shows that under this conditions, the mock module cools down to $-43\,°C$. This shows that Kapton has a significant influence on the thermal performance of the device. Therefore alternative insulating materials were considered.

Preliminary Tests with a Semi-Electrical R0 Module

After showing in Section 4.4.1 that the coldbox was able to reach the target temperature inside the mock module, the test was repeated with a semi-electrical R0 module[4]. During the test, module and heat-pads are turned on. With the module added, the coldbox is now set up exactly as in Figure 4.8. Since attaching a sensor inside the transport box of the R0 module would have damaged it, humidity was measured on the mock module. As can be seen in Figure 4.10, the dew point is well below the temperature on the module,

[3] The side of the sensor opposite to hybrids and powerboard.
[4] A mechanical dummy sensor with the real electronics on top.

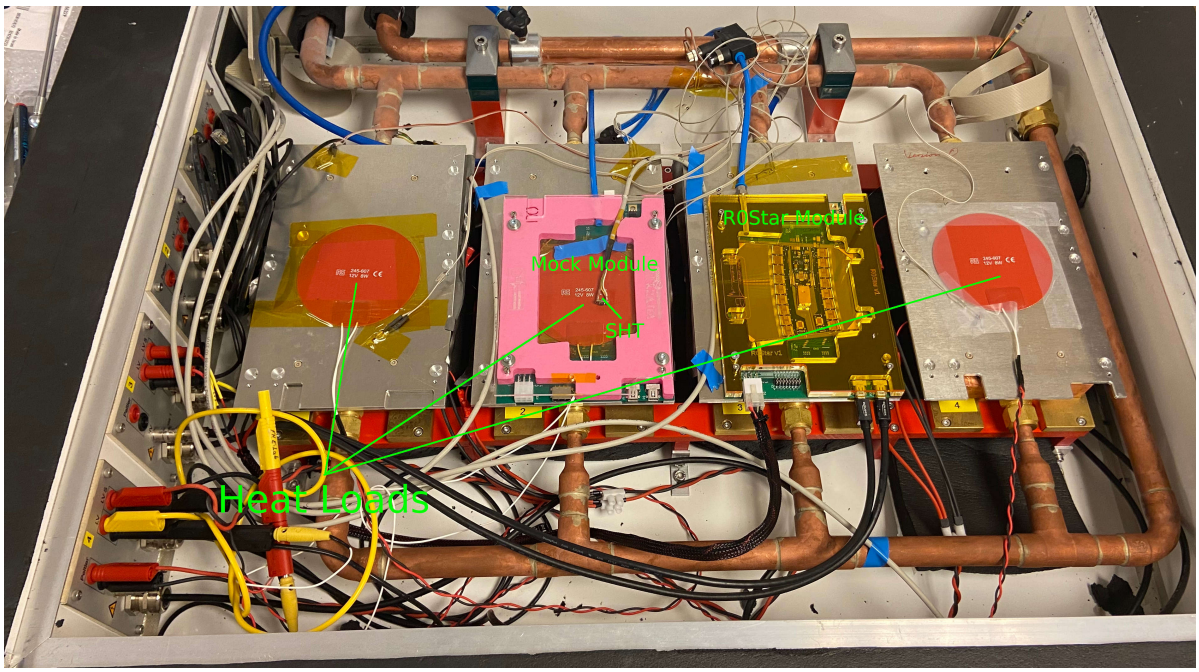

Figure 4.8.: The R0 module is placed on chuck 3, the mock module on chuck 2. The marking "SHT" indicates the position of the combined humidity and temperature sensor inside the mock module.

thus there is no risk of condensation. However, the minimum temperature reached in one of the hybrids was −34.4 °C, which is slightly below the target temperature. It is not clear why the other hybrid was significantly warmer. For the powerboard, a higher temperature is expected, as the power supply for the module, one DC-DC converter with an inductor coil, is placed there. The testing sequence was aborted when the readout of the module failed, thus it was not possible to run a temperature cycle.

Conclusions from the Preliminary Tests

- Kapton, even in thin layers, provides too much thermal insulation. A material with better heat transfer properties that still insulates electrically has to be found.
- Two Peltier elements are not enough to cool the module below −35 °C, but might be with a different electrical insulator
- Air convection has a significant impact on the thermal performance of the setup. Therefore, chucks and coolant pipes have to be insulated well against the air inside the box.
- The mock module seems to be able to reach lower temperatures than the R0 module.

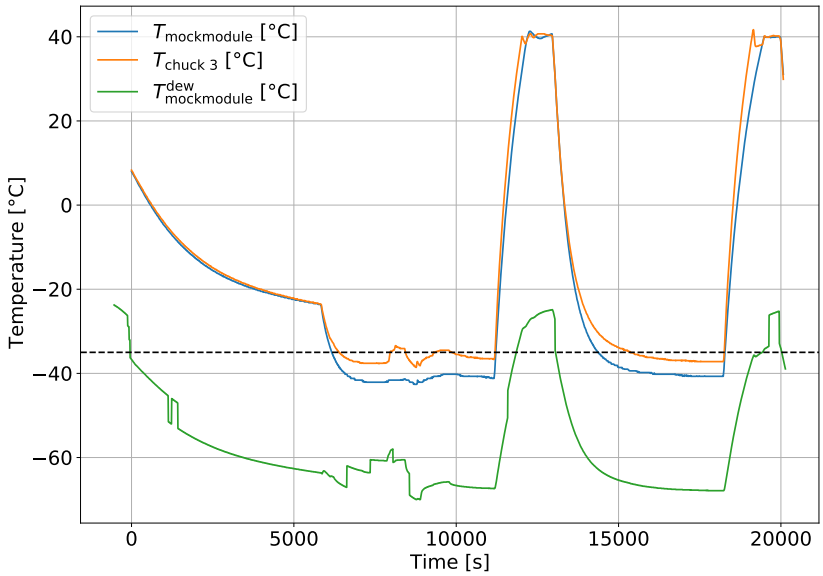

(a)

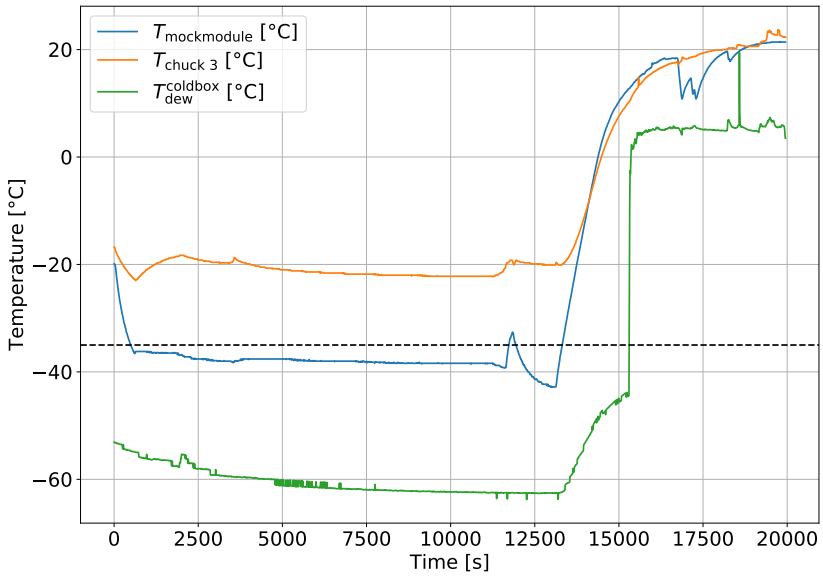

(b)

Figure 4.9.: Preliminary test results with (4.9a) and without (4.9b) Kapton foil between the mock module and the chuck. After performing the latter measurement, it was noticed that the temperature sensor on chuck 3 did not have proper contact with the chuck and thus showed higher temperatures.

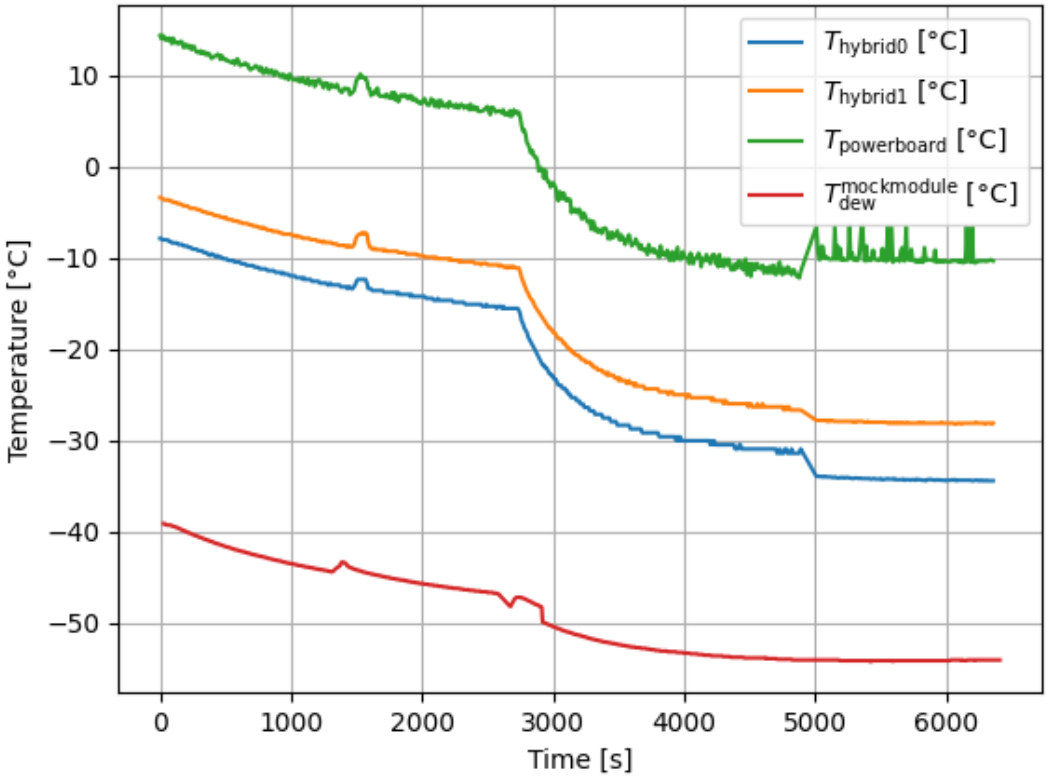

Figure 4.10.: Temperature of the hybrids and the powerboard of the semi-electrical R0 module. At $t \approx 5000\,\text{s}$, the readout of the temperature sensors module was changed to automatically adjust the sensor range for the most accurate reading.

4.4.2. Insulation Upgrade

After the preliminary tests, the chucks were insulated both from the sides and from the bottom with a new design, which now is the one already shown in Figure 4.6. Also, an electrically insulating foil of type TCIN-5,0S45F [68] with approximately twice the heat transfer of Kapton has been obtained. Since two Peltier elements have already proven to be only barely sufficient, the chucks holding module and mock module were equipped with three Peltier elements.

Surprisingly, a repetition of the test in Section 4.4.1 showed worse performance. In retrospect, it was most likely forgotten to cover the top of the modules with a foam mat, as has been done previously.

A dual channel Philipps PM 2812 [69] power supply was added to the periphery, so that the Peltier elements of each chuck now have a dedicated power source. Chuck 2 and 4 were connected to this power supply, whereas chuck 1 and 3, the latter carrying the mock module, was connected to the TTi CPX400DP. The PM 2812 is limited to $U_{\max} \cdot I_{\max} = 60\,\mathrm{W}$ per output, a limitation that is quickly reached during warmup. In contrast, the TTi CPX400DP can supply up to 420 W per output with currents and voltages exceeding the maximum values of the Peltier elements. This explains why in Figure 4.11 chuck 4 is warming up way slower than the mock module on chuck 3.

More interesting is the behaviour of the chiller temperature. $T_{\mathrm{coolant}}^{\mathrm{internal}}$ is measured in the bath of the chiller, while $T_{\mathrm{coolant}}^{\mathrm{external}}$ is measured at the coolant inlet of chuck 4. It can be seen clearly when the Peltiers are first turned on at $t \approx 8\,000\,\mathrm{s}$. During warm up, starting at $t \approx 10\,000\,\mathrm{s}$, the Peltier elements do at first cool down the coolant. But after a short time, their warm side is hot enough to also transfer heat to the cold side, thus causing a slow rise in coolant temperature. Starting at $t \approx 21\,000\,\mathrm{s}$, an alternative setup with two chucks cooling down and the other two heating up was tried. This does not lead to a rise in coolant temperature.

From these tests, it is concluded that

- the insulation of the top sides of the chucks against the air has a large influence.
- controlling two chucks with the same power supply does not allow accurate temperature control, which is especially important during the warm tests.
- during warm up, the Peltier elements will still heat up the coolant.
- in order to quickly reach +40 °C, a significantly stronger power supply than a PM 2812 is needed.

4.4.3. Thermal Cycling with Improved Setup

For a new set of measurements, chucks 1 and 2 are equipped with three Peltier elements, whereas chuck 3 and 4 were equipped with four. On top of chuck 1 and 3, TCIN-5,0S45F was applied. The latter also held the mock module. During the cooling phases, the current is regulated so that the Peltier elements generate 80 W waste heat per chuck.

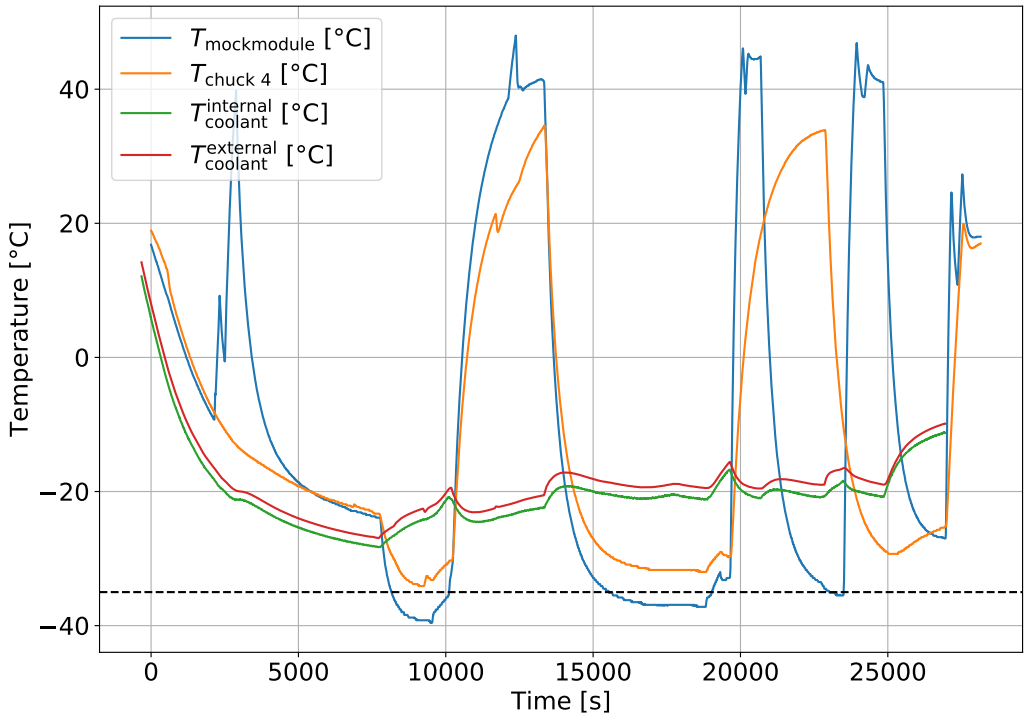

Figure 4.11.: Temperature inside the mock module (placed on TCIN-5,0S45F) and on top of a chuck as well as the coolant temperature. During cool down, it was realised that the module could not be operated and was therefore replaced by a heat-pad. Module and mock module were heated during this operation in order to avoid condensation.

This is done by measuring the temperature between one chuck and the aluminium plate on top of it as proxy for the temperature across the Peltier elements. This temperature difference is then used to calculate the current needed to generate the correct waste heat from the top right plot of Figure 4.12. Thus, it is ensured that the waste heat generated by the Peltier elements is still manageable by the chiller. Comparing the temperatures of chuck 2 and 4 in Figure 4.13 shows that four Peltier elements do offer superior cooling performance under these constraints.

Finally, the R0 module is tested again with the improved setup. R0 and mock module were placed both TCIN-5,0S45F. During previous tests, it was observed that the Peltier elements warm up the coolant also when the modules are heated (cf. Section 4.4.2). To mitigate this, the introduction a bypass valve that separates the coldbox from the coolant cycle is considered and implemented after this series of tests. It can easily be approximated by setting the chiller to "internal cycling," meaning that only 20 % of the coolant flow passes through the box, while the remainder circulates internally in the chiller. The internally circulating coolant could then reach far lower temperatures than during normal operations. Ideally, the influx of this into the coldbox at the beginning of the cool down would reduce the temperature inside the box at the lower side of the Peltier more than continuous cooling of the Peltier elements during warm up would. At the time of this test, it was not yet clear that the confirmation tests would take approximately 5 min each, thus the temperature extremes were held for longer time. Adding this number to the warm up and cooling times shown in Table 4.1 shows that one cycle can be performed in 1.3 h. The first cycle is ca. 14 min shorter than the second cycle. The most likely cause is the difference in coolant temperature that can be seen in Figure 4.14. Due to time constraints, a third cycle was not performed, but it is expected to have a similar duration as the second one, since the coolant reached the same temperature after the cycle as before.

Figure 4.13 shows that it takes approx. 2 h to reach −35 °C after starting the chiller. With sufficiently strong power supplies, warming the modules up from −35 °C to +40 °C (or room temperature) can be done in 10 min or less. This clearly shows that the coldbox prototype does fulfil the performance requirements laid out in Figure 4.5.

Table 4.1.: Duration of the warm up and cooling phases of the cycle displayed in Figure 4.14.

first warm up	8 min
first cool down	48 min
second warm up	10 min
second cool down	60 min

4.5. Finalisation of the Coldbox Setup

The previous tests have shown that the coldbox performs the thermal cycling sequence within the time specified in Figure 4.5, i. e. ca. 20 h. Despite this, some changes are still

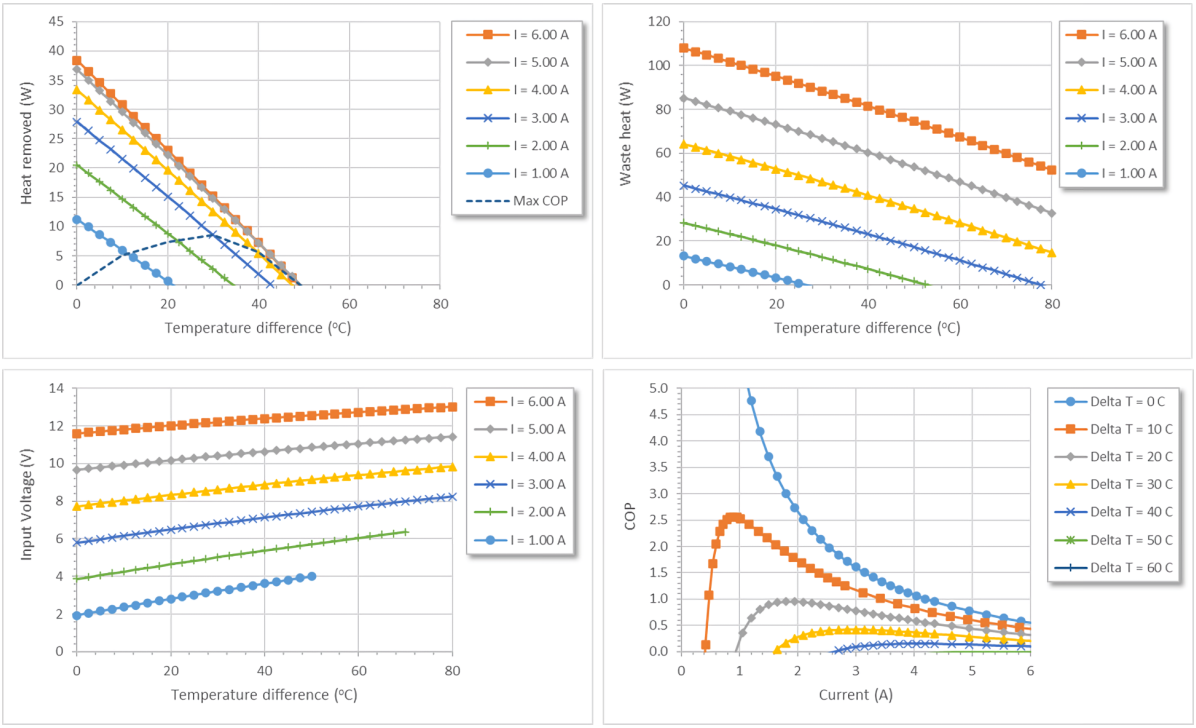

Figure 4.12.: Estimated performance of the Peltier elements with the hot side at −25 °C. Shown are the cooling power Q_C at the cold side (top left), the waste heat Q_h (top right), the voltage over the Peltier element (bottom left) and *Coefficient of Performance* (COP) $\frac{Q_C}{P_{el}}$ as functions of the applied current and the temperature difference between the hot and cold side. Figure provided by the manufacturer.

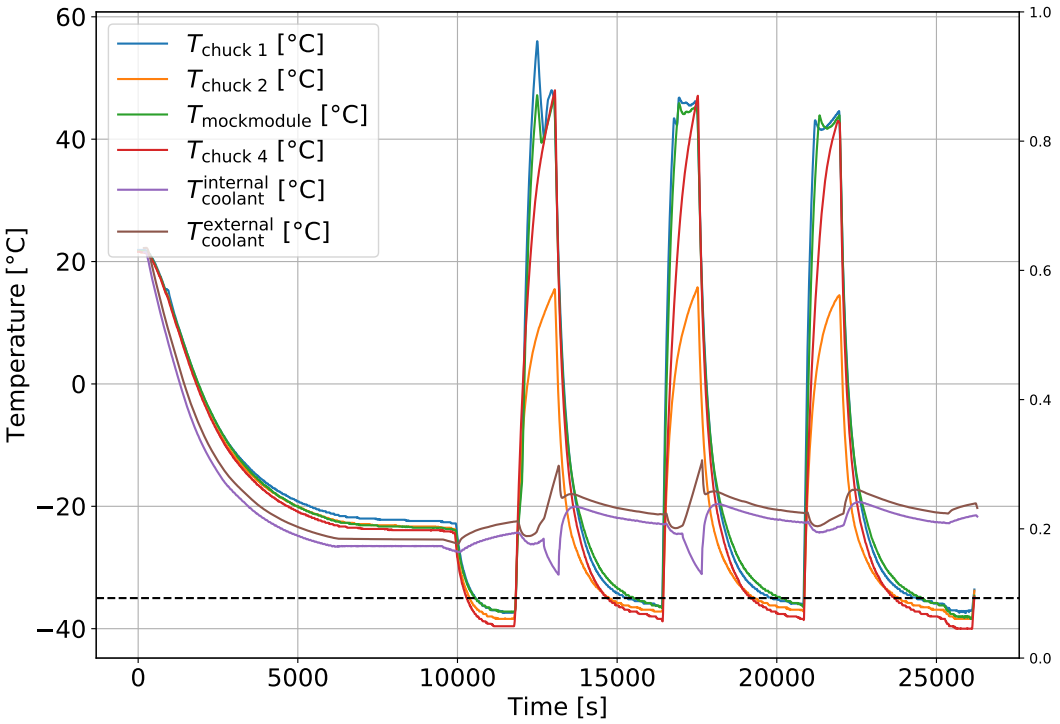

Figure 4.13.: Temperature during thermal cycling in the improved setup. $T^{\text{internal}}_{\text{coolant}}$ is measured in the chiller itself, while $T^{\text{external}}_{\text{coolant}}$ is measured at the coolant inlet of the chuck holding the module. During the first two warm up phases, the chiller is set to "internal cycling", meaning that only 20 % of the coolant circulate in the coldbox. This simulates a bypass valve that was not yet implemented.

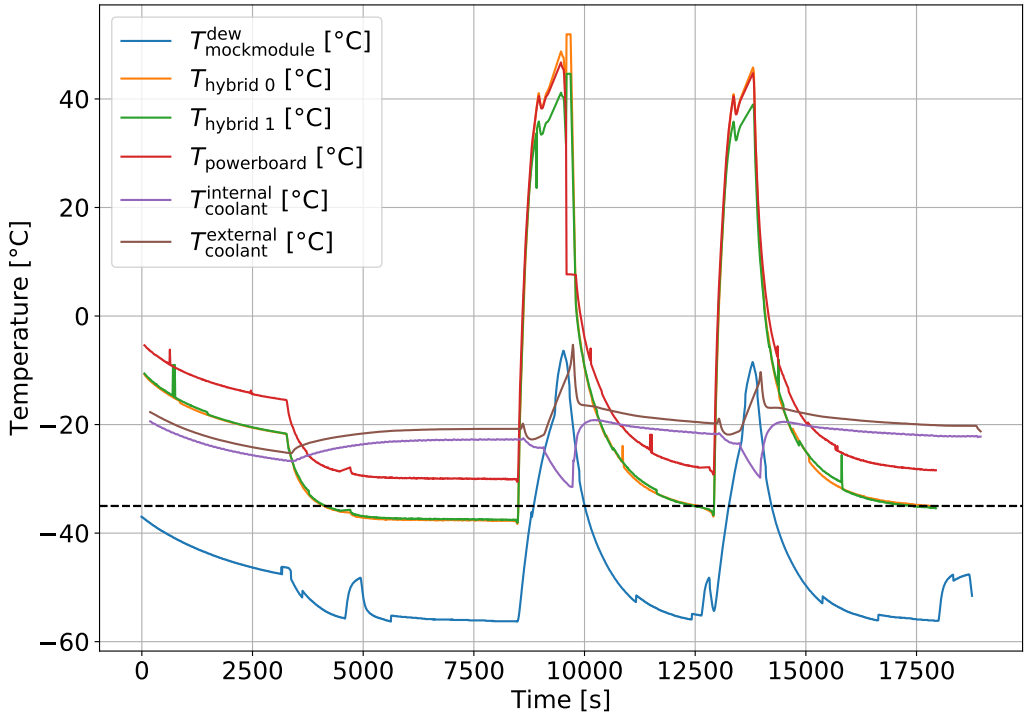

Figure 4.14.: Temperature during cycling with the R0 module in the improved setup. $T^{internal}_{coolant}$ is measured in the chiller itself, while $T^{external}_{coolant}$ is measured at the coolant inlet of the chuck holding the module. During the warm up phase, the chiller is set to "internal cycling", meaning that only 20 % of the coolant circulate in the coldbox. This simulates a bypass valve that was not yet implemented.

needed. In particular, this includes replacing the improvised sensor suite used previously and automating the thermal cycling.

4.5.1. Mechanical Changes

Two more changes are made to the coldbox design in order to reach the status described in Section 4.3. For one, all chucks are equipped with four Peltier elements. This offers slightly higher efficiency than just using three (cf. Figure 4.12). And secondly, the improvised sensor suite that has been used so far is replaced by a dedicated set of sensors. A concern during thermal cycling is to prevent corrosion damage due to condensation on the modules. Four humidity sensors are placed inside the coldbox. One sensor is placed in the dry air inlet and can detect problems with the dry air supply early on. A second sensor monitors the air volume inside the coldbox. The remaining two sensors are each placed in an enclosure connected to two module test frames (cf. Figure 4.6). In combination with a temperature sensor, they monitor the dew point inside the test frame. Temperature is measured with Pt100 *Resistance Temperature Detectors* (RTD). They are standardised components and can measure temperatures over a range much wider than that encountered inside the coldbox. Apart from the two paired with humidity sensors, each of the four chucks contains two Pt100. One is placed on the copper block (part 10 in Figure 4.7) in the centre, next to the Peltier elements. The other is placed in a cutout at the centre of the upper aluminium plate (part 30).

Finally, also the coolant also is changed. The glycol-water mixture used so far has shown to be just barely sufficient. While ethanol has performed better, it is a fire hazard due to the low flashpoint of only 13,° C. Therefore, silicone oil is used as coolant. Due to its low specific heat capacity, it is expected to perform better than both ethanol and glycol-water.

4.5.2. Automation

During module production, each coldbox[5] will test several hundred modules. Therefore, the whole thermal cycling procedure needs to be automated.

The logic for the thermal cycling will be implemented on a *Programmable Logic Controller* (PLC) from the Siemens S7-1200 series. PLCs are widely used for automation tasks in industry and can run for long times without any intervention. Extension modules for digital and analogue I/O and connection of RTDs are available and simplify the integration of the sensor suite. For this PLC series, there is also a four channel low voltage power supply available that can supply enough power to all chucks simultaneously. While the PLC will control the thermal cycling, not everything can be connected directly to it. The chiller and the modules will be connected to a regular PC. Drivers for them will be developed that can be steered from the PLC via a network connection.

Part of the work described in this thesis was writing an automation program for the PLC. A schematic of the logic applied for thermal cycling can be found in Figure 4.15.

[5]In addition to this prototype, DESY has built 15 coldboxes for collaborating institutes.

At the beginning of the cycling sequence, the setpoint of the external chiller is changed to $-28 \ldots -30\,°C$. During the initial cooldown, the chiller alone is used to reduce the temperature on all chucks below $-20\,°C$. Only after this threshold has been reached, the Peltier elements are used. A PID controller regulates the current to them so that the chucks reach their target temperature of $T_{\text{chuck}} = -35\,°C$. Additionally, the current during cooldown is restricted so that the waste heat across all chuck does not exceed a certain power. The exact value can be changed at runtime, but the tests in Section 4.4.3 suggest that 320 W of waste heat are manageable.

During warmup, the polarity of the Peltier elements is inverted so that waste heat is directed towards the top aluminium plates, whereas the copper heatsink is cooled by the Peltiers. While this works for the first minutes of the warmup phase, Figure 4.11 shows that after a while, also the bottom side of the Peltier elements gets warm and warms up the coolant. As described before, a bypass valve is used to mitigate this effect. If it is enabled, the coolant flow to the coldbox is cut off and the coolant temperature inside the chiller decreases. When the bypass is disabled again, the influx of cold coolant into the coldbox will accelerate the cooldown a bit.

After ten thermal cycles have been completed, a long testing sequence with the modules at $+20\,°C$ needs to be performed. The chiller is set to $+15\,°C$, but fine temperature control is left to the Peltier elements. This way, the coldbox can be opened immediately after the testing sequence is completed without the danger of condensation.

4.6. Thermal Cycling with the Final Setup

When these tests were performed, there were neither modules available for use during thermal cycling nor have they been interfaced with the PLC. Therefore, a 7.3 W heatload has been placed on each chuck and is turned on constantly. This is very close to the worst case of cycling four R3 modules simultaneously [70, 71], which would generate 8 W of waste heat. Smaller modules generate less wasteheat, typically ca. 5 W. Because the modules were not yet integrated, the transition between warmup and cooldown was made immediately when the target temperature was reached on all chucks. Also, the chiller hat not yet been interfaced with the PLC, therefore the setpoint was kept at $-30\,°C$ during the whole test.

Two choices of maximum waste heat are investigated: 320 W (which looks feasible according to Section 4.4.3) and 400 W. The results of these two configuration are shown in Figures 4.16a and 4.16b, respectively. One thermal cycle starts with a warmup from $-35\,°C$ to $+40\,°C$ and ends when all four chucks have reached $-35\,°C$ again. Ten cycles with a maximum waste heat of 320 W were performed in 6:18 h, whereas with a maximum waste heat of 400 W, all cycles were finished after only 5:37 h. The by far largest part of this difference originates from the first cycle. There, warming up to $+40\,°C$ took 31 min, but only 9 min with the higher waste heat. This is due to the setpoint of the chiller being lower than the equilibrium temperature reached after a few cycles. Similarly, the cooldown phase of the first cycle was ca. 12 min shorter with the higher waste

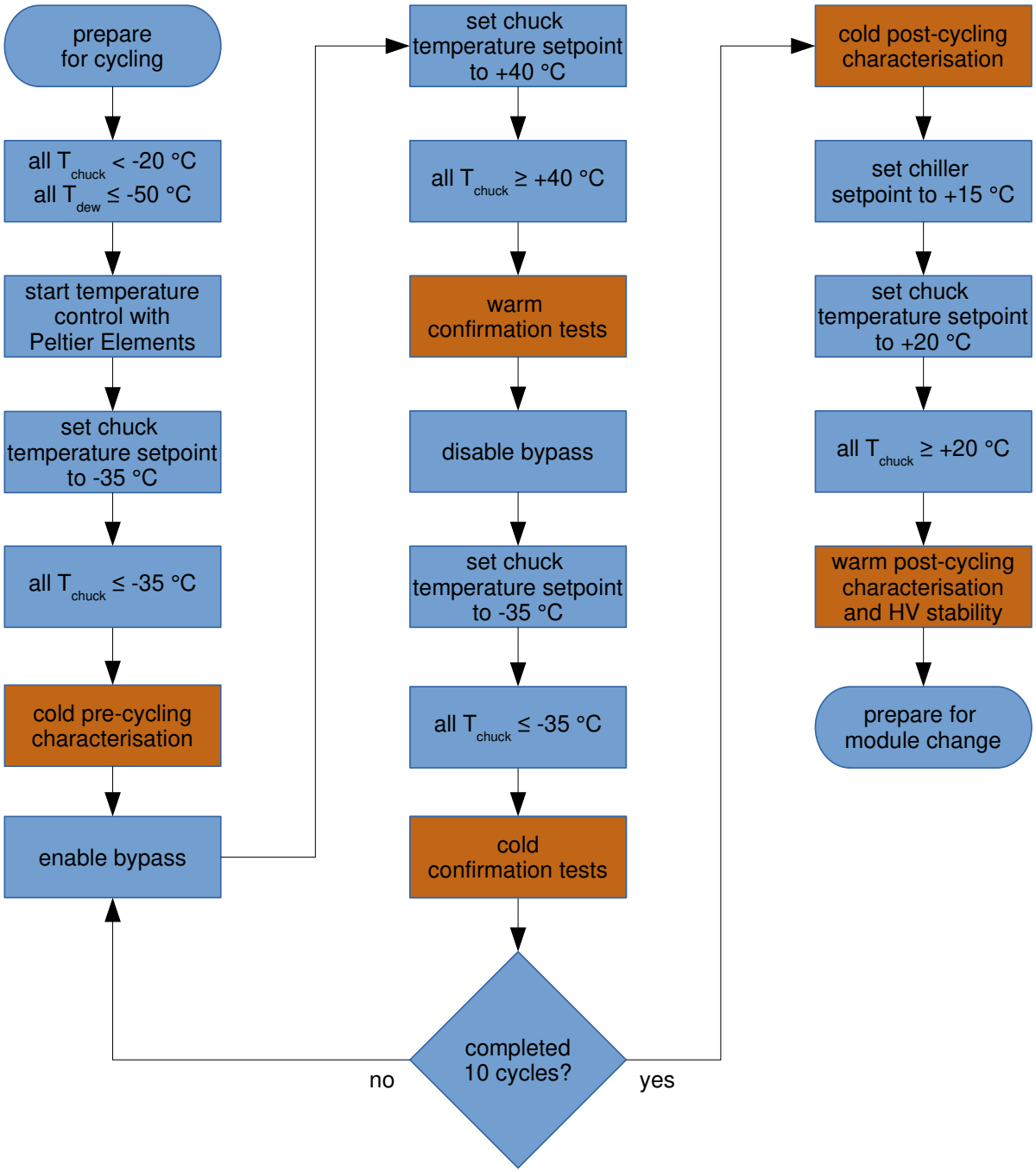

Figure 4.15.: Flow chart of the thermal cycling logic implemented on the PLC. At all times during thermal cycling, the environmental conditions must be monitored. If they change in a way that could endanger the modules (especially through condensation), the actions specified in [63] must be taken – which may include aborting the cycling sequence. Operations on modules (orange) may take several minutes and must not block the monitoring and control loop.

heat. Therefore, it is concluded that only 7 min of the difference in cycling time can be explained due to the increase in the waste heat budget.

At the end of the second cycling sequence, a temperature stability test was performed. The chucks were warmed up to +20 °C, but, since the chiller had not been interfaced with the PLC, it remained at its low setpoint. Chuck temperature is held very precisely. During the ca. 8 h of the stability test, deviations of 0.1 K of the actual chuck temperature from the setpoint were observed only rarely. Larger deviations did not occur. Also, the temperatures are read out with a resolution of only 0.1 K, so deviations smaller than one step will not show up in the outputs.

From these two tests, we can conclude that the coldbox can very well deliver the required performance. This test did not consider the warm and cold confirmation tests of ca. 5 min each that are performed every cycle. Also, the pre- and post-cycling characterisation tests were not performed, which are assumed to take ca. 2 h each. Allowing some time for the initial cooldown and the final warmup, the whole testing sequence described in Figure 4.5 can be performed in $\lesssim$ 14 h, significantly shorter than the 20 h specified. During warmup, the chuck temperature overshot the target temperature a by ca. 1 °C at a target temperature of +40 °C. In the final warmup to +20 °C, the chuck temperature overshoots typically by 3 to 4 °C, with an exception of one chuck overshooting by up to 25 °C. This indicates that the PID parameters need to be finetuned. Increasing the maximum allowed waste heat during cooldown shortens the whole thermal cycling sequence only by ca. 7 min. It would be more effective to tune the PID parameters more aggressively, but this may lead to overshooting the target temperature. Another observation was that the coolant temperature will fluctuate around −25 °C after a few cycles. The chiller setpoint could be set to a temperature closer to this equilibrium range, as cooling down further does nothing but lengthen the first thermal cycling. A final concern during cycling is the temperature difference across the Peltier elements. It was found to not exceed 65 K, staying well below the limit of 74 K specified by the manufacturer.

4.7. Supplementary Studies

4.7.1. Feasibility of Lower Current Power Supplies

Some institutes in the collaboration were planning to use power supplies limited to 30 V/3 A to power the Peltier elements in their coldboxes. Occasional monitoring of the power supply showed higher currents than 3 A, especially during warmup[6]. In order to check the effect of using such low current power supplies, thermal cycling was attempted with the Peltier power supply limited to a maximum current of 3 A. With this current, the voltage across the Peltier elements is expected to stay well below 24 V (cf. Figure 4.12). Similar to the previous tests, all chucks were equipped with a 7.3 W heatload. While it was possible to reach −35 °C during the initial cooldown, the warmup to +40 °C took

[6]The power supply for the Peltier elements that was installed together with the PLC can deliver 24 V/10 A per channel.

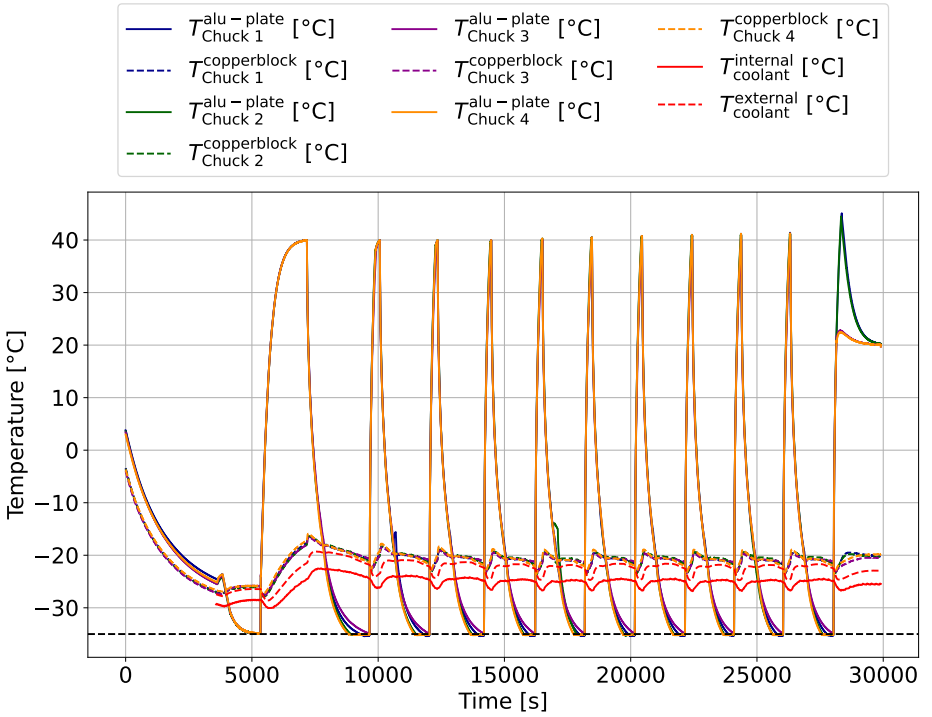

(a)

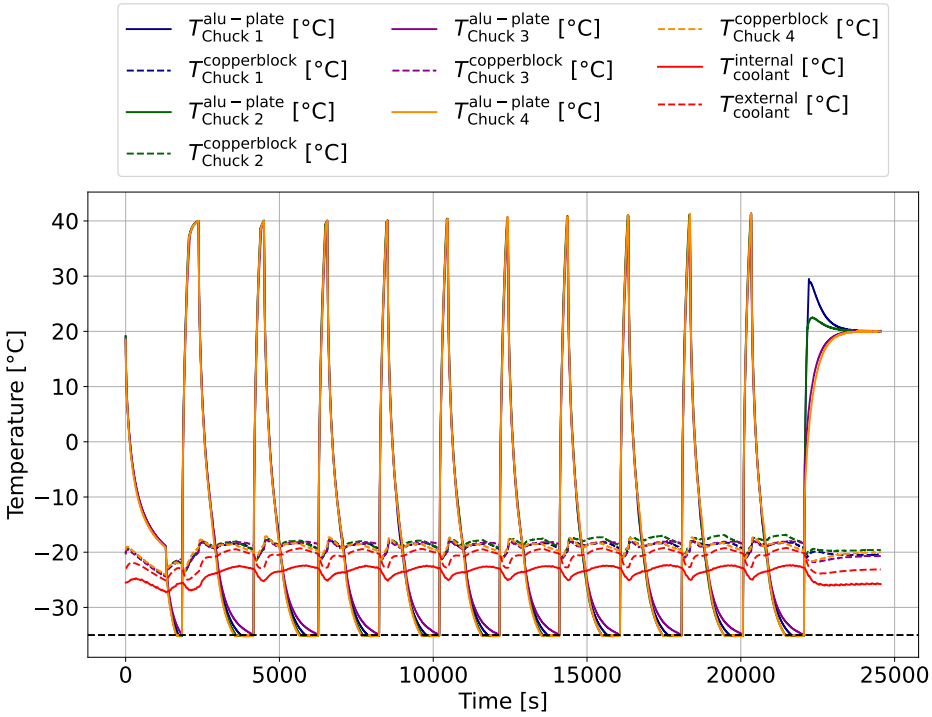

(b)

Figure 4.16.: Thermal cycles with restricted waste heat with the final design of the cold-box. The waste heat generated by the Peltier elements is regulated to not exceed 320 W (a) or 400 W (b).

1:18 h. Two out of the four chucks could then not cool down to −35 °C (Figure 4.17a). For a second attempt, the heatloads were turned off. While it was possible to perform two thermal cycles in this configuration, the cycles are unacceptably long (Figure 4.17b).

In conclusion, the Peltier elements need to be supplied with a current higher than 3 A to meet the performance goals of the coldbox. Shortly after these tests have been performed, a suitable low-cost power supply capable of delivering 36 V/10 A was found that could be used by other institutes. Therefore, it was not necessary to test different maximum currents.

4.7.2. Chiller Performance

There are several different coolants with different properties available. In general, a lower heat capacity of the coolant should enable a higher cooling power, i. e. the chiller can remove more waste heat. To measure the performance of different coolants, the current to the Peltier elements is regulated such that they give off a constant amount of waste heat Q_h. The temperature across the Peltier elements is measured and the required current then determined from the top right plot in Figure 4.12. If the waste heat is left constant for a long time, the coolant will reach an equilibrium temperature. However, due to the large thermal inertia of the coldbox, waiting for it to reach equilibrium temperature is unpractical. The change in temperature is proportional to the difference between waste heat of the Peltier elements and the chiller cooling power. For temperatures in the range $-30 \ldots 0\,^\circ\mathrm{C}$, the cooling power is approximately proportional to the temperature [64]. Thus, we can assume that

$$\frac{dT(t)}{dt} \propto \Delta T(t) = T_\mathrm{eq} - T(t) \tag{4.1}$$

From this, we can describe the coolant temperature as

$$T(t) = T_o + c \int_0^t (T_\mathrm{eq} - T(t'))dt' \tag{4.2}$$

The measurement starts at a temperature T_0 at $t = 0$ and c is a constant that describes the thermal inertia of the coldbox. Integrating and rearranging Equation (4.2) leads to

$$T(t) = \frac{T_0}{1 + ct} + \frac{T_\mathrm{eq}}{\frac{1}{ct} + 1}. \tag{4.3}$$

The above function is fit to data for each waste heat with a least squares fit. As can be seen from the figures in Appendix A.1, this provides an accurate approximation. A short-period oscillation with an amplitude of $\lesssim 0.1\,^\circ\mathrm{C}$ arises from non-optimised PID parameters of the chiller. Should the amplitude of these oscillations increase significantly, they might become problematic for the safe operation of the coldbox and testing of the modules. In that case, the PID parameters need to be tuned to remove these oscillations.

The performance studies with the glycol-water mixture (sold under the name *Thermal G*) and ethanol as coolant were performed with the "improved setup" described in Section 4.4.3. Of particular note should be that only two of the four chucks were controlled

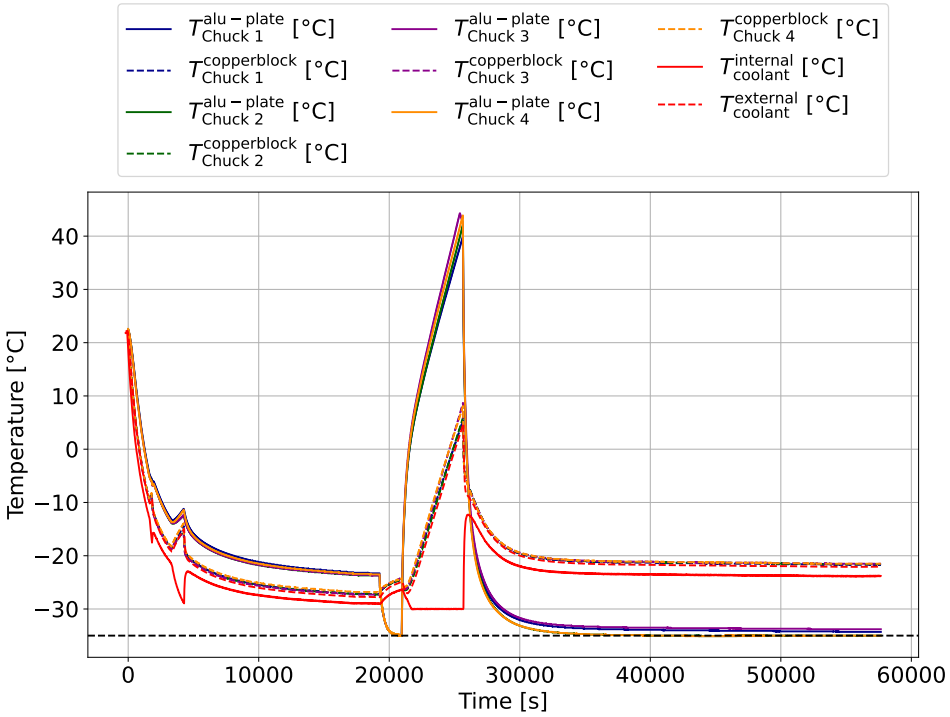

(a)

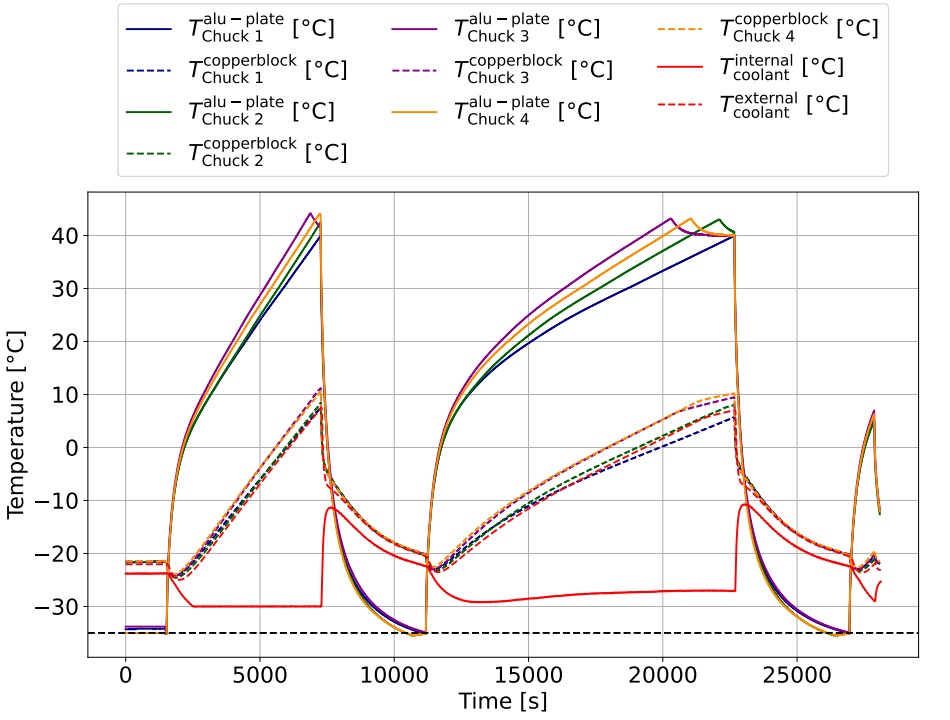

(b)

Figure 4.17.: Thermal cycling with a maximum current of 3 A supplied to the Peltier elements. In (a), a 7.3 W heatload was placed on each chuck, for (b), it was removed.

automatically, whereas power to the other two had to be adjusted manually. Also, only one chuck was equipped with a temperature sensor on the copper block, which was assumed to describe the temperature in all chucks. Thus, the waste heat figure given for glycol-water and ethanol in table 4.2 are not very precise.

While the silicone oil performance studies were performed with the same insulation, the coldbox was automated with the PLC (Section 4.5.2) for these measurements. The most noteworthy difference is that the temperature across the Peltier elements could be measured on all chucks and all Peltier power supplies have been controlled automatically. Thus, the waste heat given here is more accurate than for ethanol or water-glycol. Same as for ethanol, the chiller setpoint is $-28\,°\mathrm{C}$. Silicone oil is hygroscopic, i. e. it will attract humidity from its surrounding. In order to avoid condensation (and thus ice forming in the coolant), a constant stream of dry air is blown into the bath of the chiller. The dry air flow is reduced to a very small rate[7], which is still sufficient to compensate for the loss of coolant volume during cooldown, thus avoiding to attract humidity from the environment. Assuming air at room temperature entering the chiller bath at a rate of $1\,\frac{\mathrm{l}}{\mathrm{min}}$, this will introduce

$$\begin{aligned} Q_{\mathrm{air}} &= \dot{V}\Delta T C_{p,V}^{\mathrm{air}} && (4.4)\\ &= 1\,\frac{\mathrm{l}}{\mathrm{min}} \cdot 50\,\mathrm{K} \cdot 1.21\,\frac{\mathrm{J}}{\mathrm{l}\cdot\mathrm{K}} && (4.5)\\ &\approx 1\,\mathrm{W}. && (4.6) \end{aligned}$$

This is negligible compared to the expected cooling power of the chiller.

The glycol-water mixture (marketed as *Thermal G* [72]) has a specific heat capacity of $c = 3.2\,\frac{\mathrm{kJ}}{\mathrm{kg}}$, whereas ethanol has a lower heat capacity of $2.1\,\frac{\mathrm{kJ}}{\mathrm{kgK}}$. From these statistics, on would expect the latter to have roughly 50 % more cooling power. Comparing equilibrium temperatures between the two coolants in Table 4.2, this relation is roughly reflected in the measurements. Silicone oil (of type *Thermal H5* [72]) has a specific heat capacity of ca. $1.5\,\frac{\mathrm{kJ}}{\mathrm{kgK}}$ in the temperature range relevant for coldbox operation. Naively, this should result in a 40 % improvement in cooling power over ethanol. However, this is not reflected in the measurement. The cause of this discrepancy is not clear. Before the measurement, the silicone oil was heated to $+60\,°\mathrm{C}$ for an extended period of time in order to let any humidity evaporate. However, since the lid was bolted to the chiller, a visual inspection for ice was not possible. Considering that the coolant had been in use for over a year at the time of this measurement, this discrepancy may be caused by aging of the silicone oil.

To conclude, ethanol offers roughly 50 % more cooling power than the glycol-water mixture. This corresponds to the expected improvement based on their specific heat capacities. No corresponding improvement for silicone oil was observed, most likely because the coolant has degraded with age. Since cleaning silicone oil from the setup would be rather laborious, it was not feasible to repeat the glycol-water and ethanol performance measurement with the identical setup.

[7] The dry air flow into the chiller is not measured, but reduced so far that it is only barely noticeable on the back of a hand. The author estimates that the rate is not larger than roughly 1 l/min.

Table 4.2.: Equilibrium coolant temperatures for different waste heat Q_h. Note that the performance measurements with the glycol-water mixture (*Thermal G*) and ethanol were performed with the *improved setup* described in Section 4.4.3, whereas the silicone oil was tested using the finalised setup controlled by the PLC, as described in Sections 4.5.2 and 4.6. Thus, the latter can not be directly compared to the former two, though a tendency should still be clear. The uncertainty is the uncertainty of the fitted equilibrium temperature.

Q_h [W]	$T_\mathrm{internal}^\mathrm{Thermal\ G}$ [°C]	$T_\mathrm{internal}^\mathrm{Ethanol}$ [°C]	$T_\mathrm{internal}^\mathrm{Silicon\ Oil}$ [°C]
112	-26.50 ± 0.00	—	—
160	—	—	-24.93 ± 0.00
168	-26.50 ± 0.00	—	—
200	—	—	-22.86 ± 0.04
224	-26.50 ± 0.00	—	—
280	-25.09 ± 0.02	-28.00 ± 0.00	-19.00 ± 0.06
320	—	-28.00 ± 0.00	-18.12 ± 0.09
336	-23.35 ± 0.02	—	—
360	—	-27.97 ± 0.05	-16.96 ± 0.08
400	—	-26.76 ± 0.63	-15.73 ± 0.01
450	—	-24.75 ± 0.08	-7.89 ± 0.02
514	—	-21.61 ± 0.07	—
576	—	-19.66 ± 0.02	—

4.8. Conclusions and Outlook

This section presented the work that the author performed within the framework of this thesis on the prototype of the endcap thermal cycling setup. Tests with a preliminary design using the sensors and power supplies available in the laboratory could identify weaknesses in the design, which were subsequently corrected. As part of this work, software for a PLC was written to perform automated thermal cycling. This program has been used to perform ten thermal cycles in ca. 6 h with the finalised coldbox design. Even though these tests did not include module tests, it can be concluded that the sequence specified in Figure 4.5 can be performed in $\lesssim 14$ h, significantly shorter than required.

5. Majorana Neutrinos in Same-Sign $W^{\pm}W^{\pm}$ Scattering

The origin of neutrino masses is one of the current open questions of the SM. There are several theories such as the Type I Seesaw model or EFT descriptions such as the Weinberg operator that try to explain the origin of neutrino masses. At particle colliders, these models can be probed in final states with all lepton flavours, whereas nuclear experiments are sensitive only to final states with electrons.

After a review of the current experimental knowledge about neutrino masses and their origin in Section 5.1, this chapter investigates the sensitivity of a novel t-channel process towards neutrino mass models. The results of this study has been published in [24, 25].

5.1. Current Experimental Knowledge on Heavy Neutrinos

Models for neutrino masses are probed at several experiments. For $m_N \gtrsim 10\,\text{GeV}$, this includes experiments using nuclear decays (Section 5.1.1) and collider searches (Section 5.1.2). Section 5.1.3 reviews the current knowledge about the absolute value of neutrino masses.

5.1.1. Direct Constraints from Nuclear Decays

One way to search for heavy Majorana neutrinos is the search for *neutrinoless double-β decays*. A double beta decay $(A, Z) \to (A, Z+2) + 2e^- + 2\bar{\nu}_e$ can occur only in a few nuclei. Here, A denotes the number of nucleons and Z the number of protons. A double-β decay may occur only if a regular β decay is forbidden due to the difference in binding energies between the involved isotopes. The half-life of such a nucleus is very long. For the isotope ^{76}Ge, it is roughly $T^{\beta\beta}_{1/2} \approx 2 \cdot 10^{21}$ years. In other elements and isotopes, the lifetime of the double-β decay is of comparable magnitude.

If neutrinos were Majorana particles, a double-β decay *without* emission of neutrinos would be possible. The whole energy would be carried by the two electrons, such that their spectrum would show a peak at $Q_{\beta\beta} = 2039.06\,\text{keV}$ [73]

Currently, the best limits on neutrinoless double-β decay come from the GERDA experiment [21]. The experiment is using Germanium detectors, which are ca. 87 % pure in the isotope ^{76}Ge, which is known to have double-β decays. The detectors are surrounded by a LAr cryostat and a water tank, which both serve as shielding and are

also instrumented to veto background events. With an exposure of $127.2\,\mathrm{kg}\cdot\mathrm{yr}$, no evidence for neutrinoless double-β decay was found. The 90 % confidence level estimate for the half life of such decays in ^{76}Ge is

$$T_{1/2}^{0\nu\beta\beta} > 1.8\cdot 10^{26}\,\mathrm{yr}. \tag{5.1}$$

Assuming that a neutrinoless double-β decay would be mediated only by W bosons and heavy neutrinos[1] in a t-channel process, this half-life can be translated into limits on the masses and mixing parameters of the heavy neutrinos. The momentum transfer in this t-channel process would be $\mathcal{O}(0.1\,\mathrm{GeV})$. Under the assumption that the heavy neutrinos have masses at or above the electroweak scale, one can derive limits on their masses and mixing paramters [24].

$$|\sum_{k=4}^{n_s+3}\frac{V_{ek}^2}{m_k}| < (2.33\ldots 4.12)\cdot 10^{-6}\,\mathrm{TeV}^{-1} \tag{5.2}$$

5.1.2. Direct Constraints from Collider Searches

Both ATLAS and CMS have performed several searches for heavy neutrinos in final states with electrons and muons. These searches have mostly considered only the s-channel production process, which leads to sensitivity predominantly at low m_N.

A heavy neutrino with mass $m_N \lesssim 15\,\mathrm{GeV}$ is *long-lived*, i. e. it will decay in a significant distance from the pp collision. Both ATLAS and CMS have searched for long-lived heavy neutrinos in the $pp \to l_i l_j l_k + E_{\mathrm{T}}^{\mathrm{miss}}$ final state with $139\,\mathrm{fb}^{-1}$ of data collected at $\sqrt{s} = 13\,\mathrm{TeV}$. They are most sensitive at $m_N \approx 10\,\mathrm{GeV}$, where a mixing parameter $|V_{\mu N}|^2 < 3\cdot 10^{-7}$ can be excluded with 95 % confidence level [75, 76].

Searches for the prompt decay of a heavy neutrino can probe higher m_N. ATLAS has performed a search in the $pp \to l_i l_j l_k + E_{\mathrm{T}}^{\mathrm{miss}}$ final state in $35.9\,\mathrm{fb}^{-1}$, which is sensitive to $m_N < 50\,\mathrm{GeV}$ [77]. Mixing parameters $|V_{\mu N}|^2 < 3\cdot 10^{-5}$ can be excluded in this mass range. The CMS search in the $pp \to l^{\pm}l^{\pm}jj$ final state has approximately the same sensitivity at $m_N = 50\,\mathrm{GeV}$. However, this analysis also includes the $W\gamma$ fusion production mode for heavy neutrinos. Thus, it can extend sensitivity to higher masses. At $m_N \approx 100\,\mathrm{GeV}$, mixing parameters $|V_{\mu N}|^2 < 2\cdot 10^{-3}$ are excluded. The sensitivity of this analysis extends up to 1.4 TeV [78].

All these searches also investigate the mixing with electrons $|V_{eN}|^2$, which is not of relevance for this thesis. Heavy neutrinos with $m_N < 10\,\mathrm{GeV}$ are investigated in many smaller experiments. An overview of their results can be found in [79].

5.1.3. Constraints on Neutrino Masses

The decay of tritium $^3\mathrm{H} \to ^3\mathrm{He}^+ + e^- + \bar{\nu}_e$ is used by the KATRIN experiment as a direct probe of the electron neutrino mass. This decay releases an energy of $E_0 = 18.58\,\mathrm{keV}$ [80]. A massive neutrino will cause a distortion of the electron energy spectrum near E_0.

[1] See [74] for a study of possible processes.

However, no such distortion was observed, which leads to an upper limit on the neutrino mass at 90 % confidence level [20] of

$$m_{\nu_e} < 0.8\,\text{eV}. \tag{5.3}$$

Cosmological observables are also affected by the exact value of neutrino masses. A recent study [81] interpreted measurements of the cosmic microwave background, big bang nucleosynthesis and the large-scale structure of the universe in the context of seven different neutrino mass models. These models are sensitive only to the sum of neutrino masses. At 95 % confidence level, the sum of neutrino masses is found to be

$$\sum_{i=1}^{3} m_{\nu_i} \lesssim 0.26\,\text{eV}. \tag{5.4}$$

5.1.4. Indirect Constraints

For heavy neutrinos with masses above the electroweak scale, indirect constraints were derived from a combination of electroweak precision measurements, searches for unitarity violation in the CKM matrix and searches for lepton flavour violation [82]. Constraints are derived for the parameter $\eta_{ll'}$, which encodes a small unitarity violation of the PMNS matrix arising from the presence of heavy neutrinos. Assuming the existence of $n_R = 3$ sterile neutrinos, it is related to the heavy neutrino – light neutrino mixing parameter via

$$\sqrt{2|\eta_{ll'}|} = \sum_{k'=4}^{6} \sqrt{V_{lk'} V^*_{l'k'}}.$$

For the $l = l' = \mu$ scenario considered in this work, the limit of $\sqrt{2|\eta_{\mu\mu}|} < 0.021$ translates to

$$|V_{\mu N}|^2 < 4.41 \cdot 10^{-4} \text{ at } 95\,\%\text{ CL}. \tag{5.5}$$

5.2. Cross Sections Estimates

Current collider searches are sensitive to heavy neutrinos with masses up to 1.4 TeV. Production of heavy neutrinos in a t-channel process (Figure 5.1a) might allow to probe significantly higher masses. This process would result in a final state with two leptons of the same electric charge, but *without* $E_{\text{T}}^{\text{miss}}$. Such a clear signature would give sensitivity towards new physics already at a small expected number of events.

The first check to perform for a new model is whether it has a sufficiently large cross section at the LHC's centre-of-mass energy of 13 TeV. For a very clean final state like the one investigated in this thesis, $\mathcal{O}(10)$ events in the whole LHC Run 2 dataset are expected to be sufficient to have some sensitivity. This corresponds to a cross section of roughly $\approx 0.05 \ldots 0.1$ fb. Using MadGraph 2.6.7 [83], cross sections for various points in parameter space are calculated at *Next-to-Leading Order* (NLO).

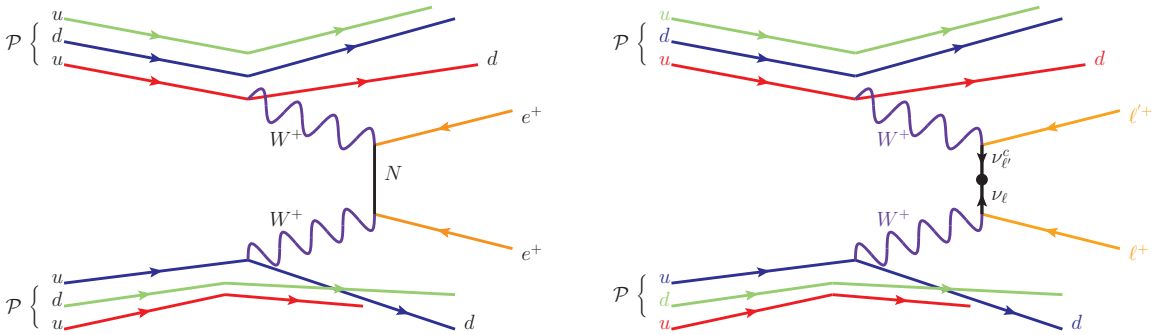

Figure 5.1.: Feynman diagrams of the t-channel process facilitated by the Type I Seesaw model (a) or Weinberg operator (b).

As a preparatory measure, cross sections for the $W\gamma$ fusion and s-channel (labelled $CCDY$) are calculated. They are found to be in good agreement with the cross sections given in [84], which shows that MadGraph and the Type I Seesaw model as implemented in the `HeavyN` library [84, 85, 86] are properly installed and configured.

The t-channel process of Figure 5.1a can be generated with the syntax

```
define p = u c d s u~ c~ d~ s~ g
define j = p
define mu = mu+ mu-

generate p p > mu+ mu+ j j $$ n1 n2 n3 w+ w- QED=4 QCD=0 [QCD]
add process p p > mu- mu- j j $$ n1 n2 n3 w+ w- QED=4 QCD=0 [QCD]
```

In addition to that, the automated check of infrared pole cancellation in MadFKS has to be disabled by setting `#IRPoleCheckThreshold=-1.0d0` in `Cards/FKS_params.dat`. This check is meant to catch the omission of virtual diagrams that are mixed QCD-EW corrections at NLO. Such diagrams do not exist in the process presented here, but the automated check does not recognise that. Thus it needs to be disabled.

Because there are two neutrino "decay" vertices in the t-channel process, $\sigma_{t-\text{channel}} \propto |V_{\mu N}|^4$ whereas the s-channel and $W\gamma$ fusion cross sections are only proportional to $|V_{\mu N}|^2$, so they are more sensitive at small mixing parameters. Assuming a mixing of unity, the t-channel is the dominant production mode for $m_N \gtrsim 750$ GeV. Reducing the mixing parameter to $V_{\mu N} = 0.5$ makes the t-channel the dominant production mode only above $m_N \gtrsim 1.8$ GeV (Figure 5.2). But even with the smaller mixing parameter, the t-channel has a large enough cross section at $m_N = 6$ TeV to have sensitivity at the LHC. As a comparison, the $W\gamma$ fusion channel has a sufficiently large cross section only up to $m_N \approx 3$ TeV and the s-channel only up to $m_N \approx 1.8$ TeV. This indicates that a

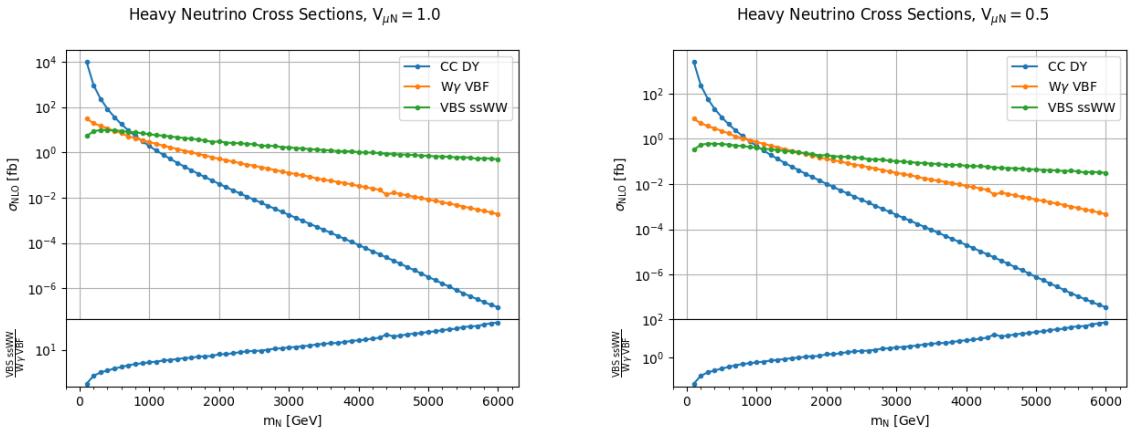

(a) (b)

Figure 5.2.: Cross section of the Type I Seesaw model for the s-channel (CC DY, blue), $W^{\pm}\gamma$ fusion (Wγ VBF, orange) and t-channel (VBS ssWW, green) processes for $V_{\mu N} = 1$ (a) as well as $V_{\mu N} = 0.5$ (b).

t-channel analysis can extend the model sensitivity to significantly higher masses than the previous searches (Figure 5.2b).

5.3. Event Generation

As presented above, the cross section for the Type I Seesaw model is large enough at $m_N = 6\,\text{TeV}$ to be detected at the LHC. But because no search for the t-channel process has been performed previously, a more thorough investigation of the possible background processes and achievable sensitivity is warranted. In addition to the Type I Seesaw model, also the sensitivity for the Weinberg operator will be determined, as the two share the same final state.

5.3.1. Generator Setup

All Monte Carlo simulations for the phenomenological study are generated with MadGraph5_aMC@NLO (version 2.7.1.2) [83] at next-to-leading order (NLO) in QCD. Events are then passed through Pythia 8 [87], version 243 for QCD and QED parton shower and hadronisation. Modelling of the underlying event or multiparton interactions is also performed by Pythia 8, as well as the decays of τ leptons and heavy-flavour hadrons. For this study, pile-up is neglected. This section contains only a brief summary of the event generation. A more thorough explanation can be found in [24, 25].

Signal Modelling

This study considers two signal models that can generate the process $q_1 q_2 \to q_1' q_2' l_i^{\pm} l_j^{\pm}$ which is of ($\mathcal{O}(\alpha^4)$) at tree level. Here, q denotes any light quark or antiquark.

Type I Seesaw model For the Type I Seesaw model, only the exchange of a heavy Majorana neutrino N in the t-channel is considered and a possible interference with the s-channel production of a heavy Majorana neutrino is neglected. At the analysis level, a large value of the dijet invariant mass m_{jj} will be required, which suppresses the s-channel contribution. As discussed above (Section 5.2), the infrared pole cancellation in MadFKS is disabled. Additionally, the generated events need to have two parton-level jets clustered with the anti-k_t algorithm [52] with a radius parameter of $R = 0.4$ that fulfil

$$p_{\mathrm{T}}^{j} > 20 \text{ GeV and } |\eta^{j}| < 5.5. \tag{5.6}$$

For the purpose of this phenomenological study, only final states with a same-sign muon pair[2] are considered. This is achieved by setting the mixing parameters to

$$|V_{\mu N}|^2 = 1, |V_{eN}|^2 = |V_{\tau N}|^2 = 0. \tag{5.7}$$

Similarly, while the model postulates up to three heavy Majorana neutrinos, this study considers only the presence of one. The other two are decoupled by setting their masses to

$$m_{N_5} = m_{N_6} = 10^7 \text{ TeV}.$$

Since there is no interference between the different heavy Majorana neutrinos, this restriction only reduces the cross section and thus leads to a more conservative estimate of the sensitivity.

The cross section for this t-channel process as a function of m_N rises up to a maximum of $\sigma \approx 20\,\mathrm{fb}$ around $m_N \approx 400\,\mathrm{GeV}$, above which it decreases again (Figure 5.3). In the low mass limit (w. r. t the $W^{\pm}W^{\pm}$ scattering scale) where $m_N, m_W \ll m_{WW}$, the cross section scales as

$$\sigma \propto g_W^4 |V_{\mu N}|^4 \frac{m_N^2}{m_W^4}. \tag{5.8}$$

In particular, the dependence on m_{WW} cancels out and the m_N^{-2} term in the heavy neutrino propagator is negligible due to the large momentum scales. Conversely, for large m_N (i. e. $m_W^2, m_{WW}^2, |t|, |u| \ll m_N^2$) the m_N^{-2} term cannot be neglected and thus the cross section scales as

$$\sigma \propto g_W^4 \frac{|V_{\mu N}|^4}{m_N^2} \frac{m_{WW}^4}{m_W^4}. \tag{5.9}$$

The cross sections for the s-channel and $W\gamma$ fusion production modes fall monotonously as a function of m_N. For a mixing parameter of $|V_{\mu N}|^2 = 1$, the t-channel process is the dominant production mode at $m_N \gtrsim 700\,\mathrm{GeV}$. Note that this crossover point moves to higher m_N for smaller $|V_{\mu N}|^2$ (Figure 5.3).

Weinberg Operator The same final state can also be generated by the Weinberg Operator (Figure 5.1b) using MadGraph syntax

[2] I. e. both muons have the same electric charge.

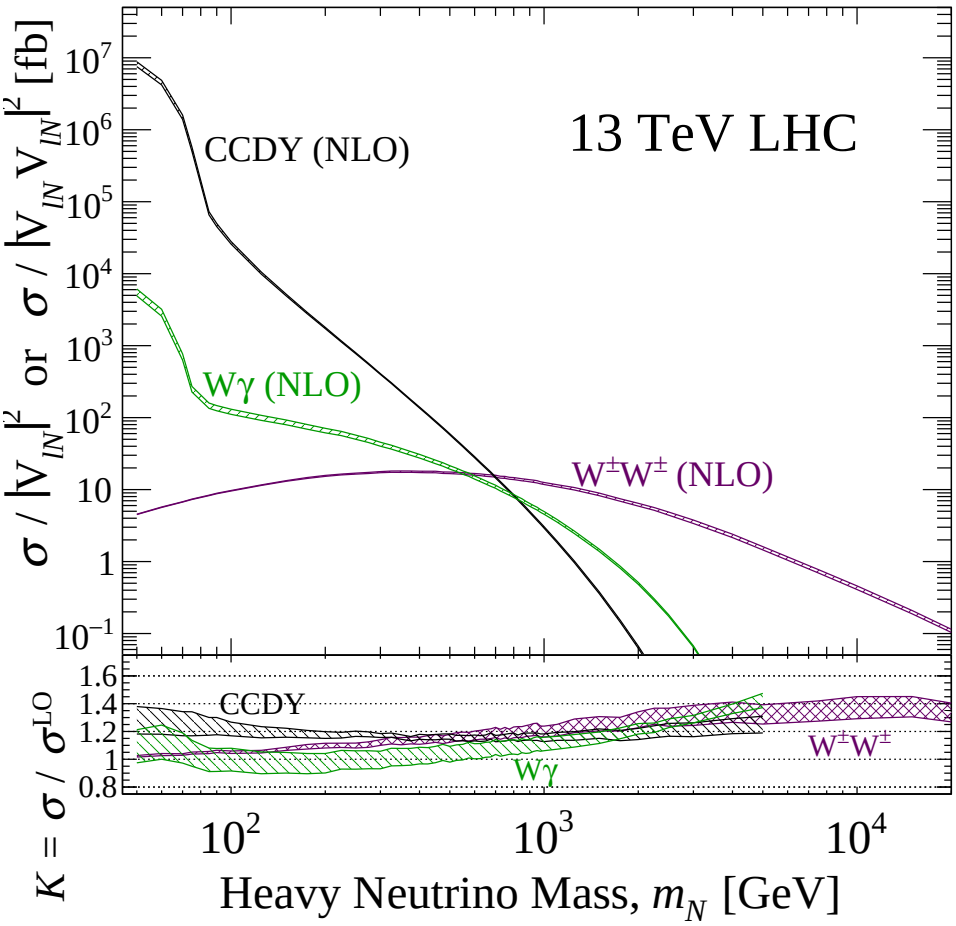

Figure 5.3.: Bare cross sections normalised to the mixing parameter $\sigma/|V_{\mu N}|^4$ for the t-channel signal process ($W^{\pm}W^{\pm}$, purple) as well as the bare cross sections $\sigma/|V_{\mu N}|^2$ for the s-channel (CCDY, black) and $W\gamma$ fusion (green) processes at NLO in QCD. The bottom panel shows the QCD K-factor for each process, i. e. the ratio of NLO to LO cross section. The band thickness corresponds to the residual scale uncertainty.

```
import model SMWeinbergNLO
generate p p > mu+ mu+j j QED=4 QCD=0 $$w+ w- [QCD]
add process p p > mu- mu- j j QED=4 QCD=0 $$w+ w- [QCD]
```

The t-channel current $\nu_l \nu_{l'}^C$ is modelled as an unphysical Majorana neutrino with mass $m_{ll'} = C_5^{ll'} v^2/\Lambda$. This mass is calculated automatically from the cutoff scale Λ and the Wilson coefficients. Since this analysis focuses on the di-muon channel, $C_5^{\mu\mu} = 1$ and all other Wilson coefficients are set to zero. For computational reasons, the cutoff scale is set to $\Lambda = 200\,\text{TeV}$. However, the final cross section can be scaled to arbitrary values of $C_5^{\mu\mu}/\Lambda$.

Background Modelling

The t-channel signal process considered in this study has a few unique aspects. It creates two forward jets with large energy (at tree level) and two same-sign muons with high transverse momentum, but no outgoing neutrinos. Having strict cuts at the analysis level on e. g. the muon momentum and m_{jj} allows to effectively reject many common backgrounds. In particular, this includes the production of single top quarks tX and top quark pairs in association with a boson $t\bar{t}X, X \in W^{\pm}, Z, \gamma*, h$ as well as triboson processes WWV with $V \in Z, \gamma*$. This leaves two main backgrounds: same-sign W bosons $W^{\pm}W^{\pm}jj$ (the pure electroweak and the mixed EW-QCD diagrams are generated separately) and diboson $W^{\pm}V$.

QCD Production of $W^{\pm}W^{\pm}jj$ The mixed electroweak-QCD production of $pp \to W^{\pm}W^{\pm}jj$ (simply labelled s QCD) has similar topology and kinematics to the signal processes, but features a t-channel gluon. Events are generated using the syntax

```
import model loop_sm
generate p p > w+ w+ j j QED=2 QCD=2 [QCD]
add process p p > w- w- j j QED=2 QCD=2 [QCD]
```

Generator-level jets are required to fulfil the same requirements codified in Equation (5.6) as the signal processes. W bosons are decayed into muons before the parton shower. The leptonic modes of $W \to \tau\nu$ are neglected.

EW Production of $W^{\pm}W^{\pm}jj$ Another large background consists of the purely electroweak production of $pp \to W^{\pm}W^{\pm}jj$. It is generated using the syntax

```
generate p p > w+ w+ j j $$ a z w+ w- QCD=0 QED=4 [QCD]
add process p p > w- w- j j $$ a z w+ w- QCD=0 QED=4 [QCD]
```

As for the QCD production, the requirements of Equation (5.6) have to be fulfilled and the W bosons are decayed into muons before the parton shower.

Inclusive Production of $WZ \to lll\nu$ The inclusive production of $pp \to lll\nu + X$ has a cross section roughly an order of magnitude larger than the $W^{\pm}W^{\pm}jj$ processes described above. It may contribute to the backgrounds if the lepton with opposite electric charge

is not reconstructed, e. g. due to being too low in p_T or outside of detector acceptance. In addition to the requirements of Equation (5.6), charged leptons need to fulfil

$$m_\mathrm{os}^{ll} > 8\,\mathrm{GeV} \quad \text{and} \quad |\eta^l| < 4.0 \tag{5.10}$$

in order to suppress contributions from mesonic resonances, as they are not modelled in MadGraph. Events with up to one additional jet at NLO are generated using the syntax

```
define ell = e+ mu+ ta+ e- mu- ta-
define vv = ve vm vt ve~ vm~ vt~
generate p p > ell ell ell vv QED=4 QCD=0 [QCD] @0
add process p p > ell ell ell vv j QED=4 QCD=1 [QCD] @1
```

and FxFx merging [88]. Events generated this way will have limited statistics at high $p_\mathrm{T}^{\mu_2}$. To compensate for that, samples with different generator-level cuts on $p_\mathrm{T}^{\mu_2}$ are made and combined without overlap at the analysis stage.

5.3.2. Truth-Level Kinematics

The kinematics of the t-channel heavy Majorana neutrino process at truth level, i. e. before detector simulation, are studied using MadAnalysis 5 [89, 90, 91]. After parton showering, jets are clustered with the anti-k_t algorithm [52] and jet and lepton candidates have to fulfil

$$p_\mathrm{T}^{e(\mu)[\tau_\mathrm{h}]\{j\}} > 10(27)[20]\{25\}\,\mathrm{GeV} \tag{5.11}$$

$$|\eta^{e(\mu)[\tau_\mathrm{h}]\{j\}}| < 2.5(2.7)[2.5]\{4.5\}. \tag{5.12}$$

This encodes the thresholds above which objects would be considered for analysis, but without any detector effects such as p_T mismeasurement or identification efficiencies smaller than one.

Of particular interest are the jet kinematics (Figure 5.4), because during analysis, a large m_{jj} will be required to suppress some background processes (cf. Section 5.3.1). On a first look, the distribution of the leading and subleading jet transverse momenta peaks roughly at $p_\mathrm{T} \approx m_W/2$ (Figures 5.4a and 5.4b). As expected for a VBS process, the jets are created symmetrically in the forward region with the maximum of the distribution at $|\eta| \gtrsim 3$, central jet activity is suppressed (Figures 5.4c and 5.4d). The invariant mass m_{jj} of the leading jet pair (Figure 5.4e) has a maximum in the $1 \ldots 1.2\,\mathrm{TeV}$ range, and slowly falls off at higher values. A second peak is observed for $m_{jj} \ll 500\,\mathrm{GeV}$. This is a feature of NLO generation and can be explained by one of the final state quarks emitting a gluon. In the $\Delta\eta_{jj}$ distribution (Figure 5.4f), a corresponding peak at $\Delta\eta_{jj} \approx 0$ can be observed. Apart from this, the leading jet pair is well separated with $|\Delta\eta_{jj}| \gtrsim 6$.

Since the $pp \to \mu^\pm\mu^\pm jj$ signal process is modelled at NLO+PS, it also includes the three-jet variant $pp \to \mu^\pm\mu^\pm jjj$ at LO+PS. The third jet is low in p_T, usually just barely above the threshold of 25 GeV (Figure 5.5a). Usually, the third jet is very forward ($|\eta| \gtrsim 2$), whereas central activity is heavily suppressed (Figure 5.5b). Note that this

Table 5.1.: Object reconstruction thresholds for the DELPHES simulation of the ATLAS detector. Jets are clustered using the anti-k_t algorithm with a radius parameter of $R = 0.4$.

	p_{T}	$\lvert\eta\rvert$
electrons	> 10 GeV	< 2.5
muons	> 10 GeV	< 2.7
jets	> 25 GeV	< 4.5

figure does not prove the absence of central QCD radiation, just that it is below the jet threshold of 25 GeV applied here.

Finally, Figure 5.6 shows the distribution of missing transverse momentum. As expected from a signal process without neutrinos in the final state, it shows a clear peak at zero $E_{\mathrm{T}}^{\mathrm{miss}}$. Since this distribution was plotted after parton shower, it also contains light mesons inside the jets. Some of these light mesons decay to neutrinos, thus explaining the small tail in the $E_{\mathrm{T}}^{\mathrm{miss}}$ distribution.

5.3.3. Detector Simulation and Object Reconstruction

Hadron-level events are then passed through a fast simulation of the ATLAS detector using DELPHES (version 3.4.2) [92]. While this study uses the standard reconstruction and isolation criteria for electrons and muons, the jet clustering is modified. Jets are clustered using the anti-k_t algorithm [52] with a radius parameter of $R = 0.4$. This jet radius is commonly used in recent ATLAS data analyses, unlike the default value of $R = 0.6$. Also, the p_{T} threshold for jets is raised to 25 GeV from the default value of 20 GeV, because $p_{\mathrm{T}}^{j} > 20$ GeV is already applied at generator-level (Equation (5.6)). Raising the threshold will ensure that the energy resolution of the detector does not bias the observed event yields. The object reconstruction criteria are summarised in Table 5.1. The contribution of pile-up is neglected, because real experiments use dedicated algorithms to remove pile-up contributions.

5.4. Signal Region Design

5.4.1. Preselection

Before studying possible signal regions, events need to pass a *preselection*. The selection criteria are motivated by the signature of the process of interest and e. g. the performance of the detector.

A key feature of the model is a final-state with two same-sign leptons. The study presented here is restricted to the $\mu^{\pm}\mu^{\pm}$ channel, thus at preselection, two muons of the same electric charge are required. If the event contains a third lepton, it will be rejected. In addition to the object definition cuts, the leading muon is required to have $p_{\mathrm{T}}^{\mu_1} > 27$ GeV in order to select only events for which the ATLAS muon trigger is fully

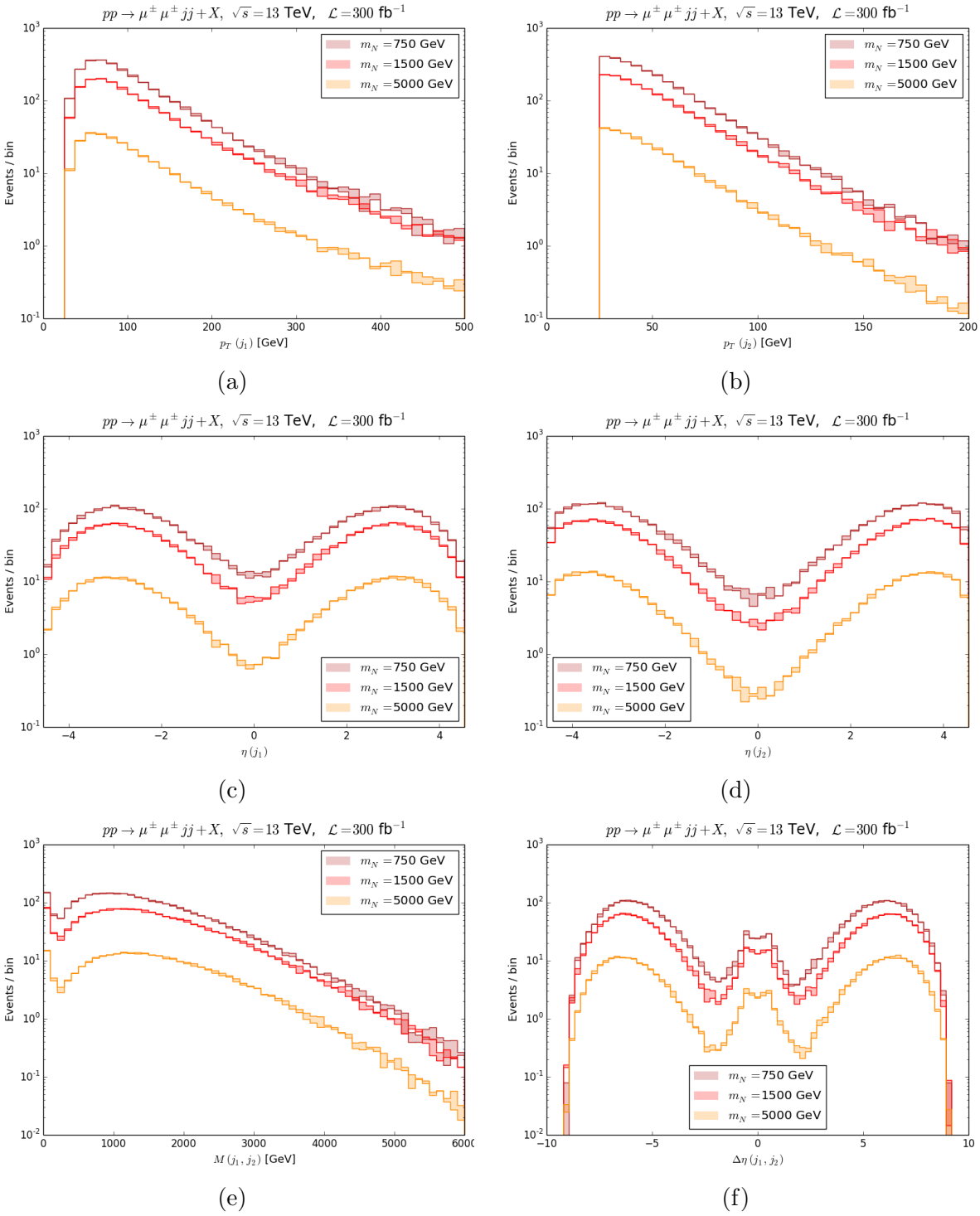

Figure 5.4.: Truth level p_T (a, b) and η (c, d) for the leading (a, c) and subleading (b, d) jet as well as the invariant mass m_{jj} (e) and separation in pseudorapidity $\Delta\eta$ (f) of the leading jet pair.

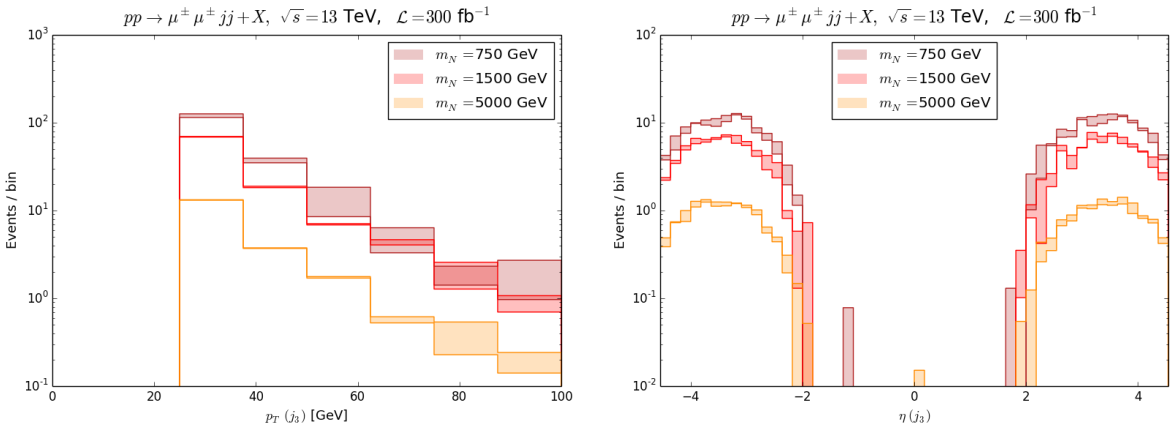

(a) (b)

Figure 5.5.: Truth-level p_{T} (a) and η (b) distributions of the third jet.

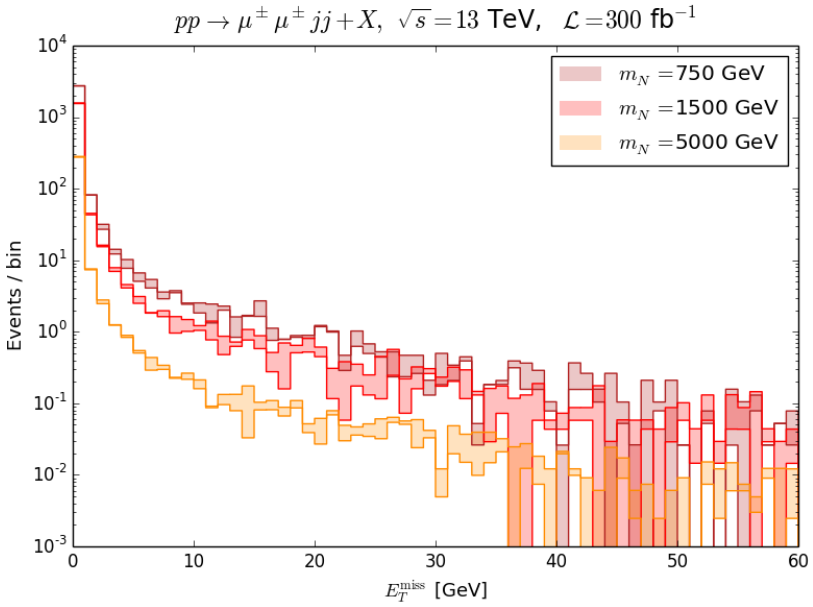

Figure 5.6.: Missing transverse momentum $E_{\mathrm{T}}^{\mathrm{miss}}$ at truth level.

Table 5.2.: Preselection cuts.

$p_{\mathrm{T}}^{\mu_1\,(\mu_2)}$	$> 27\ (10)\,\mathrm{GeV}$	p_{T}^{j}	$> 25\,\mathrm{GeV}$
$\lvert\eta^{\mu}\rvert$	< 2.7	$\lvert\eta^{j}\rvert$	< 4.5
n_{μ}	$= 2$	n_j	≥ 2
$n_e(n_\tau)$	$= 0\ (0)$	m_{jj}	$> 700\,\mathrm{GeV}$
$Q_{\mu_1} \cdot Q_{\mu_2}$	$= 1$		

efficient. While no trigger is applied in this phenomenological study, such a cut would be part of a real collider analysis.

Furthermore, an event has to contain at least two jets clustered with the anti-k_t algorithm with a radius parameter of $R = 0.4$. All jets are required to have $p_{\mathrm{T}}^{j} > 25$ GeV in order to be above the generator-level threshold of $p_{\mathrm{T}}^{j} > 20$ GeV plus a margin to allow for detector resolution effects.

Finally, events with a VBS-like topology are selected by requiring $m_{jj} > 700\,\mathrm{GeV}$. This cut removes some backgrounds, such as top quark production, completely. While a lower cut on m_{jj} might be sufficient to design a good SR, the chosen cut removes some backgrounds, such as top quark production, completely and thus simplifies the event generation (Section 5.3.1).

Kinematics at Preselection

Many observables have been checked for their potential to discriminate the different signal samples from the background, Figure 5.7 shows those that show at least some potential for this purpose. A very pronounced difference can be seen in the transverse momentum distributions of the leading (Figure 5.7a) and subleading (Figure 5.7b) muon. For the t-channel signal processes, the four-momentum of an outgoing lepton is given as

$$p_l = p_W - p_N. \tag{5.13}$$

From this, it is clear that the momentum of leading and subleading muon only differ by the momentum of their respective W bosons p_W and that large m_N also leads to large muon p_{T}. On the other hand, at small m_N and for the Weinberg operator, the lepton transverse momenta are lower and the difference is more pronounced. While $p_{\mathrm{T}}^{\mu_1}$ behaves nearly like the backgrounds, the $p_{\mathrm{T}}^{\mu_2}$ distribution of the backgrounds falls off steeper than all signals and thus offers great discrimination power.

The invariant mass of the leading jet pair (m_{jj}, Figure 5.7c) shows only a less pronounced difference. While the signals seem to have a local maximum around $1 \ldots 1.5\,\mathrm{TeV}$, their shape at higher m_{jj} is very similar to the monotonously falling backgrounds. However, the sum of jet momenta $H_{\mathrm{T}} = \sum_{i\in\{\mathrm{jets}\}} p_{\mathrm{T}}^{j_i}$ (Figure 5.7d) shows that the signal processes have significantly weaker hadronic activity. This is due to the lack of intermediate colour flow. Especially the QCD background, the diagrams of which have an internal quark or gluon, has large H_{T}.

Another characteristic of the signal processes is the absence of final state neutrinos. Naively, one would expect the maximum of the $E_{\mathrm{T}}^{\mathrm{miss}}$ distribution at zero. However, due to the finite detector resolution, some $E_{\mathrm{T}}^{\mathrm{miss}}$ due to mismeasurement arises also for the signal processes (Figure 5.7e). At large m_N, the mismeasurement of high-p_{T} muons gives a significant contribution to $E_{\mathrm{T}}^{\mathrm{miss}}$ and the tails are very similar in shape to the backgrounds.

Finally, the ratio $H_{\mathrm{T}}/p_{\mathrm{T}}^{\mu_1}$ (Figure 5.7f) combines the high lepton momenta and small hadronic activity in the signals. The discrimination is especially strong for large m_N due to the large $p_{\mathrm{T}}^{\mu_1}$ in such samples.

5.4.2. Statistical Evaluation

The significance of observing n_s signal events in addition to n_b background events is determined using the recommendations of [93]. This section summarises the derivation of the recommended formula.

Assuming that the number of observed events n follows a Gaussian distribution and that the background rate is n_b, the significance is $Z = \frac{n-n_b}{\sqrt{n_b}}$. However, this formula assumes a perfect background estimate, which of course is not possible. A simple way to account for the background uncertainty is to split the background into two contributions: One Gaussian distribution with mean n_b and standard deviation $\sqrt{n_b}$ and one with mean 0 and standard deviation σ_b that is the *systematic* uncertainty of the background estimate. The new background distribution will also be Gaussian with mean n_b and a standard deviation of $\sqrt{n_b + \sigma_b^2}$, thus resulting in the significance

$$Z = \frac{n - n_b}{\sqrt{n_b + \sigma_b^2}}. \tag{5.14}$$

However, in the case of a low number of observed or background events, the Gaussian assumption does not hold anymore and this formula will give too high significances. Therefore, the number of observed and background events has to be modelled with a Poisson distribution. The probability of observing n events given an expectation value n_b is given by

$$P(n|n_b) = \frac{n_b^n}{n!} e^{-n_b}. \tag{5.15}$$

When neglecting the background uncertainty, the likelihood of observing n_s signal events is given simply as $L(n_s) = P(n|n_s + n_b)$ ($n_s = 0$ would be the background-only hypothesis). In an actual experiment, the number of background events n_b is unknown. It can be constrained by an auxiliary measurement n_{CR} to which a transfer factor $\tau = \frac{n_b}{\sigma_b^2}$ is applied to convert n_{CR} into a background estimate n_b[3]. The likelihood function in this case is given by

[3] In LHC experiments, the auxiliary measurement is made in a *Control Region* (CR), which is kinematically similar to the signal region, but free of signal events.

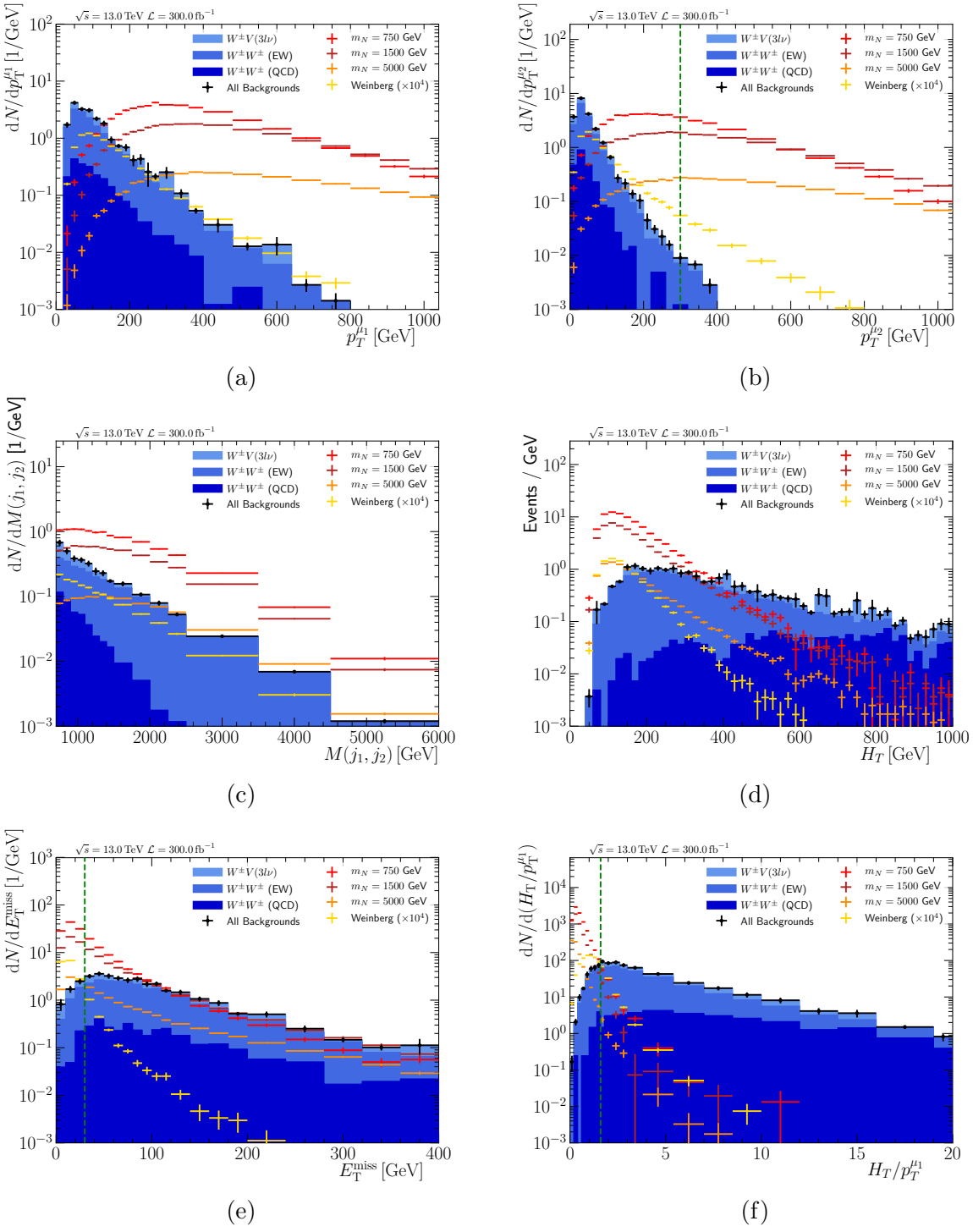

Figure 5.7.: Distributions at preselection for the leading (a) and subleading (b) muon p_{T}, the invariant mass of the leading jet pair m_{jj} (c), the direct sum of jet momenta H_{T} (d), $E_{\mathrm{T}}^{\mathrm{miss}}$ (e) and the ratio $H_{\mathrm{T}}/p_{\mathrm{T}}^{\mu_1}$ (f). The dashed vertical lines indicate where a cut for either of the two signal regions is placed (cf. Table 5.3).

$$L(n_s, n_b) = P(n|n_s + n_b)P(n_{\mathrm{CR}}|\tau n_b). \tag{5.16}$$

For calculating significance, $n_{\mathrm{CR}} = \tau n_b$ is "observed" — which does not have to be an integer. From this likelihood function, the significance is obtained using Wilks' theorem [94]. In the case of the background-only hypothesis, the likelihood is maximised for $\tilde{n_b} = \frac{n+n_{\mathrm{CR}}}{1+\tau}$ and $n_s = 0$, whereas the likelihood of the signal hypothesis is maximised for $\hat{n_s} = n - \hat{n_b}$ and $\hat{n_b} = \frac{n_{\mathrm{CR}}}{\tau}$. With this, the likelihood ratio is is defined as

$$\lambda(0) = \frac{L(0, \tilde{n_b})}{L(\hat{s}, \hat{n_b})}. \tag{5.17}$$

In the case of $n \geq \frac{n_{\mathrm{CR}}}{\tau}$, i. e. at least as many events observed as background events expected, Wilks' theorem defines the significance as $Z = \sqrt{-2\ln\lambda(0)}$[4]. Thus, the significance of observing n events while expecting n_b background events is

$$Z = \sqrt{2(n\ln\left(\frac{n(n_b+\sigma_b^2)}{n_b^2+n\sigma_b^2}\right) - \frac{n_b^2}{\sigma_b^2}\ln\left(1+\frac{\sigma_b^2(n-n_b)}{n_b(n_b+\sigma_b^2)}\right))} \tag{5.18}$$

with σ_b being the systematic uncertainty of the background estimate.

5.4.3. Scan of Possible Signal Region Cuts

The preselection presented above is only a baseline to start studies, it does not offer any sensitivity to the investigated models of new physics. However, one can already check the signal and background distributions of different observables and identify observables that allow a separation of the two (Figure 5.7). Combining cuts on two or more observables may be more efficient than just using a single observable. Thus, "designing a signal region" means to find the combination of cuts that offer the most sensitivity. The ideal signal region can therefore exclude the largest portion of the parameter space of the model of interest at 95 % CL[5].

Type I Seesaw Model

In the Type I Seesaw model, the relation $\sigma \propto |V_{\mu N}|^4$ allows to easily transform event counts into limits on the mixing parameter for a given mass point. Limits will be given in terms of $|V_{\mu N}|^2$ to allow an easy comparison with existing studies.

To find a suitable SR, combinations of cuts on the observables shown in Figure 5.7 are scanned. Each of them offers some degree of signal-background separation. For

[4] In the case of less events observed than background events expected, this turns into $Z = -\sqrt{-2\ln\lambda(0)}$. Some models of new physics could interfere destructively with SM processes, which would would lead to a deficit of observed events. However, none of the models considered in this thesis show this behaviour, thus it is not further considered.

[5] Of course, one could also use "discover with 5σ significance" as criterion — after all, searches are performed to *find* new physics, not to set exclusion limits. However, optimising for discovery would show no sensitivity in large parts of the parameter space where exclusion would still be possible. And in the part where a discovery could be made, both criteria will give the same results.

each combination of cuts, the smallest $|V_{\mu N}|^2$ that could be excluded at 95 % CL is determined. This is done by setting $Z = 2$ in Equation (5.18) and solving the resulting equation for n_s, which then can be easily converted in a limit on $|V_{\mu N}|^2$. It is assumed that the systematic uncertainty of the background estimate will be $\delta_b = 20\,\%$, which is a conservative estimate based on recent measurements of the $W^{\pm}W^{\pm}$ scattering process [95, 96]. The ideal cuts are often somewhat different for different choices of m_N. To exploit the main advantage of the t-channel process, the possibility to probe higher masses than existing searches (and reduce the the amount of information), the cut scans are performed only for a few points with $m_N \geq 1\,\text{TeV}$.

It turns out that a cut on $p_{\text{T}}^{\mu_2} > 300\,\text{GeV}$ is already sufficient to give very good sensitivity. The sensitivity could still be slightly improved ($\Delta|V_{\mu N}|^2 \approx 0.01$) by additionally requiring $E_{\text{T}}^{\text{miss}}/p_{\text{T}}^{\mu_1} < 0.3$. However, this additional cut (or a tighter cut on $p_{\text{T}}^{\mu_2}$) would leave only small background MC statistics. Thus, special care would have to be taken to ensure that the result is not influenced by statistical fluctuations of the backgrounds. Considering that the gain in sensitivity is only marginal and the total expected number of background events is already well below 1, the SR is defined by requiring $p_{\text{T}}^{\mu_2} > 300\,\text{GeV}$ in addition to the preselection.

Weinberg Operator

For the Weinberg operator, the same optimisation procedure is performed as for the Type I Seesaw model. Limits are expressed in terms of the Wilson coefficient $C_5^{\mu\mu}$ and the cutoff parameter Λ, which can be obtained from event counts via the relation $\sigma \propto (|C_5^{\mu\mu}|/\Lambda)^2$. There is no observable that offers such a clear separation of signal and background as $p_{\text{T}}^{\mu_2}$ for the Type I Seesaw model[6] (Figure 5.7). Instead, the fact that the final state of the signal does not contain any neutrinos is used by requiring $E_{\text{T}}^{\text{miss}} < 30\,\text{GeV}$. Due to the finite detector resolution, the $E_{\text{T}}^{\text{miss}}$ distribution of the signal process does not have its maximum at 0, but slightly above 10 GeV. The lack of QCD colour flow between the outgoing hadrons (Figure 5.1b) leads to significantly milder hadronic activity in the signal process than in the QCD and $W^{\pm}V$ background processes. As suggested in [98, 99, 100], the ratio of the scalar sum of jet transverse momenta (H_{T}) and leading muon transverse momentum makes this difference very visible. Thus an upper limit of $H_{\text{T}}/p_{\text{T}}^{\mu_1} < 1.6$ is imposed in the Weinberg operator signal region. Figure 5.8 confirms this choice of cuts.

5.5. Sensitivity at the LHC

Applying the selection described above and summarised in Table 5.3 to the combination of the LHC Run 2 and 3 datasets ($\mathcal{L} = 300\,\text{fb}^{-1}$) would allow to probe $|V_{\mu N}|^2 \gtrsim$

[6] For small $m_N \lesssim 100\,\text{GeV}$, the kinematics of the two models are actually very similar. While the Weinberg operator selection would then offer better sensitivity to heavy Majorana neutrinos of $m_N \lesssim 300\,\text{GeV}$ (Table 5.5), searches targeting the s-channel process are several orders of magnitude more sensitive at low m_N [97].

Table 5.3.: Preselection and signal region cuts.

Preselection cuts							
$p_{\mathrm{T}}^{\mu_1(\mu_2)}$	$> 27(10)\,\mathrm{GeV}$	$\lvert\eta^{\mu}\rvert$	< 2.7	n_{μ}	$= 2$	$Q_{\mu_1} \times Q_{\mu_2}$	$= 1$
p_{T}^{j}	$> 25\,\mathrm{GeV}$	$\lvert\eta^{j}\rvert$	< 4.5	n_j	≥ 2	m_{jj}	$> 300\,\mathrm{GeV}$
Type I Seesaw Signal Region cuts							
$p_{\mathrm{T}}^{\mu_2} > 300\,\mathrm{GeV}$							
Weinberg Operator Signal Region cuts							
$E_{\mathrm{T}}^{\mathrm{miss}} < 30\,\mathrm{GeV}$						$H_{\mathrm{T}}/p_{\mathrm{T}}^{\mu_1}$	< 1.6
Changes to preselection and Weinberg Operator SR cuts at $\sqrt{s} = 100\,\mathrm{TeV}$							
$\lvert\eta^{e(\mu)[j]}\rvert$	$< 4.0(4.0)[5.5]$	m_{jj}	$> 1\,\mathrm{TeV}$	$E_{\mathrm{T}}^{\mathrm{miss}}$	$< 20\,\mathrm{GeV}$	$H_{\mathrm{T}}/p_{\mathrm{T}}^{\mu_1}$	< 0.6

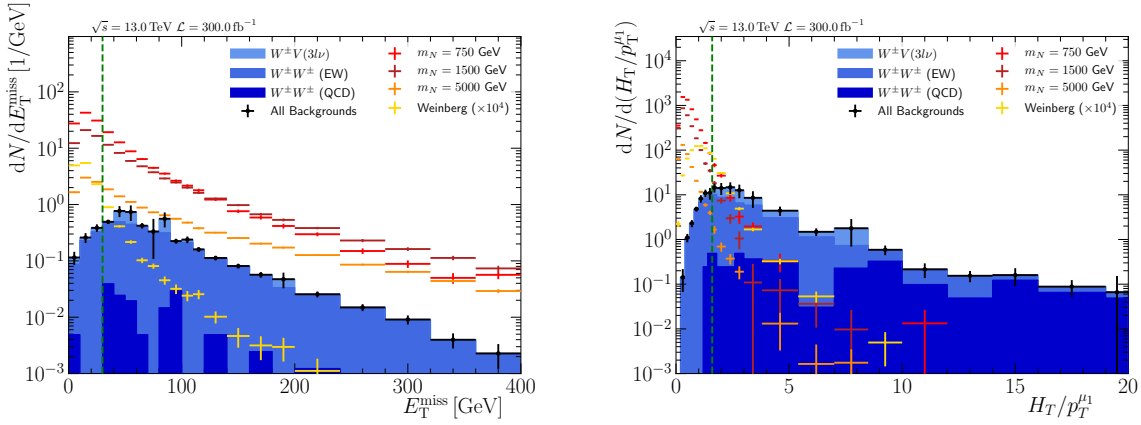

(a) (b)

Figure 5.8.: N-1 distributions in the Weinberg Operator signal region for $E_{\mathrm{T}}^{\mathrm{miss}}$ (a) and $H_{\mathrm{T}}/p_{\mathrm{T}}^{\mu_1}$ (b).

$0.06 \ldots 0.6$ at 95 % CL for $m_N = 50\,\text{GeV} \ldots 20\,\text{TeV}$, with a maximum sensitivity around $m_N = 1\,\text{TeV}$. A tenfold increase in luminosity at the HL-LHC would extend the sensitivity to $|V_{\mu N}|^2 \gtrsim 0.03 \ldots 0.3$ (Table 5.4). The shape of the limit corresponds to the shape of the cross section for the Type I Seesaw model as function of m_N (Figure 5.3). However, the sensitivity is shifted toward higher values of m_N. At higher m_N, the momentum of the outgoing muons is also higher (Figures 5.7a and 5.7b), thus more events pass the $p_{\text{T}}^{\mu_2} > 300\,\text{GeV}$ cut in the signal region. Figure 5.9 compares the sensitivity of the proposed t-channel analysis to a recent result on the s- and $W\gamma$ fusion channel processes by the CMS experiment [78]. That analysis is very sensitive at small m_N, probing $|V_{\mu N}|^2 \gtrsim 2 \cdot 10^{-5}$ at $m_N \lesssim 50\,\text{GeV}$. Sensitivity decreases rapidly with increasing m_N and is approximately the same as the t-channel analysis around $m_N \approx 750\,\text{GeV}$ and reaches $|V_{\mu N}|^2 = 1$ at $m_N = 1.4\,\text{TeV}$. In a projection to the HL-LHC ($3000\,\text{fb}^{-1}$), the t-channel analysis becomes the dominant production mode for $m_N \gtrsim 1\,\text{TeV}$. However, even with the increased luminosity, it will not be able to compete with the $|V_{\mu N}|^2 < 4.41 \cdot 10^{-4}$ indirect limits (Section 5.1.4).

Similarly, the Weinberg Operator could be probed at 95 % CL with $300\,\text{fb}^{-1}(3\,\text{ab}^{-1})$ at scales up to

$$\frac{\Lambda}{C_5^{\mu\mu}} \lesssim 8.3(11)\,\text{TeV}. \tag{5.19}$$

This corresponds to an effective Majorana mass of $|m_{\mu\mu}| \gtrsim 7.3(5.4)\,\text{GeV}$. For comparison, a search for lepton number violation in $K^\pm \to \pi^\mp \mu^\pm \mu^\pm$ decays at the NA-62 experiment probes $m_{\mu\mu} \gtrsim 55\,\text{GeV}$ [101] with the 2017 dataset using the prescription from [102] to convert the results into limits on $m_{\mu\mu}$. The LHCb experiment could probe $m_{\mu\mu} > 9\,\text{MeV}$ in $B^\pm \to \pi^\mp \mu^\pm \mu^\pm$ decays using $300\,\text{fb}^{-1}$ of data. While the search here presents a significant improvement over previous results, it cannot probe the $m_{\mu\mu}$ range allowed by a fit to neutrino oscillation data. The exact range depends on the mass hierarchy and mass of the lightest neutrino [103]. Assuming normal mass ordering (NO) and a lightest neutrino lighter than $10^{-2}\,\text{eV}$, only values in the range $2 \cdot 10^{-2}\,\text{eV} \lesssim m_{\mu\mu} \lesssim 3 \cdot 10^{-2}\,\text{eV}$ are allowed. In the same mass range, the inverted mass ordering allows roughly $10^{-3}\,\text{eV} \lesssim m_{\mu\mu} \lesssim 2 \cdot 10^{-2}\,\text{eV}$. For a lightest neutrino of 1 eV mass, the allowed range of $0.1\,\text{eV} \lesssim m_{\mu\mu} \lesssim 1\,\text{eV}$ is identical for both mass orderings. Figure 5.10 summarises the above mentioned limits and constraints.

Finally, a first estimate of the sensitivity to the Weinberg operator at an LHC successor with $\sqrt{s} = 100\,\text{TeV}$ is performed. This requires some modifications to the analysis detailed at the bottom of Table 5.3. Future detectors are expected to have a larger coverage in $|\eta|$ and the larger event rates allow to apply tighter cuts. Also, future experiments are expected to have better resolution and better control region modelling, therefore the background systematic uncertainty is reduced to $\delta_b = 5\,\%$. Note that the cuts were chosen to be a minimal modification to those applied at $\sqrt{s} = 13\,\text{TeV}$ and a thorough optimisation procedure may yield better results. Also, a statistical uncertainty of the $W^\pm V$ MC sample of ca. 30 % is neglected. This uncertainty arises even though 10^7 events were generated at NLO + PS.

Table 5.4.: Expected exclusion (excl.) and discovery (disc.) limits at the LHC (300 fb^{-1}) and HL-LHC (3 ab^{-1}) on the squared heavy neutrino mixing with the muon $|V_{\mu N}|^2$ following the analysis described in the text, as well as acceptance and efficiency with respect to the generator-level cross section.

m_N [GeV]	$\mathcal{L} = 300\,\text{fb}^{-1}$		$\mathcal{L} = 3\,\text{ab}^{-1}$		$\frac{\sigma^{\text{SR}}}{\sigma^{\text{Gen.}}}$ [%]
	$\lvert V_{\mu N}^{\text{excl.}}\rvert^2$	$\lvert V_{\mu N}^{\text{disc.}}\rvert^2$	$\lvert V_{\mu N}^{\text{excl.}}\rvert^2$	$\lvert V_{\mu N}^{\text{disc.}}\rvert^2$	
50	0.55	0.81	0.31	0.53	0.6
150	0.13	0.24	0.072	0.13	3.9
300	0.080	0.15	0.044	0.077	7.8
450	0.064	0.12	0.035	0.062	12.1
600	0.058	0.10	0.032	0.056	15.6
750	0.057	0.10	0.031	0.054	18.2
900	0.056	0.10	0.031	0.054	21.1
1000	0.056	0.10	0.031	0.054	22.2
1250	0.059	0.11	0.033	0.057	24.2
1500	0.063	0.12	0.034	0.060	26.2
1750	0.067	0.12	0.037	0.064	27.1
2000	0.071	0.13	0.039	0.068	28.4
2500	0.081	0.15	0.044	0.078	29.4
5000	0.14	0.25	0.074	0.13	31.4
7500	0.19	0.36	0.11	0.19	32.2
10000	0.25	0.46	0.14	0.24	32.5
15000	0.34	0.62	0.18	0.32	32.6
20000	0.49	0.81	0.27	0.47	32.6

In conclusion, a search for heavy Majorana neutrinos in the t-channel at the LHC will be able to extend the mass reach by an order of magnitude over existing searches. However, the sensitivity to the Weinberg operator would be bad even with a dedicated SR. Thus it seems prudent to design a search for heavy Majorana neutrinos and see whether a minor modification of it can enhance the sensitivity to the Weinberg operator.

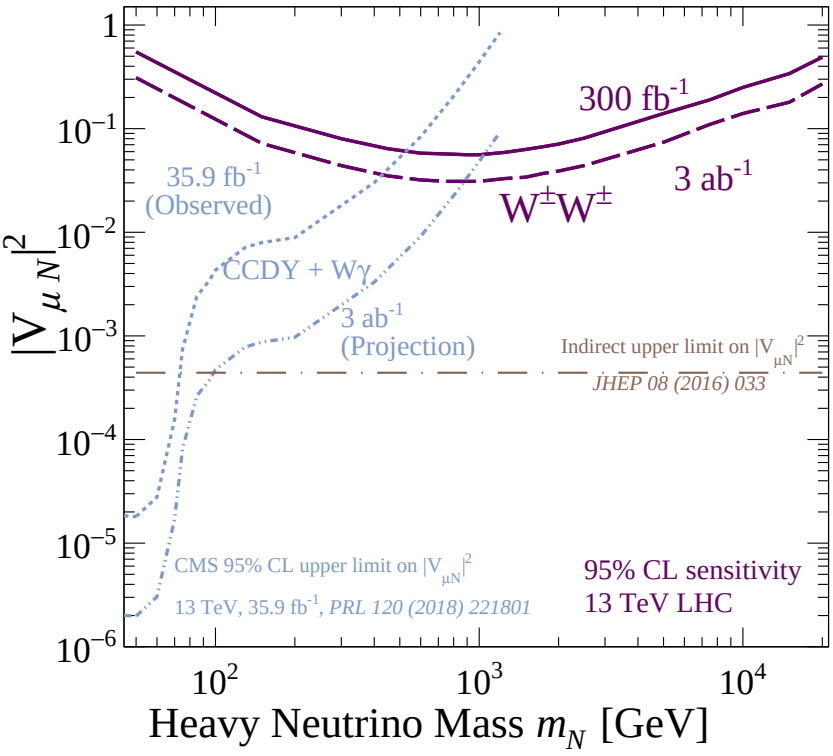

Figure 5.9.: Expected sensitivity at 95 % CL for the Type I Seesaw model at the LHC (300 fb^{-1}) and HL-LHC (3 000 fb^{-1}) (purple). For comparison, the direct limits set by CMS in the $W\gamma$ fusion and s-channels [97], their extrapolation to the HL-LHC and indirect limits on $|V_{\mu N}|^2$ [82] are shown.

Table 5.5.: Expected exclusion limits at the LHC ($\mathcal{L} = 300\,\text{fb}^{-1}$) on the squared heavy neutrino mixing with the muon $|V_{\mu N}|^2$ applying the selection optimised for the Weinberg operator.

m_N [GeV]	$\lvert V_{\mu N}^{\text{excl.}}\rvert^2$
50	0.22
150	0.10
300	0.08
450	0.08
600	0.09
750	0.09
1000	0.10
1500	0.13
5000	0.34
10000	0.67
15000	0.89

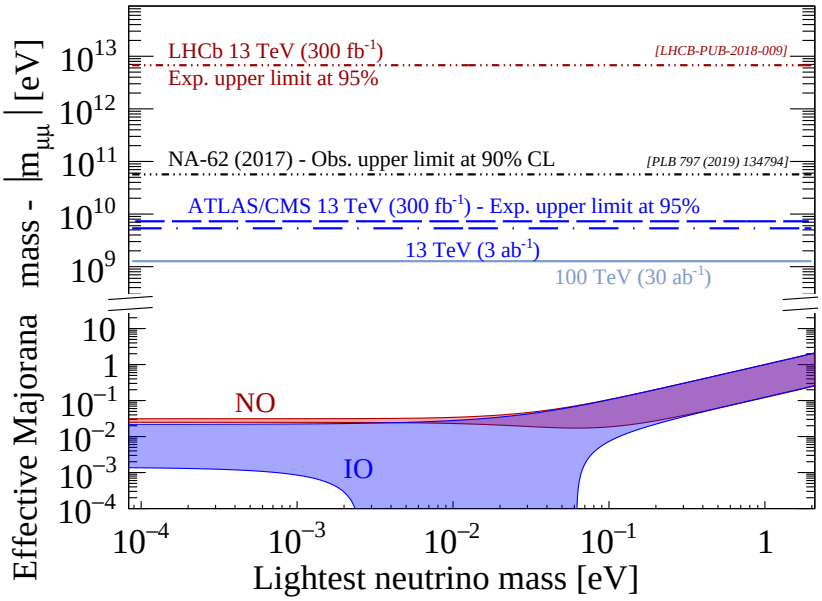

Figure 5.10.: Expected sensitivity to $|m_{\mu\mu}|$ at the LHC compared to observed limits from the NA-62 experiment [101] and constraints from fits to neutrino oscillation data [103] For comparison, the estimated sensitivity of the LHCb experiment with the combined LHC Run 2 and 3 datasets [104] is also shown.

6. Search for Majorana Neutrinos in Same-Sign $W^{\pm}W^{\pm}$ Scattering with the ATLAS Experiment

The phenomenological study presented in Chapter 5 has shown that LHC experiments are sensitive to the t-channel process of the Type I Seesaw model. In particular, this process can probe heavy neutrinos up to $m_N \gtrsim 20\,\text{TeV}$, whereas the best s-channel searches only are sensitive up to $m_N \approx 1\,\text{TeV}$. This promising outlook justifies performing a search with the ATLAS experiment. As in the phenomenological study, this will be limited to the $\mu^{\pm}\mu^{\pm}$ final state. While the $\tau^{\pm}\tau^{\pm}$ final state would also be highly interesting, it is much more difficult experimentally and thus more suited for a later analysis. On the other hand, the $e^{\pm}e^{\pm}$ final state can also be probed in nuclear physics experiments (e. g. the GERDA experiment [21]), thus it is less novel.

In addition to the Type I Seesaw, the Weinberg Operator will be considered as an alternative signal model.

6.1. Data and Simulated Samples

The analysis is performed with the full Run 2 dataset of $140\,\text{fb}^{-1}$ of proton-proton collisions at $\sqrt{s} = 13\,\text{TeV}$ collected from 2015 to 2018. Data is collected using the lowest unprescaled[1] muon trigger for each period (Table 6.1). For the 2015 dataset, this is the `HLT_mu20_iloose_L1MU15` trigger, which triggers on a CB muon candidate with $p_{\text{T}} > 20\,\text{GeV}$. Additionally, the scalar sum of track p_{T} within $\Delta R < 0.2$ of the muon track must be less than 12 % of the muon p_{T} [105]. The 2016-2018 datasets are collected with the `HLT_mu26_ivarmedium` trigger. It selects a CB muon with $p_{\text{T}} > 26\,\text{GeV}$ and a different isolation criterion. The sum of track p_{T} within $\Delta z < 6(2)\,\text{mm}$ must be less than 7 % of the muon p_{T}, the tighter criterion applies to only to the 2018 dataset. Throughout all of Run 2, these triggers are complemented by the `HLT_mu50` trigger. It triggers on a CB muon with $p_{\text{T}} > 50\,\text{GeV}$ and is used to compensate inefficiencies of the other triggers at high p_{T}. No isolation criterion is applied [105, 106].

SM and signal expectations are obtained from MC simulations. All samples are passed through the full ATLAS detector simulation [107] based on GEANT 4 [108]. The influence of pile-up is determined using dedicated simulations that are then overlayed with the simulations of the hard process. Pile-up events are generated using PYTHIA 8.186 [87]

[1] i. e. collecting every event that passes the trigger.

Table 6.1.: Triggers used during data-taking.

years	trigger
2015	HLT_mu20_iloose_L1MU15
2016 — 2018	HLT_mu26_ivarmedium
2015 - 2018	HLT_mu50

using the NNPDF2.3lo PDF set [109] with the A3 tune [110]. Events are weighted to reproduce the expected pile-up profile in the 2015-16 and 2018 datasets. For the 2017 dataset, the actual pile-up profile is used, since it differs significantly from the expected pileup profile.

6.1.1. Signal MC

While the signal processes have been generated before (Section 5.3.1), event generation needs to be repeated inside the ATLAS software framework. This will create events in a file format suitable for use with the simulation and reconstruction software used in ATLAS. Apart from these technical changes, the phase space cuts need to be adjusted. ATLAS reconstructs jets with $p_{\mathrm{T}} > 20\,\mathrm{GeV}$, whereas in Section 5.3.1, a generator-level cut of $p_{\mathrm{T}}^{j} > 20\,\mathrm{GeV}$ was used. In order to avoid effects on the reconstructed distributions, the p_{T} cut at generator needs to be ca. 5 GeV lower than the reconstruction threshold. Reducing the generator-level cut to $p_{\mathrm{T}}^{j} > 15\,\mathrm{GeV}$ makes it necessary to add or adjust generator-level cuts on other observables in order to keep the matrix element calculation time within acceptable levels.

Type I Seesaw

For the Type I Seesaw model, the initial event generation was done using MadGraph5_aMC@NLO (version 2.7.3) [83] with NNPDF3.0nlo [109] combined with Pythia 8 (version 243) [87] for parton shower simulation using the A14 tune [111] and NNPDF2.3lo [109]. Decays of hadrons containing b or c quarks are simulated with EvtGen (version 1.7.0) [112]. The process of Figure 5.1a is generated with the same syntax as in Section 5.2. The automated infrared pole cancellation check is disabled (cf. Section 5.2) and generator-level cuts on transverse momentum and pseudorapidity of jets and leptons as well as on the dilepton invariant mass are applied in order to reduce the matrix element calculation time (Table 6.2). The cuts were chosen such that they have negligible impact on the signal kinematics after a standard reconstruction is applied. For all event generation, the heavy neutrino is chosen to mix exclusively with muons, i. e. $|V_{\mu N}|^2 = 1, |V_{eN}|^2 = |V_{\tau N}|^2 = 0$. Since this parameter affects only the cross section, samples can be rescaled arbitrarily.

Five *benchmark points* with heavy neutrino masses of $m_N = 0.5, 1, 3, 5, 10\,\mathrm{TeV}$ are generated in order to design the analysis. The amount of events is chosen so that a statistical uncertainty of $\lesssim 1\,\%$ is expected in the signal region based on the acceptance

Table 6.2.: Generator-level cuts for the Type I Seesaw model.

$p_{\mathrm{T}}^{j} > 15\,\mathrm{GeV}$	$\lvert\eta^{j}\rvert < 5.2$
$p_{\mathrm{T}}^{l} > 10\,\mathrm{GeV}$	$\lvert\eta^{l}\rvert < 2.9$
$m_{ll} > 15\,\mathrm{GeV}$	

and efficiency observed in the phenomenological study (Table 5.4). The simulations are validated by comparing truth-level distributions with the shapes expected from the phenomenological study (Appendix B.1).

When determining the signal contamination in the different regions, the mixing parameters of the 500 GeV and 1 TeV samples are set to the exclusion limits determined in [97], $|V_{\mu N}|^2 = 0.08$ and $|V_{\mu N}|^2 = 0.45$, respectively.

The statistical evaluation is performed on 20 mass points between 50 GeV and 25 TeV with $|V_{\mu N}|^2 = 1$. Those samples were generated with the same configuration as described above, but using MadGraph5_aMC@NLO version 2.9.9 and Pythia 8 version 307. A comparison of the benchmark points between the two generator versions showed no significant differences.

Weinberg Operator

The alternative signal model considered in this analysis is the Weinberg operator. It is generated using MadGraph_aMC@NLO (version 2.9.3) [83] with the `NNPDF3.1luxQED` [109] parton distribution function and then parton showered using Pythia 8 (version 245) [87] with the `A14` tune [111] and `NNPDF2.3lo` [109]. Decays of hadrons containing b and c quarks are simulated with EvtGen (version 1.7.0) [112]. The same model implementation and syntax as in Section 5.3.1 are used, but the generator-level phase space cuts are changed to

$$p_{\mathrm{T}}^{j} > 15\,\mathrm{GeV} \qquad\qquad |\eta^{j}| < 5.5.$$

For event generation, a cutoff scale of $\Lambda = 200\,\mathrm{TeV}$ is chosen and all Wilson coefficients are set to zero with the exception of $C_5^{\mu\mu} = 1$. Since these two parameters affect only the cross section according to $\sigma \propto (C_5^{\mu\mu}/\Lambda)^2$, arbitrary values of the ratio can be probed. This model has never before been used in ATLAS and is thus validated extensively (Appendix B.2).

6.1.2. Background Samples

Samples for background processes are produced centrally in ATLAS and shared among many analyses. In the following paragraphs, the two main background samples are described. A multitude of minor backgrounds is considered in this analysis. They will not be shown separately, but grouped as *other*. Their processes and generators are listed in Table 6.3.

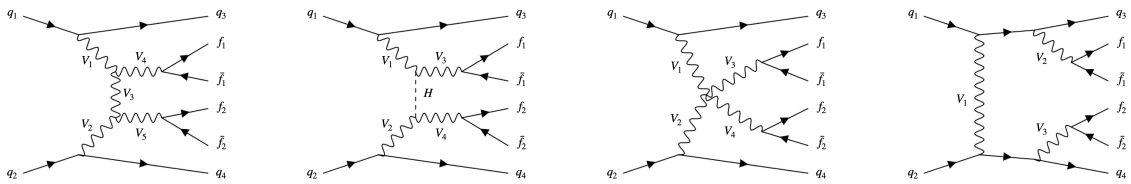

Figure 6.1.: Representative Feynman diagrams of the electroweak diboson production.

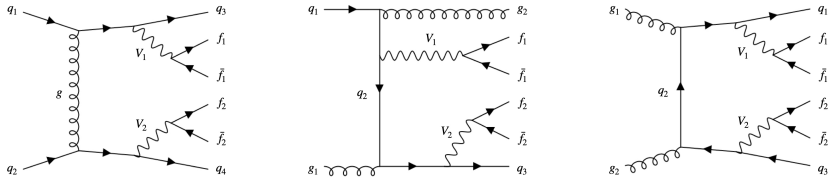

Figure 6.2.: Representative Feynman Diagrams of the mixed electroweak-QCD diboson production.

Same-Sign WW

For the SM production of two same-charge W bosons, the electroweak (Figure 6.1), mixed electroweak-QCD (Figure 6.2, referred to as QCD) and their interference terms are considered. All three processes are generated separately at LO in QCD using MadGraph5_aMC@NLO (version 2.6.7) and then parton-showered with Pythia 8 (version 244) using the `A14` tune. However, the default configuration of Pythia 8 generates too much radiation in the central region for VBS processes. This is mitigated with a novel dipole-recoil scheme in which only one parton takes the recoil of an emission instead of the whole final state [113]. This method has a better agreement with data from deep inelastic scattering [113] and offers an improved theoretical description of VBS $W^{\pm}W^{\pm}$ [114] and $W^{\pm}Zjj$ production [115]. Note that the dipole recoil scheme is used only for this background sample and not for the signal samples. Currently, it cannot be used for NLO samples generated with MadGraph5_aMC@NLO. In some figures, the $W^{\pm}W^{\pm}$ background is labelled as *ssWW*.

In order to evaluate systematic uncertainties related to the parton shower, these samples are compared to alternative samples that were generated with MadGraph5_aMC@NLO, but used Herwig (version 7.2) [116] for the parton shower. The alternative samples use the `NNPDF3.0nlo` PDF set.

Other Diboson Processes

Other diboson processes (VV) are simulated with Sherpa version 2.2.1 or 2.2.2 [117], depending on the exact process. The fully and semileptonic final states of the mixed EW-QCD processes (Figure 6.2, also referred to as QCD) are generated at NLO with up to one additional parton and LO accuracy for up to three additional partons. The

Table 6.3.: Overview of the different MC generators, PDFs and, if applicable, parton shower tunes used for the various samples used in this analysis. Samples marked *(EW)* contain only electroweak processes, whereas those marked *(QCD)* contain the mixed EW-QCD processes.

Type I Seesaw	MG5_aMC@NLO (NLO)+ Pythia 8	NNPDF3.0nlo/A14
Weinberg Operator	MG5_aMC@NLO (NLO) + Pythia 8	NNPDF3.0nlo/A14
$W^{\pm}W^{\pm}$	MG5_aMC@NLO (NLO) + Pythia 8	NNPDF3.0nlo/A14
$W^{\pm}W^{\pm}$ (alternative)	MG5_aMC@NLO (LO) + Herwig 7	NNPDF3.0nlo/A14
other diboson (QCD)	Sherpa 2.2.1/2	NNPDF3.0nnlo
other diboson (EW)	Sherpa 2.2.2	NNPDF3.0nnlo
other diboson (truth studies)	PowhegBox v2 (NLO)+ Pythia 8	CT10/AZNLO
triboson (excl. $VVV(\rightarrow jj)$)	Sherpa 2.2.2 (NLO)	NNPDF3.0nnlo
$t\bar{t}V$	MG5_aMC@NLO (NLO) + Pythia 8	NNPDF3.0nlo/A14
other V+top(s)	MG5_aMC@NLO (NLO) + Pythia 8	NNPDF3.0nlo/A14
V+jets	Sherpa 2.2.11 (NLO)	NNPDF3.0nnlo
$V+\gamma$ (QCD)	Sherpa 2.2.11 (NLO)	NNPDF3.0nnlo
$V+\gamma$ (EW)	MG5_aMC@NLO (NLO) + Pythia 8	NNPDF3.0lo/A14
$t\bar{t}$ pairs	PowhegBox v2 (NLO) + Pythia 8	NNPDF3.0nlo/A14
single top	PowhegBox v2 (NLO) + Pythia 8	NNPDF3.0nlo/A14
γ+jets	Sherpa 2.2	NNPDF3.0nnlo
multijet	Pythia 8 v230	NNPDF2.3lo/A14

loop-induced $gg \rightarrow VV$ process is calculated at LO for up to one additional parton. All samples are parton-showered with the Sherpa implementation based on Catani-Seymour dipole factorisation [118, 119] using the MEPS@NLO prescription [120, 121, 122, 123] and virtual QCD corrections from the OpenLoops library [124, 125, 126]. Parton distributions are taken from the NNPDF3.0nnlo PDF set.

The electroweak diboson production $VVjj$ includes also $VVV(\rightarrow jj)$ and is generated at LO with the NNPDF3.0nnlo PDF set. Parton showering is based on the Catani-Seymour dipole factorisation using the MEPS@LO method.

Out of the diboson processes, only WZ will be separately shown in the analysis, combining both production modes. Other diboson processes were found to have only a small impact and will therefore be grouped with the "other" backgrounds.

The truth record of events generated with Sherpa is formatted in a way that makes in unfeasible to trace back particle decay chains. Therefore, an alternative sample of mixed EW-QCD WW, WZ and ZZ is generated with PowhegBox (version 2) [127, 128, 129] and used for truth-level studies. Events are generated at NLO using the CT10 PDF set [130] and then parton-showered with Pythia 8 (version 186) using the AZNLO tune [131] and CTEQ6L1 PDF set [132].

6.2. Object Definitions

Out of the various possible working points for object reconstruction, a combination needs to be chosen that works well for the Type I Seesaw and Weinberg operator signal models. Both predict two muons of the same electric charge and at least two jets, which are likely to be in the forward regions of the detector. For most objects, two different sets of requirements are defined. *Baseline* objects fulfil some loose reconstruction criteria. They are used for vetos as well as for the $E_{\mathrm{T}}^{\mathrm{miss}}$ calculation and as input to overlap removal. Objects that survive overlap removal and fulfil more stringent selection criteria are used as *signal* objects. Typically, these are the main objects of interest in a selection.

Since this analysis targets the $\mu^{\pm}\mu^{\pm}$ final state, electrons are only of interest for lepton vetoes. Thus, only a baseline electron selection is made with the `LooseLH` working point and requires an $E_{\mathrm{T}} > 4.5\,\mathrm{GeV}$. No isolation is required.

Baseline muons are also identified at the `Loose` working point (WP) without any isolation criteria. They have $p_{\mathrm{T}} > 3\,\mathrm{GeV}$ and $|\eta| < 2.7$ as well as a d_0 significance smaller than 15 and $|z_0| < 1.5\,\mathrm{mm}$. Signal muons are identified at the `Medium` WP with tight isolation criteria. They need to have $p_{\mathrm{T}} > 10\,\mathrm{GeV}$ and $|\eta| < 2.5$, i. e. be in the part of the detector also instrumented by the Inner Detector. Additionally, they need to have a d_0 significance smaller than 3.0. Specifically for muons, there is a third object definition used to estimate the non-prompt muon background. *Spurious* muons are identified also at the `Medium` working point, but need to fulfil only loose isolation criteria. They also require a d_0 significance < 10.0, but otherwise the selection criteria are the same as for the signal muons. However, spurious muons must not pass the signal muon definition.

Jets are reconstructed from particle flow objects with the anti-k_t algorithm and a radius parameter of $R = 0.4$. Baseline jets need to have $p_{\mathrm{T}} > 20\,\mathrm{GeV}$ and $|\eta| < 4.5$. Pile-up in the central region of the detector ($|\eta| < 2.4$) is suppressed by requiring a score of more than 0.6 in the JVT algorithm for jets with $p_{\mathrm{T}} < 60\,\mathrm{GeV}$. Similarly, forward jets ($2.5 < |\eta| < 4.5$) below this p_{T} threshold need to score less than 0.5 in the fJVT algorithm and have a timing difference smaller than 10 ns. Signal quality jets have a higher p_{T} threshold of 25 GeV. Jets originating from b quarks are identified with the `DL1r` algorithm at the 85 % working point.

$E_{\mathrm{T}}^{\mathrm{miss}}$ is reconstructed from baseline objects using the track-based soft term. The definition of baseline objects corresponds to the `Tight` $E_{\mathrm{T}}^{\mathrm{miss}}$ working point[2].

6.2.1. Overlap removal

The reconstruction algorithms for electrons, muons and jets are running in parallel. Thus, the same detector response may end up in several reconstructed objects. Ambiguities are resolved by a dedicated *overlap removal* (OR) procedure described below. This procedure uses the rapidity y to calculate distances instead of the more common pseudorapidity: $\Delta R_y = \sqrt{\Delta y^2 + \Delta\phi^2}$.

[2]Note that the definition of this working point has changed since [60] was published.

Electrons and muons are considered to be overlapping when they share a track in the ID. If the muon is of the *Calo muon* type (cf. Section 3.3.3), the muon is rejected. Otherwise, the electron is rejected and the muon kept.

In general, electrons are discarded if they are within $\Delta R_y < 0.4$ of a jet. Only if the jet is not b-tagged, the distance is smaller than 0.2 and the electron has $E_{\mathrm{T}} < 100\,\mathrm{GeV}$ the jet is rejected and the electron kept.

If a muon is within $\Delta R_y < 0.4$ of a jet, it is generally rejected. One exception to this rule are jets that are identified to be most likely a fake. Also, jets that are not b-tagged, have less than three tracks and where either the jet is within $\Delta R_y < 0.2$ of the muon or the track of the muon in the ID is ghost-associated[3] to the jet.

6.3. Event Selection

6.3.1. Preselection

A very basic *Preselection* encodes the basic properties of the signal models. This preselection serves as a starting point for more detailed studies, such as the design of control and signal regions. Events need to pass the lowest unprescaled muon trigger, which varies between the different data taking periods (cf. Table 6.1) and the following requirements.

Two or more same-sign muons of signal quality, as this is the main feature of both models considered in this analysis. The leading and subleading lepton need to have $p_{\mathrm{T}} > 27\,\mathrm{GeV}$. This ensures that the triggers are fully efficient. Additionally, an event needs to have at least two jets of signal quality. The leading jet must have $p_{\mathrm{T}}^{j_1} > 30\,\mathrm{GeV}$ in order to reduce the contribution of pile-up. Further jets have $p_{\mathrm{T}}^{j} > 25\,\mathrm{GeV}$ due to their object definition. Also, $m_{jj} > 150\,\mathrm{GeV}$ or the presence of a third baseline lepton is required. The former cut selects events with a VBS-like topology – which is predicted for both signal models. The latter cut allows more flexibility to define a three-lepton control region. Both filters are essential to reduce the size of the dataset to fit into the available disk space. Finally, events including a *bad* baseline muon are vetoed. A muon is flagged as bad if the relative uncertainty on its momentum is larger than the momentum uncertainty on the individual track fits in ID and MS. This indicates that the muon was not reconstructed properly.

MC events are subject to an additional truth-level selection. The leading and subleading muon have to be either prompt or be a fake originating from a photon. This avoids double-counting of non-prompt muons arising from hadrons or charge-flipped muons, as both of these backgrounds are estimated from data.

Distributions of the six observables used in the analysis design after preselection are shown in Figure 6.3. Note that the main backgrounds will be normalised to data for the

[3]The muon ID track is considered to be a very soft constituent of the jet. The concept of infinitely soft *ghost particles* was introduced in [133, 134] to study some aspects of jet algorithms. The exact criteria used for ghost association in ATLAS were to the best knowledge of the author never published.

statistical evaluation, so that the slight systematic excess visible in these histograms is of no concern.

6.3.2. Signal Region

Previous studies (Chapter 5) have shown that the t-channel can vastly extend the mass range of searches for the Type I Seesaw mechanism over the existing s-channel searches [97]. Therefore, the analysis presented here will have a signal region optimised for $m_N \gtrsim 1\,\text{TeV}$. Since both the Type I Seesaw model as well as the Weinberg operator predict exactly two same-sign leptons, events with a third baseline lepton are vetoed. This greatly helps in reducing the WZ background. Also, events containing a b-jet are vetoed. Such events are very likely to contain a non-prompt muon. This leaves four main observables:

- The subleading muon transverse momentum $p_{\text{T}}^{\mu_2}$ was found have very strong separation power in Section 5.4.3.
- The invariant mass of the leading jet pair m_{jj} can be used to select a VBS-like topology.
- Similarly, the rapidity gap between the leading two jets ΔY_{jj} can also be used to select a VBS-like topology.
- Since both signals do not have outgoing neutrinos, their $E_{\text{T}}^{\text{miss}}$ arises only from mismeasurement. Thus, $E_{\text{T}}^{\text{miss}}$ significance can be used to distinguish them from backgrounds with outgoing neutrinos.

The signal region is designed with a simultaneous scan of different cuts on $p_{\text{T}}^{\mu_2}$, m_{jj} and ΔY_{jj} that takes correlations between these observables into account. Like in the phenomenological study (cf. Section 5.4.3), the Poisson significance as recommended by [93] is used to calculate potential exclusion limits on $|V_{\mu N}|^2$ for each cut combination. A systematic uncertainty of 15 % of the background estimate is assumed for optimisation. Apart from that, the exact same methodology is used.

The optimal cut choices vary for each mass point. Requiring $m_{jj} > 300\,\text{GeV}$ and $\Delta Y_{jj} > 4$ in the SR is a compromise that works well for all mass points. In general, the cut on $p_{\text{T}}^{\mu_2}$ should be as high as possible for maximum sensitivity. However, a cut of of $p_{\text{T}}^{\mu_2} > 200\,\text{GeV}$ or more, as recommended by the optimisation routine, would result in an unreliable background estimation due to low statistics. Additionally, sensitivity towards the Weinberg operator would be reduced significantly. Thus, it was decided to not cut on this observable, but instead bin in $p_{\text{T}}^{\mu_2}$ with bin boundaries at $[27, 40, 60, 80, 100, 120, \infty]\,\text{GeV}$. Each bin is expected to have at least approx. two background events.

An additional cut on $E_{\text{T}}^{\text{miss}}$ significance < 4.5 was introduced to make the SR orthogonal to the $W^{\pm}W^{\pm}$ control and validation regions. Since the signal has no true $E_{\text{T}}^{\text{miss}}$, this cut gives a small improvement in sensitivity.

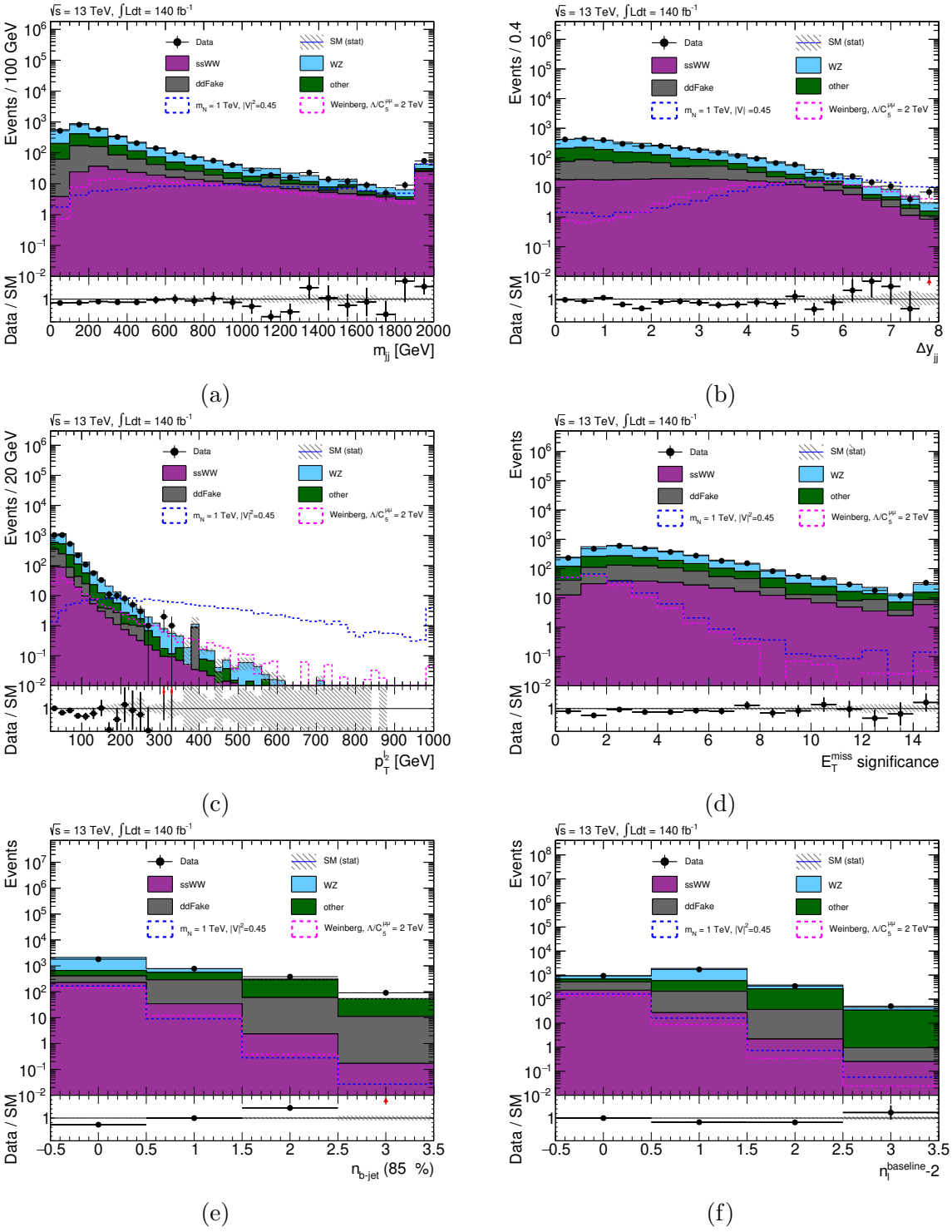

Figure 6.3.: Distribution after preselection of the six observables used for the design of the signal region: m_{jj} (a), ΔY_{jj} (b), $p_{\mathrm{T}}^{\mu_2}$ (c), $E_{\mathrm{T}}^{\mathrm{miss}}$ significance (d), $n_{b-\mathrm{jet}}$ (e) and number of extra baseline leptons n_l^{baseline}-2 (f). The last bin includes the overflow and the lower panel y-axis ranges spans from 0.5 to 1.5 (one tick $\hat{=}$ 0.1 unit). The $m_N = 1$ TeV signal sample was rescaled to the exclusion limits from [97] to check for potential signal contamination. The Weinberg Operator signal is scaled to some realistic cut-off scale matching the analysis sensitivity. For the non-prompt muon background, only the data-driven estimate (*ddFake*, grey) is shown (cf. Section 6.4.4).

Figure 6.4 shows a set on $N-1$ plots, i. e. distributions where all signal region cuts except for the cut on the shown observable are applied. These plots confirm the choice of cuts.

The prospects of a dedicated SR for the Weinberg operator were also investigated (Appendix C), but in the end, a binned fit in a common SR turned out to be the best approach.

6.4. Background Estimation

To probe BSM models, a reliable estimate of the SM processes entering the SR is needed. Since this search probes the kinematic tails of SM distributions, MC simulations may be inaccurate. This search has three main backgrounds: $W^{\pm}W^{\pm}$, $W^{\pm}Z$ and non-prompt muons. For two of these, $W^{\pm}W^{\pm}$ and $W^{\pm}Z$, dedicated control regions will be defined. In these, the normalisation of the respective background will be determined so that it matches with the observed data. The non-prompt muon background is measured with a data-driven method, which is expected to have a high systematic uncertainty. Other processes account for approx. 2 % of the SR so that using the MC simulations as they are is sufficient.

A summary of the control and signal region definitions can be found in Table 6.4 and an overview of the expected and observed amount of events in Table 6.5.

6.4.1. Control Region for $W^{\pm}W^{\pm}$

The SM production of $W^{\pm}W^{\pm} \to \mu^{\pm}\nu\mu^{\pm}\nu$ is the dominant background in the SR. It has two same-sign muons, like the signal, but outgoing neutrinos and thus real $E_{\mathrm{T}}^{\mathrm{miss}}$. A dilepton control region is expected to have a significant contribution originating from non-prompt muons. However, the non-prompt muon background is determined with a data-driven method and assumed to have an uncertainty of 100 % (i. e. $\sigma_{\mathrm{non-prompt}} = n_{\mathrm{non-prompt}}$). A too large non-prompt muon contribution would cause a large uncertainty of the background estimate in the $W^{\pm}W^{\pm}$ CR, which in turn would lead to a large uncertainty on the $W^{\pm}W^{\pm}$ prediction in the signal region. Vetoing events with b-jets reduces the non-prompt muon background significantly, but not enough to remove this concern. The uncertainty in the control region should be dominated by the statistical uncertainty of the background processes. Therefore, the CR needs to fulfil

$$\sqrt{\sigma^2_{\mathrm{b,\ stat}} + \sigma^2_{\mathrm{non-prompt}}} \leq 1.2 \cdot \sigma_{\mathrm{b,\ stat}}. \tag{6.1}$$

Also, signal contamination was a major concern in the design of this control region. In order to avoid any bias due to signal events in the control region, the amount of signal events in the CR should be small w. r. t. the expected statistical uncertainty of the background estimate. From a very preliminary guess, a CR would have $30 \ldots 50$ events, corresponding to a statistical uncertainty of $\sigma_{\mathrm{b,\ stat}} \approx 14 \ldots 18\,\%$. Thus, the signal contribution to the CR should not exceed $\approx 5\,\%$.

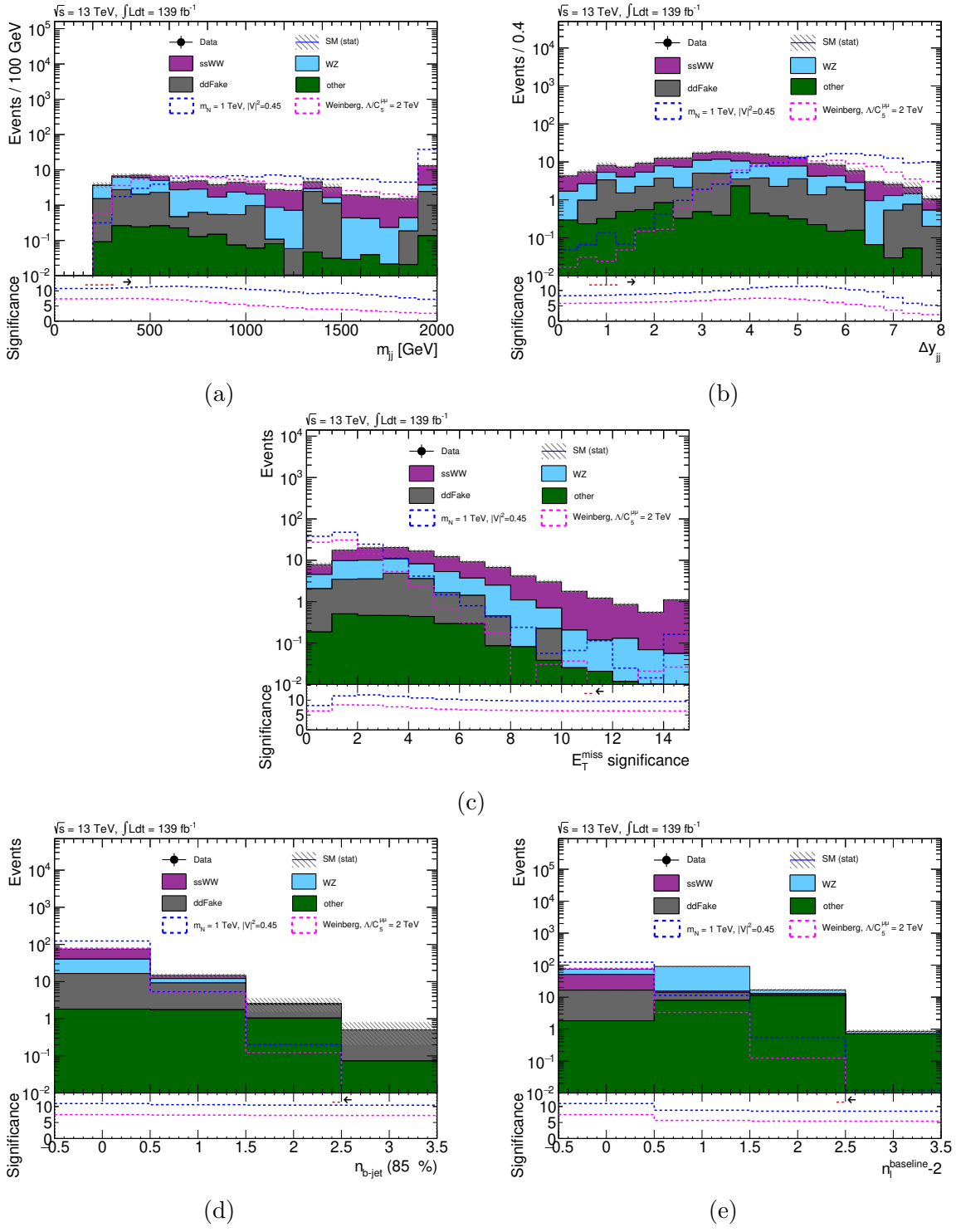

Figure 6.4.: N-1 distributions in the signal region of the five observables used for its design: m_{jj} (a), ΔY_{jj} (b), $E_{\mathrm{T}}^{\mathrm{miss}}$ significance (c), $n_{b-\mathrm{jet}}$ (d) and the number of additional baseline leptons, $n_l^{\mathrm{baseline}} - 2$ (e). The $m_N = 1\,TeV$ signal is scaled to the exclusion limits from [97] and the Weinberg operator signal to some realistic cut-off scale matching the analysis sensitivity. In the bottom panel, the significance achievable for each possible cut is shown, where the arrow indicates the direction in which the cut is tightened. For the non-prompt muon background, only the data-driven estimate (*ddFake*, grey) is shown (cf. Section 6.4.4).

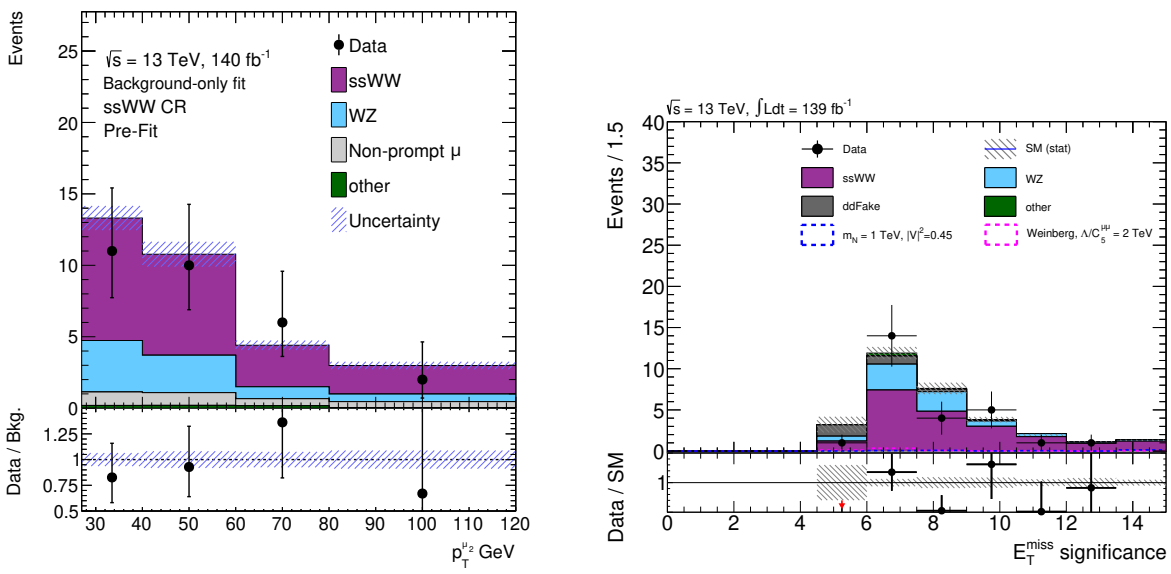

(a) (b)

Figure 6.5.: Data-MC agreement in the $W^{\pm}W^{\pm}$ control region for $p_{\mathrm{T}}^{\mu 2}$ (a) and $E_{\mathrm{T}}^{\mathrm{miss}}$ significance (b). In (b), the data-driven estimate of the non-prompt muon background is shown (*ddFake*, grey), whereas (a) uses the functional form fit (cf. Section 6.4.4).

Since the signal does not contain true $E_{\mathrm{T}}^{\mathrm{miss}}$, unlike all backgrounds, the $E_{\mathrm{T}}^{\mathrm{miss}}$ significance will be used to define the $W^{\pm}W^{\pm}$ CR[4]. After a scan of possible cut values, the $W^{\pm}W^{\pm}$ CR requires $E_{\mathrm{T}}^{\mathrm{miss}}$ significance > 5.8, while all other cuts are left as in the SR.

The decision to perform a binned fit was made quite late and large changes to the CR definition were not possible anymore. Since the signal is predominantly at high $p_{\mathrm{T}}^{\mu 2}$, an additional cut on $p_{\mathrm{T}}^{\mu 2} < 120\,\mathrm{GeV}$ is introduced and the bin boundaries are at $[27, 40, 60, 80, 120]\,\mathrm{GeV}$. It reduces the signal contamination to 1.3 % inclusively and 7.1 % in the last bin. This is negligible compared to the data statistical uncertainty of 18 % inclusively and 71 % in the last bin. 66 % of the events expected in this region are $W^{\pm}W^{\pm}$ and another 25 % come from $W^{\pm}Z$. Data and MC are found to agree well prefit (Figure 6.5). Also, a decent shape agreement between CR and SR is observed (Figure 6.6) for m_{jj} and ΔY_{jj}. The shift to somewhat higher m_{jj} in the CR is expected, because requiring a large $E_{\mathrm{T}}^{\mathrm{miss}}$ significance favours events with harder particles.

6.4.2. Validation Regions for $W^{\pm}W^{\pm}$

A dedicated region is required to check the validity of the background estimate. It is not included in the fit an can thus allow a larger signal contamination than the control regions. Kinematically, this *validation region* (VR) should be in between signal and control regions.

[4]Several other observables were also considered, but $E_{\mathrm{T}}^{\mathrm{miss}}$ significance performed best.

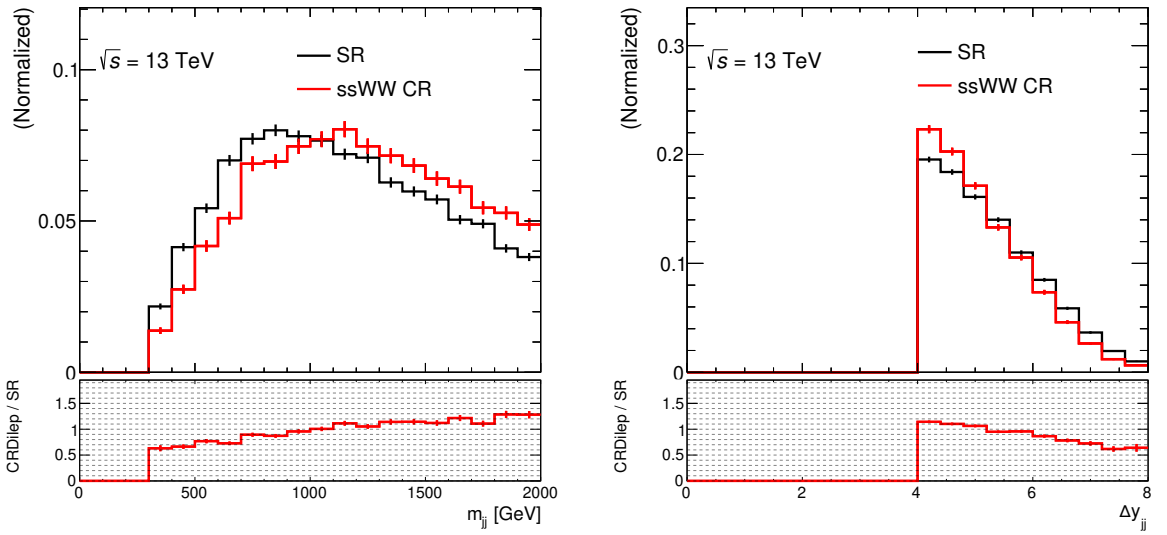

(a) (b)

Figure 6.6.: MC shape agreement between $W^{\pm}W^{\pm}$ CR (red) and SR (black) for $W^{\pm}W^{\pm}$ production. Only MC statistical uncertainties are shown.

The $W^{\pm}W^{\pm}$ validation region is defined to have a $E_{\mathrm{T}}^{\mathrm{miss}}$ significance in the range $[4.5, 5.8]$ but otherwise uses the same cuts as SR and $W^{\pm}W^{\pm}$ CR, thus it is right between them. It is binned in $p_{\mathrm{T}}^{\mu_2}$ the same way as the CR, i. e. with bin edges at $[27, 40, 60, 80, 120]$ GeV. Already before fitting, a decent agreement between data and MC is observed (Figure 6.7).

A separate VR is introduced to cover the $p_{\mathrm{T}}^{\mu_2} > 120\,\mathrm{GeV}$ range (Figure 6.8). Reducing the signal contamination here is very difficult, since the signal is also located predominantly at high $p_{\mathrm{T}}^{\mu_2}$. Starting from the $W^{\pm}W^{\pm}$ CR, the ΔY_{jj} and m_{jj} cuts are removed (leaving only the $m_{jj} > 150\,\mathrm{GeV}$ cut that is part of preselection). Requiring $p_{\mathrm{T}}^{\mu_2} > 120\,\mathrm{GeV}$ makes the high-p_{T} VR orthogonal to the $W^{\pm}W^{\pm}$ CR. Still, only six data events pass this selection, whereas 3.3 signal events are expected at the $m_N = 3\,\mathrm{TeV}$ mass point. Since this is larger than the data statistical uncertainty, the high-p_{T} VR could only detect a very large (more than 2σ) mismodelling of the background estimate.

6.4.3. Three-Lepton Control Region for $W^{\pm}Z$

The second largest background in the signal region is $W^{\pm}Z \to \mu^{\pm}\nu\mu^{\pm}\mu^{\mp}$. It has three leptons in the final state, however, if one of these three leptons is not detected (i. e. *lost*), this background may end up in the SR.

Fate of the Third Lepton

In general, there are three ways the third lepton could be lost. It might be produced outside of detector acceptance or with a low momentum below the reconstruction thresholds.

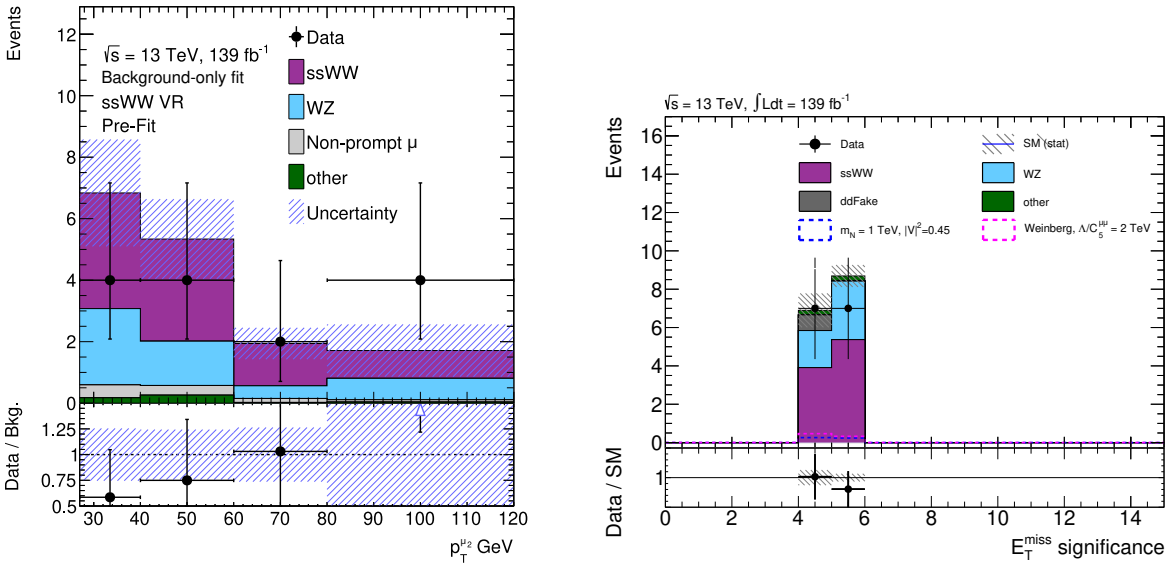

(a) (b)

Figure 6.7.: Data-MC agreement in the $W^{\pm}W^{\pm}$ validation region for $p_{\mathrm{T}}^{\mu_2}$ (a) and $E_{\mathrm{T}}^{\mathrm{miss}}$ significance (b). In (b), the data-driven estimate of the non-prompt muon background is shown (*ddFake*, grey), whereas (a) uses the functional form fit (cf. Section 6.4.4).

Or it could also be overlapping with a different object and then either be misidentified or removed by the Overlap Removal procedure (cf. Section 6.2.1). Knowing the fate of the third lepton will help with designing a control region and potentially also help to improve the background rejection in the SR.

This is investigated in a truth-level study with the alternative MC samples for WZ. The nominal samples were generated with Sherpa, which does not store the origin of a particle in the truth record. In order to validate this method, events with at least two reconstructed jets and at least three reconstructed leptons, among those an opposite-charge, same flavour pair, are selected. On a technical note, the MadGraph sample does also contain τ lepton final states, which may decay to electrons or muons. For the purpose of this study, an electron or muon originating from a prompt τ lepton is assumed to come from a $W^{\pm}$ or Z boson. Figure 6.9 shows that this method correctly identifies the leptons originating from $W^{\pm}$ and Z boson.

After validating the method, a SR-like region is formed by requiring exactly two reconstructed same-flavour, same charge leptons and at least two jets. A truth lepton is considered to be lost if there is no reconstructed lepton within $\Delta R \leq 0.1$. In the muon channel, it was found that approximately 60 % of the lost leptons are at high $|\eta|$ outside of the detector acceptance. The remaining lost muons are mostly within the central part of the detector, but at very low p_{T} and thus not reconstructed (Figure 6.10). A small fraction of lost leptons is at $|\eta| \approx 0$, where the coverage of the muon system is reduced.

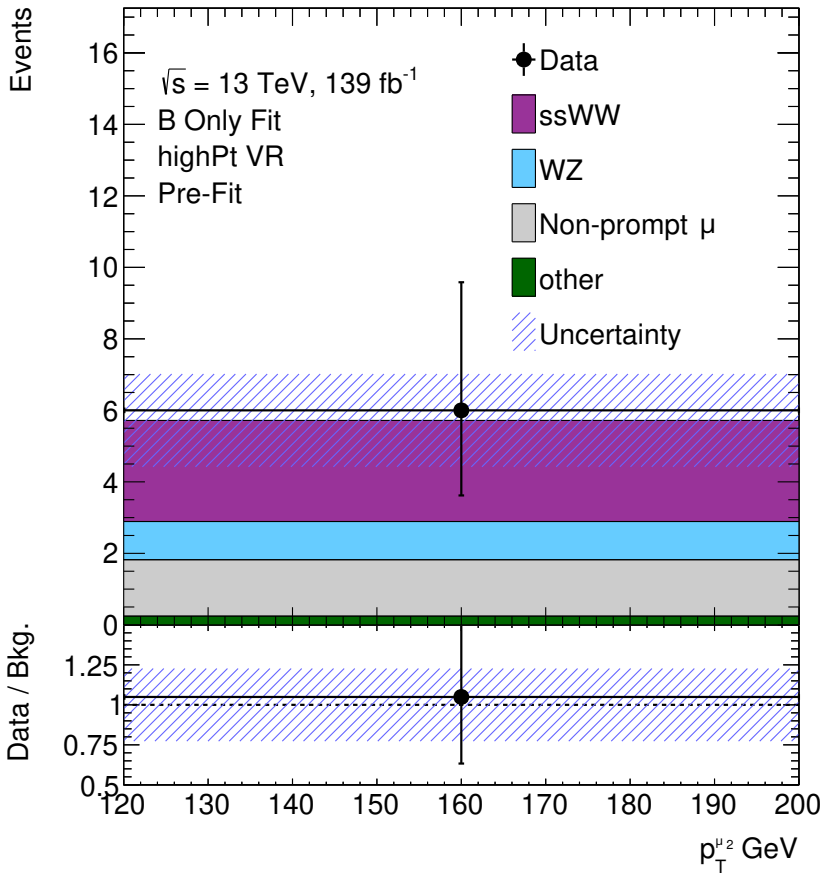

Figure 6.8.: Data-MC agreement in the high-p_{T} validation region.

It is also noted that the lost lepton always originates from the Z boson and has the opposite electric charge of the same-sign lepton pair.

Defining a Three-Lepton Control Region

The WZ background is constrained in a three-lepton CR. This CR requires exactly three leptons of signal quality. Events containing a fourth baseline lepton are vetoed to reduce the contribution of ZZ (Figure 6.11a, part of the *other* backgrounds). Among these three leptons, there needs to be a Z *boson candidate*, which is defined to be an opposite-sign same flavour lepton pair. This requirement completely removes $W^{\pm}W^{\pm}$ and the signal processes from the control region. Also, $t\bar{t}X$ backgrounds are reduced by approximately 60 %. A cut on $m_{lll} > 100\,\text{GeV}$ makes the $W^{\pm}Z$ CR orthogonal to a region used to study non-prompt muons from photons, but has only negligible effect on the composition of the CR (Figure 6.11b). The remaining cuts remain as in the signal region: $m_{jj} > 300\,\text{GeV}$, $\Delta Y_{jj} > 4$ and $E_{\text{T}}^{\text{miss}}$ significance < 4.5. In the fit, the binning in $p_{\text{T}}^{\mu_2}$ is chosen to be as similar to the SR binning as the statistics allows: $[27, 40, 60, 80, 100, \infty]\,\text{GeV}$.

This definition leads to a region with 59.4 expected SM events, thereof 88 % $W^{\pm}Z$. Neither $W^{\pm}W^{\pm}$ nor signal events pass this selection and the largest process in the *other backgrounds* category is ZZ with 2.5 out of 4.4 events. A good agreement between data and MC predictions is observed (Figure 6.12).

Comparing the shape of the $W^{\pm}Z$ process between the CR defined here and both the SR and the $W^{\pm}W^{\pm}$ control region shows good agreement in jet-based observables. The latter is important since the $W^{\pm}W^{\pm}$ CR comprises approx. 25 % $W^{\pm}Z$. This check of shape agreements (Figures 6.13 and 6.14) shows that there is only a small extrapolation on the jet-based part of the event selection. This also avoids extrapolations from non-VBS to VBS phase space, which can introduce large systematic uncertainties.

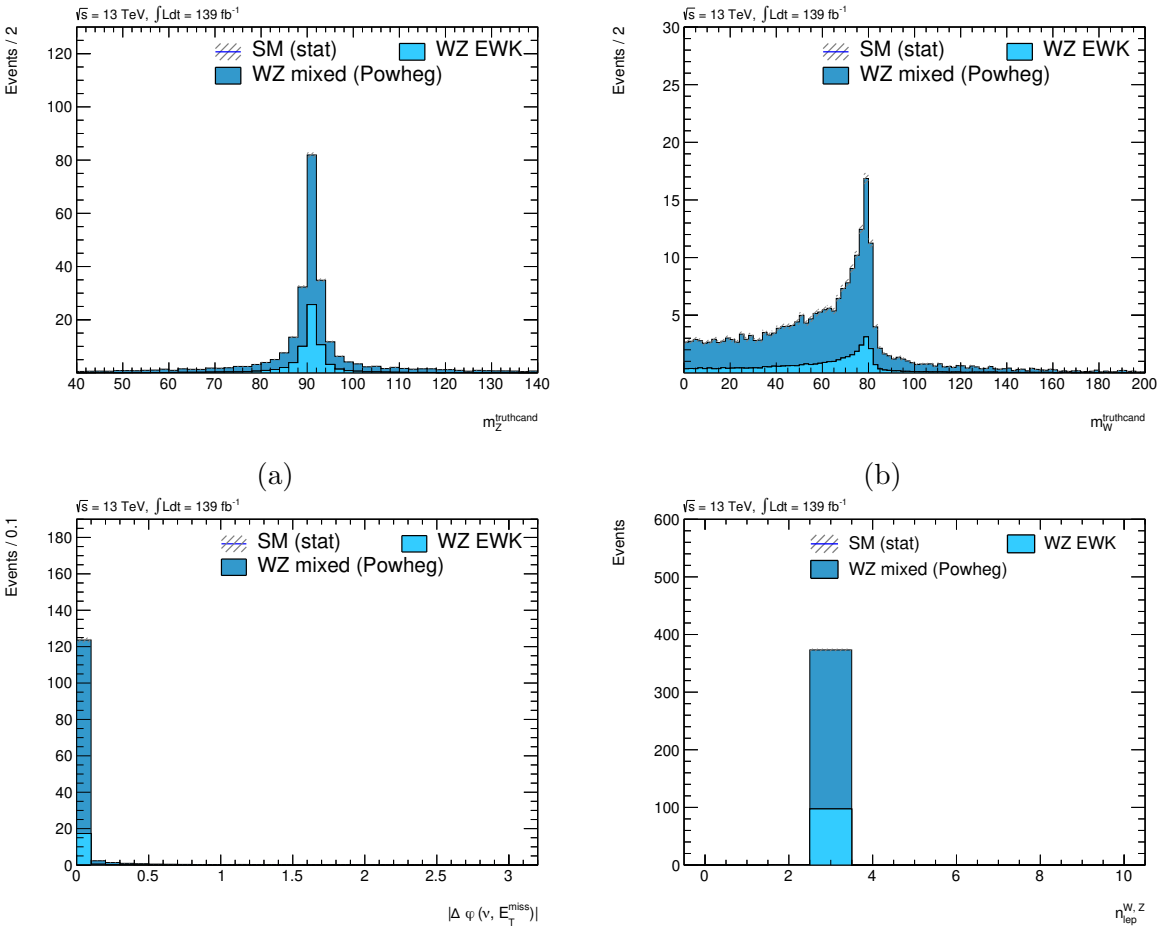

Figure 6.9.: Validation plots for the truth studies investigating the fate of the third lepton. After selecting three reconstructed leptons, the invariant mass of the truth lepton pair originating from the Z (a) boson and transverse mass of the lepton-neutrino pair originating from the $W^{\pm}$ (b) boson are shown. The sharp peaks at 90 GeV and 80 GeV respectively indicate correct identification of the Z and $W^{\pm}$ bosons. Also plotted is the distance in ϕ between the neutrino from the $W^{\pm}$ boson and $E_{\mathrm{T}}^{\mathrm{miss}}$ (c) as well as the number of leptons originating from a $W^{\pm}$ or Z boson (d).

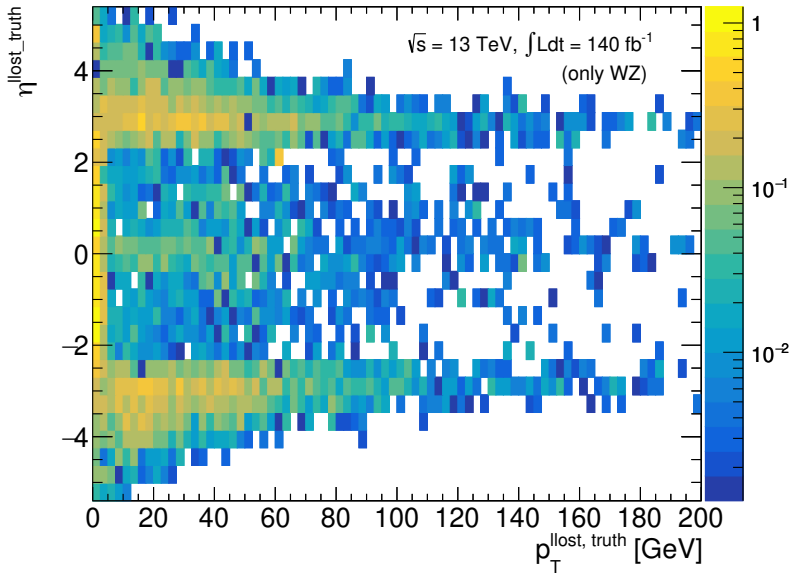

Figure 6.10.: Truth p_{T} and η of the lost muon. In addition to the preselection, exactly two *reconstructed* muons are required. Note that this plot only shows $W^{\pm}Z$.

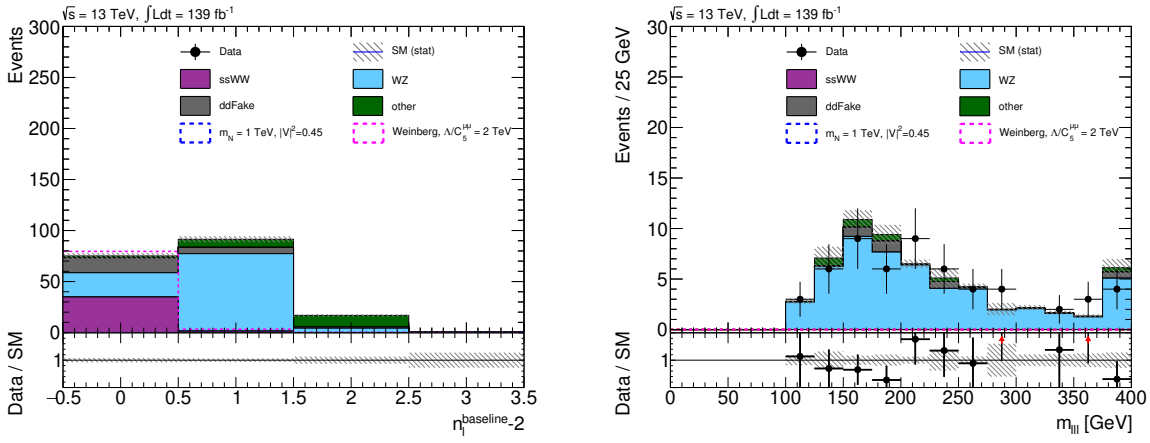

(a) (b)

Figure 6.11.: Number of baseline leptons in addition to the two signal leptons $n_l^{\mathrm{baseline}} - 2$ (a) and the three-lepton invariant mass m_{lll} in the $W^{\pm}Z$ CR without the cut on m_{lll} applied (b). In (a), the third lepton veto and Z candidate requirement are not applied. For the non-prompt muon background, only the data-driven estimate (*ddFake*, grey) is shown (cf. Section 6.4.4).

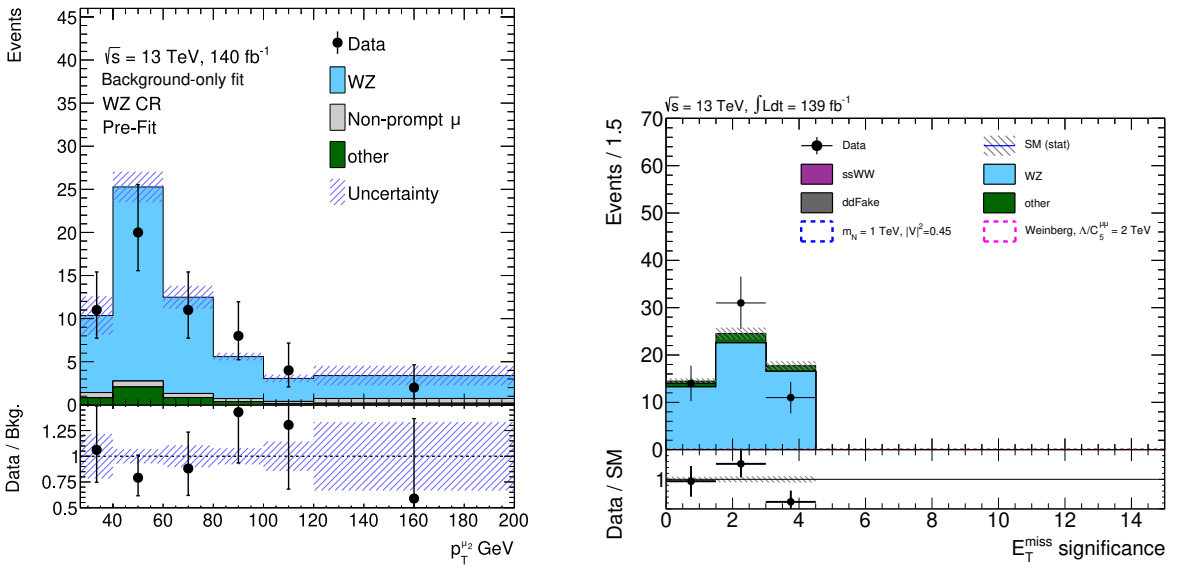

(a) (b)

Figure 6.12.: Data-MC agreement in the $W^{\pm}Z$ CR for the subleading muon transverse momentum $p_{\mathrm{T}}^{\mu_2}$ (a) and the $E_{\mathrm{T}}^{\mathrm{miss}}$ significance (b). In (b), the data-driven estimate of the non-prompt muon background is shown (*ddFake*, grey), whereas (a) uses the functional form fit (cf. Section 6.4.4).

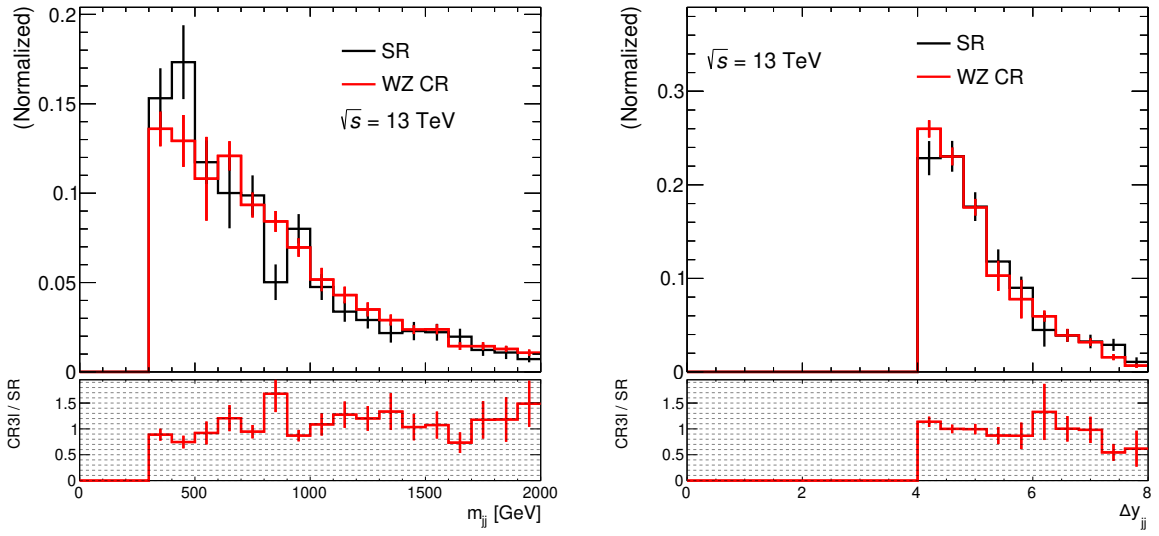

(a) (b)

Figure 6.13.: Shape agreement for the $W^{\pm}Z$ background between $W^{\pm}Z$ CR (red) and SR (black). Only MC statistical uncertainties are shown.

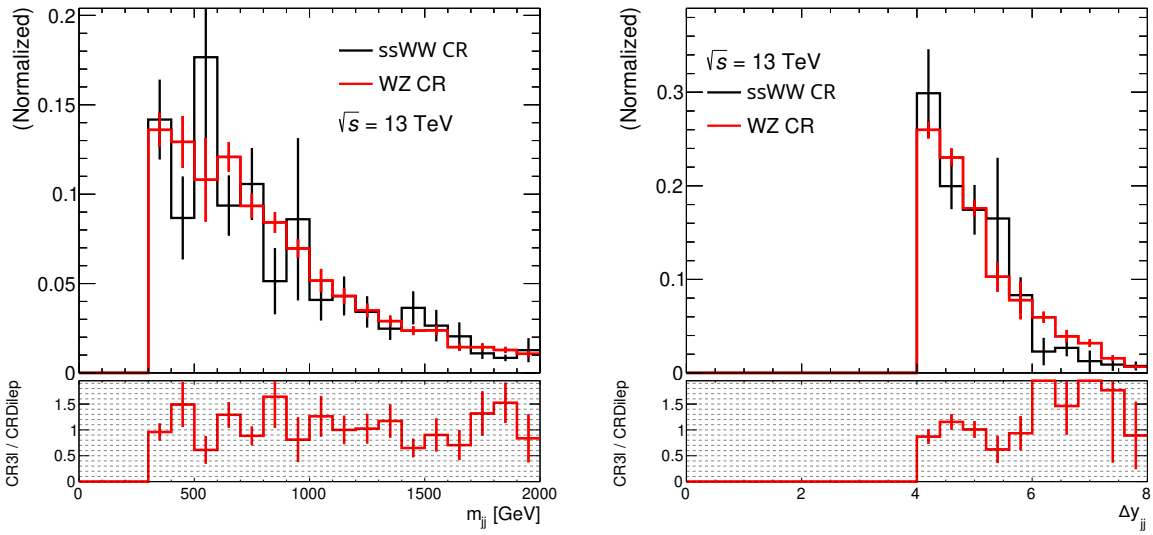

(a) (b)

Figure 6.14.: Shape agreement for the $W^{\pm}Z$ background between $W^{\pm}W^{\pm}$ CR (red) and $W^{\pm}Z$ CR (black). Only MC statistical uncertainties are shown.

6.4.4. Non-Prompt Muon Background

Muons that do not originate from a $W^{\pm}$ or Z boson decay are referred to as non-prompt muons[5]. There are several possible sources for non-prompt muons, which are investigated at truth level. While the vast majority of leptons is prompt (i. e. from a $W^{\pm}$ or Z boson decay), roughly 10 % of the events passing preselection or the SR selection are marked as non-prompt in the MC simulations. These non-prompt muons originate mostly from b or c jets. While also a small amount of non-prompt muons from prompt photons was present after preselection, this background was found to be irrelevant in a thorough study.

Rare detector effects have a strong influence on non-prompt muons. Since they are not well modelled in simulation, the non-prompt background is estimated with the data-driven *fake factor* method.

The Fake Factor Method

The fake factor method can be used to estimate the number of events with at least one non-prompt muon from hadron decays, often somewhat wrongly called *fake* muons. A reconstructed object can be either real (R) or fake (F). However, this distinction can be made only in MC by checking the truth record. But in data, a difference between good (G) and bad (B) leptons can be made. The former fulfil the signal lepton criteria, while the latter fulfil the somewhat looser spurious lepton criteria (Section 6.2).

In the signal region, both leptons are required to be good (GG). The fake factor method is used to estimate how many GG events contain a fake, i. e. are RF, FR or FF. This is done via control regions that are identical to the signal region, except for containing at least one bad lepton (i. e. GB, BG or BB). They are made pure in fakes in the bad lepton by subtracting the prompt MC contribution from data. Then, those regions are multiplied with the *fake factor*: a transfer factor that, figuratively speaking, turns a bad into a good lepton.

The fake factor is determined in a dedicated set of control regions. They do not need to have any similarity with the SR, as long as the origin of the non-prompt muons is reasonably similar. Same as before, this region is made pure in fakes by subtracting the prompt MC contribution form data.

The non-prompt muon estimate obtained with this method is labelled *ddFake* in plots and tables.

Functional Form Fit

After applying the full selection of the signal or control regions, the data-driven non-prompt muon background has low statistics. This manifests as having only few ddFake events with a rather large weight, spaced too coarse to accurately place cuts or do statistical evaluation. But since this is a data-driven method, it is not possible to improve the available statistics.

[5]While Higgs boson decays also create prompt leptons, they are negligible in this analysis.

Instead, the distributions will be approximated with a functional form. Three possible distributions are considered: a power law, a Gaussian distribution and an exponential function. These functions are fit to the $p_{\mathrm{T}}^{\mu_2}$ distributions in the range $[0, 200]$ GeV in each region. Bins with negative bin content are set to zero. The range of the fit is reduced to the upper edge of the last bin with a positive event count.

The three functional forms are fitted with a weighted log likelihood method. It uses the integral of the function over the bin instead of the default function value at the bin centre. Input histograms are corrected for the bin widths so that the fit results in a density function.

The exponential function was found to perform well in SR, $W^{\pm}W^{\pm}$ VR, and the $W^{\pm}W^{\pm}$ and $W^{\pm}Z$ control regions (Figure 6.15). In order to evaluate the impact that the choice of functional form has, the power law will be used as an alternative function. Yields are extrapolated up to 1 TeV.

The non-prompt muon estimated with this method is labelled *ffFake* in figures and tables.

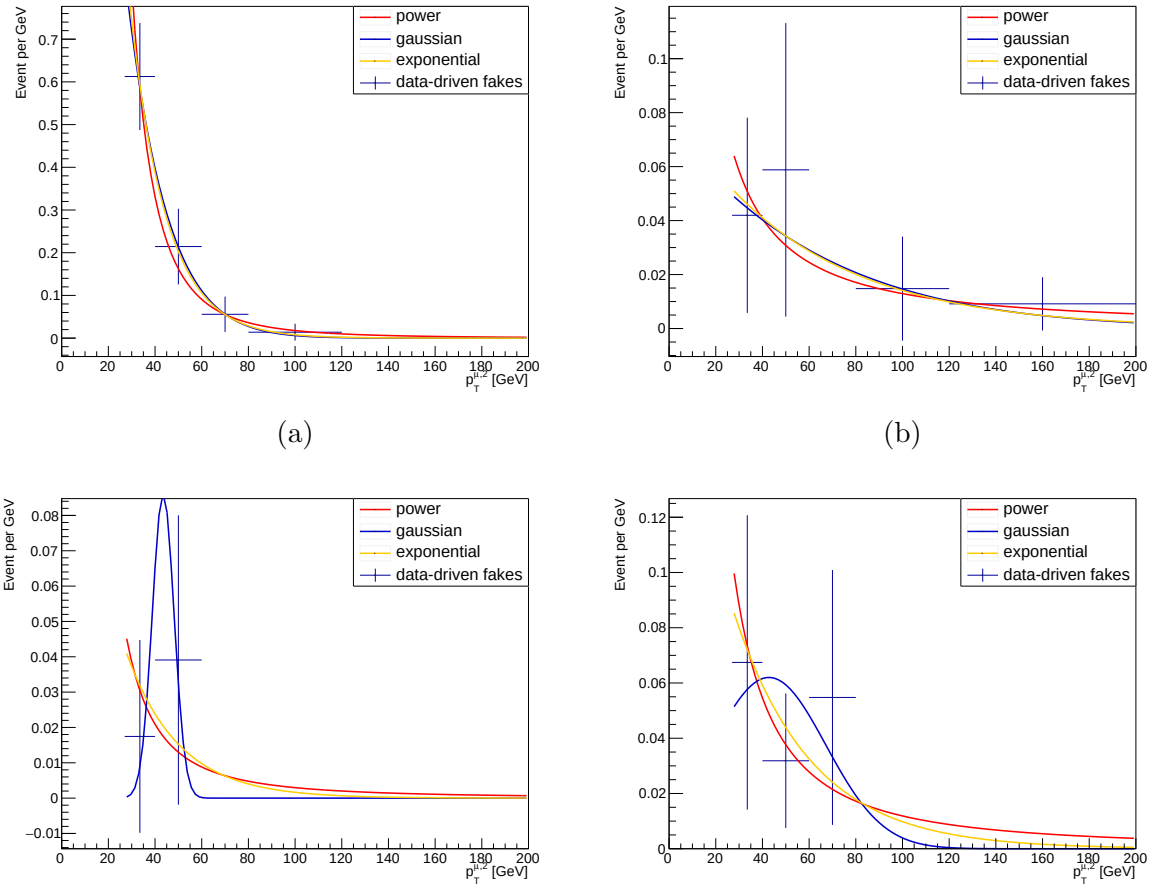

Figure 6.15.: Functional form fits of the non-prompt muon background in the signal region (a), $W^{\pm}Z$ (b) and $W^{\pm}W^{\pm}$ (d) control regions as well as the $W^{\pm}W^{\pm}$ validation region (c). Several fit functions are shown. Nominal fit estimates input to the final fit described in Chapter 7 as non-prompt component are taken from the exponential functions for the signal and the control regions, respectively. The power function will be used to derive systematic uncertainties related to the choice of fit function, whereas the Gaussian functions are not used further due to the poorer goodness of fit. Note that the bin contents are normalised to the bin width, thus the result of the fit is a density function.

Table 6.4.: Event selection criteria for signal, control and validation regions in addition to the preselection criteria described in section 6.3.1. All regions are further binned in $p_{\mathrm{T}}^{\mu_2}$. The VR is not included in the final fit.

Observable	SR	$W^{\pm}W^{\pm}$ VR	$W^{\pm}W^{\pm}$ CR (high p_{T} VR)	$W^{\pm}Z$ CR
b-jet veto	✓	✓	✓	✓
m_{jj}	$> 300\,\mathrm{GeV}$	$> 300\,\mathrm{GeV}$	$> 300\,\mathrm{GeV}$ (—)	$> 300\,\mathrm{GeV}$
ΔY_{jj}	> 4	> 4	> 4 (—)	> 4
third lepton	$= 0$ (baseline)	$= 0$ (baseline)	$= 0$ (baseline)	$= 1$ (signal)
Z cand. (OSSF only)	—	—	—	✓
$E_{\mathrm{T}}^{\mathrm{miss}}$ sign.	< 4.5	$\in [4.5, 5.8]$	> 5.8	< 4.5
m_{lll}	—	—	—	$> 100\,\mathrm{GeV}$
$p_{\mathrm{T}}^{\mu_2}$	—	< 120	< 120 (> 120) GeV	—

Table 6.5.: Expected background and signal yields in the signal, control and validation regions prefit. The *Total SM* figure is using the non-prompt muon estimate based on a functional form fit, the data-driven non-prompt muon estimate (*ddFake*) is given just as a comparison. All uncertainties in this table are statistical only, which is why there is no uncertainty given for the functional form non-prompt muon estimate. However, it has a large systematic uncertainty, which will be considered for the statistical evaluation (Chapter 7). All regions are further binned in $p_{\mathrm{T}}^{\mu_2}$. The VRs are not included in the final fit. The $m_N = 500\,\mathrm{GeV}$ and $m_N = 1\,\mathrm{TeV}$ mass points are rescaled to the exclusion limits from [97] ($|V_{\mu N}|^2 = 0.08$ and 0.45, respectively), while all other signals have a mixing parameter $|V_{\mu N}|^2 = 1$ as no limits are available from literature (except from the CMS analysis [135] looking at the same channel).

	SR	$W^{\pm}W^{\pm}$ VR	$W^{\pm}W^{\pm}$ CR (high p_{T} VR)	$W^{\pm}Z$ CR
$W^{\pm}W^{\pm}$	34.9 ± 0.2	9.3 ± 0.1	20.4 ± 0.2 (2.8 ± 0.1)	< 0.1
$W^{\pm}Z$	23.8 ± 1.0	5.0 ± 0.5	7.5 ± 0.7 (1.1 ± 0.1)	52.3 ± 1.7
ddFake	14.7 ± 2.8	0.8 ± 0.9	2.4 ± 1.3 (0.7 ± 1.2)	2.6 ± 1.6
non-prompt μ	13.9	0.9	2.8 (1.5)	2.9
other	1.8 ± 0.1	0.5 ± 0.1	0.6 ± 0.1 (0.2 ± 0.1)	4.4 ± 0.2
Total SM	74.4 ± 1.0	15.7 ± 0.5	31.3 ± 0.8 (5.6 ± 0.2)	59.6 ± 1.7
Data **(unblinded)**	**89**	14	29 (6)	56
$m_N = 1\,\mathrm{TeV}, \lvert V_{\mu N}\rvert^2 = 0.45$	123.8 ± 1.6	0.4 ± 0.1	0.3 ± 0.1 (1.6 ± 0.2)	< 0.1
$m_N = 3\,\mathrm{TeV}, \lvert V_{\mu N}\rvert^2 = 1.00$	171.7 ± 2.4	0.2 ± 0.1	0.5 ± 0.1 (3.3 ± 0.3)	< 0.1
$m_N = 5\,\mathrm{TeV}, \lvert V_{\mu N}\rvert^2 = 1.00$	76.1 ± 1.0	< 0.1	0.2 ± 0.1 (1.4 ± 0.1)	< 0.1
$m_N = 10\,\mathrm{TeV}, \lvert V_{\mu N}\rvert^2 = 1.00$	20.7 ± 0.3	< 0.1	< 0.1 (0.4 ± 0.0)	< 0.1
Weinberg, $\frac{C_5^{\mu\mu}}{\Lambda} = 2\,\mathrm{TeV}$	79.6 ± 1.2	0.8 ± 0.1	0.6 ± 0.1 (0.2 ± 0.1)	< 0.1

7. Results

7.1. Statistical Methods

The statistical evaluation tests the compatibility of the measured data with different hypotheses and, by extension, also tests whether one hypothesis is favoured over the other. In general, two types of hypotheses are used in particle physics analysis:

- The *background-only* (b-only) hypothesis H_b is that the observed data is solely from SM processes.
- The *signal-plus-background* ($s+b$) hypothesis H_{s+b} claims that there is also a BSM process in addition to the SM. In practice, several different $s + b$ hypotheses will be used to test different sets of parameters of the same BSM process.

The agreement of a hypothesis with the observed data is quantified using a *test statistic*. This compresses the complex question of agreement down to a single number. From the test statistics, one calculates a p-value. The p-value is the chance of finding a dataset at least as incompatible with the hypothesis H as the observed one, assuming that H was true. Results in a particle physics analysis are usually given in terms of the significance Z. It is calculated through the relation

$$Z = \Phi^{-1}(1 - p) \tag{7.1}$$

where Φ^{-1} is the inverse function of the cumulative distribution function of a standard Gaussian distribution. The common 95 % CL criterion for excluding a signal hypothesis corresponds to $Z = 1.64$ in the case of a one-sided significance (i. e. if the signal can only increase the observed number of events). To claim a discovery, the b-only hypothesis needs to be rejected at $Z = 5$, which corresponds to $p = 2.87 \cdot 10^{-7}$.

7.1.1. Profile Likelihood Fit

The result of a particle physics analysis is a dataset $\mathcal{D} = \{n_1, n_2, ...\}$ of individual measurements. These measurements are the individual bins of the histograms, and the expected number of events in a bin i is parametrised as

$$n_i^{\text{exp}} = \mu s_i(\theta) + b_i(\theta). \tag{7.2}$$

Here, s_i and b_i are the expected number of signal and background events, respectively. Both depend on a variety of nuisance parameters θ and the signal is scaled by the signal

strength parameter μ. It is constrained to $\mu \geq 0$ for the models considered in this analysis. The amount of events in each bin follows a Poisson distribution around the expected event number. For a given dataset $\mathcal{D}$, this can be encoded in the likelihood function

$$L(\mathcal{D}|\mu,\theta) = \prod_{i\in\text{bins}} \frac{(\mu s_i + b_i)_i^n}{n_i!} e^{-\mu s_i + b_i} \prod_{\theta_i \in \theta} f(0|\theta_i). \tag{7.3}$$

The second product is over the PDF f of the individual nuisance parameters. It is centred at zero by convention and they typically follow a Gaussian distribution.

From this, one can form the profile likelihood ratio

$$\lambda(\mu) = \frac{\mathrm{L}(\mu, \hat{\hat{\theta}}(\mu))}{L(\hat{\mu}, \hat{\theta})}. \tag{7.4}$$

In the denominator, $\hat{\mu}$ and $\hat{\theta}$ are the values of signal strength and nuisance parameters that maximise the likelihood. In the numerator, $\hat{\hat{\theta}}(\mu)$ are the values for the nuisance parameters that maximise the likelihood *for a given* μ, i. e. the conditional maximum likelihood estimator. This way, the compatibility of the dataset with different values of μ can be tested. The profile likelihood ratio is bound to the range $\lambda(\mu) \in [0, 1]$, where values close to 1 indicate a good agreement between data and the specified μ.

From Equation (7.4), one can define the test statistics

$$q(\mu) = \begin{cases} -2\ln \frac{L(\mu,\hat{\hat{\theta}}(\mu))}{L(\mu=0,\theta(\mu=0))} & \text{if } \hat{\mu} < 0 \\ -2\ln \lambda(\mu) & \text{if } 0 \leq \hat{\mu} \leq \mu \\ 0 & \text{if } \hat{\mu} > \mu. \end{cases} \tag{7.5}$$

This test statistics takes into account that the signal strength parameter μ cannot be negative. For sufficiently large datasets, an asymptotic distribution of this test statistics can be derived [136]. This makes it possible to calculate a p-value from the test statistics, which can then be used to determine confidence intervals.

7.1.2. Determining Sensitivity with the CL_s Method

Simply calculating the p value for the signal+background ($s + b$) hypothesis has a flaw in practice. Due to fluctuations in the data, one may observe less events than predicted from the background-only hypothesis. Testing the $s+b$ hypothesis against this data can lead to the exclusion of very small signals (or even rule out the signal completely), even though there is actually not enough sensitivity for this claim. To avoid this, the $s + b$ and b-only hypotheses need to be compared. For this, the CL_s method is widely used. It requires to use a test statistics for which larger values are expected for the b-only hypothesis than for the $s + b$ hypothesis. Given an observed value of the test statistics q_{obs}, the p-values for the two hypotheses are given as

$$p_{s+b} = P(q(\mathcal{D}|H_{s+b}) \geq q_{\text{obs}}) \tag{7.6}$$

$$p_b = P(q(\mathcal{D}|H_b) \leq q_{\text{obs}}). \tag{7.7}$$

In other words, these are the probabilities to obtain a result less compatible with either the $s + b$ or b-only hypothesis than the observed result.

With these two, the quantity CL_s [137, 138] is defined as[1]

$$\mathrm{CL}_s = \frac{p_{s+b}}{1 - p_b}. \tag{7.8}$$

Upper limits are set by requiring $\mathrm{CL}_s \leq \alpha$. Since $1 - p_b < 1$, this method is more conservative than simply requiring $p_{s+b} \leq \alpha$.

7.1.3. Smoothing

Some systematic uncertainties with only a small impact may suffer from large fluctuations that make the fit unstable. These fluctuations are unphysical and arise from low MC statistics. Their effect can be alleviated by smoothing.

A variety of smoothing algorithms is available which have different advantages. This analysis uses an algorithm called `TCHANNEL`, used first in [140].

It starts from the nominal histogram n and the systematic variation histogram ν, which will be rebinned to $\tilde{n}$ and $\tilde{\nu}$. The binwise ratios $t_i = \nu_i / n_i$ and $\tilde{t}_i = \tilde{\nu}_{j(i)} / \tilde{n}_{j(i)}$ are formed for original and rebinned histogram. $j(i)$ maps the i-th bin of the original histogram to the bin in the rebinned histogram.

Rebinning histograms should remove fluctuations while retaining the shape. Two adjacent bins are merged only if $\tilde{t}_i$ in one of them is higher or lower than in both its adjacent bins. This avoids merging when the distribution is monotonously rising or falling. Also, a merge is forbidden when this results in three consecutive $\tilde{t}_i$ that are all larger or smaller than t_i. If multiple rebinning options are valid, the one with the smallest difference $D = \sup_{j=1,\ldots,n^{\mathrm{bins}}_{\mathrm{rebinned}}} |\sum_{k=1}^{j} \tilde{t}_k - t_k|$ is chosen. This procedure is repeated until no more adjacent bin pairs are eligible for rebinning. Afterwards, the histogram is rebinned three times using the smoothing algorithm described in [141, Section 4.2] with the modification that the first and last bin remain unchanged during the first application of the running medians.

7.2. Systematic Uncertainties

The analysis is affected by various systematic uncertainties. Major sources of systematic uncertainties are the resolution of the kinematic variables and the event selection efficiency, both of which are influenced by the detector response and reconstruction algorithms. Another source of uncertainties is the modelling of the signal and background processes with MC. They can affect either only event yield or also the shape of an observable, such as $p_{\mathrm{T}}^{\mu_2}$. In the fit, they will be modelled as nuisance parameters.

Since the $W^{\pm}W^{\pm}$ and $W^{\pm}Z$ backgrounds are normalised to data, systematic variations cannot change the total yield of these process. To accurately reflect this, the histograms containing the systematic variations for these two processes are normalised

[1] This work uses the notation from [139, Chapter 40].

to the nominal across the signal and control regions. This means that shape effects, such as migration across bins, is properly accounted for.

7.2.1. Experimental Systematic Uncertainties

Muons are used in all control and signal region selection and the transverse momentum $p_{\mathrm{T}}^{\mu_2}$ of the subleading muon is the key variable used for statistical evaluation. Uncertainties arise from the efficiencies of muon reconstruction, identification and isolation, as well as from the trigger. Another set of systematic uncertainties affects the energy and momentum resolution, thus also affecting the spectrum of $p_{\mathrm{T}}^{\mu_2}$.

Due to the much more complex reconstruction and calibration procedure, a total of 37 uncertainties on jets is considered. Uncertainties on the Jet Energy Scale (JES) are arising from various detector effects such as pile-up, punch-trough and differences in calorimeter response between quark and gluon initiated jets. Also, uncertainties on the Jet Energy Resolution (JER) and related to the flavour tagging efficiencies are considered.

The estimate of the hadronic fakes has systematic uncertainties related to the derivation of the fake factors. These include the statistical uncertainty in the derivation region as well as its composition and the modelling of the prompt MC. Since the hadronic fake estimate is replaced with a functional form in the statistical evaluation, the functional form is fitted to each systematic variation. Another uncertainty arises from the choice of fit function. This is modelled by using a power law as an alternative to the exponential function used as nominal.

Since electrons are used only used for vetoes, only the energy scale and resolution are considered. Three nuisance parameters are covering the resolution and scale uncertainties of the soft $E_{\mathrm{T}}^{\mathrm{miss}}$ term. Finally, the total normalisation is affected by the luminosity uncertainty of 0.83 % [142].

7.2.2. Theory Uncertainties

Theory systematics are considered for the signal processes and the two main backgrounds, $W^{\pm}W^{\pm}$ and $W^{\pm}Z$.

The choice of the factorisation and renormalisation scales μ_f and μ_r introduces an uncertainty by cutting off higher order corrections. It is computed using using a pairwise seven-point variation, i. e. μ_r and μ_f are either halved or doubled while excluding the off-diagonal elements $(0.5\mu_r, 2\mu_f)$ and $(2\mu_r, 0.5\mu_f)$. These seven variations are then combined into an envelope.

Uncertainties arising from the choice of PDF can be modelled in two ways, which are combined in this analysis. The nominal PDF set, `NNPDF3.0`, contains variations of various internal parameters that were derived from data. The arithmetic mean of these individual variances is used as uncertainty on `NNPDF3.0`. In addition, the nominal PDF is also compared to the `CT14` and `MMHT2014` PDF sets. The total PDF uncertainty is then taken as the envelope of the `NNPDF3.0` variations and the alternative PDFs.

The running strong coupling constant has a nominal value of $\alpha_s = 0.118$ at the Z pole. Two alternative choices of α_s are considered, which give values of 0.117 and 0.119 at the Z mass. The α_s uncertainty is then computed as the mean of the up- and down variations.

Finally, the choice of MC generator is evaluated by analysing alternative samples made with a different generator. For the $W^{\pm}W^{\pm}$ process, the nominal samples were generated with aMC_MadGraph5@NLO and parton-showered with Pythia 8. The effect of the parton shower modelling is evaluated with events generated with aMC_MadGraph5@NLO that were showered with Herwig 7. A second alternative sample was generated and parton-showered with Sherpa. The nominal $W^{\pm}Z$ sample was generated with Sherpa and is compared to an alternative sample generated with Powheg and Pythia 8.

Other background processes than $W^{\pm}W^{\pm}$ and $W^{\pm}Z$ have a rather small event yield. Therefore, a simple 50 % normalisation uncertainty is applied.

The Type I Seesaw signal samples consider PDF, scale and α_s uncertainties obtained with the same prescription as for the $W^{\pm}W^{\pm}$ and $W^{\pm}Z$ backgrounds. For the Weinberg operator signal sample, the weights used to derive these uncertainties were not included when generating the signal samples. Due to computational constraints, they were evaluated at truth level, leading to uncertainties comparable with the Type I Seesaw signal. Since the α_s uncertainty was found to be smaller than 1 %, it is neglected in the following.

7.3. Background-only Fit

A background-only fit is performed in order to check the fit setup and test the background-only hypothesis against data. The fake lepton background is modelled using the functional form described in Section 6.4.4.

For the two main backgrounds, the normalisation is obtained from data as part of the fit, while the shape is taken from MC simulations. The normalisation factors are found to be $\mu_{W^{\pm}Z} = 1.17 \pm 0.23$ and $\mu_{W^{\pm}W^{\pm}} = 0.92 \pm 0.16$. Both are compatible with unity.

This analysis considers in total 88 different systematic uncertainties. In order to reduce the fitting time, systematics with a tiny effect are pruned. The pruning removes systematic uncertainties if the deviation from the nominal prediction is smaller than 0.5 %. This check is performed separately for the effect on shape (i. e. no bin deviates by more than 0.5 %) and normalisation of a systematic and if necessary, only one of them is pruned. Five of the systematic uncertainties that were not removed by the pruning step caused instabilities in the fit. These could be traced down to large statistical fluctuations in the up- and down variations. Smoothing them with the `TCHANNEL` algorithm (Section 7.1.3) removes the fluctuations such that the difference between the up- and down variation is clear. This algorithm was chosen because it works well for all five systematics that were underconstrained. Appendix D.1 shows the effect of the smoothing.

Sizeable correlations are found only between few parameters of the fit (Figure 7.1). The background normalisation factors $\mu_{W^{\pm}W^{\pm}}$ and $\mu_{W^{\pm}Z}$ are anti-correlated. Both back-

grounds contribute significantly to the SR and $W^{\pm}W^{\pm}$ control region. For similar reasons, $\mu_{W^{\pm}W^{\pm}}$ and the WZ generator uncertainty are correlated. A third correlation between $\mu_{W^{\pm}W^{\pm}}$ and one of the fake factor systematics is observed. This can be explained by a sizeable fake lepton contribution in SR and $W^{\pm}W^{\pm}$ CR, whereas there are significantly less fake leptons in the $W^{\pm}Z$ CR. Finally, $\mu_{W^{\pm}Z}$ is correlated with the other background systematic uncertainty. Since the other backgrounds constitute approximately 7 % of the $W^{\pm}Z$ CR, but only ca. 2 % of the other regions, this is also not surprising.

Good agreement between the background only-hypothesis and the observed data is found, indicated by $p_b = 9.3\,\%$. The background normalisation factors are $\mu_{W^{\pm}W^{\pm}} = 1.17 \pm 0.23$ and $\mu_{W^{\pm}Z} = 0.92 \pm 0.16$. Both are compatible with unity. In the SR (Figure 7.2), the background prediction falls monotonously as a function of $p_{\mathrm{T}}^{\mu_2}$, whereas the Type I Seesaw signal is predominantly in the last bin. The $p_{\mathrm{T}}^{\mu_2}$ distribution of the Weinberg operator has its maximum between 40 and 60 GeV. However, due to the long tail of the distribution (cf. Figure 6.3c), the $p_{\mathrm{T}}^{\mu_2} > 120\,\mathrm{GeV}$ bin is also the most sensitive bin for the Weinberg operator. A small, non-significant data excess is observed in the last two bins of the SR.

The control regions show very good agreement between data and background prediction (Figure 7.3). In the $W^{\pm}Z$ CR, the $p_{\mathrm{T}}^{\mu_2}$ distribution has a distinct maximum roughly at $M_Z/2$, whereas all backgrounds in the $W^{\pm}W^{\pm}$ control and validation regions are monotonously falling. Finally, in the high-p_{T} control region, a perfect agreement of data and background expectation is observed.

7.4. Sensitivity and Exclusion Limits

Since no significant deviation from the background-only hypothesis was found, exclusion limits are set on the model parameters. This is done using the CL_s method in the asymptotic limit. The validity of this approximation has been confirmed with pseudo experiments.

Expected and observed limits on the Type I Seesaw model are shown in Figure 7.4. Sensitivity is expected to be largest at $m_N \approx 500\,\mathrm{GeV}$ and extends to $m_N = 20\,\mathrm{TeV}$. Both the shape of the limits and the most sensitive heavy neutrino mass correspond to what can be expected purely from the cross section (Figure 5.3). Throughout the whole mass range, the observed limits are approximately one standard deviation worse than the expected limits. This difference is caused by an excess in the last bin of the SR (Figure 7.2). Such a uniform behaviour is expected, because this analysis is not sensitive to m_N. Different m_N leads to differences in the $p_{\mathrm{T}}^{\mu_2}$ spectrum, but these differences are small and would only show at high $p_{\mathrm{T}}^{\mu_2}$ (Figure 6.3c), where this analysis cannot detect differences in shape. The largest systematic uncertainty with an effect of ca. 8 % arises from the choice of functional form used for the non-prompt muon background (cf. Appendix D.3).

Determining the exclusion limits without systematic uncertainties gives nearly the same results, indicating that this analysis is indeed limited by the statistical uncer-

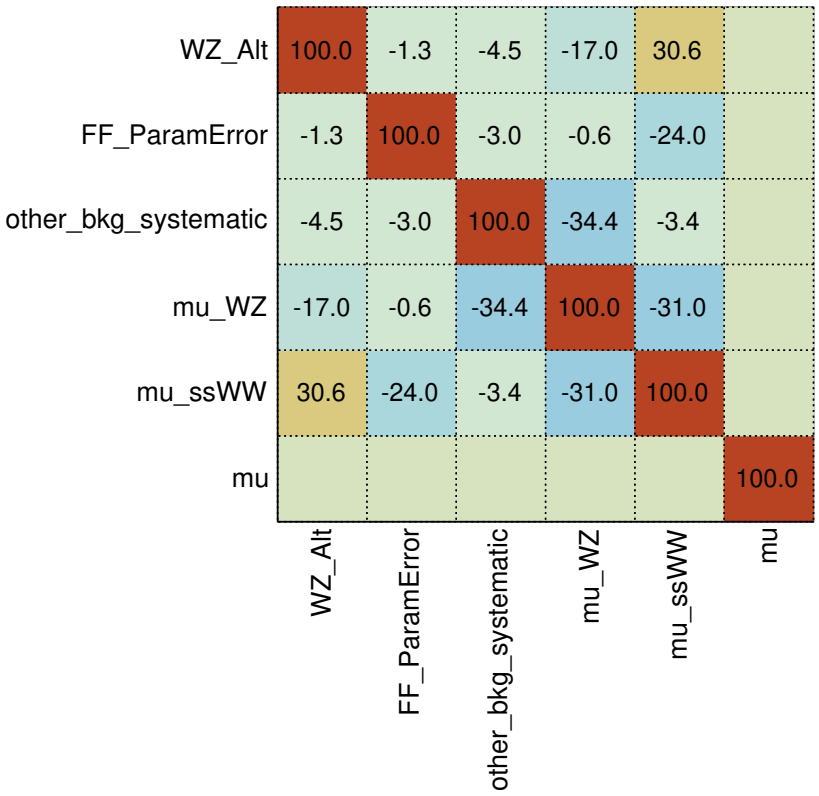

Figure 7.1.: Correlation matrix in the background only fit. Only correlations larger than 20 % are shown.

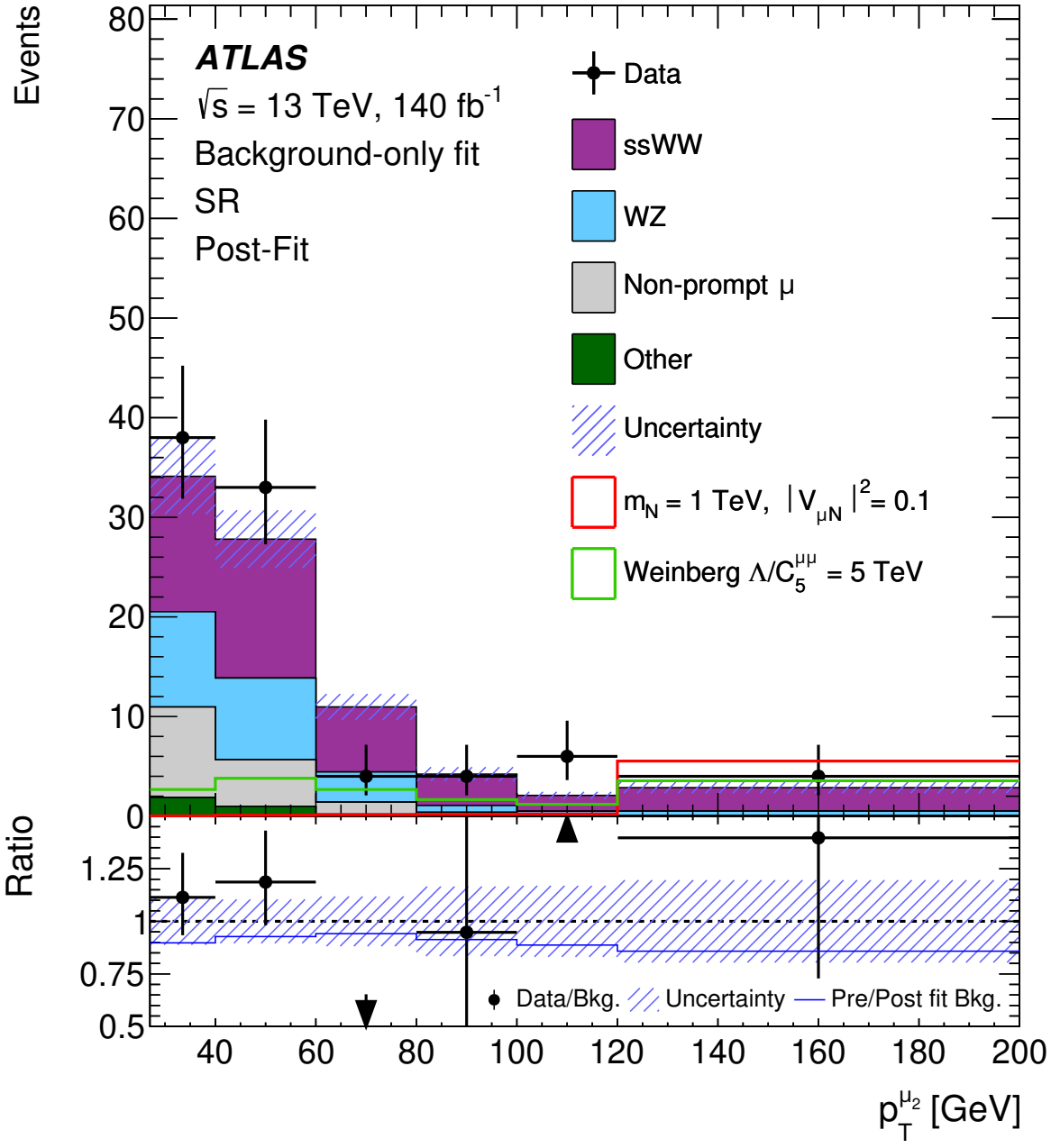

Figure 7.2.: Post-fit $p_{\mathrm{T}}^{\mu_2}$ distribution in the SR. The fit was performed under the background-only hypothesis, but two benchmark signals were overlaid using their theoretical cross section. The shaded band surrounding the background estimate indicates the total post-fit uncertainty. In the bottom panel, the ratio of data to the post-fit SM prediction is shown, whereas the blue line indicates the ratio between pre- and postfit background. Events in the *other* category are mostly ZZ and tZq.

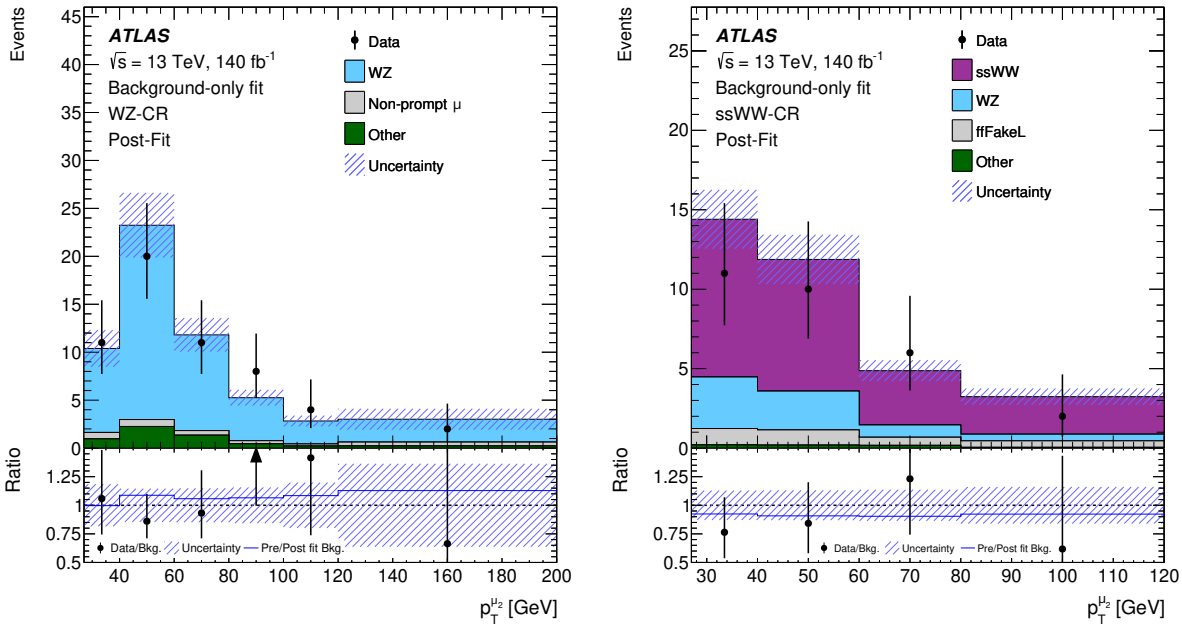

(a)

(b)

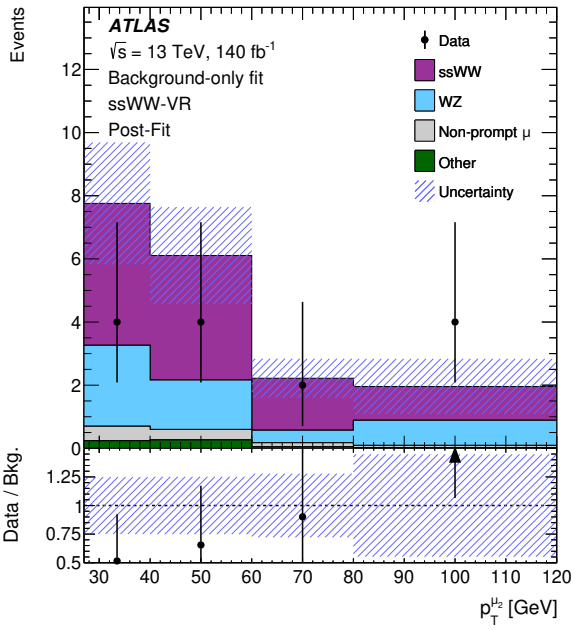

(c)

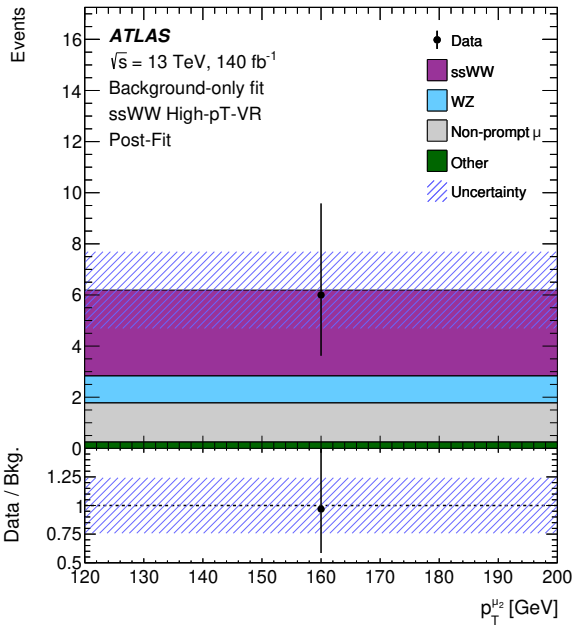

(d)

Figure 7.3.: Comparison of the post-fit $p_{\mathrm{T}}^{\mu_2}$ distributions in the $W^{\pm}Z$ (a) and $W^{\pm}W^{\pm}$ (b) control regions as well as in the $W^{\pm}W^{\pm}$ (c) and high-p_{T} (d) validation regions to data. The fit was performed under the background-only hypothesis. The shaded band surrounding the background estimate indicates the total post-fit uncertainty. In the bottom panel, the ratio of data to the post-fit SM prediction is shown, whereas the blue line indicates the ratio between pre- and postfit background. Events in the *other* category are mostly ZZ and tZq.

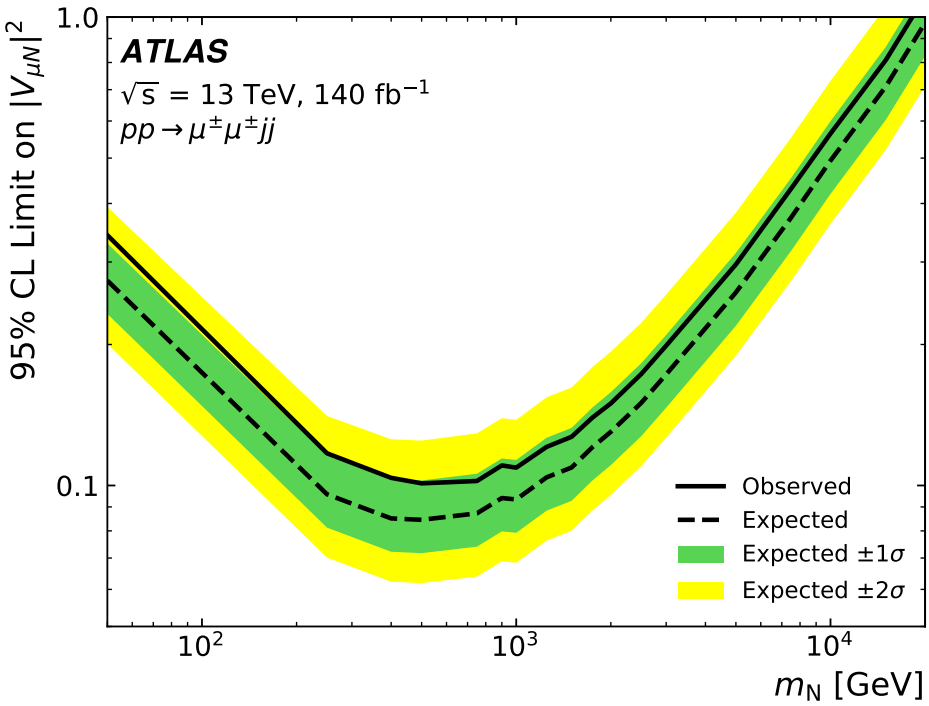

Figure 7.4.: Observed and expected 95 % CL limits on the mixing parameter $|V_{\mu N}|^2$ as a function of the heavy Majorana neutrino mass m_N in the Type I Seesaw model. The green and yellow bands indicate one and two standard deviations from the expected limit.

tainty (Table 7.1). Throughout the whole mass range, this work has at least 20 % more sensitivity than the recent CMS analysis of the same channel [135] (Table 7.1).

For the Weinberg operator, an observed (expected) lower limit of $\frac{\Lambda}{C_5^{\mu\mu}} > 3.64\,(4.61)$ TeV is determined at 95 % CL. This corresponds to an upper limit on the effective Majorana mass of $m_{\mu\mu} < 16.7\,(13.1)$ GeV. While this is slightly worse than the $m_{\mu\mu} < 12.8$ GeV limit reported by CMS [135], that analysis used a special binning of the SR to improve sensitivity to the Weinberg operator.

Table 7.1.: Expected limits on $|V_{\mu N}|^2$ from this analysis compared to the recent CMS results [135]. For this search, expected limits without systematic uncertainties are also shown and found to be nearly identical to the limits including systematic uncertainties.

m_N [TeV]	ATLAS (stat-only)	ATLAS	CMS
0.5	0.0809	0.0810	0.10
1.0	0.0895	0.0900	0.11
3.0	0.165	0.165	0.21
5.0	0.247	0.248	0.30
10.0	0.473	0.473	0.58

8. Conclusions

This thesis presents work on three distinct topics. The ATLAS experiment will receive a new tracking detector, the ITk, for the HL-LHC phase. All modules of this detector have to be thoroughly tested during production to ensure the flawless operation of the ITk. Part of these tests is a thermal cycling sequence, where modules are cycled through the whole operating temperature range of the ITk ten times. At each temperature extreme, several tests are performed. DESY has designed and built a test stand for thermal cycling, known as coldbox. Performance tests with a preliminary design were performed to identify design improvements. Additionally, the test stand has been automated with a PLC. Automated thermal cycling with the finalised design has shown that the coldbox can meet the required performance. As a result, the design could be produced in series for several other institutes in the collaboration.

The second topic presented in this thesis were two phenomenological studies. So far, heavy neutrino searches at colliders have been performed only in s-channel processes. The t-channel process, which is the high-energy equivalent of neutrinoless double-β decay, has not been investigated before. It has a very clear experimental signature of two muons of same electric charge and two jets in a VBS configuration. MC simulations of this process have shown that the cross section is large enough to be detectable in the LHC Run 2 dataset. An extensive mock analysis using a DELPHES simulation of the ATLAS detector has been designed. Assuming $300\,\text{fb}^{-1}$ of data at $\sqrt{s} = 13\,\text{TeV}$, LHC experiments should be sensitive to heavy neutrinos with masses exceeding 20 TeV while being more sensitive than previous searches for $m_N \gtrsim 750\,\text{GeV}$. This study has been published in [24].

The Weinberg operator could be probed in the same dimuon final state. LHC experiments could improve the sensitivity significantly over the results of NA-62 [101]. However, they would still be many orders of magnitude away from indirect limits from neutrino oscillations. This study was published in [25].

Both phenomenological studies have raised the interest of the CMS collaboration, who performed a search for these processes [135].

The third and main topic presented in this thesis is a search for heavy neutrinos and the Weinberg operator with the ATLAS experiment. A search was performed in the $\mu^\pm\mu^\pm jj$ final state using $140\,\text{fb}^{-1}$ of data collected at $\sqrt{s} = 13\,\text{TeV}$. Here, the main backgrounds are the SM production of two same-charge W bosons and $W^\pm Z$ production. The normalisation of these backgrounds is obtained from data in dedicated control regions. They are orthogonal to the signal region and only a negligible number of signal events is expected in them. The third large background, non-prompt muons, is estimated with a data-driven method. Since this method resulted in low statistics

of the background estimate, it is approximated by a functional form fit for statistical evaluation.

A profile likelihood fit is performed in the distribution of the subleading muon transverse momentum. This allows both the Type I Seesaw model and the Weinberg operator to be checked in the same signal region. No excess above the SM expectation was found, therefore exclusion limits are calculated at 95 % confidence level.

For the Type I Seesaw signal model, masses in the range $50\,\text{GeV} < m_N < 20\,\text{TeV}$ are probed. The analysis has the most sensitivity at $m_N = 500\,\text{GeV}$, where the observed (expected) limit on the muon-neutrino–heavy-neutrino mixing parameter is $|V_{\mu N}|^2 < 0.10(0.08)$. This limit reaches $|V_{\mu N}| = 1$ at $m_N = 20\,\text{TeV}$, which is the upper bound of the mixing parameter. All in all, the expected limits constitute a $15 \ldots 20\,\%$ improvement over the results presented in [135]. Throughout the whole mass range, the observed limits are approximately $1\,\sigma$ worse than the expected limits. This is due to a slight data excess in the last bins of the $p_{\text{T}}^{\mu_2}$ distribution. The analysis results were also interpreted in the context of the Weinberg operator. An observed (expected) limit on the effective Majorana mass $|m_{\mu\mu}| < 16.7(13.1)\,\text{GeV}$ is obtained.

Figure 8.1 presents the current observed LHC limits on the Type I Seesaw model. Searches in the t-channel are sensitive to heavy neutrinos with $50\,\text{GeV} \lesssim m_N \lesssim 20\,\text{TeV}$. For $m_N \gtrsim 700\,\text{GeV}$, they provide the best limits on $|V_{\mu N}|^2$. Below this, the best sensitivity comes from searches for a promptly decaying neutrino that is produced in the s-channel. They can probe the range $20\,\text{GeV} \lesssim m_N \lesssim 1.4\,\text{TeV}$, but are most sensitive for $m_N < m_W$, where mixing parameters $|V_{\mu N}|^2 \gtrsim 2 \cdot 10^{-5}$ can be probed. If the heavy neutrino is lighter than approximately 20 GeV, it will travel a significant distance before decaying. In the detector, this will be visible as a displaced vertex. The lifetime of the heavy neutrino will depend both on the mass and the mixing parameter, which explains the loop-like shape of the exclusion contours of the searches for long-lived neutrinos.

A combination of the t- and s-channel searches could improve sensitivity towards heavy neutrinos with masses of $400\,\text{GeV} \lesssim m_N \lesssim 1.3\,\text{TeV}$. Sensitivity to the Type I Seesaw model in the t-channel process improves only with the fourth root of the luminosity. Therefore, an analysis using the combined Run 2 and 3 LHC datasets could improve the sensitivity only by approximately 20 %. Instead, a search in the $\tau^\pm\tau^\pm$ final state should be the next focus of LHC experiments. τ leptons are experimentally more challenging than electrons or muons, therefore there are up to now only very few direct limits on $|V_{\tau N}|^2$.

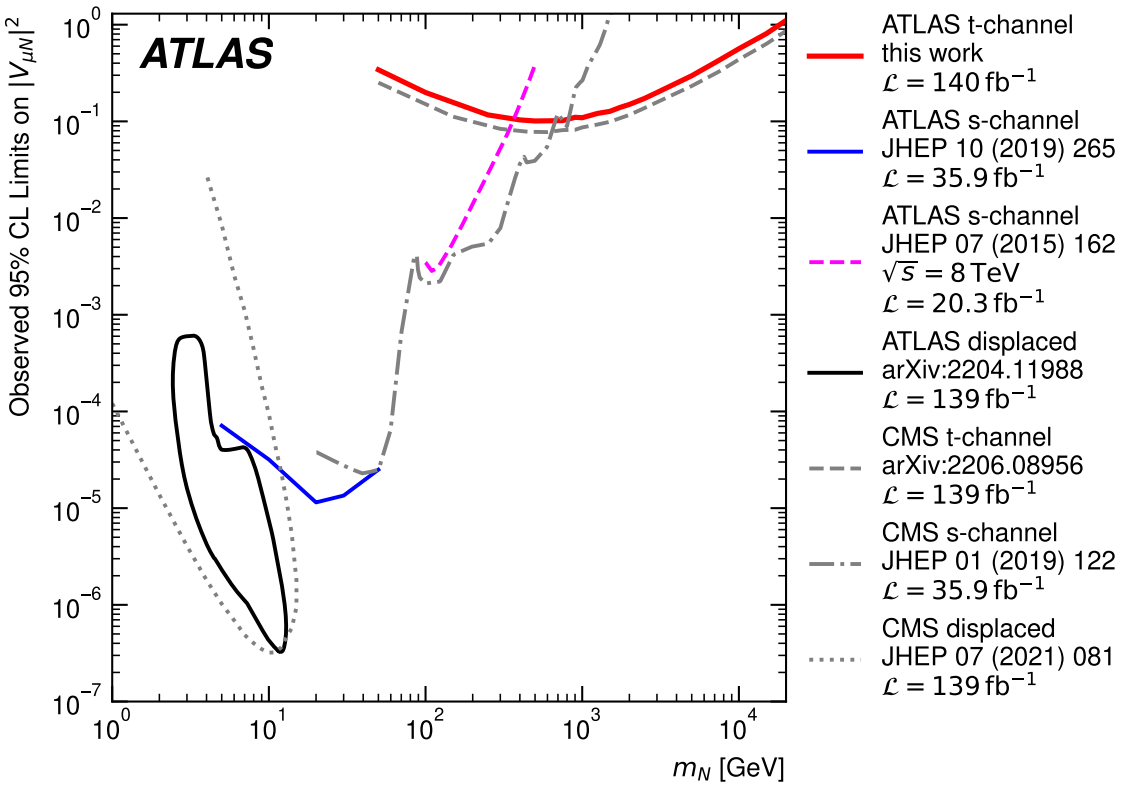

Figure 8.1.: Summary of LHC limits on heavy neutrinos.

A. Coldbox: Additional Material

A.1. Chiller Performance Studies

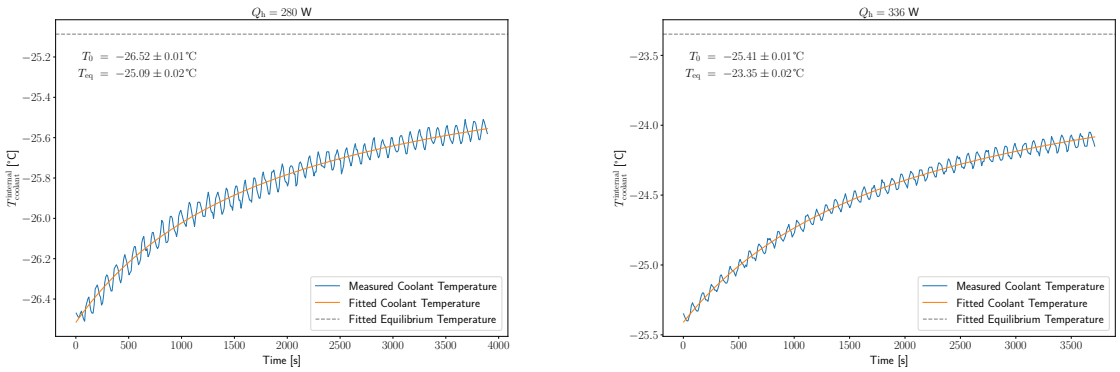

(a) (b)

Figure A.1.: Chiller performance studies using a mixture of 50 % water and 50 % ethylene glycol as coolant. These plots show the measured coolant temperatures and those predicted by an asymptotic fit for wasteheats Q_h of 280 W (a) and 336 W (b). The measured temperature oscillates with an amplitude of $\lesssim 0.1$ °C because the PID parameters of the chiller were not finetuned.

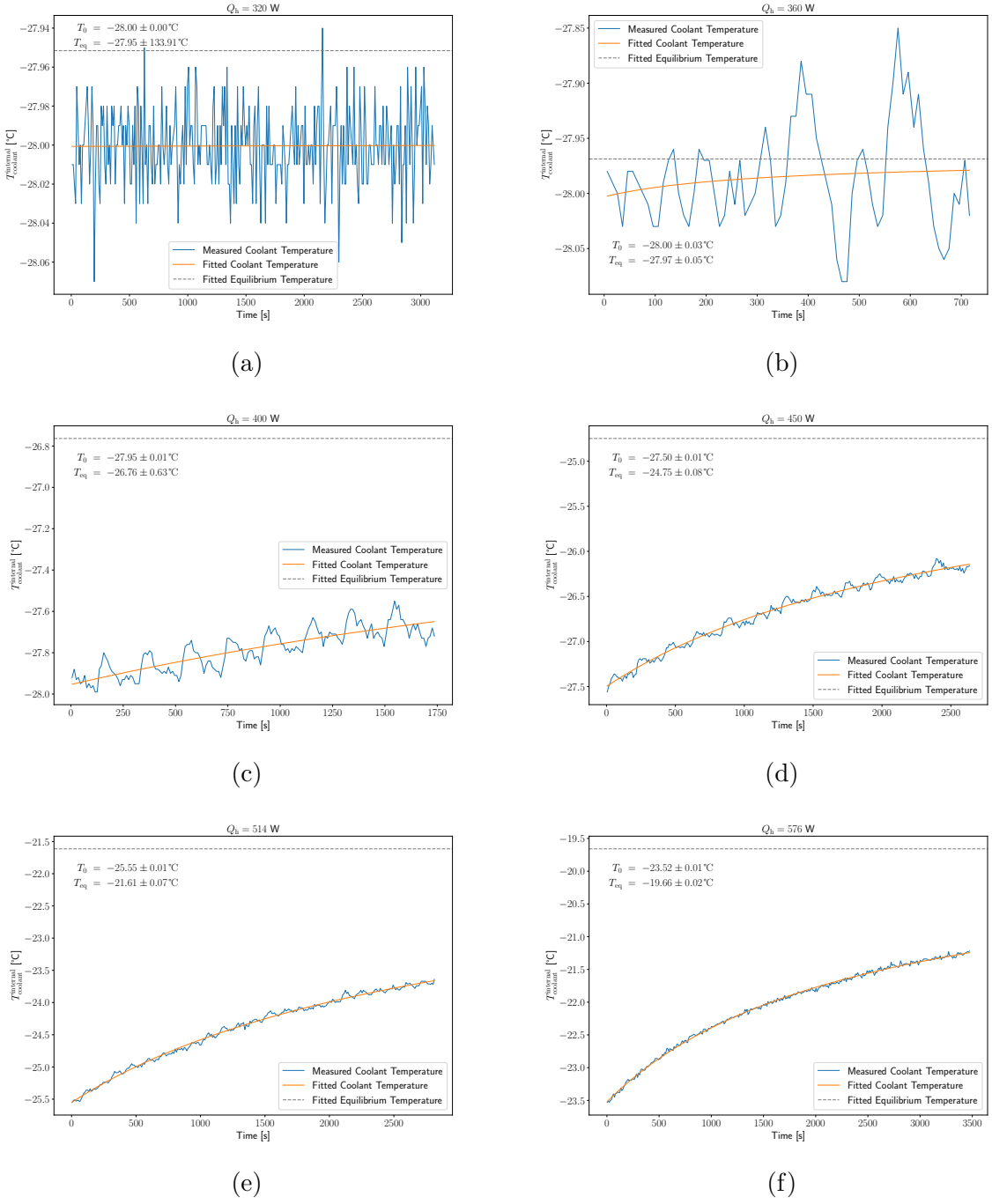

Figure A.2.: Chiller performance studies with ethanol as coolant. These plots show the measured coolant temperatures and those predicted by an asymptotic fit for wasteheats Q_h of 320 W (a), 360 W (b), 400 W (c), 450 W (d), 514 W (e) and 576 W (f). The measured temperature oscillates with an amplitude of $\lesssim 0.1\,°C$ because the PID parameters of the chiller were not finetuned. For $Q_h = 320\,W$ (a), the temperature remains constant at $T_{eq} = -28.00\,°C$, which is not described well by the asymptotic model.

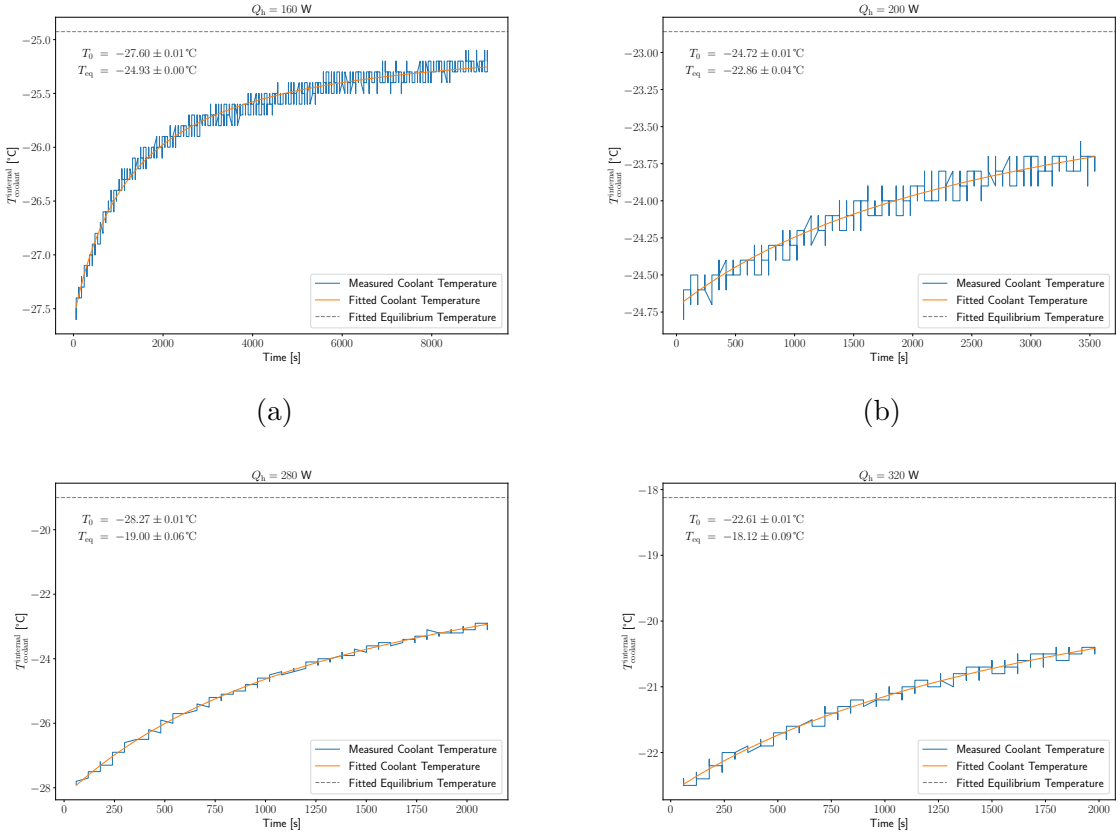

Figure A.3.: Chiller performance studies with silicon oil as coolant. These plots show the measured coolant temperatures and those predicted by an asymptotic fit for wasteheats Q_h of 160 W (a), 200 W (b), 280 W (c) and 320 W (d). This measurement was performed with the PLC, which stores temperatures only with an accuracy of 0.1 °C. Therefore the oscillations observed in Figures A.1 and A.2 are mostly hidden by the temperature resolution and only the occasional spike or seemingly abrupt change in temperature is visible.

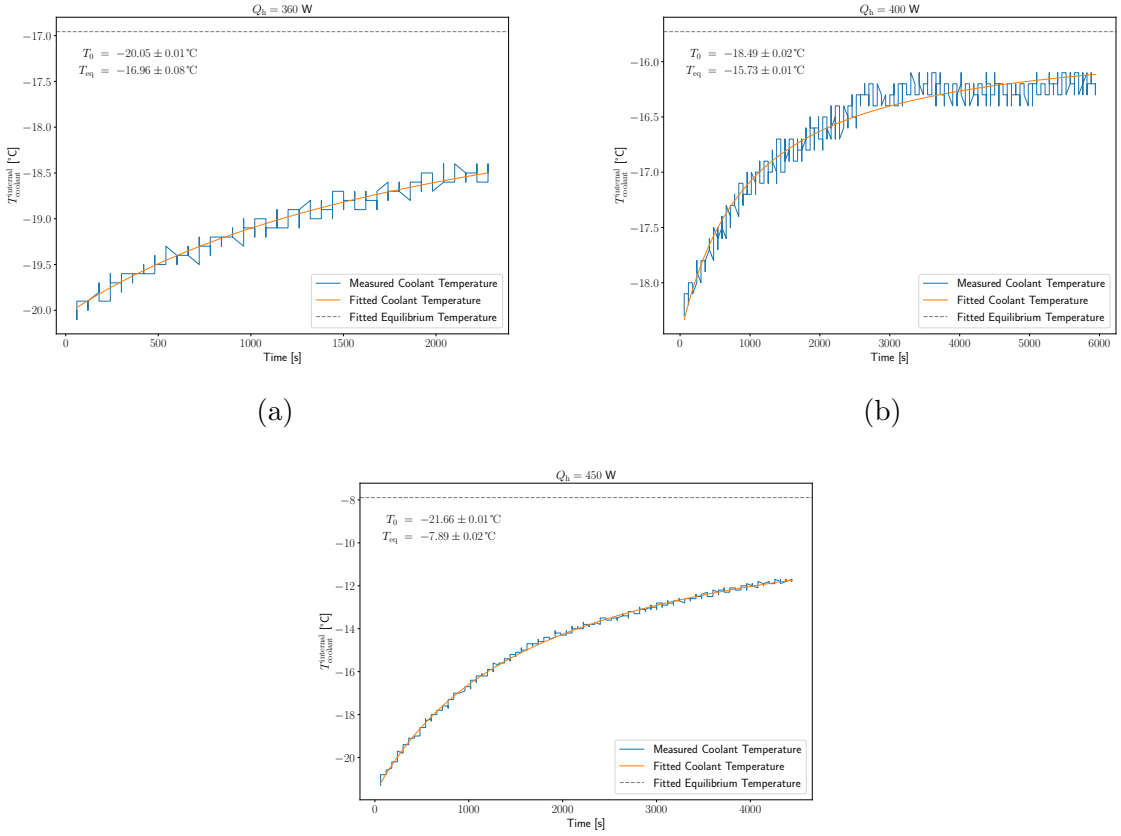

Figure A.4.: Chiller performance studies with silicon oil as coolant. These plots show the measured coolant temperatures and those predicted by an asymptotic fit for wasteheats Q_h of 360 W (a), 400 W (b) and 450 W (c). This measurement was performed with the PLC, which stores temperatures only with an accuracy of 0.1 °C. Therefore the oscillations observed in Figures A.1 and A.2 are mostly hidden by the temperature resolution and only the occasional spike or seemingly abrupt change in temperature is visible.

B. MC Validation

B.1. Type I Seesaw

Figures B.1 and B.2 show truth level distributions of the Type I Seesaw model generated within the ATLAS software framework (cf. Section 6.1.1). Comparing those with the distributions from the phenomenological study shows a good agreement in the shape of the distributions and relative cross section of the different mass points.

B.2. Weinberg Operator

The Weinberg operator samples generated for the ATLAS analysis were validated thoroughly against the samples used in the phenomenological study. The comparisons were made with a small sample generated before official ATLAS MC production. For leptons, kinematics are found to be very similar (Figure B.3). While the jet momentum distributions are also quite similar, differences in the pseudorapidity become visible (Figure B.4). For the leading and subleading jet, these differences remain small, but the third jet is at significantly higher pseudorapidities in the pheno study than in the ATLAS analysis. Ultimately, this difference is due to the parton shower. The pheno study used an improved parton shower based on [99, 143] that is supposed to better model colour flow in VBS processes. After discussion, it was concluded to not use this description for the ATLAS analysis in order to remain consistent with the background samples. Other observables that include jets are also affected to a varying degree by this difference (Figure B.5).

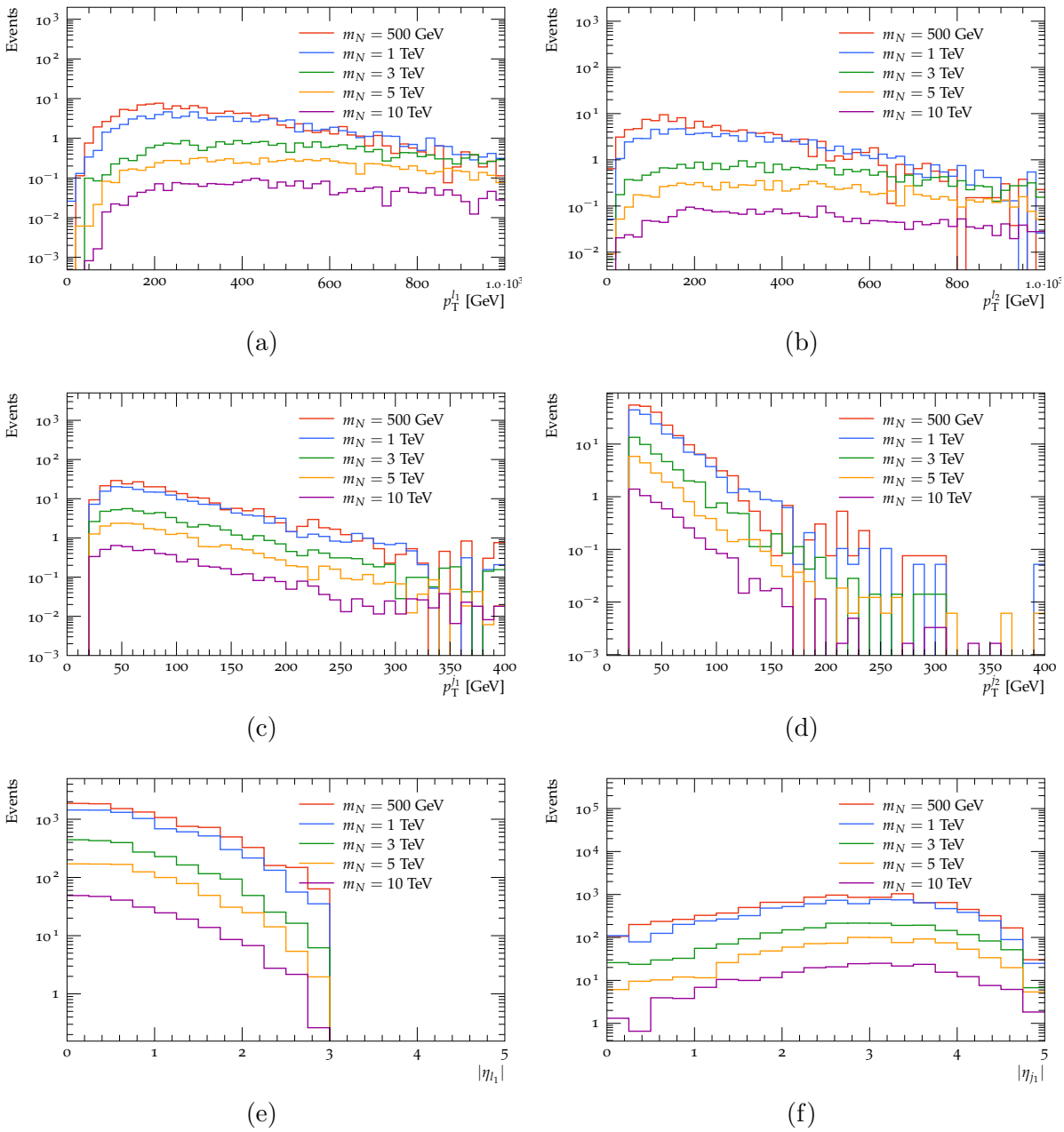

Figure B.1.: Truth-level distributions of the leading (a) and subleading (b) muon p_T, leading (c) and subleading (d) jet p_T, as well as the pseudorapidity of the leading muon (e) and jet (f) for the five benchmark mass points of the Type I Seesaw signal sample.

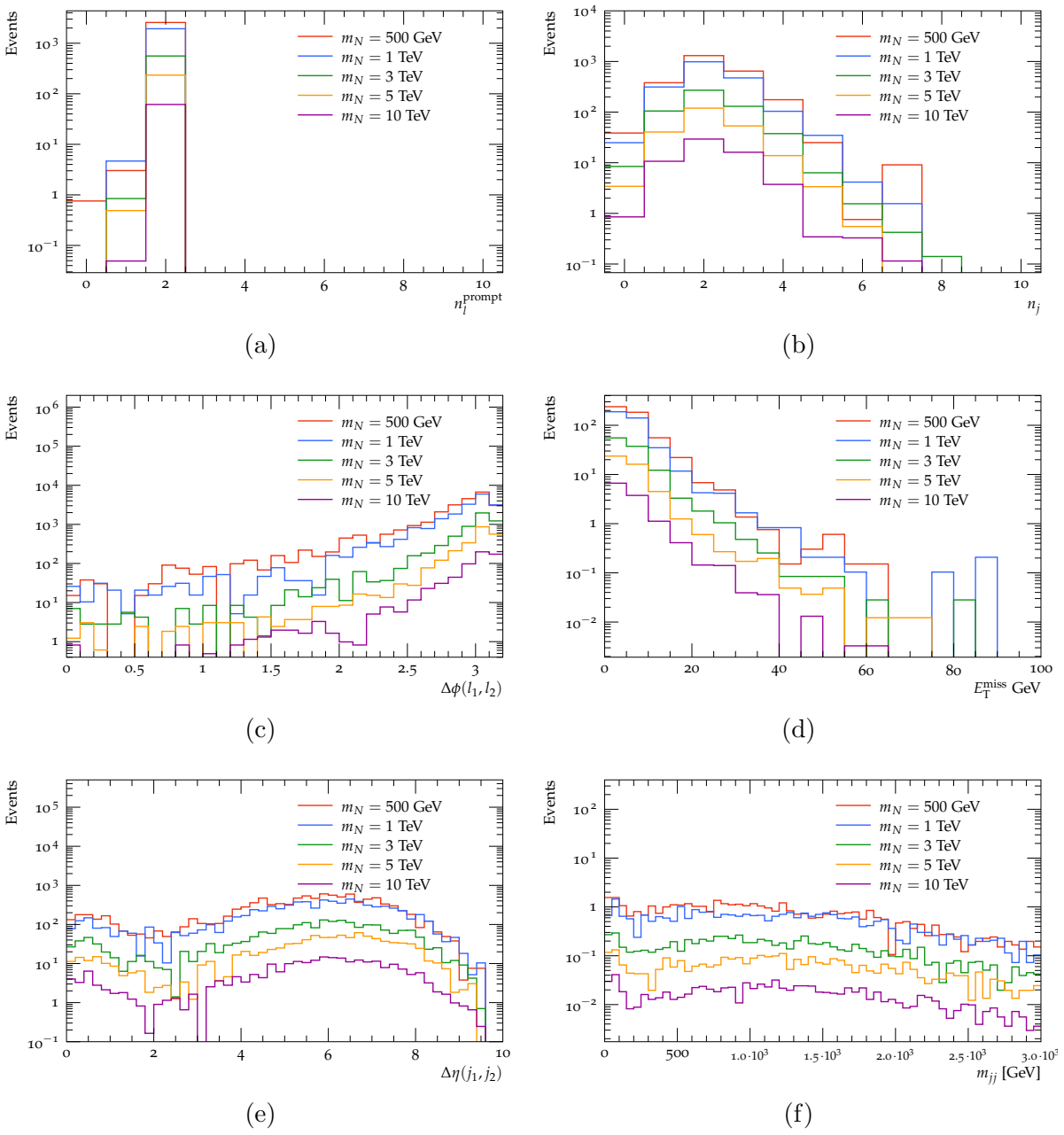

Figure B.2.: Truth-level distributions of the muon (a) and jet (b) multiplicities, the separation in ϕ of the leading and subleading muon (c), $E_{\text{T}}^{\text{miss}}$ (d), the pseudorapidity gap between the leading two jets (e) and their invariant mass (f) for five benchmark mass points of the Type I Seesaw model.

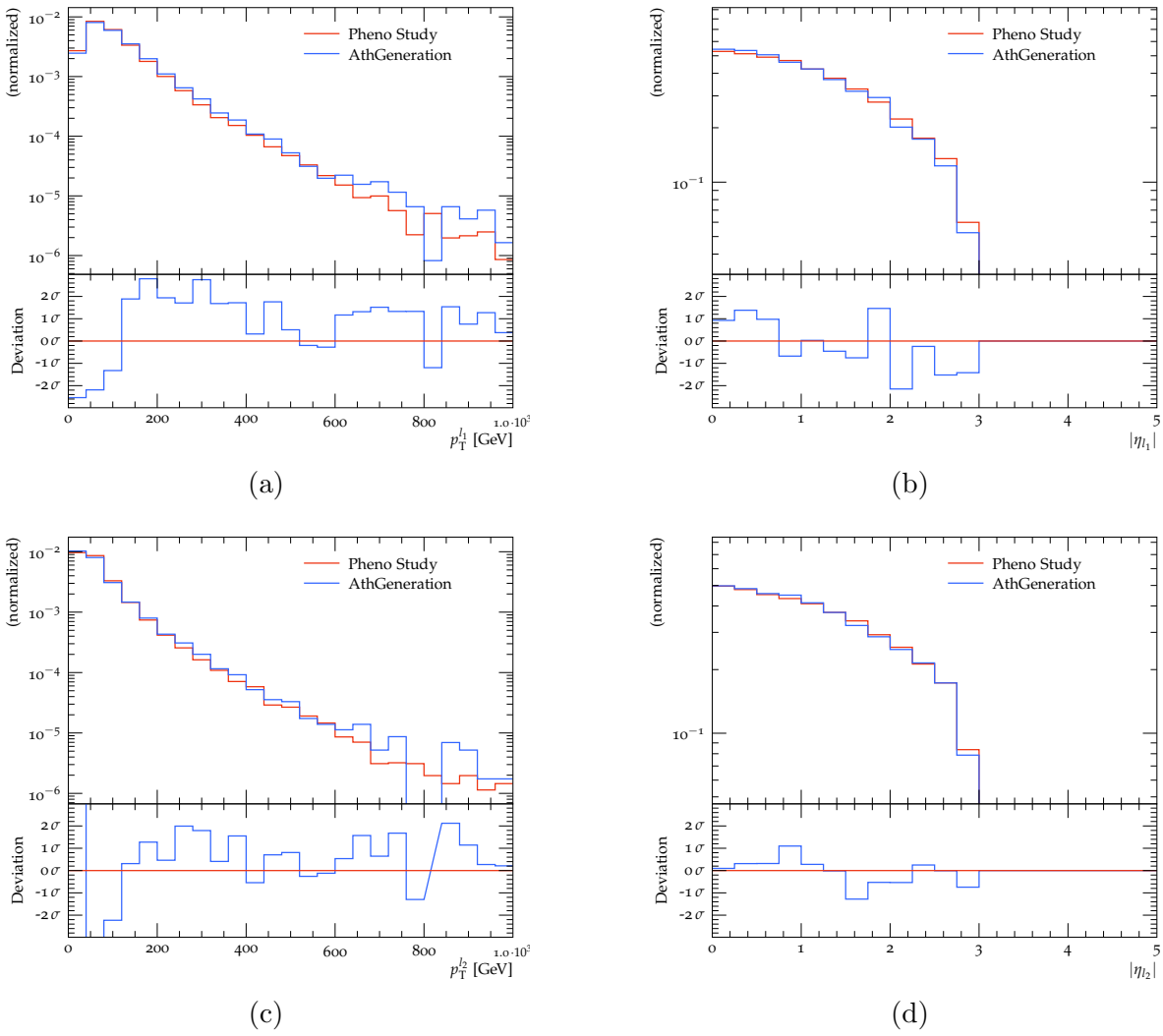

Figure B.3.: Transverse momentum (a,c) and pseudorapidity (b,d) of the leading (a,b) and subleading (c,d) lepton in the Weinberg operator signal sample. The sample used in the phenomenological study (Chapter 5) is marked red, the sample generated for the ATLAS analysis (Section 6.1.1) is marked blue.

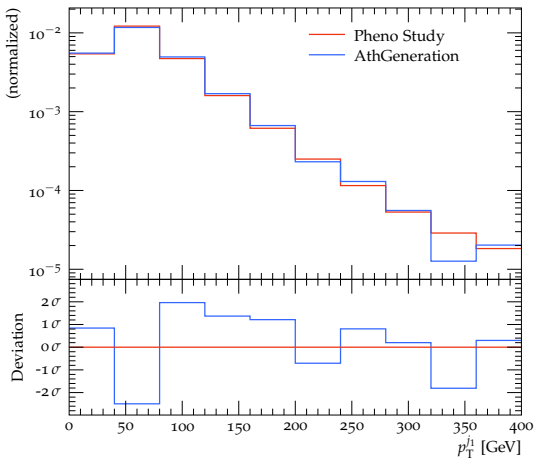

(a)

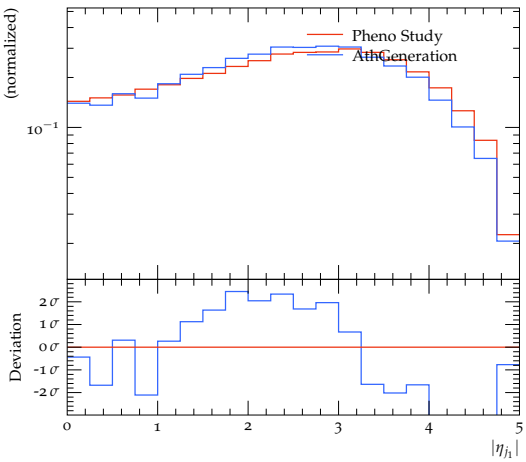

(b)

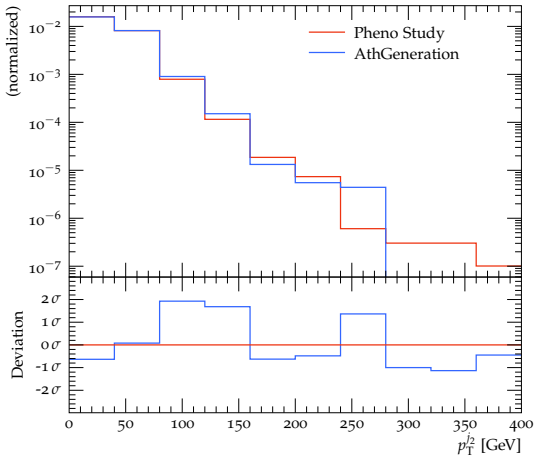

(c)

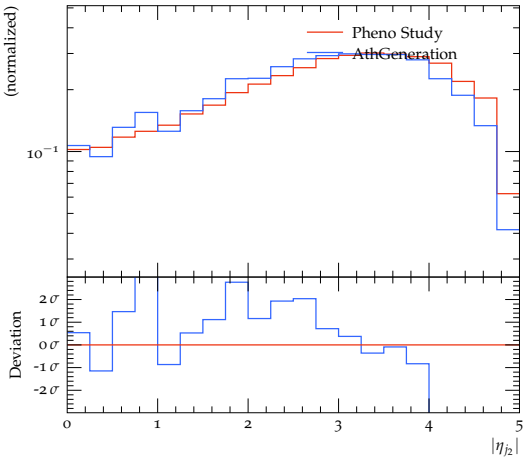

(d)

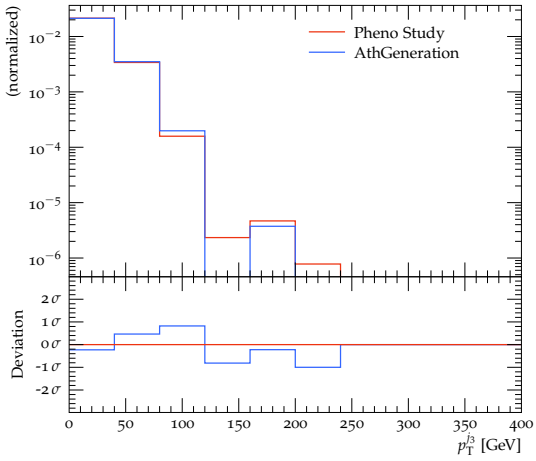

(e)

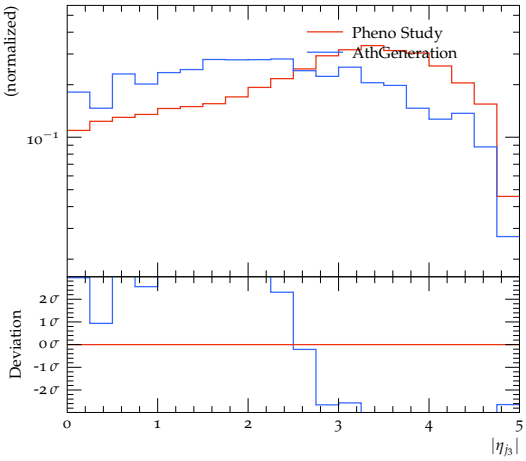

(f)

Figure B.4.: Truth-level distributions of transverse momentum (a,c,e) and pseudorapidity (b,d,f) for the leading (a,b), subleading (c,d) and third jet (e,f). The sample used in the phenomenological study (Chapter 5) is marked red, the sample generated for the ATLAS analysis (Section 6.1.1) is marked blue.

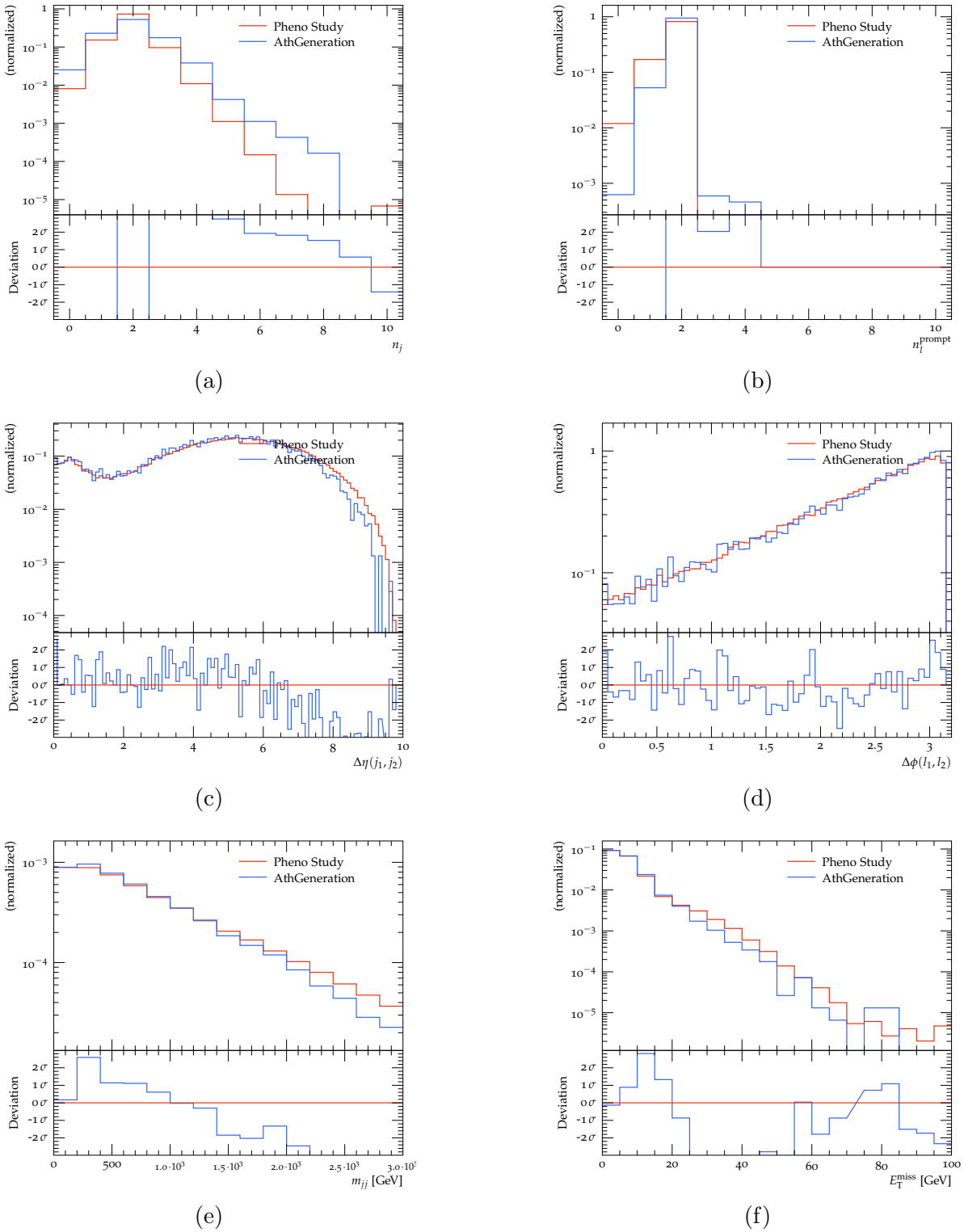

Figure B.5.: Truth-level distributions of jet (a) and lepton (b) multiplicity, pseudorapidity gap between the leading two jets $\Delta\eta(j_1, j_2)$ (c), angular distance between the leading two leptons (d), dijet invariant mass m_{jj} (e) and $E_{\text{T}}^{\text{miss}}$ (f) for the Weinberg operator signal sample. The sample used in the phenomenological study (Chapter 5) is marked red, the sample generated for the ATLAS analysis (Section 6.1.1) is marked blue.

C. Studies on a Dedicated Weinberg Operator Signal Region

The signal region design was in the beginning focused on the Type I Seesaw model. These preliminary studies considered a cut on $p_{\mathrm{T}}^{\mu_2}$, which is very effective at separating signal and background events for this model. However, this observable is less effective at selecting Weinberg operator events (Figure 5.7b). Therefore, the prospects of a dedicated Weinberg operator signal region were studied. Note that these studies were performed with a preliminary SR that, in addition to the $p_{\mathrm{T}}^{\mu_2} > 75\,\mathrm{GeV}$ cut, also had a different $E_{\mathrm{T}}^{\mathrm{miss}}$ significance cut.

C.1. Adjusting the Existing SR

One possibility is to add or modify some cuts of the signal region optimised for the Type I Seesaw model in order to increase sensitivity to the Weinberg operator. For each observable, the limit on $\Lambda/C_5^{\mu\mu}$ is determined and shown in Table C.1. Improvements are possible with a very tight cut on $E_{\mathrm{T}}^{\mathrm{miss}}$ significance or $E_{\mathrm{T}}^{\mathrm{miss}}$, but especially the latter would leave only small background statistics, making an estimate difficult. Cuts based on the leading jet p_{T} offer an even better sensitivity. However, such a Weinberg operator SR would most likely require dedicated control regions. Considering that even the improved sensitivity would be many orders of magnitude worse than the indirect limits from neutrino oscillation data, it was decided that it is not worth the effort to have a dedicated SR.

C.2. Performance of the Phenostudy Selection in ATLAS

In order to check the potential of a thoroughly optimised SR for the Weinberg operator, the selection used in the phenomenological study (Table C.2) is applied within the ATLAS frameworks. The event yields are listed in Table C.3 and correspond to sensitivity to scales scales below $\Lambda/|C_5^{\mu\mu}| \lesssim 4.8\,\mathrm{TeV}$ at 95 % confidence level. This is somewhat better than the sensitivity achievable by slightly adjusting the SR for the Type I Seesaw model (Table C.1), but cannot compete with the sensitivity estimate given in Section 5.5.

In order to find the origin of this difference, the yields from Table C.3 are rescaled to $300\,\mathrm{fb}^{-1}$ and divided by the yields from the phenomenological study (Table C.4). Some of the difference, especially at preselection, can be explained by the looser $p_{\mathrm{T}}^{\mu_2} > 10\,\mathrm{GeV}$

Table C.1.: Potential additions to the SR cuts of Section 6.3.2 in order to increase sensitivity to the Weinberg operator. The first line shows an unmodified SR for comparison. **Study done with non-final $E_{\mathrm{T}}^{\mathrm{miss}}$ significance and $p_{\mathrm{T}}^{\mu_2}$ cut but conclusion still holds.**

Modif. to SR	n_{b}	limit on $\frac{\Lambda}{C_5^{\mu\mu}}$ [TeV]
none	11.98	3.8
$E_{\mathrm{T}}^{\mathrm{miss}}$ sign. ≤ 1.8	4.65	4.3
$E_{\mathrm{T}}^{\mathrm{miss}}$ sign. ≤ 1.6, $p_{\mathrm{T}}^{\mu_2} > 82\,\mathrm{GeV}$	2.98	4.4
$E_{\mathrm{T}}^{\mathrm{miss}} \leq 25\,\mathrm{GeV}$	1.77	4.4
$p_{\mathrm{T}}^{j_1} > 115\,\mathrm{GeV}$	4.57	4.4
$p_{\mathrm{T}}^{j_1}/H_{\mathrm{T}}^{ll} \leq 0.4$	4.31	4.5
$\Delta Y_{jj} > 5.2$	4.87	4.0

Table C.2.: Selection for the dedicated Weinberg operator SR proposed in [25]. These criteria are applied in addition to the preselection defined in Section 6.3.1.

$m_{jj} > 700\,\mathrm{GeV}$	$E_{\mathrm{T}}^{\mathrm{miss}} < 30\,\mathrm{GeV}$	$\frac{H_{\mathrm{T}}}{p_{\mathrm{T}}^{\mu_1}} < 1.6$

cut applied in the phenostudy as part of the preselection instead of the $p_{\mathrm{T}}^{\mu_2} > 27\,\mathrm{GeV}$ cut used in ATLAS. After applying the full selection, the ATLAS analysis only expects half of the signal events as the phenostudy, but the same amount of background events. In both cases, $W^{\pm}W^{\pm}$ is the main background, followed by $W^{\pm}Z$. However, when applying the selection in ATLAS, there are approx. two $W^{\pm}W^{\pm}$ events for every $W^{\pm}Z$ event, whereas this ratio was closer to 6:1 in the phenostudy. Additionally, 13 % of the background events come from processes that were neglected in the phenostudy.

Looking at the marginal cut efficiencies[1], it can be clearly seen that the $E_{\mathrm{T}}^{\mathrm{miss}} < 30\,\mathrm{GeV}$ cut removes more signal in the ATLAS analysis than in the phenostudy. This is an indication that $E_{\mathrm{T}}^{\mathrm{miss}}$ originating from mismeasurement is badly described by the fast detector simulation Delphes.

[1]The percentage of events passing all other cuts that will also pass the given cut.

Table C.3.: Event yields when applying the dedicated Weinberg SR selection from Table C.2, $\mathcal{L} = 139\,\text{fb}^{-1}$.

	Weinberg	$W^\pm W^\pm$ EWK	$W^\pm W^\pm$ QCD	$W^\pm Z$	total bkg.
Preselection	0.0135	183.73	111.49	424.33	1426.75
+ $m_{jj} > 700\,\text{GeV}$	0.0062	90.37	11.41	27.18	165.75
SRWeinberg	0.0028	2.02	0.01	1.03	3.50
w/o $E_\text{T}^\text{miss} < 30\,\text{GeV}$ cut	0.0046	13.19	0.06	4.52	21.11
w/o $\frac{H_\text{T}}{p_\text{T}^{\mu_1}} < 1.6$ cut	0.0039	9.92	1.02	3.95	18.88

Table C.4.: Ratio of the ATLAS event yield scaled to $300\,\text{fb}^{-1}$and the event yield of the phenomenological study (Chapter 5).

	Weinberg	$W^\pm W^\pm$ EWK	$W^\pm W^\pm$ QCD	$W^\pm Z$	total bkg.
Preselection	0.83	0.87	0.50	0.34	0.85
+ $m_{jj} > 700\,\text{GeV}$	0.74	0.68	0.53	0.66	0.85
SRWeinberg	0.48	0.68	—	1.92	1.00
w/o $E_\text{T}^\text{miss} < 30\,\text{GeV}$ cut	0.68	0.65	0.09	1.19	0.85
w/o $\frac{H_\text{T}}{p_\text{T}^{\mu_1}} < 1.6$ cut	0.52	0.71	0.70	0.50	0.81

Table C.5.: Marginal cut efficiencies in a dedicated Weinberg operator SR (cf. Table C.2 for both the ATLAS analysis and the phenomenological study (Chapter 5). Note that the $m_{jj} > 700\,\text{GeV}$ cut is part of the preselection in the phenomenological study, therefore it is not easily possible to obtain a marginal cut efficiency for it.

		$E_\text{T}^\text{miss} < 30\,\text{GeV}$	$\frac{H_\text{T}}{p_\text{T}^{\mu_0}} < 1.6$
Weinberg Operator	ATLAS	60.9 %	72.4 %
	Phenostudy	87.0 %	79.2 %
ssWW EWK	ATLAS	15.3 %	20.4 %
	Phenostudy	14.6 %	21.3 %
ssWW QCD	ATLAS	12.9 %	0.8 %
	Phenostudy	0.0 %	0.0 %
WZ	ATLAS	22.8 %	26.1 %
	Phenostudy	14.1 %	6.8 %
total SM	ATLAS	16.6 %	18.5 %
	Phenostudy	14.1 %	15.1 %

D. Systematic Uncertainties

D.1. Smoothed Systematics

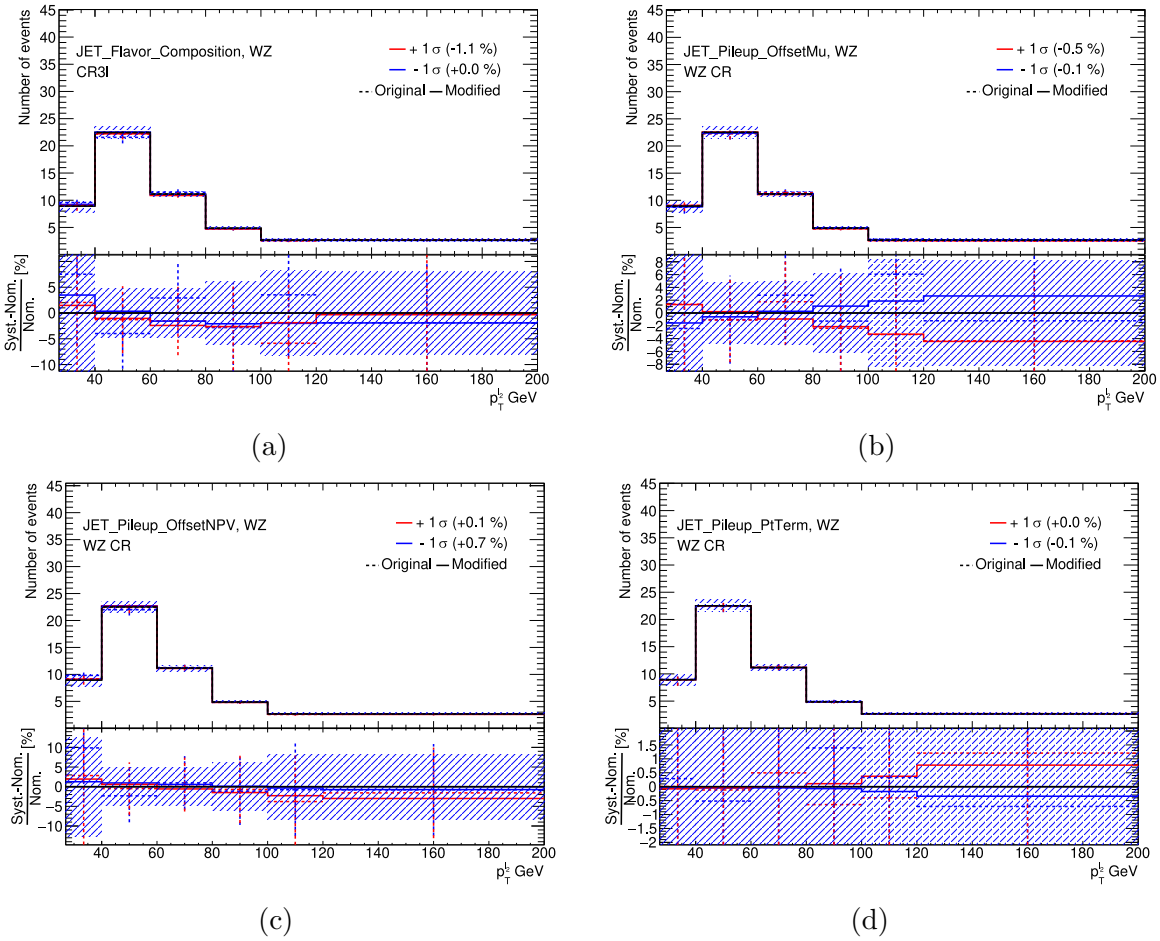

Figure D.1.: The four underconstrained fitting parameters that became stable after t-channel smoothing. It can be seen that solid post-smoothing lines have much more clearer up down variations than the previously statistically fluctuating variations (dotted). This is shown with the $W^{\pm}Z$ CR histogram as the effect is most visible.

D.2. Leading Systematics

Here we show a selection of the leading systematic variations from the S+B fit.

D.2.1. MC Systematics

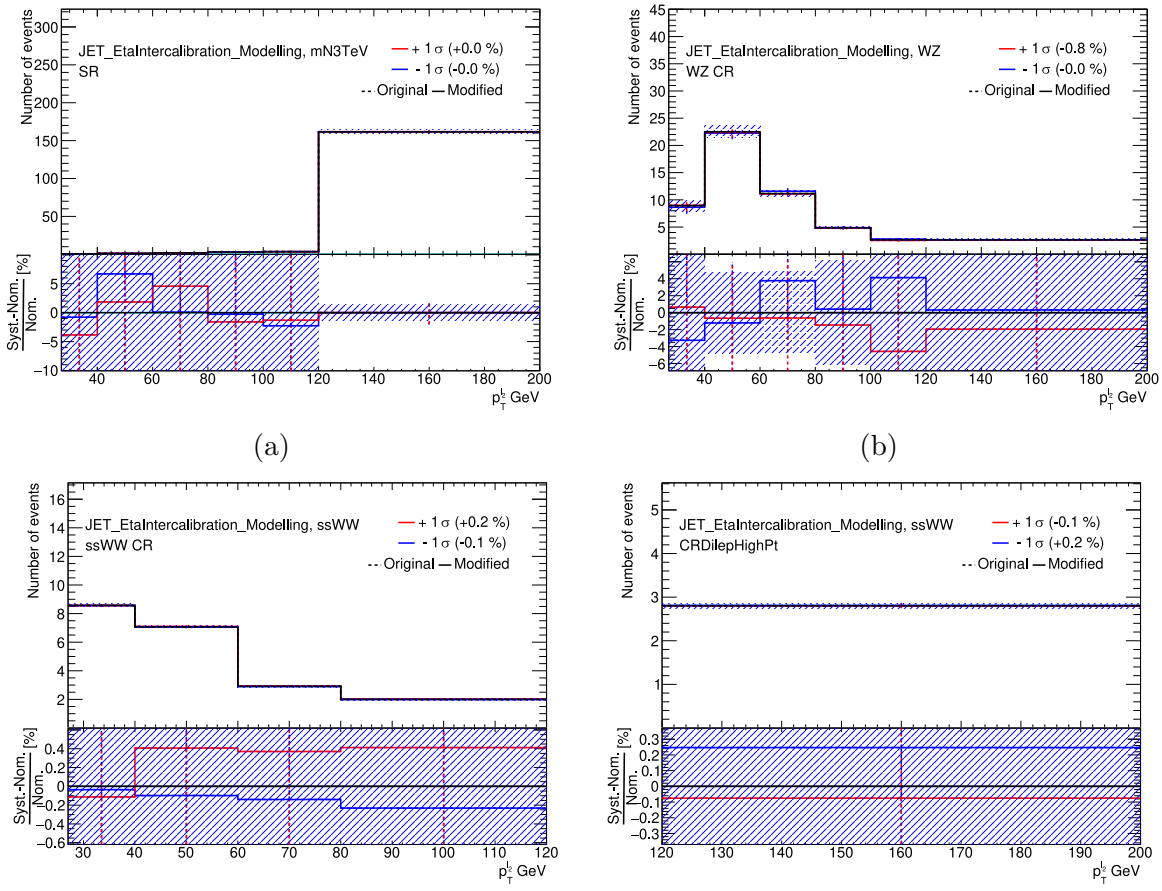

Figure D.2.: Systematic uncertainty related to η intercalibration (`JET_EtaIntercalibration_Modelling`).

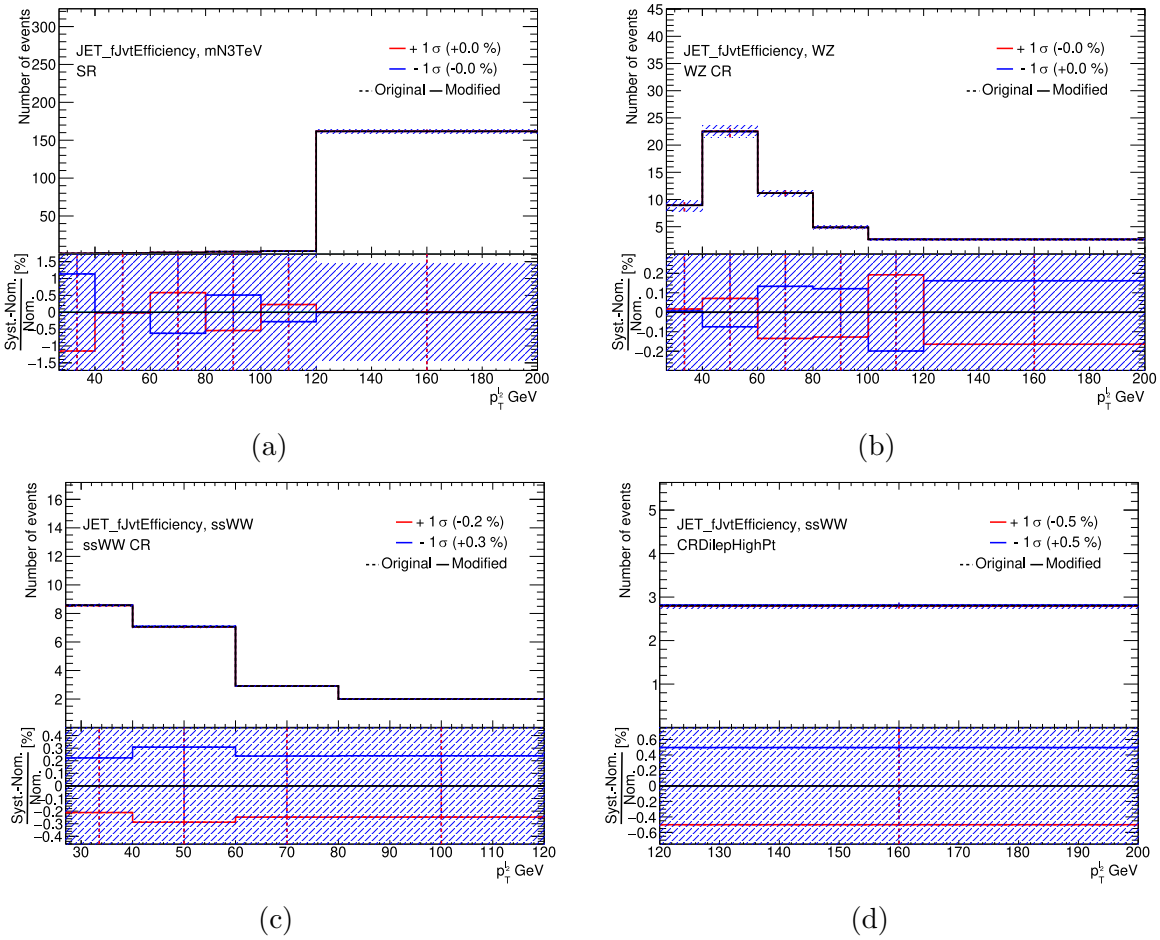

Figure D.3.: Systematic uncertainty related to the forward pile-up identification efficiency (`JET_fJvtEfficiency`).

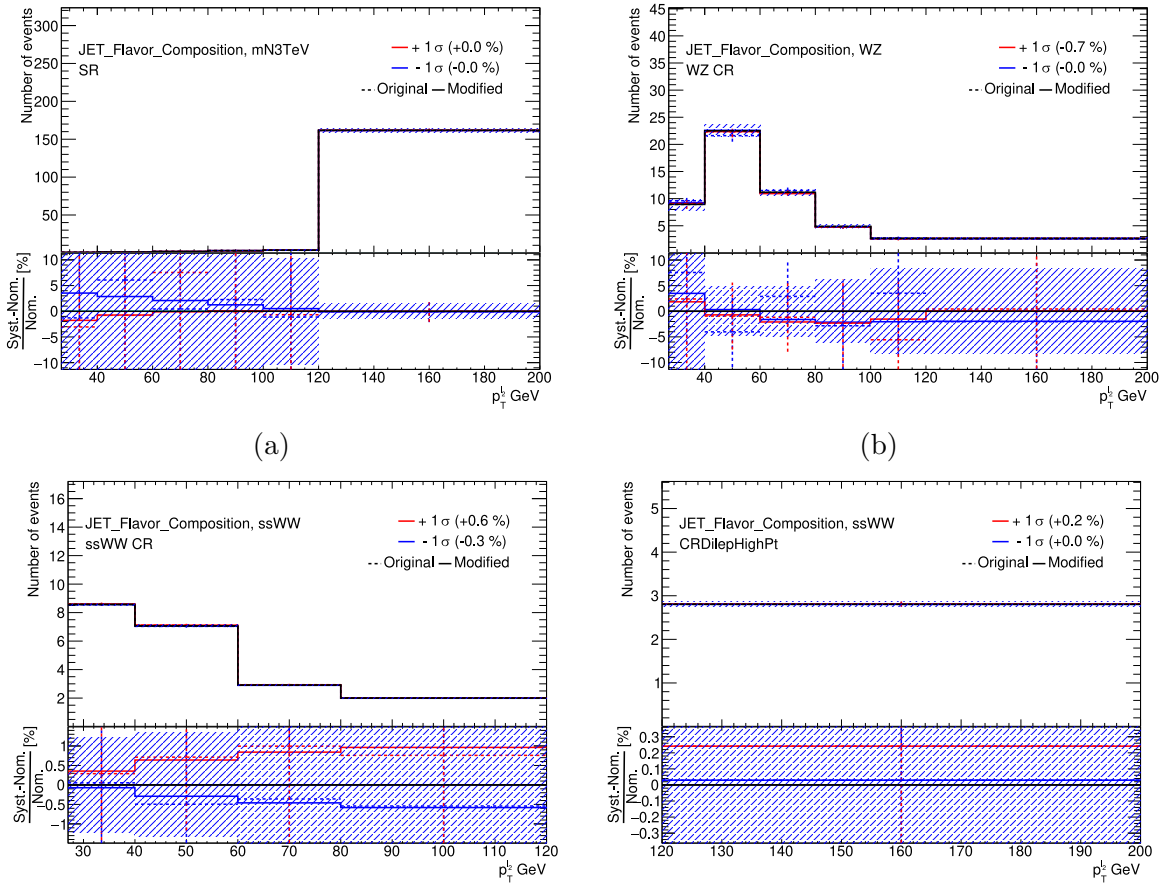

Figure D.4.: Systematic uncertainty related to the quark flavours present in jets (`JET_Flavor_Composition`).

D.3. Ranking

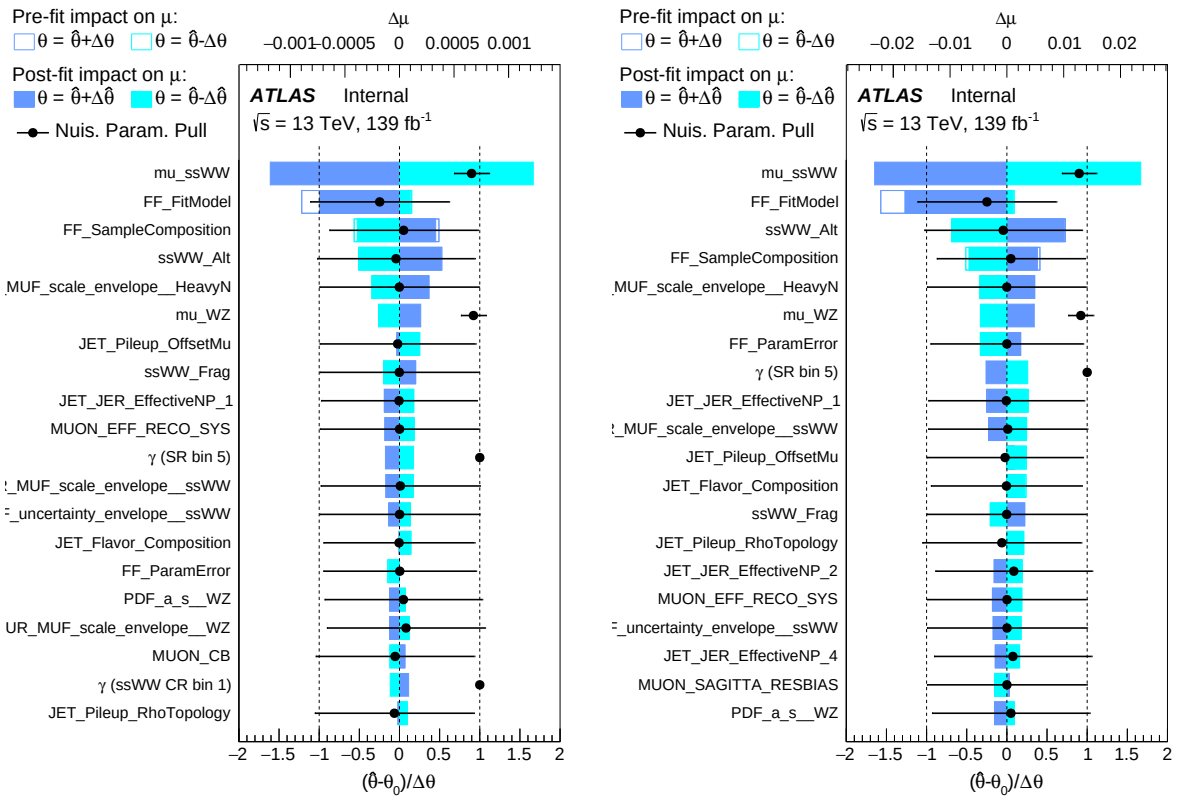

Figure D.5.: Ranking plots for the Type I Seesaw model with $m_N = 1\,\text{TeV}$ (a) and $m_N = 10\,\text{TeV}$ (a) with an injected mixing parameter of $|V_{\mu N}|^2 = 0.22$ and $|V_{\mu N}| = 1$, respectively.

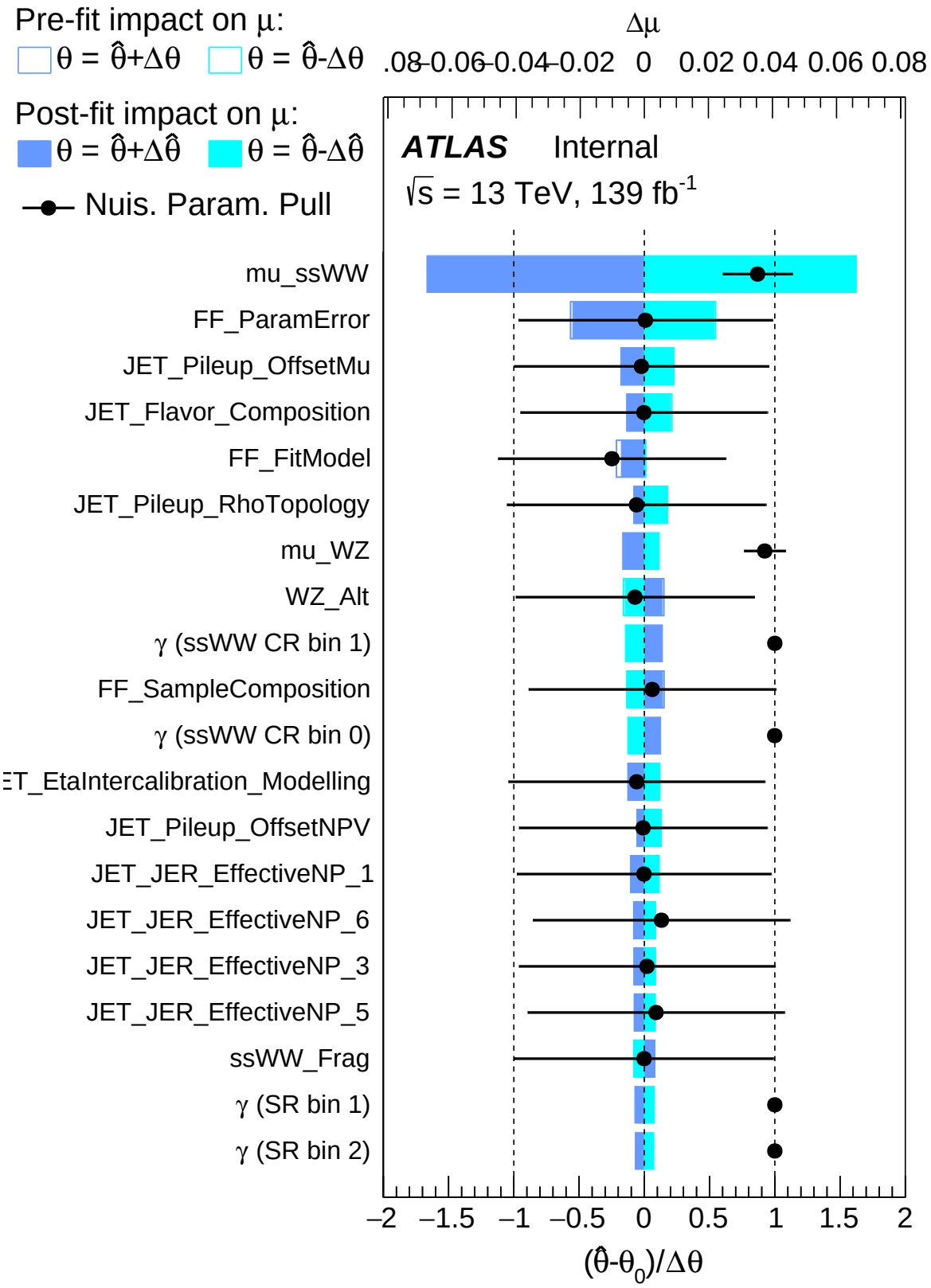

Figure D.6.: Ranking plot for the Weinberg Operator signal assuming a signal strength of $\mu = 1$

Bibliography

[1] Murray Gell-Mann. "A Schematic Model of Baryons and Mesons". In: *Phys. Lett.* 8 (1964), pp. 214–215. DOI: 10.1016/S0031-9163(64)92001-3.

[2] G Zweig. *An SU_3 model for strong interaction symmetry and its breaking; Version 1.* Tech. rep. CERN-TH-401. Geneva: CERN, Jan. 1964. URL: https://cds.cern.ch/record/352337.

[3] G Zweig. "An SU_3 model for strong interaction symmetry and its breaking; Version 2". In: CERN-TH-412 (Feb. 1964). Version 1 is CERN preprint 8182/TH.401, Jan. 17, 1964, 80 p. URL: https://cds.cern.ch/record/570209.

[4] Steven Weinberg. "A Model of Leptons". In: *Phys. Rev. Lett.* 19 (1967), pp. 1264–1266. DOI: 10.1103/PhysRevLett.19.1264.

[5] Abdus Salam and John Clive Ward. "Electromagnetic and weak interactions". In: *Phys. Lett.* 13 (1964), pp. 168–171. DOI: 10.1016/0031-9163(64)90711-5.

[6] Makoto Kobayashi and Toshihide Maskawa. "CP Violation in the Renormalizable Theory of Weak Interaction". In: *Prog. Theor. Phys.* 49.KUNS-242 (1973), pp. 652–657. DOI: 10.1143/PTP.49.652.

[7] F. Englert and R. Brout. "Broken Symmetry and the Mass of Gauge Vector Mesons". In: *Phys. Rev. Lett.* 13 (1964). Ed. by J. C. Taylor, pp. 321–323. DOI: 10.1103/PhysRevLett.13.321.

[8] Peter W. Higgs. "Broken Symmetries and the Masses of Gauge Bosons". In: *Phys. Rev. Lett.* 13 (1964). Ed. by J. C. Taylor, pp. 508–509. DOI: 10.1103/PhysRevLett.13.508.

[9] G. S. Guralnik, C. R. Hagen and T. W. B. Kibble. "Global Conservation Laws and Massless Particles". In: *Phys. Rev. Lett.* 13 (1964). Ed. by J. C. Taylor, pp. 585–587. DOI: 10.1103/PhysRevLett.13.585.

[10] M. Banner et al. "Observation of Single Isolated Electrons of High Transverse Momentum in Events with Missing Transverse Energy at the CERN anti-p p Collider". In: *Phys. Lett. B* 122.CERN-EP-83-25 (1983), pp. 476–485. DOI: 10.1016/0370-2693(83)91605-2.

[11] G. Arnison et al. "Experimental Observation of Isolated Large Transverse Energy Electrons with Associated Missing Energy at $\sqrt{s} = 540$ GeV". In: *Phys. Lett. B* 122.CERN-EP-83-13 (1983), pp. 103–116. DOI: 10.1016/0370-2693(83)91177-2.

[12] G. Arnison et al. "Experimental Observation of Lepton Pairs of Invariant Mass Around 95-GeV/c**2 at the CERN SPS Collider". In: *Phys. Lett. B* 126.CERN-EP-83-73 (1983), pp. 398–410. DOI: 10.1016/0370-2693(83)90188-0.

[13] F. Abe et al. "Observation of top quark production in $\bar{p}p$ collisions". In: *Phys. Rev. Lett.* 74.FERMILAB-PUB-95-022-E, CDF-PUB-TOP-PUBLIC-3040, ANL-HEP-PR-95-44 (1995), pp. 2626–2631. DOI: 10.1103/PhysRevLett.74.2626. arXiv: hep-ex/9503002.

[14] S. Abachi et al. "Observation of the top quark". In: *Phys. Rev. Lett.* 74.FERMILAB-PUB-95-028-E, D0-2698, D0-PUB-95-7 (1995), pp. 2632–2637. DOI: 10.1103/PhysRevLett.74.2632. arXiv: hep-ex/9503003.

[15] Georges Aad et al. "Observation of a new particle in the search for the Standard Model Higgs boson with the ATLAS detector at the LHC". In: *Phys. Lett. B* 716.CERN-PH-EP-2012-218 (2012), pp. 1–29. DOI: 10.1016/j.physletb.2012.08.020. arXiv: 1207.7214 [hep-ex].

[16] Serguei Chatrchyan et al. "Observation of a New Boson at a Mass of 125 GeV with the CMS Experiment at the LHC". In: *Phys. Lett. B* 716.CMS-HIG-12-028, CERN-PH-EP-2012-220 (2012), pp. 30–61. DOI: 10.1016/j.physletb.2012.08.021. arXiv: 1207.7235 [hep-ex].

[17] Vera C. Rubin and W. Kent Ford Jr. "Rotation of the Andromeda Nebula from a Spectroscopic Survey of Emission Regions". In: *Astrophys. J.* 159 (1970), pp. 379–403. DOI: 10.1086/150317.

[18] Y. Fukuda et al. "Evidence for oscillation of atmospheric neutrinos". In: *Phys. Rev. Lett.* 81.BU-98-17, ICRR-REPORT-422-98-18, UCI-98-8, KEK-PREPRINT-98-95, LSU-HEPA-5-98, UMD-98-003, SBHEP-98-5, TKU-PAP-98-06, TIT-HPE-98-09 (1998), pp. 1562–1567. DOI: 10.1103/PhysRevLett.81.1562. arXiv: hep-ex/9807003.

[19] B. Pontecorvo. "Neutrino Experiments and the Problem of Conservation of Leptonic Charge". In: *Zh. Eksp. Teor. Fiz.* 53 (1967), pp. 1717–1725.

[20] M. Aker et al. "Direct neutrino-mass measurement with sub-electronvolt sensitivity". In: *Nature Phys.* 18.2 (2022), pp. 160–166. DOI: 10.1038/s41567-021-01463-1. arXiv: 2105.08533 [hep-ex].

[21] M. Agostini et al. "Final Results of GERDA on the Search for Neutrinoless Double-β Decay". In: *Phys. Rev. Lett.* 125.25 (2020), p. 252502. DOI: 10.1103/PhysRevLett.125.252502. arXiv: 2009.06079 [nucl-ex].

[22] K. H. Ackermann et al. "The GERDA experiment for the search of $0\nu\beta\beta$ decay in ^{76}Ge". In: *Eur. Phys. J. C* 73.3 (2013), p. 2330. DOI: 10.1140/epjc/s10052-013-2330-0. arXiv: 1212.4067 [physics.ins-det].

[23] M. Agostini et al. "Upgrade for Phase II of the Gerda experiment". In: *Eur. Phys. J. C* 78.5 (2018), p. 388. DOI: 10.1140/epjc/s10052-018-5812-2. arXiv: 1711.01452 [physics.ins-det].

[24] Benjamin Fuks et al. "Majorana neutrinos in same-sign $W^{\pm}W^{\pm}$ scattering at the LHC: Breaking the TeV barrier". In: *Phys. Rev. D* 103.5 (2021), p. 055005. DOI: 10.1103/PhysRevD.103.055005. arXiv: 2011.02547 [hep-ph].

[25] Benjamin Fuks et al. "Probing the Weinberg operator at colliders". In: *Phys. Rev. D* 103.11 (2021), p. 115014. DOI: 10.1103/PhysRevD.103.115014. arXiv: 2012.09882 [hep-ph].

[26] Georges Aad et al. "Search for Majorana neutrinos in same-sign WW scattering events from pp collisions at $\sqrt{s} = 13$ TeV". In: *Eur. Phys. J. C* 83.9 (2023), p. 824. DOI: 10.1140/epjc/s10052-023-11915-y. arXiv: 2305.14931 [hep-ex].

[27] S. L. Glashow. "Partial Symmetries of Weak Interactions". In: *Nucl. Phys.* 22 (1961), pp. 579–588. DOI: 10.1016/0029-5582(61)90469-2.

[28] "Standard Model Summary Plots October 2023". In: (2023).

[29] CMS Collaboration. *CMS Standard Model summary plots*. 11th Nov. 2023. URL: https://twiki.cern.ch/twiki/bin/view/CMSPublic/PhysicsResultsCombined.

[30] K. Abe et al. "Evidence of Electron Neutrino Appearance in a Muon Neutrino Beam". In: *Phys. Rev. D* 88.3 (2013), p. 032002. DOI: 10.1103/PhysRevD.88.032002. arXiv: 1304.0841 [hep-ex].

[31] Y. Abe et al. "Indication of Reactor $\bar{\nu}_e$ Disappearance in the Double Chooz Experiment". In: *Phys. Rev. Lett.* 108 (2012), p. 131801. DOI: 10.1103/PhysRevLett.108.131801. arXiv: 1112.6353 [hep-ex].

[32] N. Agafonova et al. "Observation of a first ν_τ candidate in the OPERA experiment in the CNGS beam". In: *Phys. Lett. B* 691 (2010), pp. 138–145. DOI: 10.1016/j.physletb.2010.06.022. arXiv: 1006.1623 [hep-ex].

[33] Q. R. Ahmad et al. "Measurement of the rate of $\nu_e + d \to p + p + e^-$ interactions produced by ^{8}B solar neutrinos at the Sudbury Neutrino Observatory". In: *Phys. Rev. Lett.* 87.UPR-0240E (2001), p. 071301. DOI: 10.1103/PhysRevLett.87.071301. arXiv: nucl-ex/0106015.

[34] Steven Weinberg. "Baryon and Lepton Nonconserving Processes". In: *Phys. Rev. Lett.* 43.HUTP-79-A050 (1979), pp. 1566–1570. DOI: 10.1103/PhysRevLett.43.1566.

[35] Yi Cai et al. "From the trees to the forest: a review of radiative neutrino mass models". In: *Front. in Phys.* 5 (2017), p. 63. DOI: 10.3389/fphy.2017.00063. arXiv: 1706.08524 [hep-ph].

[36] "LHC Machine". In: *JINST* 3 (2008). Ed. by Lyndon Evans and Philip Bryant, S08001. DOI: 10.1088/1748-0221/3/08/S08001.

[37] Esma Mobs. "The CERN accelerator complex - August 2018. Complexe des accélérateurs du CERN - Août 2018". In: (2018). General Photo. URL: https://cds.cern.ch/record/2636343.

[38] G. Aad et al. "The ATLAS Experiment at the CERN Large Hadron Collider". In: *JINST* 3 (2008), S08003. DOI: 10.1088/1748-0221/3/08/S08003.

[39] M. Capeans et al. "ATLAS Insertable B-Layer Technical Design Report". In: CERN-LHCC-2010-013, ATLAS-TDR-19 (Sept. 2010).

[40] "ATLAS Insertable B-Layer Technical Design Report Addendum". In: CERN-LHCC-2012-009, ATLAS-TDR-19-ADD-1 (May 2012).

[41] Georges Aad et al. "Operation of the ATLAS trigger system in Run 2". In: *JINST* 15.10 (2020), P10004. DOI: 10.1088/1748-0221/15/10/P10004. arXiv: 2007.12539 [physics.ins-det].

[42] Georges Aad et al. "ATLAS data quality operations and performance for 2015–2018 data-taking". In: *JINST* 15.04 (2020), P04003. DOI: 10.1088/1748-0221/15/04/P04003. arXiv: 1911.04632 [physics.ins-det].

[43] T. Cornelissen et al. "Concepts, Design and Implementation of the ATLAS New Tracking (NEWT)". In: ATL-SOFT-PUB-2007-007, ATL-COM-SOFT-2007-002 (Mar. 2007). Ed. by A. Salzburger.

[44] M. Aaboud et al. "Performance of the ATLAS Track Reconstruction Algorithms in Dense Environments in LHC Run 2". In: *Eur. Phys. J. C* 77.10 (2017), p. 673. DOI: 10.1140/epjc/s10052-017-5225-7. arXiv: 1704.07983 [hep-ex].

[45] "Performance of primary vertex reconstruction in proton-proton collisions at $\sqrt{s}$ =7 TeV in the ATLAS experiment". In: ATLAS-CONF-2010-069 (July 2010).

[46] R. Fruhwirth, W. Waltenberger and P. Vanlaer. "Adaptive vertex fitting". In: *J. Phys. G* 34.CERN-CMS-NOTE-2007-008, CMS-NOTE-2007-008 (2007), N343. DOI: 10.1088/0954-3899/34/12/N01.

[47] Georges Aad et al. "Topological cell clustering in the ATLAS calorimeters and its performance in LHC Run 1". In: *Eur. Phys. J. C* 77.CERN-PH-EP-2015-304 (2017), p. 490. DOI: 10.1140/epjc/s10052-017-5004-5. arXiv: 1603.02934 [hep-ex].

[48] Georges Aad et al. "Electron and photon performance measurements with the ATLAS detector using the 2015–2017 LHC proton-proton collision data". In: *JINST* 14.12 (2019), P12006. DOI: 10.1088/1748-0221/14/12/P12006. arXiv: 1908.00005 [hep-ex].

[49] Morad Aaboud et al. "Electron reconstruction and identification in the ATLAS experiment using the 2015 and 2016 LHC proton-proton collision data at $\sqrt{s}$ = 13 TeV". In: *Eur. Phys. J. C* 79.8 (2019), p. 639. DOI: 10.1140/epjc/s10052-019-7140-6. arXiv: 1902.04655 [physics.ins-det].

[50] Georges Aad et al. "Muon reconstruction and identification efficiency in ATLAS using the full Run 2 *pp* collision data set at $\sqrt{s}$ = 13 TeV". In: *Eur. Phys. J. C* 81.7 (2021), p. 578. DOI: 10.1140/epjc/s10052-021-09233-2. arXiv: 2012.00578 [hep-ex].

[51] Morad Aaboud et al. "Jet reconstruction and performance using particle flow with the ATLAS Detector". In: *Eur. Phys. J. C* 77.7 (2017), p. 466. DOI: 10.1140/epjc/s10052-017-5031-2. arXiv: 1703.10485 [hep-ex].

[52] Matteo Cacciari, Gavin P. Salam and Gregory Soyez. "The anti-k_t jet clustering algorithm". In: *JHEP* 04.LPTHE-07-03 (2008), p. 063. DOI: 10.1088/1126-6708/2008/04/063. arXiv: 0802.1189 [hep-ph].

[53] S. Catani et al. "Longitudinally invariant K_t clustering algorithms for hadron hadron collisions". In: *Nucl. Phys. B* 406.CERN-TH-6775-93, LU-TP-93-2 (1993), pp. 187–224. DOI: 10.1016/0550-3213(93)90166-M.

[54] Yuri L. Dokshitzer et al. "Better jet clustering algorithms". In: *JHEP* 08.CAVENDISH-HEP-97-06 (1997), p. 001. DOI: 10.1088/1126-6708/1997/08/001. arXiv: hep-ph/9707323.

[55] M. Wobisch and T. Wengler. "Hadronization corrections to jet cross-sections in deep inelastic scattering". In: *Workshop on Monte Carlo Generators for HERA Physics (Plenary Starting Meeting)*. PITHA-99-16. Apr. 1998, pp. 270–279. arXiv: hep-ph/9907280.

[56] Georges Aad et al. "Jet energy scale and resolution measured in proton–proton collisions at $\sqrt{s} = 13$ TeV with the ATLAS detector". In: *Eur. Phys. J. C* 81.8 (2021), p. 689. DOI: 10.1140/epjc/s10052-021-09402-3. arXiv: 2007.02645 [hep-ex].

[57] Georges Aad et al. "Performance of pile-up mitigation techniques for jets in pp collisions at $\sqrt{s} = 8$ TeV using the ATLAS detector". In: *Eur. Phys. J. C* 76.11 (2016), p. 581. DOI: 10.1140/epjc/s10052-016-4395-z. arXiv: 1510.03823 [hep-ex].

[58] *Forward jet vertex tagging using the particle flow algorithm*. Tech. rep. All figures including auxiliary figures are available at https://atlas.web.cern.ch/Atlas/GROUPS/PHYSICS/PUB PHYS-PUB-2019-026. Geneva: CERN, 2019. URL: http://cds.cern.ch/record/2683100.

[59] "ATLAS flavour-tagging algorithms for the LHC Run 2 pp collision dataset". In: CERN-EP-2022-226 (Nov. 2022). arXiv: 2211.16345 [physics.data-an].

[60] *E_T^{miss} performance in the ATLAS detector using 2015-2016 LHC pp collisions*. Tech. rep. ATLAS-CONF-2018-023. June 2018. URL: http://cds.cern.ch/record/2625233?ln=en.

[61] *Object-based missing transverse momentum significance in the ATLAS detector*. Tech. rep. ATLAS-CONF-2018-038. July 2018. URL: http://cds.cern.ch/record/2630948?ln=en.

[62] *Technical Design Report for the ATLAS Inner Tracker Strip Detector*. Tech. rep. CERN-LHCC-2017-005. Geneva: CERN, Apr. 2017. URL: http://cds.cern.ch/record/2257755.

[63] *QC: Thermal/Electrical QC Proc. - Modules*. Tech. rep. EDMS 2228451. CERN, 2022. URL: https://edms.cern.ch/document/2228451.

[64] *Dyneo DD. Einhänge-, Bad- Kältethermostate. Bedienungsanleitung*. Julabo. Seelbach, Germany. URL: https://www.julabo.com/sites/default/files/betriebsanleitung/1.950.1300.de.V06.pdf.

[65] *ETH-127-14-15-S Peltier cooler module*. European Thermodynamics. Market Harborough, England. URL: https://www.europeanthermodynamics.com/products/datasheets/4-ETH-127-14-15-S.pdf.

[66] *CPX 400DP Instruction Manual*. Thurlby Thandar Instruments. Huntingdon, England. URL: https://resources.aimtti.com/manuals/CPX400DP_Instruction_Manual-Iss1.pdf.

[67] *DuPont Kapton. Summary of Properties*. DuPont de Nemours Inc. Jan. 2022. URL: https://www.dupont.com/content/dam/dupont/amer/us/en/ei-transformation/public/documents/en/EI-10142_Kapton-Summary-of-Properties.pdf.

[68] *Insulators TCIN Series 5,0 W/m*K*. MTC Micro Tech Components. Dillingen. URL: https://www.mtc.de/sites/default/files/tables/data_sheets/tcin_50s45f.pdf.

[69] *PM2812 Users Manual*. Fluke Philipps. URL: http://manuals.chudov.com/Fluke-PM2813-User-Manual.pdf.

[70] Alessia Renardi. "The silicon strip detector of the ATLAS Inner Tracker: from individual sensing units to multi-module petal structures". Dissertation, University of Dortmund, 2022. Dissertation. Hamburg: University of Dortmund, 2022, p. 153. DOI: 10.3204/PUBDB-2022-01931. URL: https://bib-pubdb1.desy.de/record/477203.

[71] Graham Beck et al. "Thermo-electrical modelling of the ATLAS ITk Strip Detector". In: *Nucl. Instrum. Meth. A* 969 (2020), p. 164023. DOI: 10.1016/j.nima.2020.164023. arXiv: 2003.00055 [physics.ins-det].

[72] *Die Temperierflüssigkeiten*. Julabo. Seelbach, Germany. URL: https://m.europages.com/filestore/gallery/89/c/19757340_62f5e1c7.pdf.

[73] Brianna J. Mount, Matthew Redshaw and Edmund G. Myers. "Double-beta-decay Q values of Se-74 and Ge-76". In: *Phys. Rev. C* 81 (2010), p. 032501. DOI: 10.1103/PhysRevC.81.032501.

[74] J. Schechter and J. W. F. Valle. "Neutrinoless Double beta Decay in SU(2) x U(1) Theories". In: *Phys. Rev. D* 25 (1982), p. 2951. DOI: 10.1103/PhysRevD.25.2951.

[75] G. Aad et al. "Search for Heavy Neutral Leptons in Decays of W Bosons Using a Dilepton Displaced Vertex in s=13 TeV pp Collisions with the ATLAS Detector". In: *Phys. Rev. Lett.* 131.6 (2023), p. 061803. DOI: 10.1103/PhysRevLett.131.061803. arXiv: 2204.11988 [hep-ex].

[76] Armen Tumasyan et al. "Search for long-lived heavy neutral leptons with displaced vertices in proton-proton collisions at $\sqrt{s}$ =13 TeV". In: *JHEP* 07 (2022), p. 081. DOI: 10.1007/JHEP07(2022)081. arXiv: 2201.05578 [hep-ex].

[77] Georges Aad et al. "Search for heavy neutral leptons in decays of W bosons produced in 13 TeV pp collisions using prompt and displaced signatures with the ATLAS detector". In: *JHEP* 10 (2019), p. 265. DOI: 10.1007/JHEP10(2019)265. arXiv: 1905.09787 [hep-ex].

[78] Albert M Sirunyan et al. "Search for heavy Majorana neutrinos in same-sign dilepton channels in proton-proton collisions at $\sqrt{s}$ = 13 TeV". In: *JHEP* 01.CMS-EXO-17-028, CERN-EP-2018-159 (2019), p. 122. DOI: 10.1007/JHEP01(2019)122. arXiv: 1806.10905 [hep-ex].

[79] Prateek Agrawal et al. "Feebly-interacting particles: FIPs 2020 workshop report". In: *Eur. Phys. J. C* 81.11 (2021), p. 1015. DOI: 10.1140/epjc/s10052-021-09703-7. arXiv: 2102.12143 [hep-ph].

[80] E. G. Myers et al. "Atomic Masses of Tritium and Helium-3". In: *Phys. Rev. Lett.* 114.1 (2015), p. 013003. DOI: 10.1103/PhysRevLett.114.013003.

[81] Arthur Loureiro et al. "On The Upper Bound of Neutrino Masses from Combined Cosmological Observations and Particle Physics Experiments". In: *Phys. Rev. Lett.* 123.8 (2019), p. 081301. DOI: 10.1103/PhysRevLett.123.081301. arXiv: 1811.02578 [astro-ph.CO].

[82] Enrique Fernandez-Martinez, Josu Hernandez-Garcia and Jacobo Lopez-Pavon. "Global constraints on heavy neutrino mixing". In: *JHEP* 08 (2016), p. 033. DOI: 10.1007/JHEP08(2016)033. arXiv: 1605.08774 [hep-ph].

[83] J. Alwall et al. "The automated computation of tree-level and next-to-leading order differential cross sections, and their matching to parton shower simulations". In: *JHEP* 07.CERN-PH-TH-2014-064, CP3-14-18, LPN14-066, MCNET-14-09, ZU-TH-14-14 (2014), p. 079. DOI: 10.1007/JHEP07(2014)079. arXiv: 1405.0301 [hep-ph].

[84] Celine Degrande et al. "Fully-Automated Precision Predictions for Heavy Neutrino Production Mechanisms at Hadron Colliders". In: *Phys. Rev. D* 94.5 (2016), p. 053002. DOI: 10.1103/PhysRevD.94.053002. arXiv: 1602.06957 [hep-ph].

[85] Anupama Atre et al. "The Search for Heavy Majorana Neutrinos". In: *JHEP* 05.FERMILAB-PUB-08-086-T, NSF-KITP-08-54, MADPH-06-1466, DCPT-07-198, IPPP-07-99 (2009), p. 030. DOI: 10.1088/1126-6708/2009/05/030. arXiv: 0901.3589 [hep-ph].

[86] Daniel Alva, Tao Han and Richard Ruiz. "Heavy Majorana neutrinos from $W\gamma$ fusion at hadron colliders". In: *JHEP* 02.PITT-PACC-1407 (2015), p. 072. DOI: 10.1007/JHEP02(2015)072. arXiv: 1411.7305 [hep-ph].

[87] Torbjörn Sjöstrand et al. "An introduction to PYTHIA 8.2". In: *Comput. Phys. Commun.* 191.LU-TP-14-36, MCNET-14-22, CERN-PH-TH-2014-190, FERMILAB-PUB-14-316-CD, DESY-14-178, SLAC-PUB-16122 (2015), pp. 159–177. DOI: 10.1016/j.cpc.2015.01.024. arXiv: 1410.3012 [hep-ph].

[88] Rikkert Frederix and Stefano Frixione. "Merging meets matching in MC@NLO". In: *JHEP* 12 (2012), p. 061. DOI: 10.1007/JHEP12(2012)061. arXiv: 1209.6215 [hep-ph].

[89] Eric Conte, Benjamin Fuks and Guillaume Serret. "MadAnalysis 5, A User-Friendly Framework for Collider Phenomenology". In: *Comput. Phys. Commun.* 184 (2013), pp. 222–256. DOI: 10.1016/j.cpc.2012.09.009. arXiv: 1206.1599 [hep-ph].

[90] Eric Conte et al. "Designing and recasting LHC analyses with MadAnalysis 5". In: *Eur. Phys. J. C* 74.10 (2014), p. 3103. DOI: 10.1140/epjc/s10052-014-3103-0. arXiv: 1405.3982 [hep-ph].

[91] Eric Conte and Benjamin Fuks. "Confronting new physics theories to LHC data with MADANALYSIS 5". In: *Int. J. Mod. Phys. A* 33.28 (2018), p. 1830027. DOI: 10.1142/S0217751X18300272. arXiv: 1808.00480 [hep-ph].

[92] J. de Favereau et al. "DELPHES 3, A modular framework for fast simulation of a generic collider experiment". In: *JHEP* 02 (2014), p. 057. DOI: 10.1007/JHEP02(2014)057. arXiv: 1307.6346 [hep-ex].

[93] *Formulae for Estimating Significance*. Tech. rep. ATL-PHYS-PUB-2020-025. All figures including auxiliary figures are available at https://atlas.web.cern.ch/Atlas/GROUPS/PHYSICS/PUBNOTES/ATL-PHYS-PUB-2020-025. Geneva: CERN, Sept. 2020. URL: http://cds.cern.ch/record/2736148.

[94] S. S. Wilks. "The Large-Sample Distribution of the Likelihood Ratio for Testing Composite Hypotheses". In: *The Annals of Mathematical Statistics* 9.1 (1938), pp. 60–62. DOI: 10.1214/aoms/1177732360. URL: https://doi.org/10.1214/aoms/1177732360.

[95] Morad Aaboud et al. "Observation of electroweak production of a same-sign W boson pair in association with two jets in pp collisions at $\sqrt{s} = 13$ TeV with the ATLAS detector". In: *Phys. Rev. Lett.* 123.16 (2019), p. 161801. DOI: 10.1103/PhysRevLett.123.161801. arXiv: 1906.03203 [hep-ex].

[96] Albert M Sirunyan et al. "Measurements of production cross sections of WZ and same-sign WW boson pairs in association with two jets in proton-proton collisions at $\sqrt{s} = 13$ TeV". In: *Phys. Lett. B* 809 (2020), p. 135710. DOI: 10.1016/j.physletb.2020.135710. arXiv: 2005.01173 [hep-ex].

[97] Albert M Sirunyan et al. "Search for heavy neutral leptons in events with three charged leptons in proton-proton collisions at $\sqrt{s} = 13$ TeV". In: *Phys. Rev. Lett.* 120.22 (2018), p. 221801. DOI: 10.1103/PhysRevLett.120.221801. arXiv: 1802.02965 [hep-ex].

[98] Benjamin Fuks et al. "Sleptons without Hadrons". In: *Phys. Rev. D* 100.7 (2019), p. 074010. DOI: 10.1103/PhysRevD.100.074010. arXiv: 1901.09937 [hep-ph].

[99] Silvia Pascoli, Richard Ruiz and Cedric Weiland. "Heavy neutrinos with dynamic jet vetoes: multilepton searches at $\sqrt{s} = 14$, 27, and 100 TeV". In: *JHEP* 06.CP3-18-77, IPPP/18/111, PITT-PACC-1821, VBSCAN-PUB-10-18 (2019), p. 049. DOI: 10.1007/JHEP06(2019)049. arXiv: 1812.08750 [hep-ph].

[100] Silvia Pascoli, Richard Ruiz and Cedric Weiland. "Safe Jet Vetoes". In: *Phys. Lett. B* 786.IPPP/18/36, IPPP-18-36 (2018), pp. 106–113. DOI: 10.1016/j.physletb.2018.08.060. arXiv: 1805.09335 [hep-ph].

[101] Eduardo Cortina Gil et al. "Searches for lepton number violating K^+ decays". In: *Phys. Lett. B* 797 (2019), p. 134794. DOI: 10.1016/j.physletb.2019.07.041. arXiv: 1905.07770 [hep-ex].

[102] Anupama Atre, Vernon Barger and Tao Han. "Upper bounds on lepton-number violating processes". In: *Phys. Rev. D* 71 (2005), p. 113014. DOI: 10.1103/PhysRevD.71.113014. arXiv: hep-ph/0502163.

[103] Ivan Esteban et al. "The fate of hints: updated global analysis of three-flavor neutrino oscillations". In: *JHEP* 09 (2020), p. 178. DOI: 10.1007/JHEP09(2020)178. arXiv: 2007.14792 [hep-ph].

[104] Roel Aaij et al. "Physics case for an LHCb Upgrade II - Opportunities in flavour physics, and beyond, in the HL-LHC era". In: (Aug. 2018). arXiv: 1808.08865 [hep-ex].

[105] Morad Aaboud et al. "Performance of the ATLAS Trigger System in 2015". In: *Eur. Phys. J. C* 77.5 (2017), p. 317. DOI: 10.1140/epjc/s10052-017-4852-3. arXiv: 1611.09661 [hep-ex].

[106] Georges Aad et al. "Performance of the ATLAS muon triggers in Run 2". In: *JINST* 15.09 (2020), P09015. DOI: 10.1088/1748-0221/15/09/p09015. arXiv: 2004.13447 [physics.ins-det].

[107] G. Aad et al. "The ATLAS Simulation Infrastructure". In: *Eur. Phys. J. C* 70 (2010), pp. 823–874. DOI: 10.1140/epjc/s10052-010-1429-9. arXiv: 1005.4568 [physics.ins-det].

[108] S. Agostinelli et al. "GEANT4–a simulation toolkit". In: *Nucl. Instrum. Meth. A* 506 (2003), pp. 250–303. DOI: 10.1016/S0168-9002(03)01368-8.

[109] Richard D. Ball et al. "Parton distributions for the LHC Run II". In: *JHEP* 04 (2015), p. 040. DOI: 10.1007/JHEP04(2015)040. arXiv: 1410.8849 [hep-ph].

[110] "The Pythia 8 A3 tune description of ATLAS minimum bias and inelastic measurements incorporating the Donnachie-Landshoff diffractive model". In: (Aug. 2016).

[111] "ATLAS Pythia 8 tunes to 7 TeV data". In: (Nov. 2014).

[112] D. J. Lange. "The EvtGen particle decay simulation package". In: *Nucl. Instrum. Meth. A* 462 (2001). Ed. by S. Erhan, P. Schlein and Y. Rozen, pp. 152–155. DOI: 10.1016/S0168-9002(01)00089-4.

[113] Baptiste Cabouat and Torbjörn Sjöstrand. "Some Dipole Shower Studies". In: *Eur. Phys. J. C* 78.3 (2018), p. 226. DOI: 10.1140/epjc/s10052-018-5645-z. arXiv: 1710.00391 [hep-ph].

[114] Michael Rauch and Simon Plätzer. "Parton Shower Matching Systematics in Vector-Boson-Fusion WW Production". In: *Eur. Phys. J. C* 77.5 (2017), p. 293. DOI: 10.1140/epjc/s10052-017-4860-3. arXiv: 1605.07851 [hep-ph].

[115] Barbara Jager, Alexander Karlberg and Johannes Scheller. "Parton-shower effects in electroweak $WZjj$ production at the next-to-leading order of QCD". In: *Eur. Phys. J. C* 79.3 (2019), p. 226. DOI: 10.1140/epjc/s10052-019-6736-1. arXiv: 1812.05118 [hep-ph].

[116] Johannes Bellm et al. "Herwig 7.0/Herwig++ 3.0 release note". In: *Eur. Phys. J. C* 76.4 (2016), p. 196. DOI: 10.1140/epjc/s10052-016-4018-8. arXiv: 1512.01178 [hep-ph].

[117] Enrico Bothmann et al. "Event Generation with Sherpa 2.2". In: *SciPost Phys.* 7.3 (2019), p. 034. DOI: 10.21468/SciPostPhys.7.3.034. arXiv: 1905.09127 [hep-ph].

[118] Tanju Gleisberg and Stefan Hoeche. "Comix, a new matrix element generator". In: *JHEP* 12 (2008), p. 039. DOI: 10.1088/1126-6708/2008/12/039. arXiv: 0808.3674 [hep-ph].

[119] Steffen Schumann and Frank Krauss. "A Parton shower algorithm based on Catani-Seymour dipole factorisation". In: *JHEP* 03 (2008), p. 038. DOI: 10.1088/1126-6708/2008/03/038. arXiv: 0709.1027 [hep-ph].

[120] Stefan Hoeche et al. "A critical appraisal of NLO+PS matching methods". In: *JHEP* 09 (2012), p. 049. DOI: 10.1007/JHEP09(2012)049. arXiv: 1111.1220 [hep-ph].

[121] Stefan Hoeche et al. "QCD matrix elements + parton showers: The NLO case". In: *JHEP* 04 (2013), p. 027. DOI: 10.1007/JHEP04(2013)027. arXiv: 1207.5030 [hep-ph].

[122] S. Catani et al. "QCD matrix elements + parton showers". In: *JHEP* 11 (2001), p. 063. DOI: 10.1088/1126-6708/2001/11/063. arXiv: hep-ph/0109231.

[123] Stefan Hoeche et al. "QCD matrix elements and truncated showers". In: *JHEP* 05 (2009), p. 053. DOI: 10.1088/1126-6708/2009/05/053. arXiv: 0903.1219 [hep-ph].

[124] Federico Buccioni et al. "OpenLoops 2". In: *Eur. Phys. J. C* 79.10 (2019), p. 866. DOI: 10.1140/epjc/s10052-019-7306-2. arXiv: 1907.13071 [hep-ph].

[125] Fabio Cascioli, Philipp Maierhofer and Stefano Pozzorini. "Scattering Amplitudes with Open Loops". In: *Phys. Rev. Lett.* 108 (2012), p. 111601. DOI: 10.1103/PhysRevLett.108.111601. arXiv: 1111.5206 [hep-ph].

[126] Ansgar Denner, Stefan Dittmaier and Lars Hofer. "Collier: a fortran-based Complex One-Loop LIbrary in Extended Regularizations". In: *Comput. Phys. Commun.* 212 (2017), pp. 220–238. DOI: 10.1016/j.cpc.2016.10.013. arXiv: 1604.06792 [hep-ph].

[127] Simone Alioli et al. "A general framework for implementing NLO calculations in shower Monte Carlo programs: the POWHEG BOX". In: *JHEP* 06 (2010), p. 043. DOI: 10.1007/JHEP06(2010)043. arXiv: 1002.2581 [hep-ph].

[128] Stefano Frixione, Paolo Nason and Carlo Oleari. "Matching NLO QCD computations with Parton Shower simulations: the POWHEG method". In: *JHEP* 11 (2007), p. 070. DOI: 10.1088/1126-6708/2007/11/070. arXiv: 0709.2092 [hep-ph].

[129] Paolo Nason. "A New method for combining NLO QCD with shower Monte Carlo algorithms". In: *JHEP* 11 (2004), p. 040. DOI: 10.1088/1126-6708/2004/11/040. arXiv: hep-ph/0409146.

[130] Hung-Liang Lai et al. "New parton distributions for collider physics". In: *Phys. Rev. D* 82 (2010), p. 074024. DOI: 10.1103/PhysRevD.82.074024. arXiv: 1007.2241 [hep-ph].

[131] Georges Aad et al. "Measurement of the Z/γ^* boson transverse momentum distribution in pp collisions at $\sqrt{s} = 7$ TeV with the ATLAS detector". In: *JHEP* 09 (2014), p. 145. DOI: 10.1007/JHEP09(2014)145. arXiv: 1406.3660 [hep-ex].

[132] J. Pumplin et al. "New generation of parton distributions with uncertainties from global QCD analysis". In: *JHEP* 07 (2002), p. 012. DOI: 10.1088/1126-6708/2002/07/012. arXiv: hep-ph/0201195.

[133] Matteo Cacciari and Gavin P. Salam. "Pileup subtraction using jet areas". In: *Phys. Lett. B* 659 (2008), pp. 119–126. DOI: 10.1016/j.physletb.2007.09.077. arXiv: 0707.1378 [hep-ph].

[134] Matteo Cacciari, Gavin P. Salam and Gregory Soyez. "The Catchment Area of Jets". In: *JHEP* 04 (2008), p. 005. DOI: 10.1088/1126-6708/2008/04/005. arXiv: 0802.1188 [hep-ph].

[135] Armen Tumasyan et al. "Probing Heavy Majorana Neutrinos and the Weinberg Operator through Vector Boson Fusion Processes in Proton-Proton Collisions at s=13 TeV". In: *Phys. Rev. Lett.* 131.1 (2023), p. 011803. DOI: 10.1103/PhysRevLett.131.011803. arXiv: 2206.08956 [hep-ex].

[136] Will Buttinger. "Asymptotic Formula for a General Double-Bounded Custom-Sided Likelihood Based Test Statistic". In: (Feb. 2013). arXiv: 1302.2799 [physics.data-an].

[137] Thomas Junk. "Confidence level computation for combining searches with small statistics". In: *Nucl. Instrum. Meth. A* 434 (1999), pp. 435–443. DOI: 10.1016/S0168-9002(99)00498-2. arXiv: hep-ex/9902006.

[138] Alexander L. Read. "Modified frequentist analysis of search results (The CL(s) method)". In: *Workshop on Confidence Limits*. Aug. 2000, pp. 81–101.

[139] R. L. Workman et al. "Review of Particle Physics". In: *PTEP* 2022 (2022), p. 083C01. DOI: 10.1093/ptep/ptac097.

[140] "Measurement of t-channel production of single top quarks and antiquarks in pp collisions at 13 TeV using the full ATLAS Run 2 dataset". In: (2023).

[141] Jerome H. Friedman. "Data Analysis Techniques for High-Energy Particle Physics". In: *3rd CERN School of Computing*. Oct. 1974, p. 271.

[142] "Luminosity determination in pp collisions at $\sqrt{s} = 13$ TeV using the ATLAS detector at the LHC". In: (Dec. 2022). arXiv: 2212.09379 [hep-ex].

[143] Barbara Jäger et al. "Parton-shower effects in Higgs production via Vector-Boson Fusion". In: *Eur. Phys. J. C* 80.8 (2020), p. 756. DOI: 10.1140/epjc/s10052-020-8326-7. arXiv: 2003.12435 [hep-ph].

Acknowledgments

Conducting the work presented on the previous pages would not have been possible without the support of various people.

First and foremost, I would like to thank my supervisor, Krisztian Peters for offering me a position as doctoral researcher and introducing me to the heavy neutrino project. His guidance and advice and our frequent discussions were what made it possible to succeed in completing the thesis. I would also like to thank Matthias Saimpert for the close collaboration. His expertise in the technical aspects of a physics analysis, always being open for my questions, greatly helped me to push forward. I also have to thank Richard Ruiz for patiently explaining the theory behind neutrino masses and helping to find a path through the weird ways of MadGraph.

My work on the coldbox would have been impossible without Sören Ahrens and Torsten Külper. Thank you for sparking my joy for laboratory work and for sharing your expertise in all things hardware. A thanks to Sergio Díez Cornell for introducing me to this project and for his advice.

I would also like to thank Jackson Barr, Nicola de Biase, Sergio Díez Cornell, Philipp Gadow, Gediminas "G" Glemža and Craig Wells for proofreading parts of this thesis. I also have to thank Mrs. von der Weihe from the Bundesagentur für Arbeit for letting me focus on completing my thesis. Without her leniency, this thesis would have been written only years later, if at all.

Finally, I express my gratitude towards my parents, Burkhard and Susanne Neundorf, for their unwavering support throughout all those years of studying. Some of the things I learned might even be useful when repairing a coffee machine.